# DEVELOPMENT OF PASSIVE DOSIMETER CASE USING OPTICAL FIBRES FOR SPACE RADIATION DETECTION



**By**

**FARID BIN BAJURI**

**Thesis Submitted to the School of Graduate Studies, Universiti Putra Malaysia, in Fulfilment of the Requirements for the Degree of Doctor of Philosophy**

**October 2024**

**FK 2024 65**

Abstract of thesis presented to the Senate of Universiti Putra Malaysia in fulfilment of the requirement for the degree of Doctor of Philosophy

**DEVELOPMENT OF PASSIVE DOSIMETER CASE USING OPTICAL FIBRES FOR SPACE RADIATION DETECTION**

By

**FARID BIN BAJURI**

**October 2024**

**Chairman : Norkhairunnisa binti Mazlan, PhD**
**Faculty : Engineering**

In the Low Earth Orbit (LEO) lies the International Space Station (ISS), Earth observation satellites and the Chinese Tiangong Space Station. Currently, the National Aeronautics and Space Administration (NASA) is actively creating LEO economy with the production, distribution, and trade of goods and services within the LEO. However, without the protection of the Earth's atmosphere, any object existing in LEO is subject to the harsh space environment, which affects its performance. When designing a casing to be placed within the LEO, engineer needs to consider the effect of ionising radiation. To monitor this, passive dosimeters can be employed alongside the casing. Advantages of passive dosimeter compared to active dosimeter are its small size and the independency on power source, making the passive dosimeters suitable to be employed for long term radiation monitoring. In this work, a passive dosimeter casing was designed which incorporates the germanium doped optical fibres (OF) as it was found to produce high thermoluminescence (TL), having good reproducibility, dose rate-independent, angular independent, irradiation temperature-independent and

low in fading rate. The passive dosimeter casing is designed by incorporating engineering design process. The passive dosimeter casing consisted of polyetheretherketone (PEEK) case where the main body has nine blind holes to place the filters and dosimeter blocks made from PEEK that held the dosimeters. Before exposing the casing to space environment, random vibration tests, static load tests and compressive tests are conducted on the assembled casing. While producing resonance and anti-resonance region starting from approximately 445 Hz in all directions that exceeds/fall below the high/low abort, the casing is not damaged after performing random vibration test and static loads test. Mechanically, the thinnest (1 mm) part of the casing would fail at lowest compressive force of 304 N with a safety factor (SF) of 1.5 or up to 600 N (SF=2.88) meaning that the casing can work even with the possibility of force from the robotic arm being applied during attachment/detachment for exposure. On the other hand, the passive dosimeters were screened using gamma (Caesium 137), irradiated with beta (Strontium 90), gamma-neutron mixed field (Americium-Beryllium), and proton (produced by accelerator) as preliminary tests. Upon assembly, the casing was exposed to space radiation outside of the ISS for 433 days. Upon retrieval, the passive dosimeters were analysed and calibrated using proton (based on linearity, energy dependency and fading analysis) to calculate the absorbed dose received during exposure. Flat fibres doped with 6 mol% Germanium (Ge) produced the highest TL signal normalised by the core volume. All dosimeters had a high coefficient of determination of $\geq 0.98$ for all type of irradiations. The dosimeters showed up to 18% reduction in TL signal after 358 days of irradiation. Upon calibration which include linearity and fading correction, the passive dosimeters are exposed to absorbed dose rate up to about 2000 μGy/day outside of ISS. In summary, a dosimetry casing to employ passive dosimeter for space exposure is successfully conducted and found OF to be operational as a passive dosimeter for radiation detector in space.

**Keywords**: Optical Fibre, Passive Dosimeter Casing, Space Radiation Monitoring, Space Exposure, Vibration

**SDG**: GOAL 9: Industry, Innovation and Infrastructure, GOAL 17: Partnerships for the Goals

Abstrak tesis yang dikemukakan kepada Senat Universiti Putra Malaysia sebagai memenuhi keperluan untuk ijazah Doktor Falsafah

**PEMBANGUNAN SELONGSONG DOSIMETER PASIF YANG MENGGUNAKAN GENTIAN OPTIK UNTUK PENGESANAN SINARAN ANGKASA LEPAS**

Oleh

**FARID BIN BAJURI**

**Januari 2024**

**Pengerusi : Norkhairunnisa binti Mazlan, PhD**
**Fakulti : Kejuruteraan**

Di dalam Orbit Bumi Rendah (LEO), terletak Stesen Angkasa Antarabangsa (ISS), satelit pemerhatian Bumi, dan Stesen Angkasa China Tiangong. Ketika ini, *National Aeronautics and Space Administration* (NASA) secara aktifnya sedang mencipta ekonomi LEO yang melibatkan pengeluaran, pengedaran, dan perdagangan barang dan perkhidmatan dalam LEO. Walau bagaimanapun, tanpa perlindungan atmosfera Bumi, mana-mana objek yang wujud dalam LEO, terdedah kepada persekitaran angkasa yang keras. Apabila merekacipta sistem untuk diletakkan dalam LEO, jurutera perlu mempertimbangkan kesan radiasi pengionan. Untuk memantaunya, meter dos pasif boleh digunakan bersama-sama dengan peranti tersebut. Kelebihan meter dos pasif berbanding meter dos aktif adalah saiznya yang kecil dan ketidakbergantungan kepada sumber kuasa, menjadikan meter dos pasif sesuai untuk pengawasan radiasi jangka panjang. Dalam kerja ini, satu sistem dosimetri pasif direka yang menggabungkan optik gentian (OF) yang didop dengan germanium sebagai meter dos pasif kerana ia didapati menghasilkan pendarkilau haba (TL) yang tinggi, mempunyai pengulangan

penghasilan yang baik, tidak bergantung kepada kadar dos, tidak bergantung kepada sudut, tidak bergantung kepada suhu sinaran, dan rendah dalam kadar pemudaran. Sistem dosimetri pasif ini direka dengan menggabungkan proses perekaan kejuruteraan. Selongsong meter dos pasif terdiri daripada kes PEEK (polietereterketon) di mana badan utamanya mempunyai sembilan lubang untuk meletakkan penapis dan blok meter dos yang diperbuat daripada PEEK yang memegang meter dos. Sebelum mendedahkan selongsong meter dos pasif kepada persekitaran angkasa lepas, ujian getaran rawak, ujian beban statik, dan ujian pemampatan dijalankan pada sistem yang dipasang. Selongsong tersebut tidak rosak selepas menjalani ujian getaran rawak dan ujian beban statik sambil menghasilkan kawasan resonans dan anti-resonans bermula dari kira-kira 445 Hz dalam semua arah yang melebihi/tidak melebihi pengunduran tinggi/rendah. Secara mekanikal, bahagian yang paling nipis (1 mm) sistem boleh gagal pada daya pemampatan terendah 304 N dengan faktor keselamatan (SF) 1.5 atau sehingga 600 N (SF = 2.88), bermakna selongsong boleh berfungsi walaupun dengan kemungkinan daya daripada lengan robot yang digunakan semasa pemasangan/pemisahan untuk pendedahan. Sementara itu, dosimeter pasif disaring menggunakan gamma (Caesium 137), disinari dengan beta (Strontium 90), medan tercampur gamma-neutron (Americium-Beryllium), dan proton (dihasilkan oleh pemecut) sebagai ujian awal. Selepas pemasangan, selongsor tersebut telah didedahkan kepada sinaran angkasa lepas di luar ISS selama 433 hari. Setelah pengutipan semula, dosimeter pasif dianalisis dan dikalibrasi menggunakan proton (berdasarkan kelelurusan, kebergantung kepada tenaga, dan analisis pemudaran) untuk mengira dos terserap yang diterima semasa pendedahan. Gentian rata yang terdop dengan 6 mol% Germanium (Ge) menghasilkan isyarat TL tertinggi yang ternormal kepada isipadu teras. Semua dosimeter mempunyai pekali penentuan

yang tinggi ≥ 0.98 untuk semua jenis radiasi. Meter dos menunjukkan penurunan sehingga 18% dalam isyarat TL 358 hari selepas sinaran. Selepas penentukuran yang mengambilkira pemadanan lelurus dan pemudaran, meter dos pasif terdedah kepada kadar dos terserap sehingga 2000 μGy/hari di luar ISS. Secara ringkasnya, dalam kerja ini, selongso meter dos pasif yang menggunakan meter dos pasif bagi pendedahan angkasa lepas telah berjaya dilaksanakan, dan menunjukkkan kebolehgunaan OF sebagai meter dos pasif sebagai pengesan sinaran di angkasa lepas.

**Kata Kunci**: Gentian Optik, Selongsong Dosimeter Pasif, Pemantauan Sinaran Angkasan Lepas, Pendedahan Angkasa Lepas, Getaran

**SDG**: MATLAMAT 9: Industri, Inovasi dan Infrastruktur, MATLAMAT 17: Perkongsian untuk Matlamat

**ACKNOWLEDGEMENTS**

This work will not be able to be completed without the help of Agensi Angkasa Negara (MySA) especially by En. Fairul, En. Ammar, Dr. Abadi, En. Helmi and Pn. Zahira. In that sense, I am extremely grateful for their kind guidance and understanding which became the steppingstone for the success of this work. Apart from that, I would like to thank everyone that directly or indirectly contributed to the completion of this thesis. Specifically, I would like to thank my supervisory committee Assoc. Prof. Dr. Norkhairunnisa binti Mazlan, Assoc. Prof. Dr. Noramaliza binti Mohd Noor, Dr. Nizam bin Tamchek, Dr. Adi Azriff bin Basri and Assoc. Prof. Dr. Nawal Aswan bin Abdul Jalil. Additionally, I would like to thank Dr. Ernnie Basri and Dr. Tay Chai Hua for their direct help in terms of proofreading or formatting of the thesis. Not to forget, Dr. Rushdi that came alongside Dr. Nawal like a hero when we were in a crisis of not being able to conduct the required tests.

Apart from people that directly contributed to my PhD, I am very grateful for the support that I have received throughout my journey. My family that is always there for me, and my friends that always listen to me when I was in distress.

皆様、どうもありがとうございました。いつかまたどこかで会いましょう。

This thesis was submitted to the Senate of Universiti Putra Malaysia and has been accepted as fulfilment of the requirement for the degree of Doctor of Philosophy. The members of the Supervisory Committee were as follows:

**Norkhairunnisa binti Mazlan, PhD**
Associate Professor Ts. Dr.
Faculty of Engineering
Universiti Putra Malaysia
(Chairman)

**Adi Azriff bin Basri, PhD**
Senior Lecturer Dr.
Faculty of Engineering
Universiti Putra Malaysia
(Member)

**Nawal Aswan bin Abdul Jalil, PhD**
Associate Professor Dr.
Faculty of Engineering
Universiti Putra Malaysia
(Member)

**Nizam bin Tamchek, PhD**
Senior Lecturer Dr.
Faculty of Science
Universiti Putra Malaysia
(Member)

**Noramaliza binti Mohd Noor, PhD**
Associate Professor Dr.
Faculty of Medicine and Health Sciences
Universiti Putra Malaysia
(Member)

**ZALILAH MOHD SHARIFF, PhD**
Professor and Dean
School of Graduate Studies
Universiti Putra Malaysia

Date: 13 March 2025

## TABLE OF CONTENTS

# LIST OF TABLES

## LIST OF FIGURES

## LIST OF ABBREVIATIONS

| | |
|---|---|
| $^{60}Co$ | Cobalt-60 |
| $^{137}Cs$ | Caesium-137 |
| $^{241}AmBe$ | Americium-Beryllium |
| A | Acceptor |
| Al | Aluminium |
| $Al_2O_3$ | Aluminium Oxide |
| ANM | Agensi Nuklear Malaysia |
| AO | Atomic Oxygen |
| ASD | Acceleration Spectral Density |
| AT | Acceptance Tests |
| CB | Conduction Band |
| CF | Cylindrical Fibre |
| CNC | Computerised Numerical Control |
| COMOF | Commercial OF |
| CR | Cosmic Radiations |
| CSA | Canadian Space Agency |
| CSDA | Continuous Slowing Down Approximation Range |
| D | Donor |
| ECR | Extragalactic CR |
| EDX | Electron Dispersive X-Ray |
| EF | Exposed Facility |
| ESA | European Space Agency |
| EVA | Extravehicular Activity |

| | |
|---|---|
| ExHAM | Exposed Experiment Handrail Attachment Mechanism |
| FEG | Forbidden Energy Gap |
| FF | Flat Fibre |
| FGMOS | Floating-Gate MOS Transistor |
| FM | Flight Model |
| GCR | Galactic Cosmic Radiation |
| Ge | Germanium |
| $GeCl_4$ | Germanium Tetrachloride |
| GeV | Gigaelectron Volt |
| $H/H_2$ | Hydrogen |
| HEO | High Earth Orbit |
| HZE | High Atomic Number Energy |
| ISS | International Space Station |
| JAXA | Japan Aerospace Exploration Agency |
| JEMRMS | Japanese Experiment Module Remote Manipulator Casing Small Fine Arm |
| SFA | Small Fine Arm |
| KLIA | Kuala Lumpur International Airport |
| LEO | Low Earth Orbit |
| LET | Linear Energy Transfer |
| LiF: Mg, Ti | Lithium Fluoride Phosphor Doped with Magnesium and Titanium |
| MCVD | Modified Chemical Vapour Deposition |
| MEMS | Micro-Electromechanical System |
| MEO | Medium Earth Orbit |
| MEVR | Maximum Effective Vent Ratio |

| | |
|---|---|
| MFS | Multifunctional Structure for Spacecraft |
| MoA | Memorandum Of Agreement |
| MYSA | Malaysian National Space Agency |
| NASA | National Aeronautics and Space Administration |
| NIST | National Institute of Standards and Technology |
| $O/O_2$ | Oxygen |
| OF | Optical Fibre |
| OSL | Optically Stimulated Luminescence |
| OSLD | Optically Stimulated Luminescence Dosimeter |
| PADLES | Passive Dosimeter for Life Science Experiment in Space |
| PD | Passive Dosimeters |
| PADCIOF | Passive Dosimetry Casing |
| PE | Polyethylene |
| PE | Polyethylene |
| PEEK | Polyether Ether Ketone |
| PL | Photoluminescence |
| PNTD | Plastic Nuclear Track Detector |
| POM | Polyoxymethylene |
| PPS | Polypropylene Sheets |
| PSD | Power Spectral Density |
| QF | High-Quality Factor |
| QT | Qualification Test |
| RadFET | Radiation Field-Effect Transistors |
| Roscosmos | Russian Federal Space Agency |
| RPLD | Radio-Photoluminescence Dosimeter |

| | |
|---|---|
| RPLD | Radiophotoluminescent Dosimeter |
| SAA | South Atlantic Anomaly |
| SDG | Sustainable Development Goal |
| SEM | Scanning Electron Microscope |
| SEP | Solar Energetic Particles/Protons |
| Si | Silicon |
| $SiCl_4$ | Silicon Tetrachloride |
| $SiO_2$ | Silica Glass |
| SOFPADS | Passive Dosimetry in Space |
| SPE | Solar Particle Events |
| SpX-17 | SpaceX Dragon CRS-17 |
| SpX-21 | SpaceX Dragon CRS-21 |
| SR | Supernova Remnants |
| Tb | Terbium |
| TKSC | Tsukuba Space Center |
| TL | Thermoluminescence |
| TLD | Thermoluminescent Dosimeter |
| TLD-MSO-S | $Mg_2SiO_4$: Tb ($Mg_2SiO_4$ doped with Tb) |
| TPS | Treatment Planning System |
| TTP | The Time-Temperature Profile |
| UV | Ultraviolet Radiation |
| VB | Valence Band |
| VLEO | Very Low Earth Orbit |
| Z | Atomic Number |
| $Z_{eff}$ | Effective Atomic Number |

# CHAPTER 1

# INTRODUCTION

## 1.1 Overview

This chapter describes the general idea of the current work. Firstly, the theoretical foundations of this research are presented in research background. Then, in the problem statement, the current situation in the development of passive dosimeter casing (PADC) incorporating optical fibre (PADCIOF) for outer space radiation exposure is discussed. The research objective is stated in the third section. The research questions are discussed in the fourth section. The scope of the thesis is described in the final section.

## 1.2 Research Background

The Earth's orbits are separated by the distance of the orbit from the Earth. Low Earth Orbit (LEO) is the orbit with the lowest altitude from the Earth's surface that is considered as outer space. Demarcation of the Earth's atmosphere and outer space is not clearly defined as there are different school of thoughts, the functionalist that considers the nature of activity rather than location to be the determinant of space boundary or the spatialist that considers the physical boundary instead (DiPaolo, 2014). The widely (not universally) accepted space boundary is called the Karman line, where generally, the altitude for space boundary is in the range of 80-100 km since the typical satellite ballistic coefficient that is independent of solar and atmospheric condition starts from 80 km altitude (McDowell, 2018). The starting altitude of low Earth orbit (LEO) is also not definite where McDowell (2020) considers it to be at 80-100 km, below which satellite could not orbit the Earth while Lu et al. (2019) defines the initial altitude of LEO at 160 km. Considering the Karman line that demarcate the atmosphere and outer space at 80-100 km and the lowest assumed altitude of LEO that overlaps with the Karman line based on McDowell (2018) and McDowell (2020), it can be concluded that LEO is an orbit that is considered as outer space closest to the Earth.

In the LEO locates the International Space Station (ISS), Earth observation satellites and the Chinese Tiangong Space Station. Satellites are placed in LEO since the orbit is suited for Internet of Things (IoT) application alongside being more accessible for crew and servicing (Kua et al., 2021). With the National Aeronautics and Space Administration (NASA) creation of LEO economy, which involves the production, distribution, and trade of goods and services within LEO, technological advances are sought to further explore and expand the solar system (Elburn, 2021).

However, without the protection of the Earth's atmosphere, any object placed in outer space, even at the low altitude of the LEO, is exposed to the harsh space environment, especially regarding ionising radiation. The sources of ionising radiation in space are cosmic rays (CR) and the solar radiation. The main constituent of CR is mostly from protons (~98%) (Shen et al., 2019). Through solar events, energetic protons and gamma radiation are also produced (Cucinotta et al., 2009; Kocharov et al., 2021). While mostly made up of protons, space radiations are mixed radiations field with photons, electrons, high atomic number (z) and energy (HZE) ions and even neutrons

(Blasi, 2013; Shen et al., 2019; Obodovskiy, 2019; Yu et al., 2015). Apart from the ionising radiation, when placing an object in LEO, the engineer must consider the vacuum, atomic oxygen (AO), ultraviolet radiation (UV), plasma, extreme temperature, thermal cycling, and orbital debris impact (Hopkins et al., 2016).

Long-term radiation monitoring mission in space is scarce and usually will use the commercial detector such as TLD-600 and TLD-700 (Berger et al., 2013; Rabbow et al., 2015; Zhou et al., 2010). To conduct a radiation monitoring mission, importance is placed on the casing that carries the radiation detector or more commonly known as dosimeter. To develop the casing, requirements need to be identified in terms of: (1) Space radiation monitoring and (2) long term space exposure.

In the aspects of radiation monitoring at LEO altitude, passive dosimeters (PD) can be used with advantages compared to active dosimeter by being relatively small and no power sources required for the PD to be operable. This makes PD suitable for long-term radiation monitoring. Optical Fibre (OF) is oftentimes used in the telecommunications industry. However, they have also been shown to work well as Thermoluminescent Dosimeter (TLD), a type of passive dosimeter. OF doped with Germanium (Ge) has been found to be high in Thermoluminescent (TL), good reproducibility, dose rate-independent, angular independent, temperature-independent, and low in fading rate (Mohd Noor et al, 2012; Mohd Noor et al, 2014). OF has been used as a TLD in various medical fields, such as photon beam dosimetry audit, radiation therapy with proton or electron beam dosimetry, phantom study, dose verification of treatment planning (TPS) and blood irradiator dosimetry using Caesium-137 ($^{137}Cs$). OF has been found to give satisfactory results compared to the commercial TLD made of Lithium Fluoride phosphor doped with Magnesium and Titanium (LiF: Mg, Ti). Up to date, OF has not been used as a TLD for space radiation detector. Therefore, this research will pave the way of a new application for OF in the realm of space radiation.

Apart from the detector itself, for space radiation monitoring, considerations should be made for material selection on the casing in terms of water equivalence of said material. This is due to human body consisting mostly of water, hence, by placing the PD in water equivalent materials, the radiation detection mimics the condition of human body (Zuber et al., 2021). Anthropomorphic phantom (materials used to assess dose distribution on human) has been employed for space radiation monitoring using the commercial TLD, TLD-600 and TLD-700 (Berger et al., 2013; Zhou et al., 2010). As such, employing water equivalent materials for the casing allows the assumption that the casing is part of human body, as such, the detected dose of the PD is similar to what will be experienced by human if they are placed in the same location as the casing.

On the other hand, in terms of long-term space exposure, various considerations should be made as apart from the space environment condition. The considerations for long-term space exposure are as follows: (1) Transport environment, (2) exposure survivability, and (3) experimental site condition.

The transport of goods to ISS is generally by using a rocket, for example the Falcon 9 rocket by SpaceX (SpaceX, 2021). For transport of human and commercial resupply services (CRS) of the ISS, the casing will be transported in a Dragon spacecraft that is attached to the rocket (SpaceX, 2021). As such, the casing will be subjected to the vibration environment within the Dragon spacecraft produced by the Falcon 9 rocket during transport to ISS and return to the Earth. The design of the casing should consider the susceptibility of the casing to the vibration environment within the Dragon CRS spacecraft where the casing is placed during transport.

In terms of long-term exposure in LEO environment, considerations should be made due to AO erosion. Some materials are more prone to AO erosion which weakens the materials the longer they are placed in the LEO environment. De Groh et al. (2006) has exposed various materials in the LEO environment for up to three years and found some materials like polyetheretherketone (PEEK), polystyrene (PS), polytetrafluoroethylene (PTFE) and polyurethane (PU) can survive the duration of exposure and have low AO erosion rate. These materials can be considered as the material for the casing, however, other specifications as mentioned in the previous paragraphs should be considered before the final material is chosen.

Lastly, the condition of the experimental site will affect the exposure condition. For example, for the utilisation of Exposed Experiment Handrail Attachment Mechanism (ExHAM) owned by Japan Aerospace Exploration Agency (JAXA), a Japanese Experiment Module Remote Manipulator System (JEMRMS) is used to attach the ExHAM to the experiment site (JAXA, 2008). The tip of the JEMRMS can damage the casing from accidental collision during transport, attachment of ExHAM and retrieval of ExHAM. As such, materials strength and casing design come into play where the casing is required to be able to withstand the tip force of the JEMRMS in the event of a collision. This work agrees with the Sustainable Development Goal

(SDG) Goal 9 industry, innovation and infrastructure where the OF used is developed specifically for radiation detection and the requirement to develop the casing that will carry and expose the PD into the space environment. Additionally, due to the large-scale nature of this work, it fostered collaborative works with various national and international agencies such as NASA, JAXA and Malaysian Space Agency (MySA) in regards for space radiation exposure, and, Agensi Nuklear Malaysia (ANM), Hyogo Ion Beam Medical Center and University of Surrey for irradiations to analyse the PD TL responses. This aligns with SDG Goal 17 to revitalize the global partnership for sustainable development.

## 1.3 Problem Statement

The critical elements of PADCIOF to space exposure is radiation monitoring in outer space and the sustainability of the casing at space environment for extended period. Prior to exposing the PADCIOF to outer space, several considerations should be taken into account such as the design of the PADCIOF, preparation of the passive dosimeters, assembly of the PADCIOF, transport of the PADCIOF to the launching station, arrival at the ISS, attachment of the PADCIOF on the experiment site, retrieval of the PADCIOF until the read-out of the TLD that is placed within the PADCIOF. Each stage has their own challenges to be overcame. For the designed PADCIOF, the complex preparation process including from the development of the PADCIOF to exposure of radiation that is notably influenced the suitable materials used.

There are several issues related to the radiation exposure of the designed PADCIOF, namely:

1. Lack of works in the requirements to expose PADCIOF at the experiment site for extended period. Hence, issues occur where the design requirements to expose a casing at the experiment site need to be clarified in the aspects of space radiation monitoring and space exposure at the experiment site.
2. Lack of works in the structural assessment of PADCIOF for the purpose of space radiation monitoring.
3. Limitation of information regarding OF capability to detect various kind of radiations specifically at low dose of environmental radiation.
4. Limitation of information on OF capability to detect space radiation.

Therefore, the current work employs the development of PADCIOF that is designed to meet the requirements of the experiment site that is applicable for space radiation monitoring. The novelty of the current research work is the development of PADCIOF to be utilised as a space radiation monitoring system. This work incorporates the usage of customised optical fibre (CUSOF) that has never been used before for space radiation detection paving a new application for CUSOF in the realm of dosimetry. The PADCIOF developed covers from the design perspective, the structural assessments of the PADCIOF that include vibrations and structural load, the assessment of CUSOF for low dose radiation detection and the assessment of CUSOF for space radiation detection.

## 1.4 Research Objective

Performance of PADC that incorporates customised optical fibres (CUSOF) for outer space radiation detection at LEO altitude has not been reported. The aim of this research is to develop a PADCIOF to detect space radiation at LEO altitude where the PADCIOF can sustain the launching, exposure condition and retrieval while allowing accurate radiation measurement by the passive dosimeters. The development of PADCIOF is influenced by considerations made radiation monitoring perspective and long-term space exposure perspective. This led to the specific objectives of this research being as follows:

1. To develop PADCIOF based on radiation monitoring requirements and space exposure at LEO requirements.
2. To assess the structural properties of the developed PADCIOF in terms of random vibration, sine-burst and structural load.
3. To evaluate the CUSOF capability to detect low dose radiations by using the beta and mixed neutron-gamma source.
4. To examine the CUSOF ability to detect space radiation by exposing the CUSOF within the PADCIOF in space.

## 1.5 Research Questions

The research questions for this work are as follows:

1. What are the requirements for the PADCIOF to conduct a space radiation monitoring mission?

2. What are the vibration conditions during launching and retrieval of PADCIOF? Do the vibrations damage PADCIOF or the passive dosimeters placed inside?
3. What is the expected failure possibility in the event of collision (from astronaut or robotic arm) occurring during outer space exposure?
4. Can CUSOF in PADCIOF be used for low dose radiation detection?
5. What are the responses of CUSOF in PADCIOF after being exposed in space?

## 1.6 Scope of Research

The scope of the research is limited to the development of PADCIOF for the utilisation of ExHAM during the space exposure. As such, the requirements for the development of PADCIOF is constrained the dimension limitation of ExHAM, weight limitation of ExHAM, and exposure method of ExHAM. This limitation expands to the assessment of the structural assessment of the developed PADCIOF where the vibration condition assessed in this work is due to the Dragon CRS spacecraft launched using the Falcon 9 rocket by SpaceX. The structural assessment in the aspect of structural load concerns the loads expected to be received by the PADCIOF during space exposure by ExHAM utilisation.

The scope of research for the PD (CUSOF and commercial TLD) that are incorporated within the PADCIOF are for the low dose beta irradiation, low dose neutron-gamma irradiations, space radiation exposure and proton irradiation. The space radiation exposure of the PD is the same as the previous paragraph. For other irradiations, these include the design of experiment to expose the PD, preparation of PD, and sample read-out of PD.

## 1.7 Thesis Outline

This thesis consists of five chapters.

Chapter 1 provides the overview of the research background, objectives, and scope of the research.

Chapter 2 provides the previous works describing the studies on on dosimeters mechanism of radiation detection of TLD. Then the environment of LEO is discussed in depth. LEO environment does not only cover on the radiation environment, but it also covers various conditions of the LEO from the temperature, vacuum, until the AO environment. This chapter also provides the ionizing radiation environment, and further discuss on the interaction of various types of radiations in LEO.

Chapter 3 discusses the methodology adopted in this research. The conceptual technique of standard method of developing and designing the PADCIOF are explained in detail. Despite that, this chapter also explain all the experimental setups involving the properties (including vibration and mechanical) and irradiation process on the developed PADCIOF.

Chapter 4 reveals the results of the fabricated PADCIOF that is analysed qualitatively and quantitatively including the calculation results of radiation attenuation. This chapter also describes the discussion on the morphology of OF, and results of irradiations. Plus, this chapter presents the parametric studies of the results of space exposed passive dosimeters alongside the calibration with proton.

Chapter 5 gives the conclusion and recommendations for future works.

# CHAPTER 2

# LITERATURE REVIEW

## 2.1 Overview

This chapter presents a comprehensive explanation of Low Earth Orbit (LEO), where the choice of materials plays important role for Passive Dosimetry Casing Incorporating Optical Fibres (PADCIOF) and its survivability in LEO environment. Then, it is followed by the discussion on the practice by International Space Station (ISS), in which various extravehicular activity (EVA) experiments that have been conducted on ISS to be used for determining the PADCIOF design. The theoretical knowledge of vibration environment of spacecraft is discussed in the fourth section. Before concluding the chapter, the passive dosimeters that used for detecting radiation and Thermo-luminescent Dosimeter (TLD) will be presented followed by remarks of the direction of the research.

## 2.2 Low Earth Orbit Exposure

To develop a casing for radiation detection at LEO of ISS altitude, considerations should be made in terms of the exposure condition and radiation sources or environment of the experiment site. Hence, in subchapter 2.2.1, a summary of the LEO environment is made to understand the conditions which will lead to the design requirements for casing to be developed for LEO exposure. In subchapter 2.2.2, reviews of exposure mission conducted for EVA is conducted.

### 2.2.1 Low Earth Orbit Environment

As also mentioned in Chapter 1 subsection 1.2, LEO is the lowest orbit considered as outer space with an altitude of 80 km to 2000 km (McDowell, 2020). Here, various satellites reside in the LEO including the ISS. The ISS orbits the Earth with an average altitude of 400 km (Kawaguchi et al., 2016). Image of ISS is presented in

Figure **2.1**. Due to the higher constant gravitational force at LEO, the ISS is maintained at the selected altitude by re-boosting by its thrusters; e.g. Figure 2.2 shows the variations of ISS altitudes between 330-410 km from its beginning until May 2014 (Murtazin and Zaborskaya, 2014).

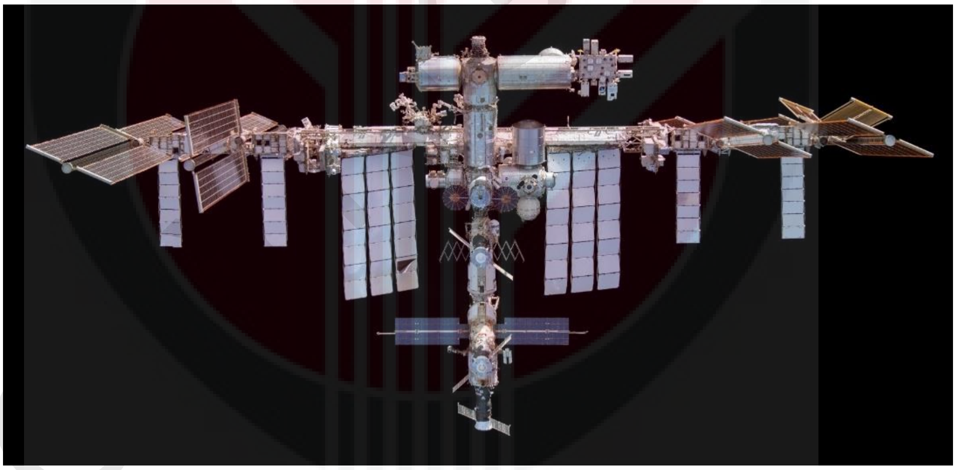

**Figure 2.1: Photograph of the ISS** (Garcia, 2024)

The ISS orbits the Earth at an inclination of 51.6°, travels at a speed of about 7.8 km/s and take about 90 minutes to orbit the Earth, producing an orbital period about 16 times a day (ESA, 2020; Furukawa et al., 2020). ISS is built by the partnership of five space agencies from 15 countries that contributed different parts to make up the ISS (Howell, 2023). The space stations that are working together are the National

Aeronautics and Space Administration (NASA), the ESA, the Canadian Space Agency (CSA), the Russian Federal Space Agency (Roscosmos), and JAXA (ESA, 2020).


**Figure 2.2: ISS altitude and solar activity from November 1998 to May 2014** (Murtazin and Zaborskaya, 2014)

Satellites orbiting at LEO altitude experience a high vacuum environment (Rabbow et al., 2017), constant atomic oxygen (AO) bombardments (Liu et al., 2016), oscillating temperature (Lei et al., 2013), low exposure to complex ionising radiation and, constant irradiation from short-wavelength solar ultraviolet (UV) radiation (Furukawa et al., 2020). Table 2.1 provides the summary of each LEO condition.

**Table 2.1: LEO environment**

| No. | Condition | Details | References |
|---|---|---|---|
| 1 | Vacuum | • Vacuum pressure of $1.33\times10^{-3}$ – $1.33\times10^{-4}$ Pa (atmospheric pressure is $1.01\times10^{5}$ Pa) during EXPOSE-R2 mission. | Rabbow et al, 2017 |
| 2 | AO | • 4.2-4.5 eV energy.<br>• $1.96\times10^{20}$ atoms/cm$^2$ for 6 months of exposure at an altitude of 500 km. | Liu et al., 2016; Wang et al., 2018 |

**Table 2.1: Continued**

| No. | Condition | Details | References |
|---|---|---|---|
| 3 | Temperature Oscillation | • Depends on location on ISS. Outside of Zvezda (Russian module of ISS) the temperature range was -24.65 to 49.47°C with internal heater within instruments.<br>• Typical cycle of ±100°C. | Berger et al.; 2015; Lei et al., 2013; Rabbow et al., 2014; Rabbow et al., 2017 |
| 4 | UV Radiation | • Include highly energetic UV-C (<285 nm wavelength) that is eliminated by stratospheric ozone layer. | Furukawa et al., 2020 |

### 2.2.2 Sources of Ionising Radiation in LEO

In this work, the PADCIOF's development is to detect radiation in the LEO specifically at ISS altitude. As such the ionising radiation environment in LEO is explored to understand the what the passive dosimeters (PD) included in PADCIOF is exposed to. The sources of radiations in outer space are from the CR and the sun producing solar energetic particles (SEP) and solar flare as shown in Figure 2.3 (Berger et al., 2017; Cucinotta et al., 2009). In LEO the harmful CR is mainly shielded by the Earth's magnetic field, called the magnetosphere (Brown et al., 2018). The Earth's radiation belts (also called Van Allen radiation belts) are the product of the Earth's magnetic field trapping charged particles from the CR and the SEP (Obodovskiy, 2019). While the radiation belt generally extends to 600 km from the Earth, a region called the South Atlantic Anomaly (SAA) of the inner radiation belt can extend to even lower altitudes due to the weakened magnetic field, hence, increasing the local particle flux (Anderson et al., 2018). As the ISS orbits the Earth approximately 16 times daily passing through SAA at regular intervals, it is exposed to strong radiation (Anderson et al., 2018).

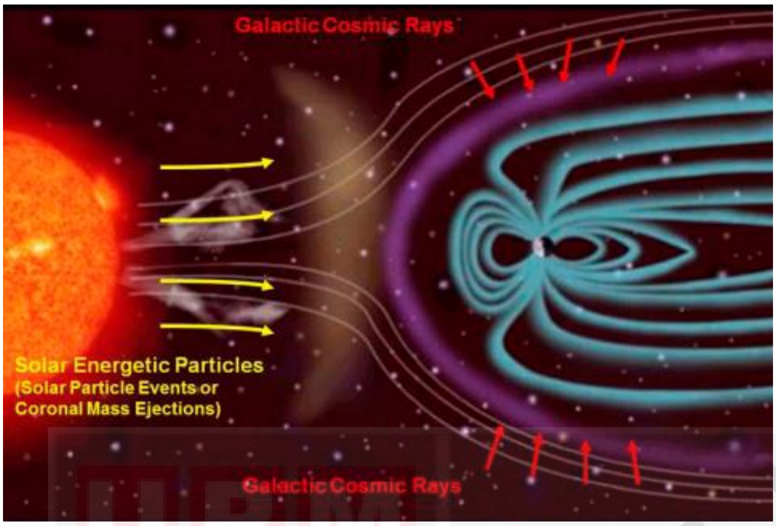


**Figure 2.3: Sources of radiations in the LEO** (Chancellor et al., 2014)

CR consists mainly of hydrogen nuclei (～98%) with some electrons and positrons (～2%), which have an energy density of about 1 eV/cm$^3$ in the Galaxy (Blasi, 2013; Shen et al., 2019). The nuclei mainly consist of approximately 90% hydrogen (H) nuclei (H nuclei consist of proton only hence can be interchangeably called as proton too), 9% helium nuclei and 1% heavier elements, generally referred to as high atomic number (Z) and energy ions (HZE ions) (Blasi, 2013; Shen et al., 2019). CR has a high flux with an intensity of about 1 particle/s.m$^2$ at ～50 GeV particle energies produced on Earth (Tjus and Merten, 2020). As illustrated in the Figure 2.4, the energy cross section of various particles produced by CR measured using the PAMELA instrument (Blasi, 2013).

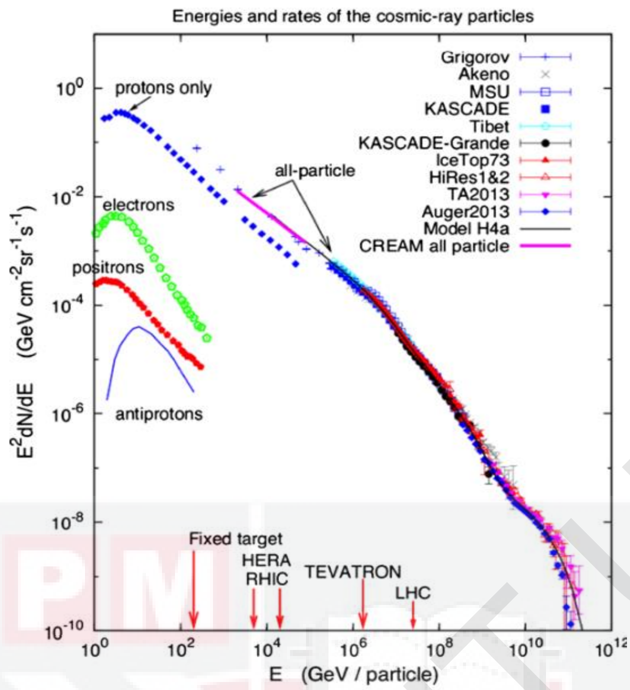


**Figure 2.4: Spectra of CR at the Earth. The all-particle spectrum measured by different experiments is plotted, together with the proton spectrum. The subdominant contributions from electrons, positrons and antiprotons as measured by the PAMELA experiment are shown** (Blasi, 2013)

The Earth is producing a constant magnetic that creates a radiation shielding known as Van Allen Radiation belt. The belts have toroidal shape with intense proton and electron fluxes in the inner and outer belt ranging from 600-60000 km from Earth (Kress et al., 2020; Obodovskiy, 2019). Since the ISS is orbiting in the range of 400 km, therefore, the radiation from the inner belt is of concern in this work. According to Obodovskiy, (2019), the density of the proton flux with energy >1 MeV in the inner radiation belt is $10^6$–$10^7$/cm$^2$s, and the density of the electron flux with energy >0.5 MeV in the outer belt is ~ up to $10^9$ cm$^2$s.

Solar events produce SEP through solar flares (SF) and coronal mass ejections (CME) (Papaioannou et al., 2016). SF are impulsive bursts of energy created by the magnetic energy around sunspots (Nishizuka et al., 2018). They are dangerous and unpredictable because they produce fluence of high energetic protons of more than $10^9$ protons/$cm^2$ (Cucinotta et al., 2009). All electromagnetic waves up to gamma radiation of > 100 MeV are also produced during SF events (Kocharov et al., 2021; Obodovskiy, 2019). CME on the other hand are large structures containing plasma and magnetic fields being expelled from the Sun into Heliosphere (Webb and Howard, 2012). CME produces proton flux of higher than 10 MeV protons (Papaioannou et al., 2016). Apart from protons and electromagnetic waves, neutrons of high energy in the range of 100-1000 MeV range, produced by accelerated charged particles colliding with the Sun's atmosphere, can survive the distance travelled from the Sun to the Earth (Share et al., 2011; Yu et al., 2015).

### 2.2.3 Passive Radiation Monitoring Missions on International Space Station during Extravehicular Activity

In this section, several passive radiation monitoring missions that were conducted in the LEO. Here, the review is based on the exposure methods rather than the PD itself. Missions reviewed here meets the following conditions: (1) Missions are conducted in LEO, (2) Missions are conducted outside of vehicle.

Zhou et al. (2010) and Berger et al. (2013) both exposed a male Alderson anthropomorphic upper-torso phantom (RANDO®, The Phantom Laboratory) at the MATROSHKA facility outside of the Russian module (Zvezda) of ISS under a mission called MATROSHKA-1 (MTR-1). The phantom is filled with urethane-based materials. The phantom is covered by Nomex®, an aramid fibre-based skin substitute to provide skin doses (poncho and hood), then the whole phantom is placed inside a carbon fibre container covered with multilayer thermal insulation (MLI) to mimic the shielding properties of and astronaut's spacesuit during EVA activity. The PD are placed inside polyethylene (PE) tubes and the tubes are placed on various locations from within the phantom to being sewn onto the poncho. Another set of PD is placed within an Al container and attached to the MLI for outside dose measurement. Exposure of the anthropomorphic phantom during MTR-1 mission provides a very good information regarding the absorbed dose received by specific organ of an astronaut during EVA. However, it only provides absorbed dose information at a specific situation, which is absorbed dose received by astronauts wearing a spacesuit. For example, if a new spacesuit is developed with better radiation protection, or an exposure using different kind of shielding materials, the authors work needs to be repeated for accurate measurement.

While Zhou et al. (2010) and Berger et al. (2013) objective was to conduct radiation monitoring on a phantom to estimate the absorbed dose astronaut will receive in the event of EVA, Rabbow et al., (2015) and Berger et al., (2015) on the other hand has conducted exposure of PD within an acrylic case that is further placed within Al courier. The objective of the exposure was to monitor the radiation received by the biological samples. Both Zhou et al. (2010) and Rabbow et al. (2015) experiments are mission specific, meaning that that the radiation monitoring conducted only applies for each application, either for human or biological samples.

Seedhouse et al. (2018) and JAXA (2015) exposed the PD within and Al dome with varying wall thicknesses of the Al dome. A 1 atm pressure was maintained within the Al dome due to the prerequisite of the PD used needing oxygen to operate. Unlike the previous exposure experiments, this monitoring mission focused on the Al shielding thicknesses of up to 4 mm. Kawaguchi et al. (2016) and Yamagishi et al. (2018) placed PD inside and Al container like Seedhouse et al. (2018). Additionally, a shield, either stainless steel or lead (Pb) is placed on top of the PD. In comparison to the previous paragraphs, here, the missions conducted eliminate some energies of the radiation by introducing different types of shielding and varying the thicknesses of the shield. Dense materials such as Pb is commonly used as radiation shield (AbuAlRoos et al., 2019; Aziz et al., 2018). The denser the material, the more it will weight. As there are limitations in terms of dimension and mass of samples allowed depending on experimental site during space exposure at most, 5 mm Pb was used by Kawaguchi et al. (2016) and Yamagishi et al. (2018) for the shielding. Limitations also can be seen where the types of radiation shielding are not varied.

Apart from the shields that are intended to attenuate the incoming radiation, the container itself will act as radiation shield. From the literatures, as gathered in Table 2.2, all LEO exposure missions have used Al as container to hold the PD. As materials like Al can also be used as radiation shield, the PD within the container received attenuated radiation even without any shielding (AbuAlRoos et al., 2019; Sathish et al., 2023). As such, materials consideration should be made to conduct a mission where the PD can detect the radiations with the least amount of attenuation without any shielding.

From the reviews made above, there are three types of radiation monitoring missions that have been conducted on ISS during EVA as follows:

1. Specific missions to estimate the absorbed radiation received by targeted application.
2. Mission employing thicknesses of shielding material.
3. Mission employing different types of shielding materials.

From the missions reviewed in this subchapter, all missions employ Al as the container to carry the PD. On Earth, as acknowledged by International Atomic Energy Agency (IAEA), the international dosimetry protocols are based on determinations of absorbed dose to water (Zuber et al., 2021). Water as a standard phantom which is used universally in radiotherapy as water has a unit density like human body (Yadav et al., 2021). As such, there is a research gap where container carrying the PD using a material that is near water equivalent as is not studied for space radiation monitoring. Also, studies reviewed show that only metallic materials have been used as shields. Unlike gamma, electrons and protons, hydrogen-rich materials are used to shield neutrons (Uğur, 2017). Since there is a possibility of neutron particles existing in LEO, there is a gap for material consideration to shield neutron in radiation monitoring mission in space.

**Table 2.2: EVA radiation monitoring missions conducted on ISS**

| References | Exposure Method | Materials | PD used | Absorbed Dose |
|---|---|---|---|---|
| Berger et al., 2013; Zhou et al., 2010 | • PD in PE tubes placed in RANDO$^{R}$ Phantom.<br>• Phantom is covered using Nomex$^{R}$.<br>• Phantom placed in carbon fibre-based container.<br>• Container wrapped in MLI.<br>• PD inside Al casing placed in MLI for outside radiation monitoring. | • PE – PD securement<br>• Urethane based resin – Phantom<br>• Aramid fibre - Nomex$^{R}$<br>• Carbon fibre composite – Container<br>• MLI – not specified | • CR- 39 PNTD<br>• TLD-600<br>• TLD-700 | • 204 – 711 µGy/day (within container)<br>• Up to 1000 mGy/day (outside of container) |
| Berger et al., 2015; Rabbow et al., 2015; Rabbow et al., 2017 | • PD in PMMA case.<br>• PMMA case placed in Al container. | • PMMA – PD securement<br>• Al - Container | • MTS-7<br>• TLD-700 | • 276-381 µGy/day |
| JAXA, 2015; Nagamatsu et al., 2013; Seedhouse, 2018; Tawara et al., 2011 | • TLD-MSO-S placed in glass tube filled with argon gas.<br>• Glass tubes placed in PMMA container.<br>• PMMA stacked in between CR-39 PNTD and sealed inside aluminised PE bag. Overall called PADLES.<br>• PADLES placed inside Al dome. | • Glass, PMMA, aluminised PE – PD securement<br>• Up to 4 mm Al - Container | • CR- 39 PNTD<br>• TLD-MSO-S | • Not reported |
| Kawaguchi et al., 2016; Kodaira et al., 2021; Yamagishi et al., 2018 | • PD placed inside Al container.<br>• Stainless steel or Pb shield placed on top of PD. | • 2 mm Al – Container<br>• 3 mm stainless steel shield<br>• 5 mm Pb shield | • Al Oxide based OSLD<br>• Silver-activated phosphate glass-based RPLD | • 771 µGy/ day for 0.55 g/cm$^2$ shield<br>• 396 µGy/ day for 2.95 g/cm$^2$ shield<br>• 381 µGy/ day for 6.23 g/cm$^2$ shield |

## 2.3 Passive Dosimeter

Dosimeters are radiation sensors/detectors and can be divided into active and passive dosimeters (PD). PD provide indirect readouts and can operate without active means. They do not require an energy source to function. PD are typically small and can be customised into the user's needs making them versatile and accurate for small-scale dosimetry. For example, Thermo Fisher Scientific's TLD-100 (LiF:Mg, Ti with natural $Li^6$ and $Li^7$ distribution) can be purchased in a variety of forms, from disk with 4.5 mm and 0.89 mm thickness, rod with 1 mm diameter and 6 mm length, to powder form, so it can be used depending on the user's needs (TLD-100™ thermoluminescent dosimetry material) (Fadzil et al., 2022). However, PD cannot provide instantaneous readouts and must be analyse after exposure. Usually, the readouts from passive dosimeters are sent to the dosimetry service provider as they require special instruments to perform the sample readout.

Active dosimeters (AD) can also be referred to as electronic, operational (DMC), or alarm dosimeters (CERN accelerating science). AD measure accumulated dose in real time and can be equipped with additional features such as a notification to the users when the accumulated dose threshold is reached or a visual indicator that enhances the quality of life when using the dosimeter. All of this means that while the active dosimeter may seem convenient compared to the passive dosimeter, it requires a power source, such as a battery to operate. This eventually leads to the need of electronic circuit board ultimately making active dosimeter bulky and inconvenient for constant monitoring for a long period of time.

There are passive dosimeters that are integrated into the active dosimetry system, such as the OSLD used during the DIME-2 experiment (McNulty et al., 2022; Poole et al., 2022). The passive dosimeters are integrated into the circuit board, allowing the small sensors to be used in a larger system. Compared to active dosimeters, passive dosimeters can cover the prioritisations for radiation monitoring, which are personal dosimetry during EVA, dosimetry in tandem with other experiments, long term monitoring and small area monitoring. Hence, these main advantages highlighted the need to further understand on using passive dosimeter for space radiation.

### 2.3.1 Types of Passive Dosimeter

Passive dosimeters have various types depending on the mechanism of detection, as in Table 2.3. TLD, OSLD, and RPLD are categorised as luminescent dosimeters. The mechanism of TLD is use the concept of thermoluminescence (TL), in which irradiated TLD emit light (photon) when heat is applied. Like TLD, for OSL, ionising radiation excites electrons from the valence band (VB) into the conduction band (CB), then electrons are trapped in the forbidden energy gap (FEG) between VB and CB (Aramrun et al., 2018; Motcheyo and Macías-Díaz; 2020). Unlike TLD, however, the trapped electrons are excited with light rather than heat (Aramrun et al., 2018). RPLD uses a mechanism in which interaction with ionising radiation forms a new luminescence centre that produces luminescence under photoexcitation or photoluminescence (PL) (Yanaginada et al., 2022). PL is defined as a process in which a photon absorbed a molecule in the visible region, before excites one of its electrons to a higher electronic excited state, before the photon being radiated as the electron coming back to a lower energy state (Munson et al., 2007).

Apart from luminescent dosimeter, other types of dosimeters such as direct ion storage (DIS) dosimeter, radiochromic films and the CR-39 PNTD, are commonly used for radiation detection. DIS dosimeter function by collecting charges generated during irradiation in a gas chamber (Aramrun et al., 2018). However, the mission exposes the weakness of the PD used, CR-39 plastic nuclear track detector (PNTD) that requires oxygen pressure to be sensitive to radiation (Kodaira et al., 2009). The monomer of the radiochromic film polymerise when the material is exposed to ionising radiation, resulting in a change in the colour of the film at the macroscopic level, with the colour of the film correlating with the radiation dose (Casolaro et al., 2019). Finally, CR-39 PNTD is specialised in detecting neutrons caused (Castillo et al., 2013). CR-39 bombarded by the particles during irradiation will show damaged regions. The material is then etched to amplify the damaged regions before visualising it with an optical microscope (Castillo et al., 2013). Both DIS dosimeters and CR-39 dosimeters require a pressurised environment to operate, which means they are difficult to deploy outside of the ISS and require a special facility (pressurised container) to function. Radiochromic film, on the other hand, can detect UV (non-ionising) radiation, which affects the accuracy of determining the level of ionising radiation in the environment of LEO.

As gathered in Table 2.3, all PD here can detect the low range of radiation in LEO exposure (at minimum 204 $\mu$ Gy/day as shown in Table 2.2). However, CR-39 PNTD is not suitable for long term exposure as there is a limitation of 250 mSv upper detection limit as space radiation exposure can be up to 1000 mGy/day (Table 2.2). DIS dosimeter, radiochromic film, and CR-39 PNTD also have limitations where they need additional considerations for LEO exposure (pressurised container, UV shield etc). As such, TLD, OSLD and RPLD are the most suitable TLD to be used for long term passive radiation monitoring.

**Table 2.3: Types of passive dosimeter**

| Dosimeter Type | Operating Environment | Detection Range | Space radiation exposure | References |
|---|---|---|---|---|
| TLD | - | 0.1 µGy-100 Gy | Short to long term | Aramrun et al., 2018 |
| OSLD | - | 10 µGy-10 Gy | Short to long term | |
| RPLD | - | 10 µGy-10 Gy | Short to long term | |
| DIS dosimeter | Pressurised | 10 µGy-10 Gy | Short to long term | |
| Radiochromic Film | Non-UV environment (can detect UV too) | 1 cGy-40 Gy | Short to long term | Tsang et al., 2017; Gafchromic™, 2023 |
| CR-39 PNTD | Pressurised | 0.2-250 mSv | Short term | El Ghazaly and Hassan, 2018; Landauer, 2024 |

### 2.3.2 Optical Fibres as Thermoluminescent Dosimeter

OF is silica glass ($SiO_2$) with a doped core generally fabricated using modified chemical vapour deposition (MCVD) to tailor the concentration of the dopant in the core suitable for dosimetry purposes (Bradley et al., 2017). In this process, germanium tetrachloride ($GeCl_4$) and silicon tetrachloride ($SiCl_4$) are typically introduced into a rotating hollow silica tube at a high temperature of 1800-2100°C which will soften the silica tube allowing the deposition on the inner walls of the silica tube (Bradley et al., 2017). This results in a preform that is pulled at elevated temperature typically used in telecommunications. OF made for dosimetry application generally consist of cylindrical fibre (CF) and flat fibre (FF). CF is produced by pulling the collapsed (solid) tube while FF is produced by pulling the un-collapsed (hollow) tube that has been doped with the germanium (Ge) dopant (Lam et al., 2019). Figure 2.5 show the cross section of OF fibre under scanning electron microscope (SEM). CUSOF fabricated for dosimetry purposes typically will have a doped core that is surrounded by undoped $SiO_2$ as shown in the figure. The CUSOF is then applied as TLD. A good TLD possesses excellent linearity, low dose rate dependence, low field size dependence, low energy dependence, low fading rate and close to tissue equivalent (Zakaria et al., 2023; Ibrahim et al., 2014).

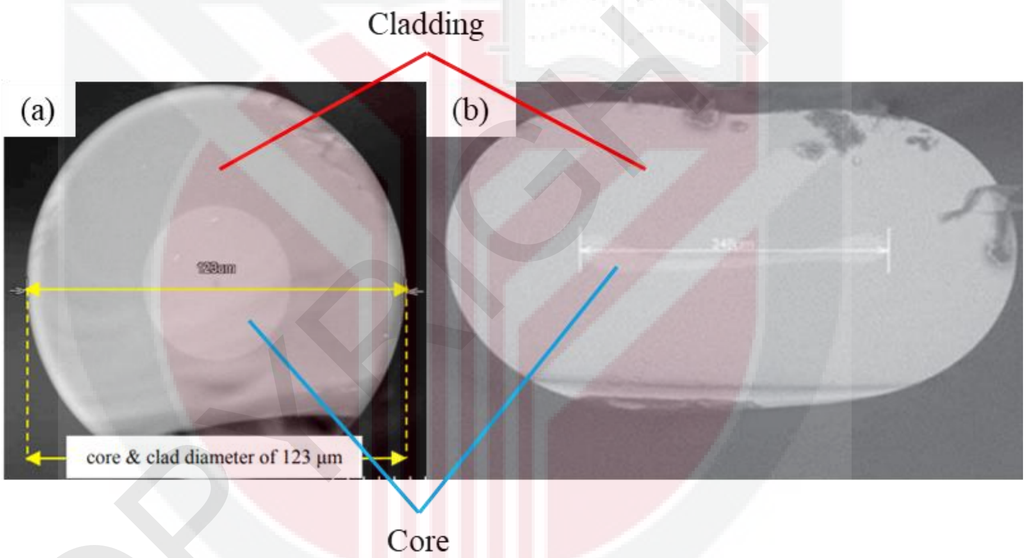


**Figure 2.5: Cross section of OF under SEM: (a) CF, (b) FF** (Lam et al., 2019; Rais et al., 2019)

Table 2.4 shows some study related to OF as a TLD. Here we can see that CUSOF has been subjected to various study using different kind of ionising radiations from photon, X-ray, gamma, electron, proton, and neutron. The application of CUSOF as TLD is also wide from radiotherapy to space radiation monitoring. Mustafa et al., 2018 is in the same team that work together with this team. From various literatures, this is the only work that has sent CUSOF to the ISS for radiation monitoring.

**Table 2.4: Various Ge-doped CUSOF study**

| Dopant Concentration | Shape | Radiation Type | Energy | Dose Range | Application | References |
|---|---|---|---|---|---|---|
| 0.1, 1, 3.5, 6.6 amd 9 wt% | CF | X-ray | 30 keV | 500 Gy | Radioactive waste monitoring | Benabdesselam et al., 2023 |
| 2.3 and 6.0 mol% | CF and FF | Electron | 6, 9 and 12 MeV | 1-5 Gy | Radiotherapy | Zakaria et al., 2020 |
| 2.3 and 6mol% | CF | Proton | 150 MeV | 1-10 Gy | Radiotherapy | Hassan et al., 2019 |
| 6 mol% | CF and FF | Photon | 6 MV | 5-80 Gy | Small-field dosimetry | Lam et al., 2019 |
| 6.0 mol% | CF and FF | Neutron-Gamma (Americium-241 Beryllium, $^{241}$AmBe) | Neutron flux of up to 11 MeV with 4.2 MeV average energy; gamma energy of 4.44 MeV | 25-200 mGy | Space radiation monitoring | Mustafa et al., 2018 |
| 3.23-3.85 mol% | CF (Core diameter: 100, 80, 60, 40, 20 μm) | Gamma (Cobalt-60, $^{60}$Co) | 1.1732 MeV, 1.3325 MeV | 1-10 Gy | - | Begum et al., 2015 |

#### 2.3.2.1 Linearity of Customised Optical Fibres

Dose linearity is the linear increment of TL responses of a TLD in tandem with the increment of absorbed dose received by the dosimeter. Hassan et al., (2019) irradiated Ge-doped CUSOF with 150 MeV proton from 1-10 Gy where the responses of the CUSOF corresponding to absorbed dose is as shown in Figure 2.6. We know the higher the dose, the higher the TL responses of the dosimeter will be. In Figure 2.6 CUSOF is highly linear with a coefficient of determination ($R^2$) of larger than 0.99 comparable or even better than that of commercial TLD-100 at an $R^2$ of 0.9988. $R^2$ value of 1.00 means that the TL responses is perfectly linear to the absorbed dose sought after by a good TLD. CUSOF's linearity to other types of radiation has been studied by Zakaria et al., (2020) where the CUSOF irradiated to 9 MeV electron beam from 1-5 Gy had $R^2$ of 0.96-0.99. The commercial OF (COMOF) originally used for telecommunication had $R^2$ value of 0.93, lower than CUSOF as to be expected since it was not tailored for radiation detection. Other than that, Begum et al. (2015) irradiated Ge-doped CUSOF to a dose of 10 Gy using Cobalt-60 ($^{60}Co$) that produces gamma radiation and found that CUSOF can be highly linear up to an $R^2$ value of 0.999. Exposure of CUSOF to a neutron-gamma source from Americium-241-Berylium (AmBe) yielded a lower linearity where the $R^2$ is 0.9707 at lowest for 6 mol% Ge-doped CF with 604 μm diameter attributed to the low dose exposure of the optical fibre from approximately 25-150 mGy (Mustafa et al., 2018). If a TLD is linear at a certain tested dose range by a particular type of radiation, does not necessarily mean that it will be linear when irradiated at a lower or higher dose or by a different type of radiation. Application of the TLD is important to determine the exposure dose and type of radiation to assess whether a TLD is satisfactory for a particular application or not.

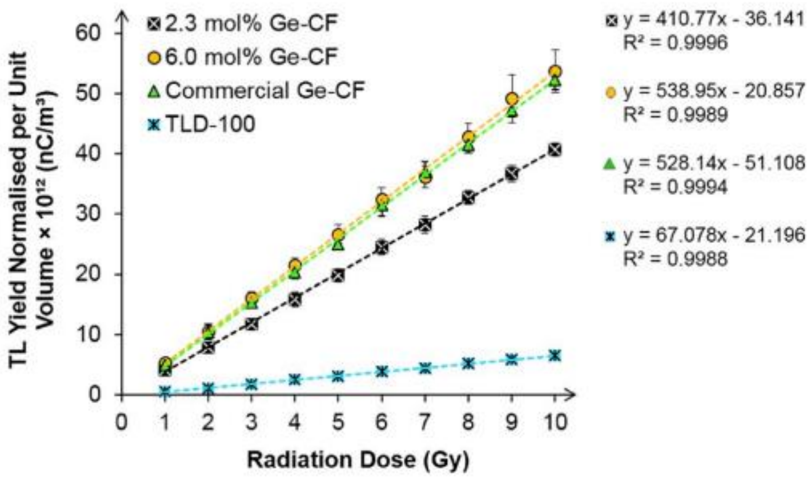


**Figure 2.6: Linearity of CUSOF irradiated with 150 MeV proton** (Hassan et al., 2019)

#### 2.3.2.2 Fading Rate of Customised Optical Fibres

In section 2.5.2 we have learned that the trappings inside the band gap can store electrons produced during irradiation and released when thermally stimulated during analysis of the irradiated TLD. These trapped electrons, however, can still be released in room temperature albeit slowly, especially for the shallower traps. This will cause the irradiated TLD to produce a lower TL response when analysed after a long period of time. This reduction in TL response is called fading rate of a TLD. A good TLD will have lower fading rate even after being stored for a long period of time. Especially for space irradiated TLD, the duration from the end of exposure from the outside of ISS until sample retrieval may take a longer period due to the processes of waiting the space shuttle flight schedule and returning the sample upon landing.

Zakaria et al., 2020 who irradiated the 2.3 and 6.0 mol% Ge-doped CUSOF with 2 Gy at 9 MeV electron found that after 204 days, the CUSOF had their TL responses drop up to 37% their original value if read at 5 days post irradiation as shown in Figure 2.7. Fading is an undesirable characteristic and if a TLD has a high fading rate, they require additional calibration to correct their responses to the actual value at an earlier read out day post irradiation. Begum et al., (2014), analysed the effect of CUSOF diameter on the fading rate of the dosimeter. 3.23-3.85 mol% Ge-doped CUSOF were irradiated under gamma radiation ($^{60}Co$ source) up to 15 days post irradiation and the author found out that CUSOF with 100 μm core diameter and 604 μm total diameter had the lowest fading of 20% where the CUSOF here has the largest core diameter and total diameter. Other studies under different types of radiation were also made. Contrary to Begum et al. (2014) findings, when irradiated with AmBe neutron-gamma source, 6 mol% Ge-doped CUSOF with a diameter of 483 μm had a lower fading rate of 10% 71 days post irradiation compared to the 604 μm that had a higher fading rate of 26% (Mustafa et al., 2018). 2.3 mol% Ge-doped CUSOF had a fading of 13% 96 days post irradiation comparable to TLD-100 that had a 10% fading under 150 MeV proton (Hassan et al., 2019).

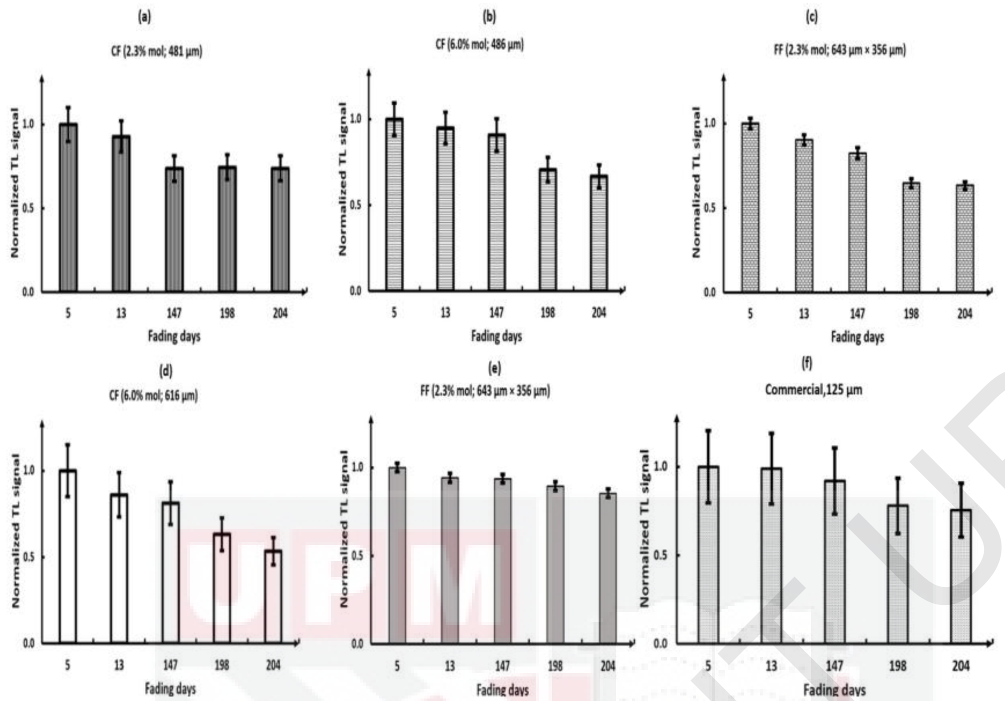


**Figure 2.7: Fading of CUSOF subjected to 2 Gy, 9 MeV electron. TL normalized versus post-irradiation days for 9 MeV electron beam irradiated fibres, as follows: a) 2.3% mol Ge, 481 µm; b) 6.0% mol Ge, 486 µm); c) 6.0%mol Ge; 620 × 165 µm); d) 6.0% mol Ge; 616 µm; e) 6.0% mol Ge; 643 × 356 µm); f) commercial, 125 µm** (Zakaria et al., 2020)

### 2.3.3 Energy Dependency of Customised Optical Fibres

Depending on the energy of radiation, sometimes correction is required to accurately calculate the actual responses. Noor et al. (2016) irradiated CUSOF with varying photon energies of 1.25 MeV from $^{60}$Co (gamma), 6 MV and 10 MV and found that 10 mol% Ge doped CF to produce the largest gradient value of 0.364 and 0.327 respective to the diameter of 241 µm and 604 µm as shown in Figure 2.8. Zabariah et al. (2020) irradiated 2.3 mol% CF with 6, 9, 12 and 15 MeV electron and found that the range of responses from CUSOF were from 0.80-1.12 respective to 6-15 MeV under 6 cm × 6 cm field size. As such, energy dependency is a consideration to be made to calibrate the dose responses of the CUSOF accurately. While a more accepted beam quality specifier such as $TPR_{20/10}$ is better, the OF used in this work has not been through $TPR_{20/10}$ preliminary assessment.

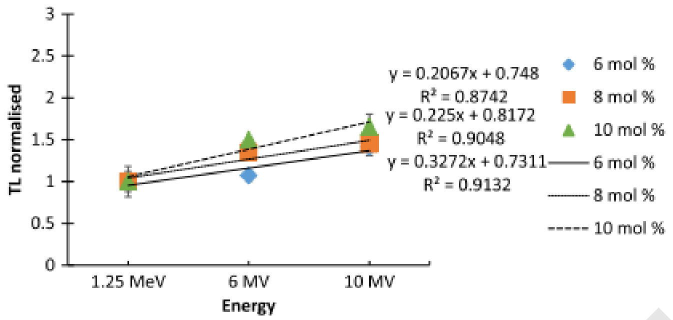


**Figure 2.8: Energy dependency of CUSOF subjected to photon of different energies** (Noor et al., 2016)

### 2.3.4 Glow Curves of Customised Optical Fibres

The intensity of the glow curve indicates the quantity of light released due to thermal stimulation. The Ge-doped CUSOF irradiated up to 500 Gy of 50 keV X-ray shows glow curves characterised by a main peak located between 200°C and 250°C, corresponding to an energy depth of the traps between 1.2 and 1.4 eV in the silica band gap as in Figure 2.9 (Benabdesselam et al., 2023). Generally, TL signal is lower with the increasing Ge amount in the fibre. The variation in position of the main peak means that, depending on the Ge concentration, different rearrangements of the trap defects associated with this dopant take place in the silica matrix. As presented in Figure 2.10, irradiation of 150 MeV proton from 1-5 Gy shows that 2.3 mol% Ge-doped FF is characterised with a single peak at approximately 80°C maximum TL while 6 mol% Ge-doped FF had two main peaks at around 60°C for the first peak and 120°C for the second peak (Hassan et al., 2019).

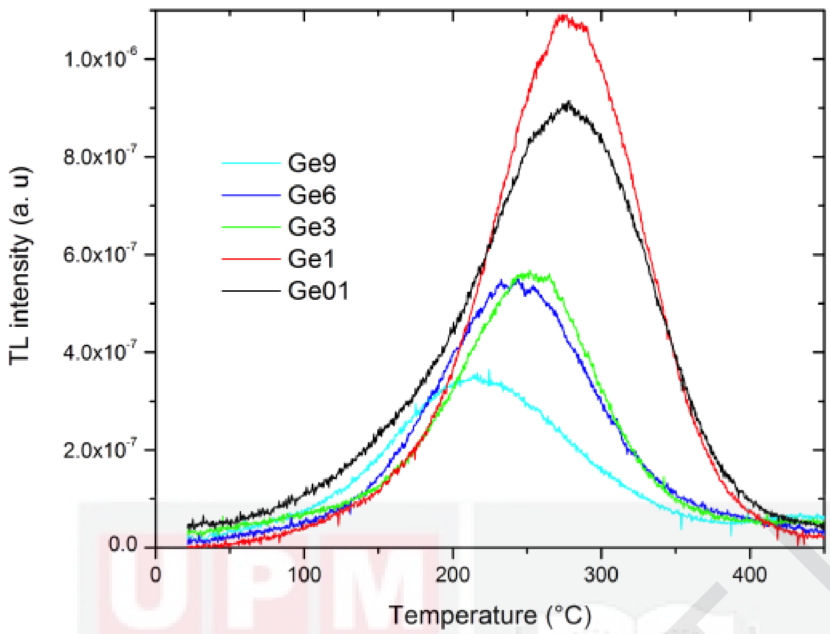


**Figure 2.9: Glow curves of Ge-doped CUSOF irradiated at 500 Gy, 50 keV X-ray** (Benabdesselam et al., 2023)

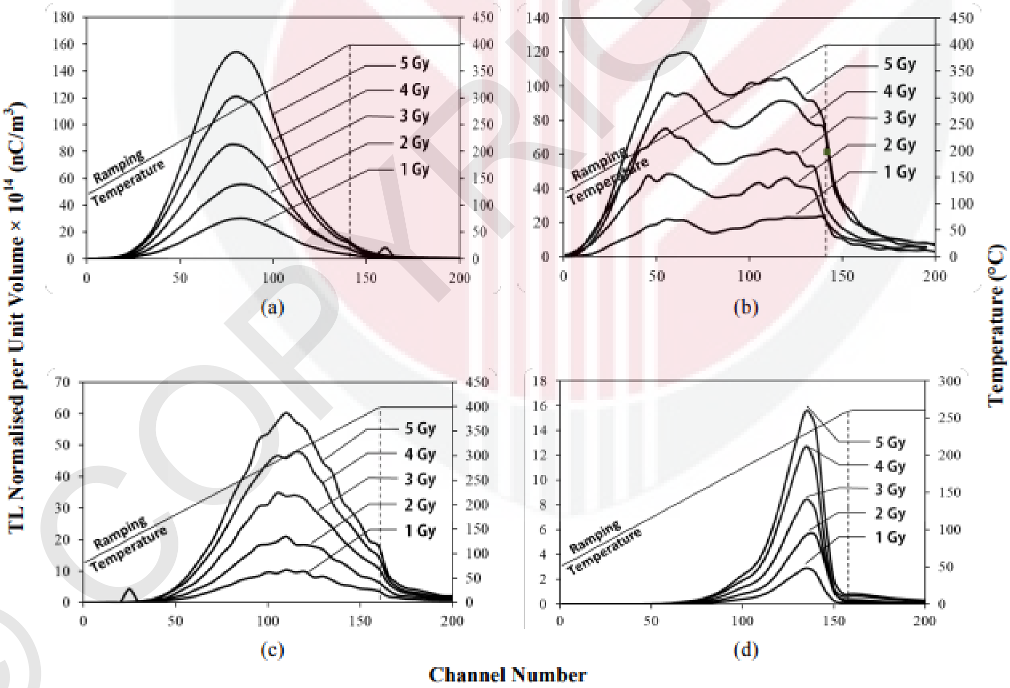


**Figure 2.10: Glow curves of 150 MeV proton irradiated CUSOF. (a) 2.3 mol% FF, (b) 6.0 mol% FF, (c) COMOF and (d) TLD-100** (Hassan et al., 2018)

## 2.4 Development of Casing for Space Exposure

This subchapter addresses the iterative development method used while conducting this work and explore them further in terms of their theory and connection to scientific literature. The materials consideration for the casing is also discussed here.

### 2.4.1 Iterative Product Development

In this work, due to the tight deadline to accommodate the shuttle schedule for launching, iterative product development fits criteria as a versatile and fast paced development procedure. Iterative product development is a cyclical process that consists of idea generation, evaluation and design improvement until the design requirement is met (Wynn and Eckert, 2017). Iterative methods are suitable for projects without clear requirements as new additions can be integrated to match the evolving requirements (García-Sánchez et al., 2024). The development process involves small changes by regularly engaging the clients for feedback which allows for flexibility in accommodating changes in product characteristics (Cooper and Sommer, 2016). Savage (1996) performed an iterative development by collecting feedbacks in three stages starting from expert reviews, user reviews and lastly conducting usability testing. From the feedbacks made by the experts and users, the author was able to conduct multiple iterations of the software being developed. Feedbacks from experts are also called heuristic evaluation (Sharma et al., 2021). Sharma et al. (2021) conducted semi-structured interviews with the users (astronauts) to and heuristic evaluation by the experts to incorporate the feedbacks into the iteration process to develop human-centred design principles for space environments. While iterative development process originally comes from software development through complete rewriting of a programming code for every new version, it also has been used to for swift advancement of hardware development (Blakstad and Tingsborg, 2023). Working closely with the client, Blakstad and Tingsborg (2023) employed iterative development process alongside action research that fits the iterative development process as shown in Figure 2.11. Blakstad and Tingsborg (2023) employed spontaneous non-structured interviews and focus group discussion to obtain feedbacks for the product development.

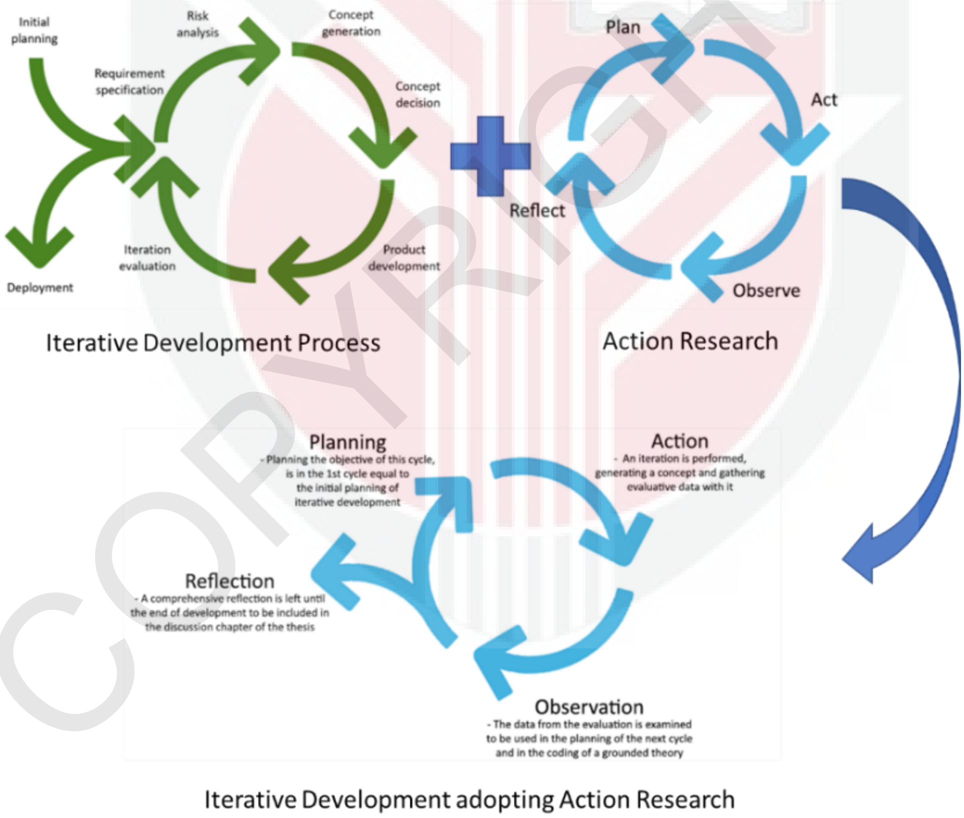


**Figure 2.11: Action research cycle adapted into iterative development process** (Blakstad and Tingborg, 2023)

### 2.4.2 Materials Selection for Casing

The main material used for the container carying the PD is the most important as while the casing is being exposed to the space environment, it still needs to contain any parts within. As this work concerns the PD, considerations should be made not just in terms of the structural integrity but also in terms of radiation exposure. The best method would be exposing the PD to free space. Nevertheless, the PD will require a container during space exposure. In section 2.2.3, all exposure reviewed used Al container even for surface dose measurement. Sathish et al. (2023) found that Al alloy is a good material for electromagnetic, neutron and Bremsstrahlung radiations. In this work, without any shielding, the PD exposed is intended to detect free space radiation as close as possible. As such, in this section, the review of potential materials to be used as PADCIOF is reviewed.

There are two categories in which the materials are reviewed:

1. Water equivalent properties
2. Survivability in LEO
   i) Strength
   ii) Actual exposure to LEO conditions

To evaluate similarities between materials in terms of interaction of ionising radiation with materials, effective atomic number ($Z_{eff}$) is often used (Zuber et al., 2021). As such, a material similarities with water can be evaluated by comparing the $Z_{eff}$ of said material with the $Z_{eff}$ of water. $Z_{eff}$ has been calculated in various works using

Equations 2.1-2.3 (Birnbacher et al., 2018; Hashim et al., 2014; Joshi et al., 2017; Kurudirek, 2014; Smith et al., 2011). Here, $a$ is the fractional contributions of each element to the total number of electrons in the mixture and $Z$ is the atomic number of each element, $N_e$ is the number of electrons per gram of each element, $N_A$ is the Avogadro's constant, $A_w$ is the atomic weight of each element and $W_i$ is the fractional weight of each element

.

$$Z_{eff} = \sqrt[2.94]{a_1 {Z_1}^{2.94} + a_2 {Z_2}^{2.94} + a_3 {Z_3}^{2.94} + \cdots + a_n {Z_n}^{2.94}} \quad (2.1)$$

$$N_{en} = {N_A Z_n W_{in}}/{A_{wn}} \quad (2.2)$$

$$a_n = {N_{en}}/{(N_{e1} + N_{e2} + \cdots + N_{en})} \quad (2.3)$$

$Z_{eff}$ of water is 7.42 and the material has the closest $Z_{eff}$ with water is polyoxymethylene (POM) with a $Z_{eff}$ of 6.95 (Birnbacher et al., 2018). Polymethylmethacrylate (PMMA), polyurethane (PU) which is the material used for the RANDO ® phantom by Berger et al. (2013) and Zhou et al. (2010), polyetheeretherketone (PEEK), and polytetrafluoroethylene (PTFE) also are also materials with similar $Z_{eff}$ to water at 6.47, 6.44, 6.38 and 8.50, respectively (Birnbacher et al., 2018; Joshi et al., 2017; Kurudirek, 2014; Smith et al., 2011). Other materials such as polyamide (PA), PE and polystyrene (PS) have $Z_{eff}$ that differs largely compared to water (Birnbacher et al., 2018; Kurudirek, 2014). Overall, in terms of water equivalence ($Z_{eff}$ like water), POM, PMMA, PU, PEEK, and PTFE are the closest from the literatures.

For survivability in LEO, one of the most important properties is the strength of the materials. Out of the materials that has been presented in the previous paragraph, PEEK is the strongest with a tensile strength of up to 118 MPa (Muhsin et al., 2019). Other polymeric materials have lower strength than PEEK with PMMA and PA being the closest at 83 MPa for both materials (Jafferson and Chatterjee, 2021; Muhsin et al., 2019). POM, being the closest to water in terms of $Z_{eff}$ is even weaker at 70 MPa (Jafferson and Chatterjee, 2021). Other polymeric materials such as ABS, PE, PU and PTFE are even weaker in strength compared to PEEK (Dhanumalayan et al., 2018; Jafferson and Chatterjee, 2021; Xu et al., 2022).

Various polymeric materials have been exposed for about 4 years in LEO environment in the ram direction of ISS where the estimated AO flux for 3 years of exposure is estimated to be $9.1 \times 10^{21}$ atoms/cm$^2$ (De Groh et al., 2006; De Groh and Banks, 2019). PTFE had the lowest erosion yield due to AO and no visible damages seen after the exposure (De Groh et al., 2006). ABS, PPU, PEEK, PA and PS have slightly higher erosion yield compared to PTFE with some discolouration after exposure (De Groh et al., 2006). Other materials such as PMMA and POM that have high erosion yield due to AO interaction eroded with residual material left (De Groh et al, 2006).

As presented in Table 2.5, PEEK is the most promising material with good water equivalence, highest strength, and low erosion yield when exposed to LEO environments. PU that has been used for radiation monitoring mission, albeit being contained inside carbon fibre container possesses lower strength compared to PEEK. POM being the closest to water equivalence has low strength and high AO yield rendering the materials unusable for space exposure. Similarly, PTFE with the lowest AO erosion has low strength making it unusable as a container for LEO exposure.

**Table 2.5: Materials selection criteria**

| Materials | Water Equivalence | Strength | AO Erosion | References |
|---|---|---|---|---|
| ABS | Bad | Bad | High | Birnbacher et al., 2018; De Groh and Banks 2019; De Groh et al., 2006; Dhanumalayan et al., 2018; Jafferson and Chatterjee, 2021; Joshi et al., 2017; Kurudirek, 2014; Muhsin et al., 2019; Smith et al., 2011; Xu et al., 2022 |
| PA | Mid | Good | High | |
| PE | Bad | Bad | Mid | |
| PEEK | Good | Best | Low | |
| PMMA | Good | Good | High | |
| POM | Best | Bad | High | |
| PS | Bad | Bad | Low | |
| PTFE | Good | Bad | Lowest | |
| PU | Good | Good | Low | |

## 2.5 Prerequisite of Payload

The transportation of goods and humans to the ISS usually will utilise Space-X spacecraft. From launching to arrival of the sample to ISS, the random vibration and sine burst are of concern (Yasaka and Onoda, 2003). After arrival of the goods onboard ISS, for deployment to the experiment site, the sample will be transported using robotic arm (JAXA, 2008). The sample will need to be able to sustain the force applied by the robotic arm without losing structural integrity.

### 2.5.1 Transport: Random Vibration Test

SpaceX's Falcon spacecraft is a two-stage launch vehicle, where, payloads attached to the payload attachment fitting (PAF) as shown in Figure 2.12 of the spacecraft will experience random vibration and shock loads during transport to ISS (SpaceX, 2021). It is divided into two categories; the Falcon 9 and the Falcon Heavy vehicle with extra two separating side cores (SpaceX, 2021). The random vibration sources at the top of PAF can be segregated as follows (SpaceX, 2021):

1. Low frequency (0-100 Hz)
    - Global vehicle motion and modes.
2. Mid frequency (100-600 Hz)
    - Aeroacoustics and aero buffet.
3. High frequency (600-2000 Hz)
    - Structure-borne vibration such as the engine.

**Figure 2.12: PAF of the SpaceX Falcon spacecraft** (SpaceX, 2021)

Random vibration test for payload is typically conducted in the range of 20-2000 Hz (García-Sánchez et al., 2024). The vibration profile is analysed in power spectral density (PSD) with the unit of $g^2$ per Hertz (García-Sánchez et al, 2024). An overall value of the PSD curve is expressed as square root of the area under the PSD with a unit of G root mean square (Grms) (Irvine, 2009). The maximum random vibration environment at the PAF is gathered in Table 2.6.

**Table 2.6: MPE at the top of PAF of Falcon** (SpaceX, 2021)

| Frequency [Hz] | | PSD [$g^2$/Hz] | | Slope [dB/OCT] |
|---|---|---|---|---|
| From | To | From | To | |
| 20 | 100 | 0.0044 | 0.0044 | 0 |
| 100 | 300 | 0.0044 | 0.01 | 2 |
| 300 | 700 | 0.01 | 0.01 | 0 |
| 700 | 800 | 0.01 | 0.03 | 25 |
| 800 | 925 | 0.03 | 0.03 | 0 |
| 925 | 2000 | 0.03 | 0.00644 | -6 |
| | Overall [Grms] | 5.13 | | |

Random vibration load is applied at acceptance level (AL) for 1 min and at qualification level (QL) for 3 min (Air Force Space Command, 2014). The AL is the envelope of the maximum predicted environment (MPE) and minimum workmanship level where the PSD requirements is presented in Table 2.7 (Air Force Space Command, 2014). The QL of random vibration load is +6 dB of the AL random vibration load (Air Force Space Command, 2014).

**Table 2.7: AL random vibration profile** (SpaceX, 2021)

| Frequency [Hz] | | PSD [$g^2$/Hz] | | Slope [dB/OCT] |
|---|---|---|---|---|
| From | To | From | To | |
| 20 | 150 | 0.0053 | 0.04 | 3 |
| 150 | 800 | 0.04 | 0.04 | 0 |
| 800 | 2000 | 0.04 | 0.00644 | -6 |
| | Overall [Grms] | 6.94 | | |

A random vibration signal includes a waveform in which frequencies whose amplitudes and phases vary randomly (Thukral et al., 2022). As shown in Table 2.8 Dellingr CubeSat by NASA was subjected to a random vibration test at an overall QL of 9.47 Grms for 3 min/axis and at AL of 5.76 Grms for 1 min/axis where the CubeSat was planned to be launched using the Falcon 9 vehicle (Clagett et al., 2017). Like Clagett et al. (2017), García-Sánchez et al. (2024) also excited an AL with an overall PSD of 5.76 Grms for 1 min/axis onto the developed CubeSat as both authors used Falcon 9 vehicle for launching. Method used to evaluate the PSD is by comparing the average values where the Grms remain similar (García-Sánchez et al., 2024). Wan Aasim et al. (2022) on the other hand, applied an MPE level load as shown in Table 2.8, of +3 dB as a proto-qualification level (PL) random vibration load on the payload. While the AL of the vibration load is not the same as shown in Table 2.7 they have higher overall Grms compared to the MPE of the launching vehicle. For experiments, not conducted at AL, they are conducted at PL which is +3 dB in comparison to the MPE. Requirements state that the spacecraft is required to comply with the vibration environment at the launch vehicle-to spacecraft interface due to the mechanical joints having risks of incurring damage if subject to an environment above the test specification.

**Table 2.8: Random vibration profiles used by various payloads (frequency range 20-2000 Hz)**

| References | Vibration Profile | Vehicle | Payload Type |
|---|---|---|---|
| Clagett et al., 2017 | • QL of overall 9.47 Grms for 3 min/axis<br>• AL of overall 5.76 Grms for 1 min/axis | Falcon 9 | 6U CubeSat |
| García-Sánchez et al. 2024 | • AL of overall 5.76 Grms for 1 min/axis | Falcon 9 | 1U CubeSat |
| Wan Aasim et al., 2022 | • PL with MPE profile (Table 2.6) + 3 dB for 1 min/axis | Falcon 9 | 3U CubeSat |
| Mariano et al., 2020 | • AL of overall 6.12 Grms for 1 min/axis<br>• QL of + 3 dB from AL for 1 min/axis | Falcon 9 | 1U CubeSat |
| Kim et al., 2019 | • QL of overall 14.1 Grms for 3 min/axis | Falcon 9 | 3U CubeSat |
| Roberts, 2018 | • QL of overall 14.1 Grms for 1 min/axis | Based on NASA's GEVS | 3U CubeSat |
| Navarro et al., 2020 | • QL of overall 14.1 Grms for 1 min/axis | Based on NASA's GEVS | 3U CubeSat |

*GEVS: Generic Environmental Verification Specification

### 2.5.2 Transport: Sine-burst Test

The sine-burst test is used for testing the strength of the payload as an alternate to static pull and centrifuge tests by applying sinusoidal acceleration at increasing, maintained, and finally decreasing amplitudes at a constant frequency (Cote et al., 2020; NASA, 2015; Sarafin et al., 2018). The purpose of sine-burst tests is to apply specified acceleration on the payload to verify that the payload can withstand the maximum expected loads during launch (NASA, 1999; NASA, 2015; Sarafin et al., 2018). At the same time, sine-burst test is conducted over short period to minimize the fatigue damage to the payload (NASA, 1999; Sarafin et al., 2018). Sinusoidal wave is applied to the payload with frequency of less than 1/3 of the fundamental natural frequency to avoid dynamic amplification during the test (Cho et al., 2019; NASA, 1999; NASA, 2015).

As gathered in Table 2.9, sine-burst test is conducted at various frequencies due to the difference in natural frequencies based on the structure of the payload. The maximum amplitude of input also differs based on the launch provider vibration profile. The number of cycles of the sinusoidal waves during input are similar ranging in between 5-10 cyles (NASA, 2015). The strongest shock loads during the flight are due to fairing deployment and spacecraft separation (SpaceX, 2021). However, for cargo and crew for commercial resupply services (CRS) the fairing is replaced with a SpaceX Dragon spacecraft instead (SpaceX, 2021). As far as the author knowledge, there is no work found doing sine-burst test on payload to be sent using the Dragon spacecraft. As such it is hard to determine the sine-burst profile of the spacecraft other than through the launch provider.

**Table 2.9: Sine-burst profiles used by some payloads**

| References | Vibration Profile (Frequency, Maximum Input Amplitude, Cycles) | Vehicle | Payload Type |
|---|---|---|---|
| Oh et al., 2017 | 100 Hz, 12 g, 7 cycles | Based on QB50 System Requirements and Recommendations (QB50, 2015) | 1U CubeSat |
| Kim et al., 2019 | 50 Hz, 18.75 g, 5 cycles | Falcon 9 | 3U CubeSat |
| Cote et al., 2020 | 13 Hz, inputs of 2.1, 4.1, and 9.0 g, 5 cycles | - | Satellite |
| Lee et al., 2015 | 12 g, 7 cycles | Based on QB50 System Requirements and Recommendations (QB50, 2015) | 1U CubeSat |
| Navarro et al., 2020 | 25 Hz, 20 g | Based on GEVS | 3U CubeSat |

## 2.6 Installation of Exposed Payload

A robotic arm, the Japanese Experiment Module Remote Manipulator System (JEMRMS), is used to install the exposed payload or deployment of CubeSats into orbit (JAXA, 2008). There is a possibility that the robotic arm applying load onto the exposed payload. The JEMRMS operates using two arms where both the main arm and small fine arm has a maximum tip force of more than 30 N (JAXA, 2008). A puncture test can be used to assess material's ability to withstand the penetrating force. PEEK has a puncture strength of up to 10.5 MPa, higher than PE with 5.65 MPa (Liu et al., 2019). This agrees with the reviews in section 2.3.2 where PEEK is also stronger in terms of tensile strength.

## 2.7 Summary

From the discussion in the literatures, this work will be focused on the research gap and limitations that has been discussed. From the review, most of the passive dosimeters used in LEO involves the usage of TLD and CR-39 PNTD where the CR-39 has its limitations in terms of long term and external exposure. OF used in the forms of TLD has been presented as having great characteristics to be applied as PD in LEO.

Another issue that has arisen in the literature is the PADCIOF used in exposure. They either always include the usage of materials that impede the accuracy of radiation detection like Al or require complex setups that will requires extensive research. In this perspective, this research will be focusing on the simplification of PADCIOF that is able to survive any adversary that comes with prolonged exposure in space, while at the same time providing valuable scientific knowledge on the usage of a new PD in the realm of space radiation dosimetry.

The literatures reviewed in this chapter influenced the methodology that is employed in Chapter 3. The sources of radiations as reviewed in subchapter 2.2.2 allow for the consideration of multi radiation fields for attenuation calculations by the filters employed within the PADCIOF. The passive dosimetry missions as reviewed in subchapter 2.2.3 are used to extract the requirements for PADCIOF. In terms of dosimetry, it influences the materials used as most missions employed Al container which is a good attenuator for various types of radiations such as photon, proton and electron. In Chapter 3, considerations are made for main body of PADCIOF to have the least influence on the incoming radiation until reaching the dosimeter unless it is purposefully attenuated by using filter materials. Subchapters 2.3 assisted in the decision-making process for the PD to be included in PADCIOF namely the TLD which are used for comparison to the PD of interest.

Subchapter 2.4.1 reviewed the methodology that is most suitable for the development of PADCIOF. Specifically, the method used by Blakstad and Tingsborg (2023) is the most fitting for this work as the PADCIOF's requirements are extracted from different party, necessitating the multiple iteration to assess the current iteration suitability to be used for space exposure. Additionally, subchapter 2.4.2 also provides the information needed to satisfy the requirements during PADCIOF development process.

Finally, subchapter 2.4.1 and 2.4.2 provided the basis for qualification throughout the transportation to the exposure facility until retrieval. As this work employs the services of SpaceX for transport and Kibo module for exposure, the base requirements need to be satisfied by the developed PADCIOF are reviewed for vibrations analysis and structural load analysis. In conclusion, the literatures reviewed in this chapter aid the processes conducted and analysis made throughout the research.

# CHAPTER 3

# METHODOLOGY

## 3.1 Overview

This chapter discusses on the flow of research methodology. After a brief introduction, a general flowchart of the research process is written in details. The third section describes the design and assembly of the passive dosimetry (PD) casing incorporating optical fibre (PADCIOF) including sample preparations. The optical fibres samples for the PADCIOF are named as Smart Optical Fibres for Passive Dosimetry in Space (SOFPADS). The PADCIOF also included other passive dosimeters such as TLD-100, TLD-600 and TLD-700. The tests conducted on PADCIOF for approval to be launched to the International Space Station (ISS) is discussed in the fourth section. Irradiation methods for calibration of space radiation are explained in the fifth section. The launching, exposure outside of ISS, retrieval, and sample extraction processes are described in the last section.

## 3.2 Research Methodology

This work is supported by the *Geran Putra Berimpak* provided by Universiti Putra Malaysia (UPM) (Grant number: 9521800). The design of the PADCIOF was derived from the requirement of the experiment site, in which referring to the exposure of extravehicular activity (EVA) on the ISS. Therefore, the material used for PADCIOF requires specific specification to sustain for space exposure. The flowchart of this research is shown in Figure 3.1.

Referring to Figure 3.1, the commencement step of Stage 1 is the design of PADCIOF by using the iterative development process where the processes is used to satisfy two types of requirements, the space radiation monitoring and the space exposure utilising Exposed Experiment Handrail Attachment Mechanism (ExHAM). The subsequent Stage 2 indicated the performance evaluation of the assembled PADCIOF through vibration and mechanical tests to validate the structural properties of the casings. The validation process of the structural properties was done by JAXA. Simultaneously with Stage 3 is conducted to prepare the SOFPADS and commercial thermoluminescent dosimeter (TLD) to be placed inside the proposed casing. In this stage, various processes such as preliminary tests, screening, final annealing, and assembly are conducted. The final design PADCIOF is subjected to the acceptance tests (AT) procedures provided by JAXA. The final stage is the space exposure of the PADCIOF from transportation to the last correlation of the exposed radiation in the space using the calibration coefficient of proton radiation.

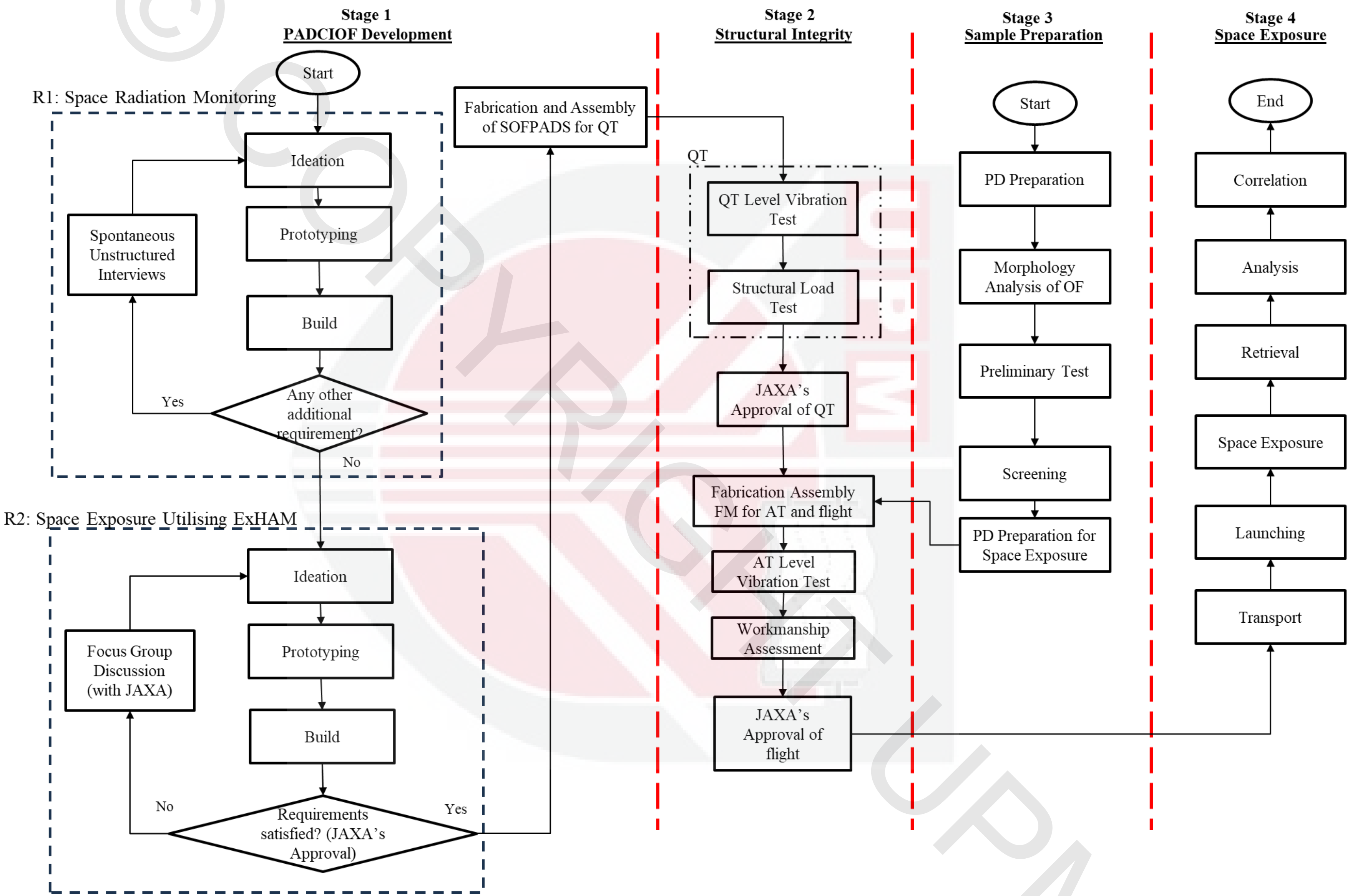


**Figure 3.1: Flowchart of research methodology**

## 3.3 Stage 1: Development of SOFPADS

### 3.3.1 Iterative Development Process

The PADCIOF development process in this work adopts similar product development method used by Blakstad and Tingsborg (2023) and Enginess (2021) as shown in Figure 3.2. Iterative development method is an incremental development method where the iteration can occur at any step as shown in Figure 3.2. The iterative development process is conducted until the confirmation on the final design was achieved. Accordingly, in this research, the final design has must abide the rigorous process of idea, prototyping, building and testing before accepted for flight and space radiation exposure. The details of the process are explained below.

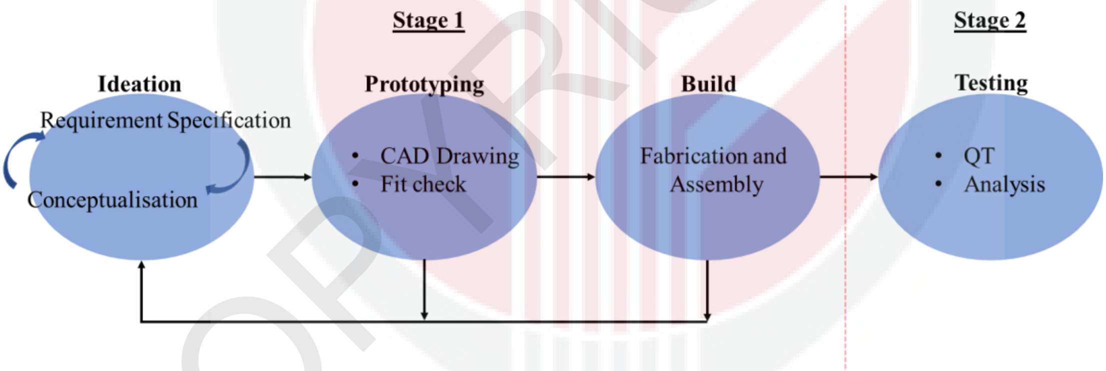


**Figure 3.2: SOFPADS development procedure**

### 3.3.2 Ideation

In the ideation stage, the requirements for the space exposure are specified, then the design was conceptualised. Iterations occurs where new requirements are added incrementally during the ideation step. The requirements in this work are determine from two point of views as gathered in Figure 3.3; (R1) Space radiation monitoring, and (R2) space exposure utilising the ExHAM.

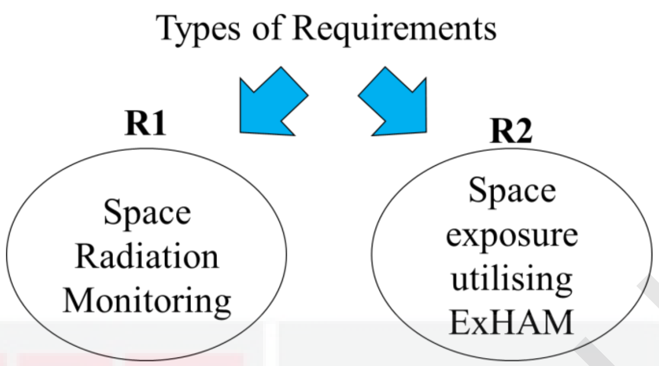


**Figure 3.3: Type of requirements**

The R1 requirements were provided by UPM experts. Two of the experts are medical physicist where one of them is an expert in dosimetry too. One of the UPM experts has an expertise in photonics and astrophysics who is also experienced in OF fabrication and characterisation which is used in this work. The experts from JAXA for R2 are the Manager and Associate Senior Engineer of the Japanese Experiment Module (JEM) Utilization Center of JAXA, and an Engineer/Researcher at the Human Spaceflight Technology Directorate of JAXA. Table 3.1 summarised the number of experts for each requirement.

**Table 3.1: Requirement specification details**

| Code | Requirements Type | Providers | Numbers of Experts |
|---|---|---|---|
| R1 | Space radiation monitoring | UPM | 3 |
| R2 | Space exposure utilising ExHAM | JAXA and UPM | 7 |

Methods used to determine the requirements are through spontaneous unstructured interviews (SUI) and focused group discussion (FGD) which were used by Blakstad and Tingsborg (2023). Generally, R1 were specified using SUI. This was conducted by doing multiple discussion with the UPM experts and developing the design concept immediately after discussion. The SUI with the UPM experts is not documented as the conceptualisation is conducted directly after the meetings and the developed concept is used for the next discussion. The discussion and development of the design concept is iterated until a satisfactory concept is developed.

On the other hand, R2 is determined by either searching online for necessary information, SUI with the UPM experts or conducting FGD where meetings are conducted with JAXA experts, UPM experts to discuss the requirements needed to improve the design concept made. The FGD are generally facilitated by Malaysian Space Agency's (MYSA) representatives as the JAXA experts are more accustomed to work with MYSA. JAXA experts and came to *Pusat Pengimejan Diagnostik* Nuklear, UPM once for a physical discussion as shown in Figure 3.4.


**Figure 3.4: JAXA's experts technical visit to PPDN, UPM for FGD**

Other discussions were conducted through teleconferences arranged by Infocomm Development Centre (iDEC) as shown in Figure 3.5, UPM. Additional discussions were conducted through email correspondences. The FGD with JAXA experts and MySA's representative is transcribed into minute of meetings (MoM). The requirements are extracted from the MoM to improve the design concept. JAXA also provided reports for further clarification if any info was missing or misunderstood during the teleconferences.

**Figure 3.5: Teleconference at iDEC, UPM**

### 3.3.3 Prototyping

The casing was modelled using computer aided design (CAD) of SolidWork software. Plainly, the proposed casing should fulfil the requirement and regulations for space exposure. The CAD file (.stl format) was also sent to JAXA for pre-fit check. JAXA 3D printed the model, specifically the casing without the internal parts and attached the model to ExHAM mock-up to verify that the developed model's geometry is suitable for ExHAM utilisation.

After the casing design geometric and feature requirement were verified, the target materials were studied for radiation purpose. The details will be explained in the following sub-sections.

### 3.3.4 Build

After the design is approved by JAXA, the casing is fabricated and assembled. For fabrication of the casing, a fabricator (K&M Infinity Engineering) was hired to machine the materials chosen into the designed geometry. Most of the base materials of the casing are purchased separately from other companies with some materials like the screws and c-clips provided by K&M Infinity Engineering. Upon assembly, a final observation was made to decide whether improvements are required or not before proceeding with QT. After acceptance of the final design, no changes in the design were made.

## 3.4 First Iteration

### 3.4.1 Ideation: Requirement Specification

Table 3.2 shows the initial requirements provided. The R1 requirements are obtained through SUI with the UPM experts while the R2 requirement is obtained from the information provided by JAXA (2018). At this stage, no FGD was conducted yet.

**Table 3.2: Initial requirements**

| Code/ Subcode | Requirements Type | Justification |
|---|---|---|
| **R1** | **Space radiation monitoring** | |
| R1-1 | CUSOF shall be used for radiation monitoring. | PD of interest |
| R1-2 | TLD-100, TLD-600 and TLD-700 shall be used for comparison. | Commercial TLD for comparison |
| R1-3 | The internal area of the casing shall have multiple areas for placing the PD | To determine the consistency of radiation exposure at different locations |
| R1-4 | Structure covering the PD facing the space should be as thin as possible. | To reduce the attenuation of radiations |
| | | |
| **R2** | **Space exposure utilising ExHAM** | |
| R2-1 | The overall maximum dimension shall be 100 mm × 100 mm × 20 mm (L×W×H). | ExHAM's sample size |

### 3.4.2 Ideation: Conceptualisation

Based on the requirements from Table 3.2, a design concept as shown in Figure 3.6 was made. Figure 3.6 (a) shows the side view of the PADCIOF indicate the compartment area for the PD. Figure 3.6 (b) shows the top view of the PADCIOF with 9 compartment area designated for PD placement The details dimension of the compartment is shown in Figure 3.6 (c). Specifically, the compartments are required from R1-1 to R1-3 and the thickness of the case cover was decided at 1 mm to satisfy condition R1-4. The overall dimension of the PADCIOF was accomplished to 100 mm × 100 mm × 20 mm according to R2-1. This iteration cycle ends at ideation.

(a)

(b)

(c)

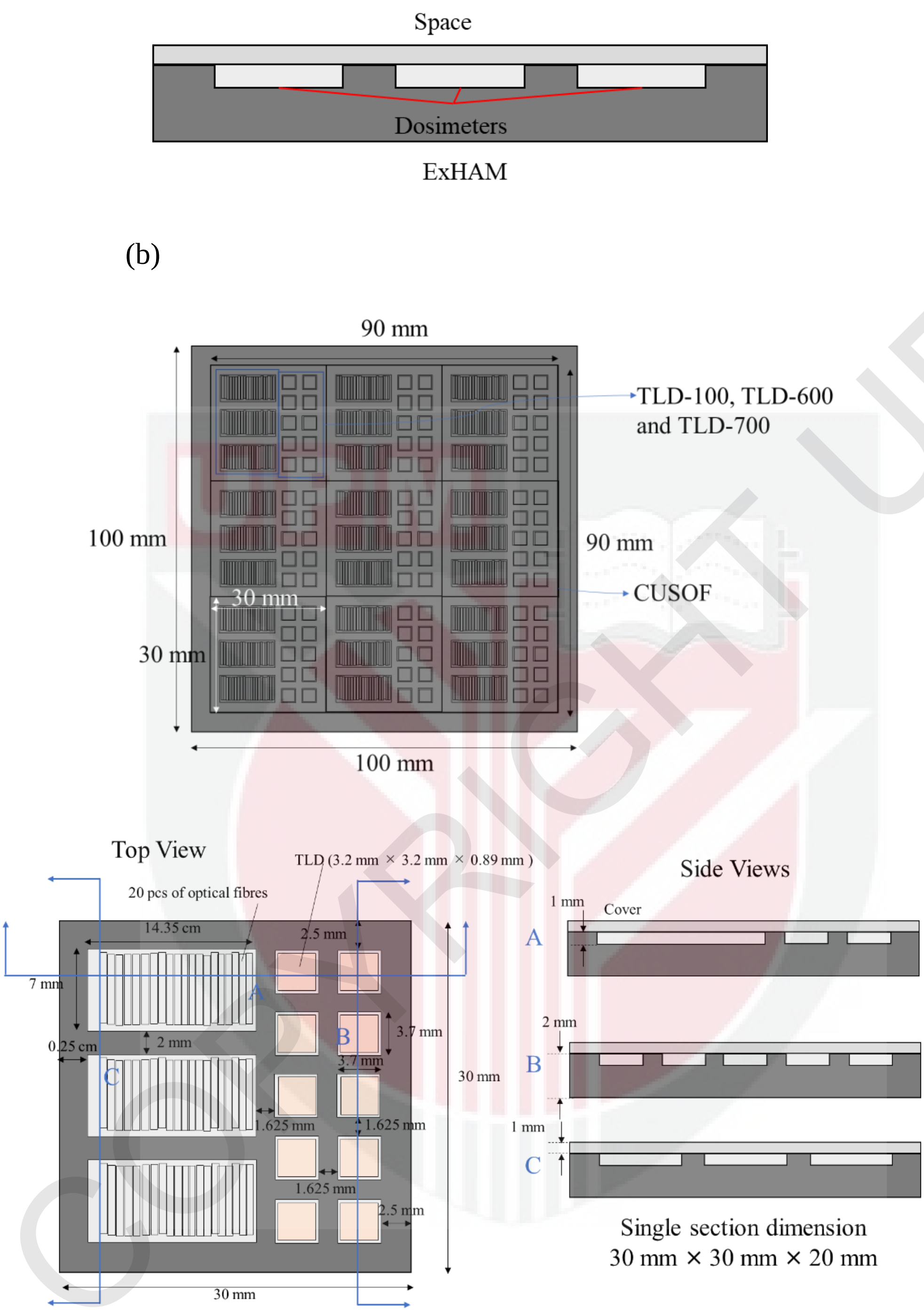


**Figure 3.6: Initial design concept. (a) Exposure method, (b) top view of the whole casing, (c) single area for PD placement**

The PD to be used are shown in Table 3.3. Here, CF is cylindrical fibres while FF is flat fibres. The CUSOF are doped with the same concentration of Germanium (Ge) but have different dimensions and core dimensions (Fadzil et al., 2022).

**Table 3.3: PD to be used in the first iteration**

| Label | Description | Diameter or Width [mm] | Length [mm] | Height [mm] |
|---|---|---|---|---|
| D9-1 | 6 mol% Ge-doped CUSOF (CF) | 0.48 | 6.00 | - |
| D9-2 | 6 mol% Ge-doped CUSOF (CF) | 0.61 | 6.00 | - |
| D9-3 | 6 mol% Ge-doped CUSOF (FF) | 0.62 | 6.00 | 0.17 |
| D10-1 | TLD-100 | 3.20 | 3.20 | 0.89 |
| D10-2 | TLD-600 | 3.20 | 3.20 | 0.89 |
| D10-3 | TLD-700 | 3.20 | 3.20 | 0.89 |

## 3.5 Second Iteration

### 3.5.1 Evaluation of Previous Iteration

Concerns were raised in the previous iteration on compartment area shown in Figure 3.6 (c) due to the space allocated for TLD placement and extraction. As such, modification to large space to accommodate multiple TLD was considered.

### 3.5.2 Ideation: Requirement Specification

The dimension of PD tabulated on Table 3.3 is carefully studied and the assembly process was simulated. According to SUI with UPM expertise, additional requirement of dimension and total area for TLD was conceptualized and additional requirement is tabulated in Table 3.4.

**Table 3.4: Additional requirement for the second iteration**

| Code/ Subcode | Requirements Type | Justification |
|---|---|---|
| **R1** | **Space radiation monitoring** | |
| R1-5 | Holes for TLD placement shall accommodate multiple pieces of the PD. | Easier placement and extraction of TLD during assembly |

### 3.5.3 Conceptualisation

The additional specification from Table 3.3 (R1-5) resulted design concept shown in Design concept for second iteration. (a) Top view of whole casing, (b) single area for PD placement. Here, each hole for TLD can hold up to two pieces of the material where the dimension for a single piece of TLD is 3.2 mm × 3.2 mm × 0.89 mm.

The design concept as added in Table 3.4 (R1-5) resulted in Figure 3.7. Here, each hole for TLD can hold up to two pieces of the material where a single piece is 3.2 mm × 3.2 mm × 0.89 mm.

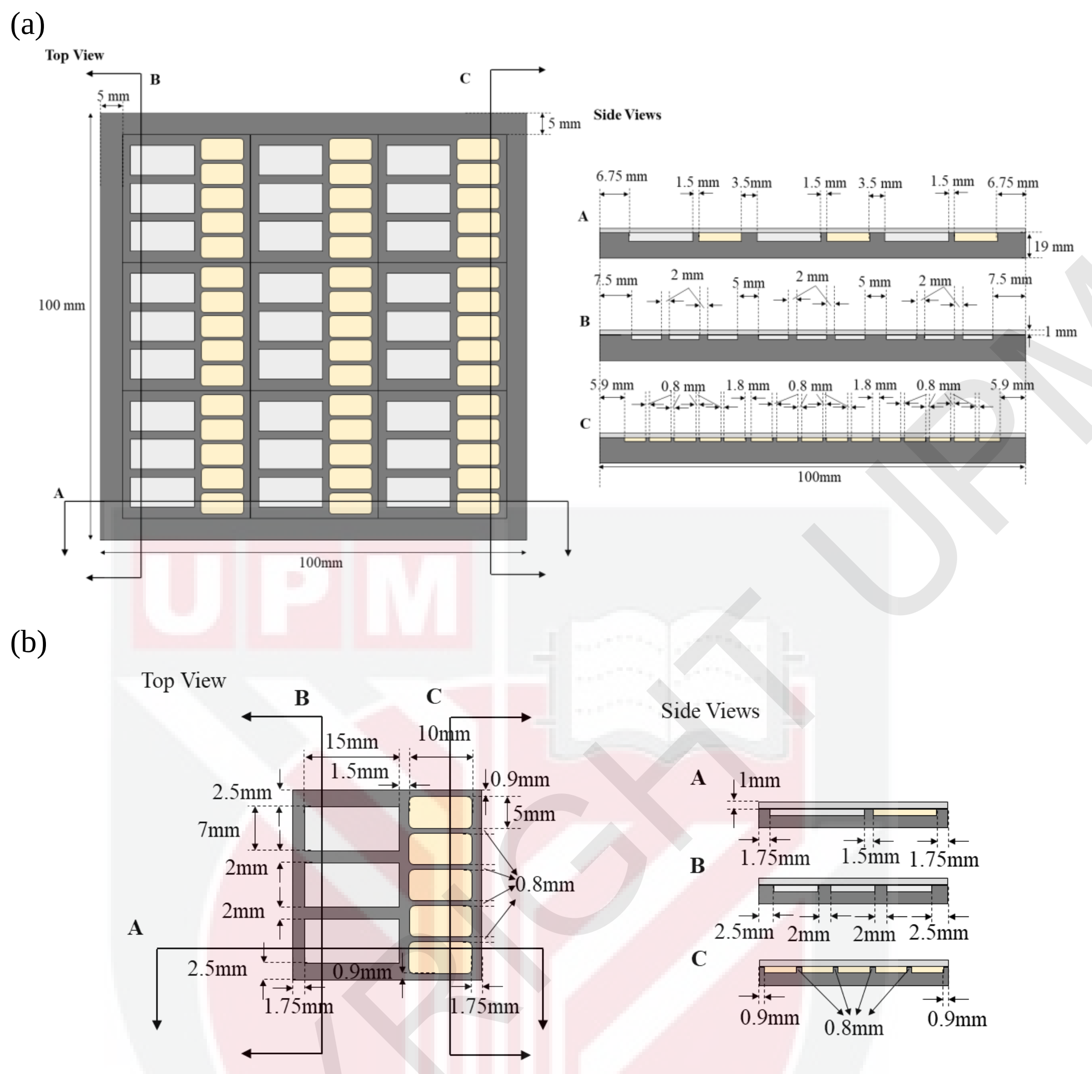


**Figure 3.7: Design concept for second iteration. (a) Top view of whole casing, (b) single area for PD placement**

## 3.6 Third Iteration

### 3.6.1 Evaluation of Previous Iteration

In the previous iterations, there are 9 individual compartment area for PD placement as shown on Figure 3.7 (a). While this will provide information on radiation source distribution, the number of repetitions is excessive and a waste of area. Other irradiation considerations such as the inclusion of radiation filters can provide more useful information. In the outer space environment, there are various types of radiation sources and energies, as discussed in Chapter 2, subsection 2.2.2. The quantification of radiation characteristics can be studied by using the mass attenuation ${}^{\mu}/_{\rho}$, and energy absorption ${}^{\mu_{en}}/_{\rho}$ of materials (ICRU Report 33 (1980)). According standard defined by ICRU Report 33 (1980), the ${}^{\mu}/_{\rho}$ is dependent on the interaction cross section between photon and atoms per unit atomic mass while ${}^{\mu_{en}}/_{\rho}$ is dependent on energy transfer for each interaction cross section between photon and atoms per unit atomic mass. The relation of both parameters is shown below in Equation (3.1 and Equation (3.2 (ICRU Report 33 (1980)).

$$ {}^{\mu}/_{\rho} = \frac{\sigma_{total}}{uA} \tag{3.1} $$

$$ {}^{\mu_{en}}/_{\rho} = \frac{f\sigma_{total}}{uA} \tag{3.2} $$

Here, the $\sigma_{total}$ is the total interaction cross section between photon and atoms, constant $u = 1.660 \times 10^{-24}$ g and *A* is the atomic mass of the element.

Therefore, according to this coefficient, the characterise of radiation in space can be studied by deducing an addition conceptual of radiation energy loss and energy deposition in materials. Hence, introducing an ample material capable to filter the radiation energy allows for the identification of the total amount of doses at different radiation types and energies.

The commercial TLD of TLD-100, TLD-600, and TLD-700 are all made of Lithium Fluoride doped with Magnesium and Titanium (LiF: Mg, Ti). In the second iteration, there are 10 pieces of TLD that will be placed in five individual areas. However, it was discovered that based only on appearance, it is impossible to distinguish between TLDs. Hence there would be a mix-up of two types of TLD in one individual area when the design concept in Figure 3.7 is used. Therefore, each type of TLD should be allocated a separate section for placement.

### 3.6.2 Ideation: Requirement Specification

Considering the evaluation of the previous iteration and SUI with the UPM experts, additional requirements for the third iteration are described in Table 3.5.

**Table 3.5: Additional requirements for third iteration**

| Code/ Subcode | Requirements Type | Justification |
|---|---|---|
| **R1** | **Space radiation monitoring** | |
| R1-6 | Each type of TLD shall have its own designated compartments. | To avoid a mix-up of different type of TLD. |
| R1-7 | One section shall be used to place other types of CUSOF. | To avoid a mix-up of different type of CUSOF. |
| R1-8 | The material for the main casing shall be made of water equivalent material. | To estimate dosimetric quantity kerma on human. |
| R1-9 | Consideration for filters shall be made based on radiation attenuation capability. | To characterise the energies of the radiation sources. |
| R1-10 | Consideration for filters shall be made based on mass. | Limitation of the total mass of the PADCIOF. |
| R1-11 | Calculations on attenuated radiation energies shall be made. | To estimate the radiation energies received by the PD. |
| | | |
| **R2** | **Space exposure utilising ExHAM** | |
| R2-2 | The total mass of SOFPADS shall be 200 g or less. | Initial mass limitation provided by JAXA. |

### 3.6.3 Ideation: Conceptualisation

The new PADCIOF is shown in Figure 3.8. The filters are placed on top of the dosimeters, secured by the case cover that facing to the space environment as shown on Figure 3.8 (a). Figure 3.8 (b) and (c) shows the PD configurations that satisfy R1-6. In this iteration the locations inside the casing are further labelled from A to I as in Figure 3.8 (b). The PD will be located to specific compartments as tabulated in Figure 3.8 (c). In the figure, section C has a different compartments dimension for the placement of OF shown in Table 3.6. These OF possess different dimensions and Ge-dopant concentrations compared to the OF in Table 3.3. Additionally, Commercial OF (COMOF) is also included to detect different type radiation energy and doses.

(a)

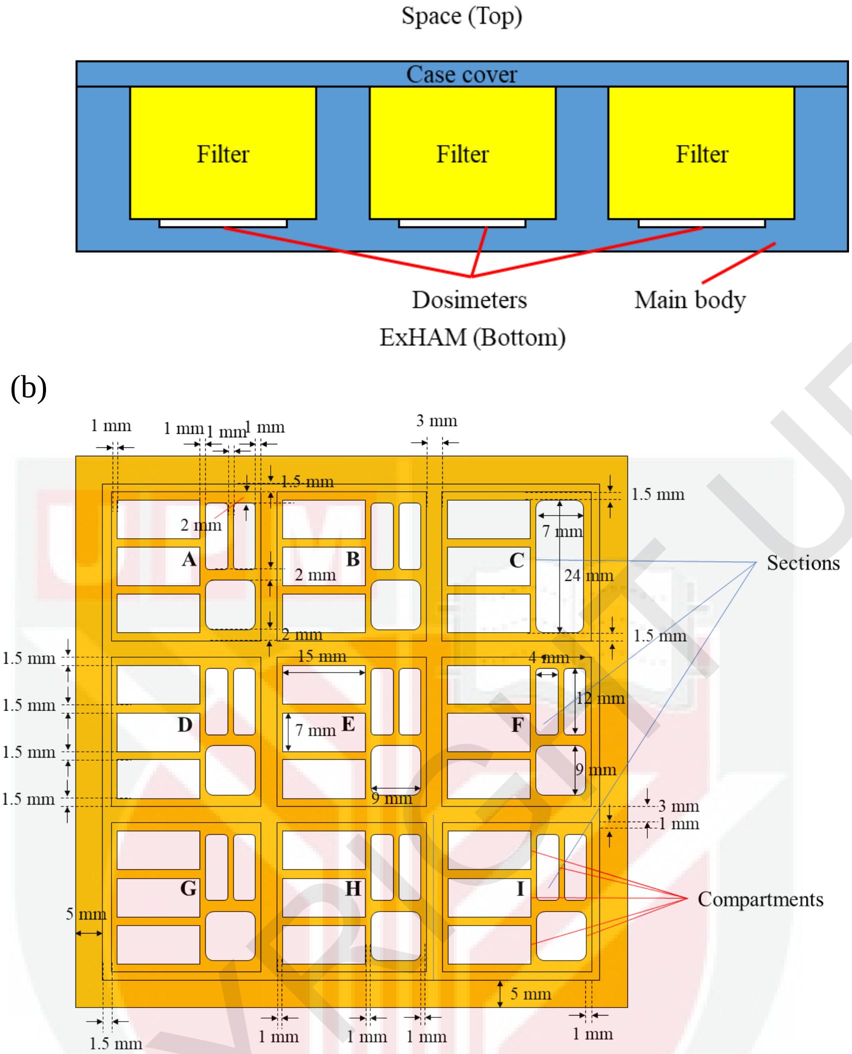


(c)

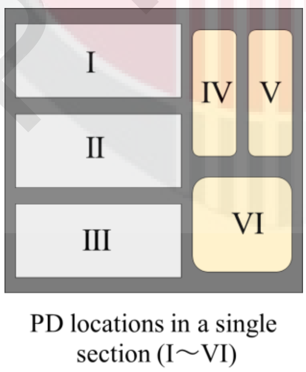


| Dosimeter location | Dosimeter type |
|---|---|
| I | D9-1 |
| II | D9-2 |
| III | D9-3 |
| IV | TLD-600 |
| V | TLD-700 |
| VI | TLD-100 |

**Figure 3.8: Design concept for third iteration. (a) Exposure method, (b) top view of the whole casing, (c) PD locations in a single section**

**Table 3.6: Additional OF to be used in the third iteration**

| Label | Description | Diameter or Width [mm] | Length [mm] | Height [mm] |
|---|---|---|---|---|
| D9-4 | 10 mol% Ge-doped CUSOF (CF) | 0.604 | 6.00 | |
| D9-5 | 2.3 mol% Ge-doped CUSOF (CF) | 0.475 | 6.00 | |
| D9-6 | 2.3 mol% Ge-doped CUSOF (FF) | 0.63 | 6.00 | 0.36 |
| D9-7 | 4 mol% Ge-doped COMOF | 0.125 | 6.00 | |

### 3.6.4 Materials Selection for the Casing Main Body and Case Cover

The current consideration for material concerns only in terms of radiation exposure which is described as R1-8 in Table 3.4. As discussed in Chapter 2, subsection 2.4.2, materials such as polyoxymethylene (POM), polymethylmethacrylate (PMMA), polyurethane (PU), polyetheeretherketone (PEEK), and polytetrafluoroethylene (PTFE) are suitable for main casing and case cover. Therefore, PMMA was suggested for the material for the main casing and case cover.

### 3.6.5 Materials Selection for the Filters

Materials selection for the filters is conducted to characterize the energies of radiation sources. The radiations energy is attenuated in accord to its path length in that particular materials as derived in Equation (3.1). Hence, high effective atomic number ($Z_{eff}$) materials are more suitable to attenuate protons, electrons, and photons while low $Z_{eff}$ materials are more suitable to attenuate neutrons (AbuAlRoos et al., 2019; Lee et al., 2020a). Aluminum (Al) is a common material used for electron shielding while PE is a common material used for neutron shielding (Cheraghi et al., 2023; Lee et al., 2020a). Even though lead is a common material used for photon shielding, this material is hazardous to the environment and humans (AbuAlRoos et al., 2019). Tungsten (W) is not toxic to the environment and has 1.4x higher shielding effect for photon radiation (Jang et al., 2018). As such, Al and W were proposed for proton, electron, and photon shields while PE was proposed for neutron shield.

In the next subsections, the method used to calculate the energies attenuated by each filter is presented. The information regarding the materials used as filters is gathered from National Institute of Standards and Technology (NIST) database (Hubbell and Seltzer, 1995). Table 3.7 shows the materials properties used as filters in this work. Hydrogen (H) and Carbon (C) are gathered too as they are the elements that constitutes PE. $Z_{eff}$ of PE is calculated using Equation (2.1) in Chapter 2, subsection 2.4.2 and its identical to result from Greene (2021) for a single chained PE.

**Table 3.7: Materials properties of filters** (Hubbell and Seltzer, 1995; Greene, 2021)

<table>
<tr><th>Material</th><th>Density, ρ [g/cm$^3$]</th><th colspan="2">Fraction by Weight</th><th>Atomic mass or molecular mass, M [g/mol]</th><th>Z / $Z_{eff}$</th></tr>
<tr><td>H</td><td>$8.37 \times 10^{-5}$</td><td colspan="2">1</td><td>2.01568</td><td>1</td></tr>
<tr><td>C</td><td>1.7 (graphite)<br>2 (amorphous)</td><td colspan="2">1</td><td>12.0107</td><td>6</td></tr>
<tr><td>W</td><td>19.3</td><td colspan="2">1</td><td>183.8</td><td>74</td></tr>
<tr><td>Al</td><td>2.7</td><td colspan="2">1</td><td>26.982</td><td>13</td></tr>
<tr><td rowspan="2">PE</td><td rowspan="2">0.94</td><td>H</td><td>C</td><td rowspan="2">28</td><td rowspan="2">5.44</td></tr>
<tr><td>0.1437</td><td>0.8563</td></tr>
</table>

### 3.6.6 Overall Mass Estimation

To consider requirement R2-2 in Table 3.5, the overall mass is estimated from the density and dimensions of each part. Table 3.8 shows the mass estimation of the main body and case cover. Density of PMMA is obtained from NIST (Hubbell and Seltzer, 1995). The mass is estimated by calculating the mass of overall dimension (97 mm × 97 mm × 19 mm) and subtracting the mass of the parts that are removed to create the compartments.

**Table 3.8: Estimated mass of SOFPADS's main body and case cover**

| Part | Material | Density, ρ [g/cm$^3$] | Length [cm] | Width [cm] | Height [cm] | Amount | Mass [g] |
|---|---|---|---|---|---|---|---|
| Main Body (without compartments) + Case Cover | PMMA | 1.19 | 9.70 | 9.70 | 1.90 | 1 | 212.74 |
| Removed compartments | PMMA | 1.19 | 2.70 | 2.70 | 1.50 | 9 | 117.11 |
| | | | | | | Mass with compartments [g] | 95.62 |
| | | | | | | Remaining allowable mass [g] | 104.38 |

Accordingly, the total mass weight of the filter materials (Al, W and PE) must less than 104.38 g as have estimated on Table 3.8. Therefore, the following dimension and configuration as shown in Table 3.9 and Figure 3.9 is proposed, such as:

1. Compartment in sections A and G do not have any filters
2. Compartment in sections B, D, E, and F will have filter material from Al and W at different thickness.
3. Compartment in section H will have 2 different filter materials at different Z numbers sandwiched to each other.
4. Comportment in section I will has filter material from PE.

**Table 3.9: Filters thicknesses and configuration for the third iteration**

| Compartment | Filters | Mass [g] |
|---|---|---|
| A | - | - |
| B | 5 mm Al | 8.44 |
| C | - | - |
| D | 15 mm Al | 25.31 |
| E | 0.5 mm W | 6.03 |
| F | 3.2 mm W | 36.19 |
| G | - | - |
| H | 0.5 mm W + 5 mm Al | 14.47 |
| I | 15 mm PE | 8.81 |
| | Total mass [g] | 99.25 |
| | Remaining allowable mass [g] | 5.13 |

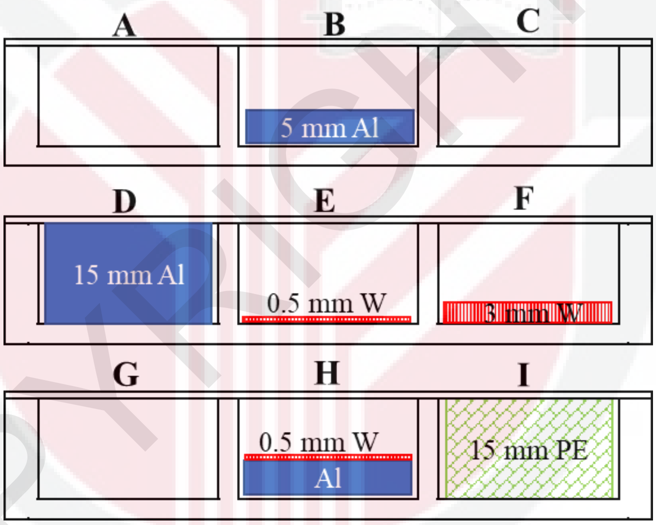


**Figure 3.9: Exposure configuration for each section for the third iteration**

Consequently, the total weight of the PADCIOF is estimated to be 194.87 g, thus allowing a mass of 5.13 g of PD to be placed in the casing (shown in Table 3.9). Table 3.10 shows the mass of the PD to be used in the PADCIOF. The mass of a single PD is calculated from a measurement made using about 10 pieces of PD in a single measurement then divided by the amount of PD used for measurement. The mass measurement was conducted using a Mettler Toledo's A&D HR-250A Analytical

Balance. Overall, the total estimated mass of the assembled SOFPADS is 198.69 g, allowing 1.31 g of extra tolerance of mass.

**Table 3.10: Mass of PD used for estimation of total mass**

| PD | Single Mass | Amount | Total Mass |
|---|---|---|---|
| D9-1 | 0.0024 | 248 | 0.599 |
| D9-2 | 0.0038 | 192 | 0.720 |
| D9-3 | 0.0014 | 192 | 0.266 |
| D9-4 | 0.0050 | 24 | 0.119 |
| D9-5 | 0.0030 | 31 | 0.094 |
| D9-6 | 0.0030 | 37 | 0.111 |
| D9-7 | 0.0001 | 120 | 0.017 |
| D10-1 | 0.0236 | 32 | 0.756 |
| D10-2 | 0.0236 | 24 | 0.567 |
| D10-3 | 0.0236 | 24 | 0.567 |
| Total mass [g] | | | 3.815 |
| Remaining allowable mass [g] | | | 1.311 |

### 3.6.7 Proton and Electron Filtered Energies

The filtered energies of protons and electrons for each material were calculated using Continuous Slowing Down Approximation Range (CSDA, unit in $cm^2/g$). The value of CSDA for each material were obtained from NIST's (National Institute of Standard and Technology) stopping power and range tables for electrons and protons, as shown in Figure 3.10. The thickness (X), required to stop electron/proton of a particular energy is shown in Equation (3.3).

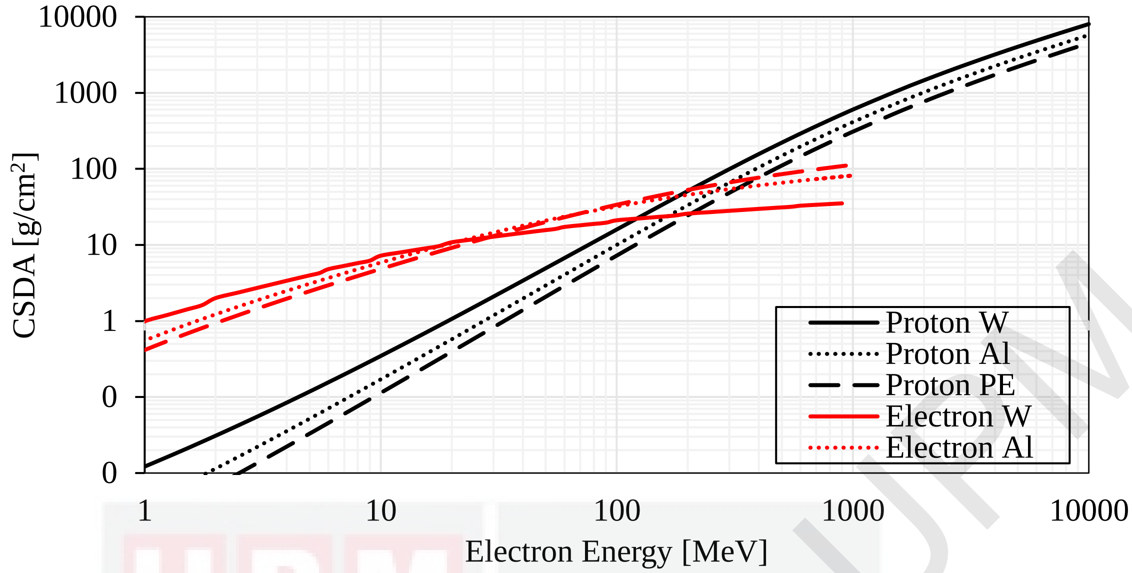


**Figure 3.10: CSDA range of proton and electron in W, Al and PE versus energy of the particles obtained from NIST**

$$X = \frac{CSDA}{\rho} \qquad (3.3)$$

### 3.6.8 Photon Attenuation

For photon, the mass attenuation coefficient (μ/ρ), where $\mu$ is the linear attenuation coefficient, for photon energies up to $10^4$ keV is shown in Figure 3.11. At lower energies, W have highest μ/ρ but around $10^3$ keV, the μ/ρ of all three materials are similar. The energy peaks in Al and W curves are due to contribution of photoelectron ejected for the element's respective shells (K-N shells) relative to binding energy of electron from each shell. The binding energies are specific to each element (Bell, 2023). Photoelectron is produced by photoelectric interaction which occur predominantly at lower energy (with energy range near to zero for negative electron affinity to over 1 MeV for core electrons in elements with a high atomic number). (Kloprogge et al., 2020; Attix, 2008). The peaks are labelled as K-edge (highest energy), followed by L-edge and continued. In radiology the K-edge properties is chosen for radiology application such as beam filters (Bell, 2023). However, for this work, the edges are occurrence that is not considered for the determination of thickness but exist. As such, there is a possibility that the attenuation of energies occurs at the edges. For W, there are three edges (K, L and M) while for Al there is one edge only. Later, from this coefficient, the attenuation strength of the radiation source is calculated using the Lambert-Beer's equation as shown in Equation (3.4) (Yildirim et al, 2016).

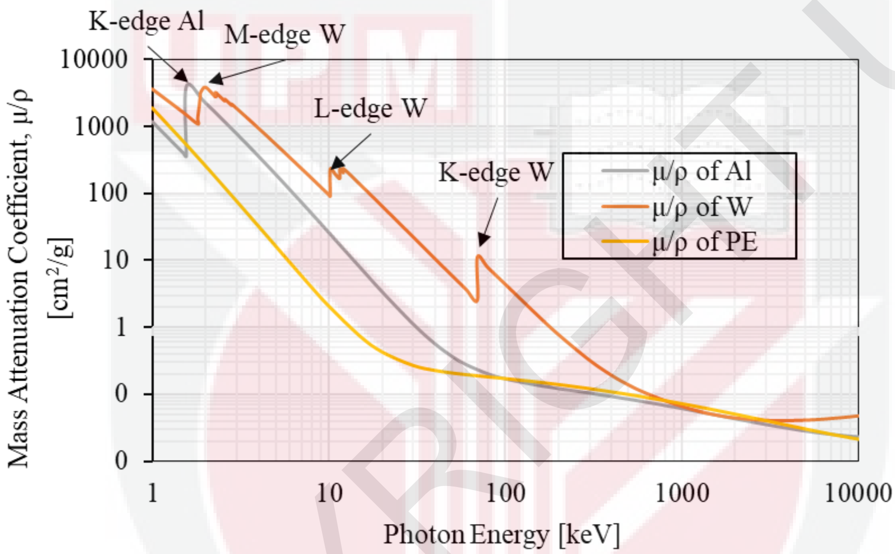


**Figure 3.11: μ/ρ of each filter obtained from NIST**

$$X = \frac{\ln \frac{I_o}{I}}{\mu/\rho} \tag{3.4}$$

Here, $I_o$ is the incident intensity and $I$ is the intensity of the photon beam at thickness X.

### 3.6.9 Neutron Attenuation

The neutron cross section ($\sigma$) for Al and W are taken from National Nuclear Data Center (NNDC, 2023) while the $\sigma$ for PE is taken from Lee et al. (2020b). Figure 3.12 shows the $\sigma$ for each neutron energy of up to $10^7$ eV. The hydrogenous PE possesses higher $\sigma$ in general especially up to $10^2$ eV, while Al and W relatively have low $\sigma$ values due to small absorption in metal. Starting from around $10^2$ eV for W and $5.9 \times 10^3$ eV for Al, there are resonance peaks showing. This is due to the energy of an incoming neutron matching the energy difference of two discrete energy states of the nucleus resulting in the absorption of the neutron by the nucleus of the matter where the nucleus adopts an excited state afterwards (Schulz et al., 2024). This occurs more prominently in higher $Z_{eff}$ materials due to the existence of more neutrons and protons that provides more possible ways for the neutron to fill the subshells resulting in more energy levels (Schulz et al., 2024).

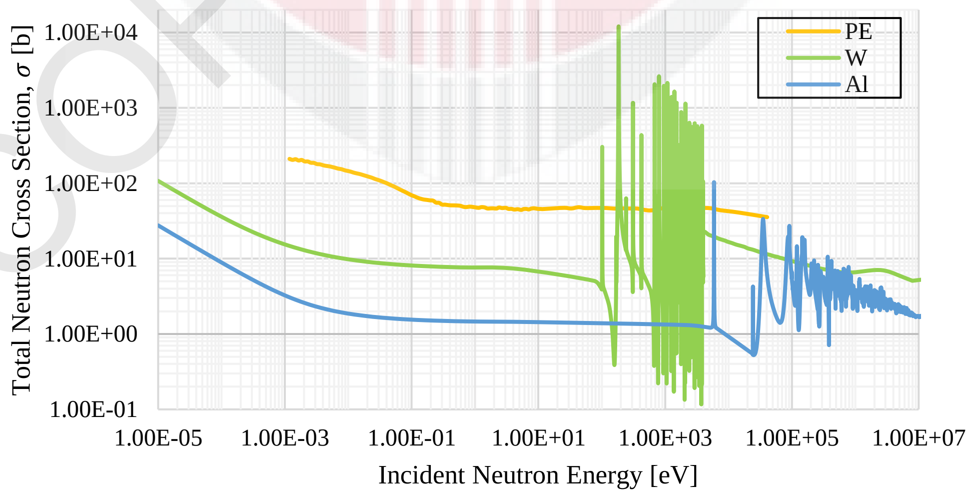


**Figure 3.12: $\sigma$ for each filter material**

Neutron attenuation is calculated using the equation by Wender et al. (2020) as in Equation (3.5) which is also a modification of the Lambert-Beer's equation.

$$\mathrm{X} = \frac{\ln \frac{I_o}{I}}{N\sigma} \tag{3.5}$$

Here, $N$ is atomic or molecular density of a compound and $\sigma$ is the total microscopic neutron cross section.

### 3.6.10 Prototyping: CAD Drawing

The CAD drawing of the design concept for the third iteration is shown in Figure 3.13. The drawing is used to fabricate the main body.

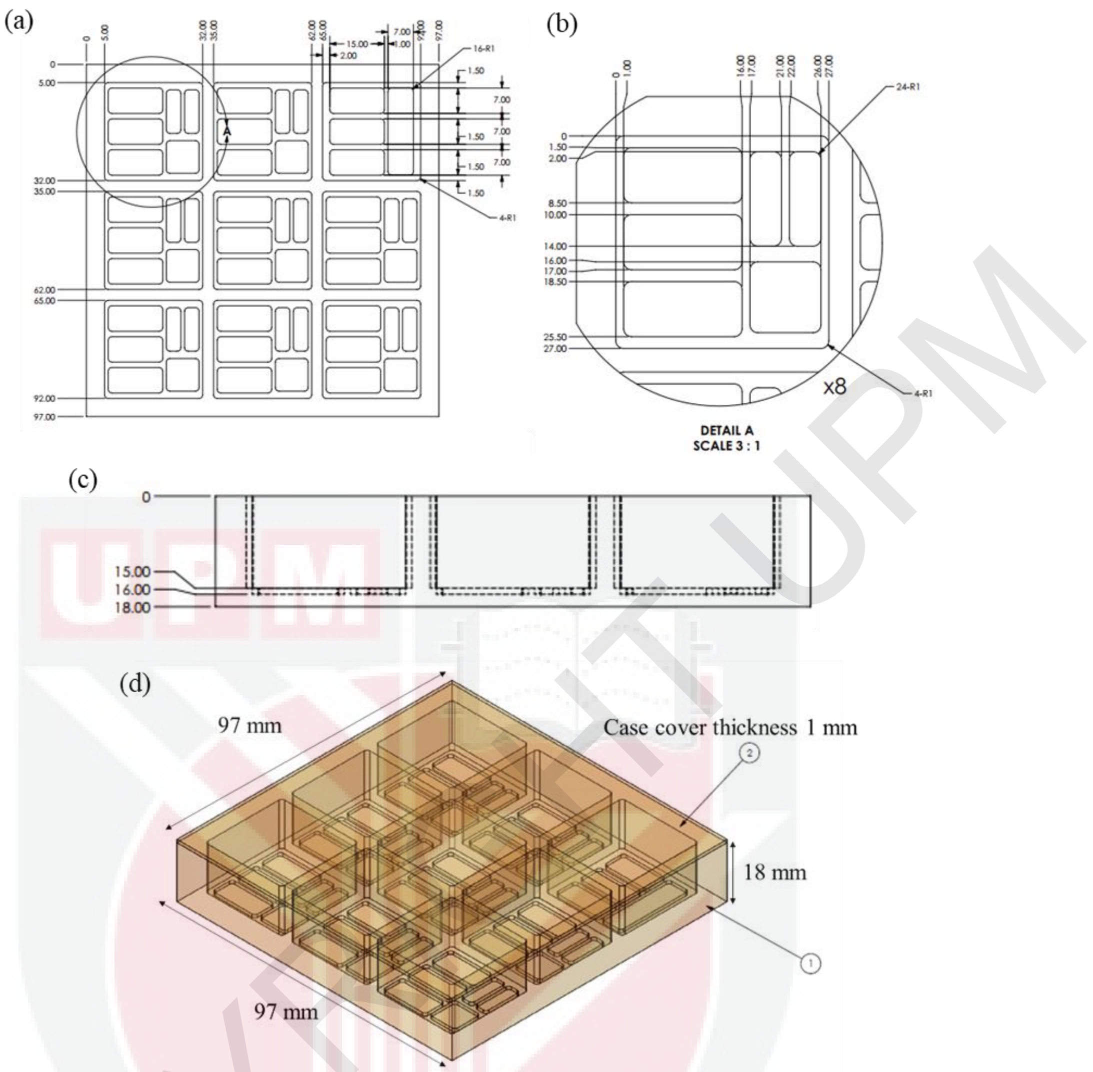


**Figure 3.13: CAD drawing of the design concept of the third iteration for the main body. (a) Top view, (b) single section top view, (c) side view, (d) orthographic view**

### 3.6.11 Build: Fabrication

The main body was fabricated by K&M Infinity Engineering using PMMA block, machined into the desired shape using Computerised Numerical Control (CNC) machine. Figure 3.14 shows the fabricated main body made from PMMA. Then, the fabricated main body in this iteration is used for FGD with JAXA. The first FGD with JAXA experts and MySA representative was conducted physically where the JAXA experts and MySA representative came to UPM. The FGD was conducted at meeting room of the Centre for Diagnostic Nuclear Imaging, UPM. This resulted in the requirements for the fourth iteration.

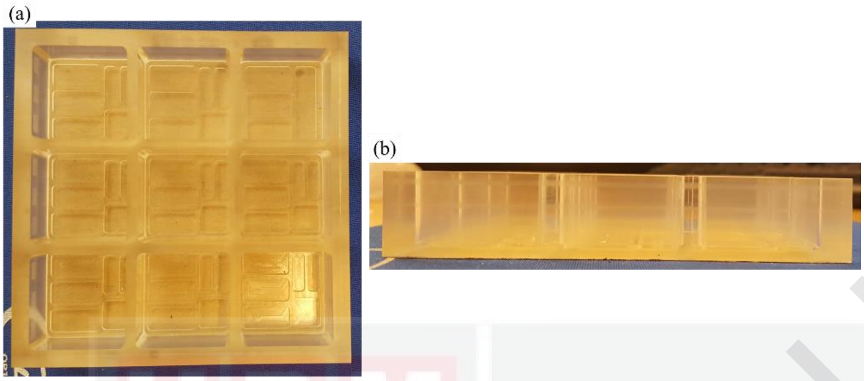


**Figure 3.14: Main body of fabricated SOFPADS during third iteration. (a) Top view, (b) side view.**

## 3.7 Fourth Iteration

### 3.7.1 Evaluation of Previous Iteration

In the previous iterations, the filter material and PD are placed in the main body directly without any mechanism to secure its. Initially, the case cover will be used to kept and secure the PD and filter materials. However, during the FGD with JAXA's experts, the securing mechanism must clearly define to avoid any damage. There are concern on displacement or movement of PD and filter materials during the transportation process.

### 3.7.2 Ideation: Requirement Specification

Table 3.11 shows the additional requirements after FGD with JAXA's experts. The table also include the amendment of R2-1 during the first iteration. Additional dimension tolerance is also added in the specification. The additional specifications are the materials for the main body and case cover, overall dimensions amendment, inclusion of shatterable materials containment, and inclusion of double lock mechanism for the case cover.

**Table 3.11: Additional and amendment of requirements for fourth iteration**

| Code/ Subcode | Requirements Type | Justification |
|---|---|---|
| **R2** | **Space exposure utilising ExHAM** | |
| R2-1 | The overall maximum dimension shall be 100 (+0/-1) mm × 100 (+0/-1) mm × 20 (+0/-2) mm (L×W×H). | ExHAM's sample size with tolerance added. |
| R2-3 | Case cover shall be secured onto the main body using a double lock mechanism. | Securement of case cover onto main body. |
| R2-4 | Empty spaces between the filters and the main body shall be occupied. | To secure the filters. |
| R2-5 | Shatterable materials shall be contained using mesh with opening of less than 50 μm. | Shatterable materials containment. |
| R2-6 | Material used for main body and case cover shall be able to sustain AO environment. | Survivability in space. |
| R2-7 | Material used for main body and case cover shall have strength to sustain damage. | Survivability in space. |
| R2-8 | All corners and edges of the case main body and the case cover shall be rounded with at least radius of 0.75 mm. | To protect crew members from sharp edges during all crew operations. |

### 3.7.3 Ideation: Conceptualisation

The double lock mechanism proposed is by using counter sunk screws to secure the case cover to the main body while locking the screws using c-clips to avoid the loosening of a singular screw (R2-3). As such, the case cover's thickness needs to be increased to accommodate the screws clips. However, increasing the thickness of the side facing the radiation source will increase the attenuation of the radiation. To avoid this a new method of exposure shown in Figure 3.15 is proposed. Here, the thickness of the side facing the space is maintained at 1 mm while the case cover is transferred to the side facing ExHAM where the thickness can be increased to 2.5 mm. The overall thickness of the case is increased to 19.5 mm to satisfy the amended requirement R2-1. Also, to satisfy R2-4, the PD are placed inside separate parts called the dosimeter holders and are contained using stainless steel mesh. The stainless-steel mesh is secured using Kapton (polyimide) tape.

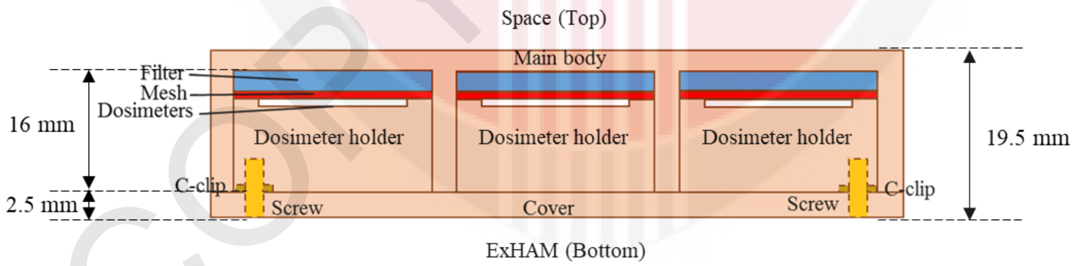

**Figure 3.15: Exposure method for the fourth iteration**

### 3.7.4 Materials Selection of Main Body and Case Cover

As reviewed in Chapter 2, subsection 2.3.2 and presented in Table 2.5, alternatively, PEEK possesses a good water equivalence at a $Z_{eff}$ of 6.38 (water's $Z_{eff}$ is 7.42), with highest strength at an ultimate tensile strength of 110 MPa in comparison to other polymers and low AO erosion at 2.99 $\times$ $10^{-24}$ $cm^3$/atom or loss of mass of 0.11 g. Previously, PEEK also have been reported to survive for three years in LEO in the ram direction of ISS with the highest AO concentration (Birnbacher et al., 2018; de Groh et al., 2006; de Groh et al., 2019; Muhsin et al., 2019).

### 3.7.5 Prototyping: CAD Drawing

From the conceptualisation made in the fourth iteration, CAD drawings were suggested as shown in Figure 3.16 to Figure 3.26. Each part of PADCIOF is labelled as presented in Table 3.12, together with its corresponding dimension. Later, the main bodies (MB1 and MB2) stl files were sent to JAXA for fit check. Countersunk screws (L1) are used to attach MB1 onto MB2 as it rests flush with the surfaces. C-clips (L2) are used to secure L1 onto MB1. The dosimeter holders (D1-D8) were used to contain the PD (D9-1 to D10-3) with further securement using stainless steel wire mesh (C1) and Kapton tape (C2). During the assembly of the PADCIOF, the filter materials (F1-F1) were placed first inside MB2 followed by the dosimeter holders (D1-D8). The quantity of PD was estimated using the dimension of the PD and the size of the allocated compartment areas in the dosimeter holder. Each part in is placed within MB2 according to the configuration in Table 3.13.

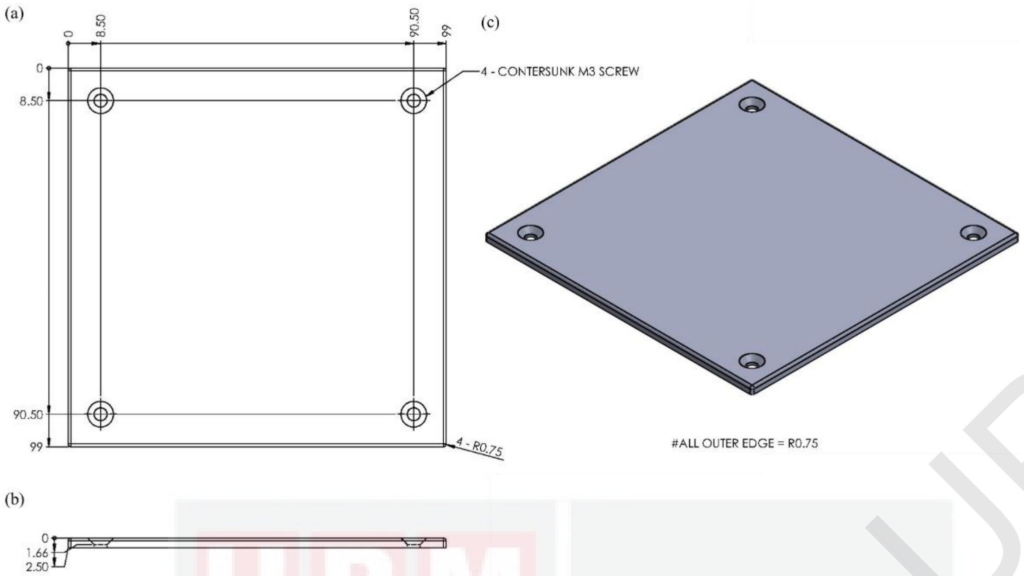


**Figure 3.16: Design of case cover (MB1): (a) Bottom view, (b) side view, (c) orthographic view**

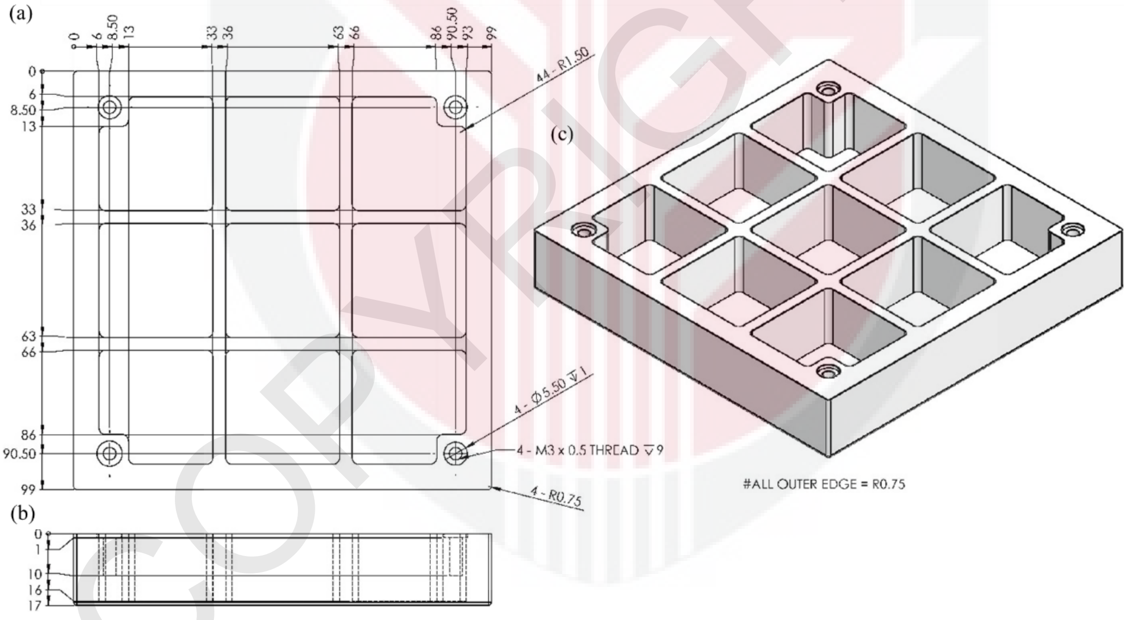


**Figure 3.17: Design of main body (MB2): (a) Bottom view, (b) side view, (c) orthographic view**

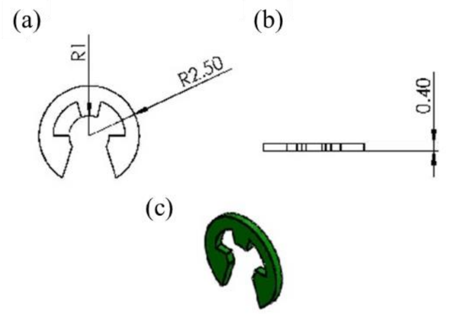


**Figure 3.18: C-clip (L2) design: (a) Top view, (b) side view, (c) orthographic view**

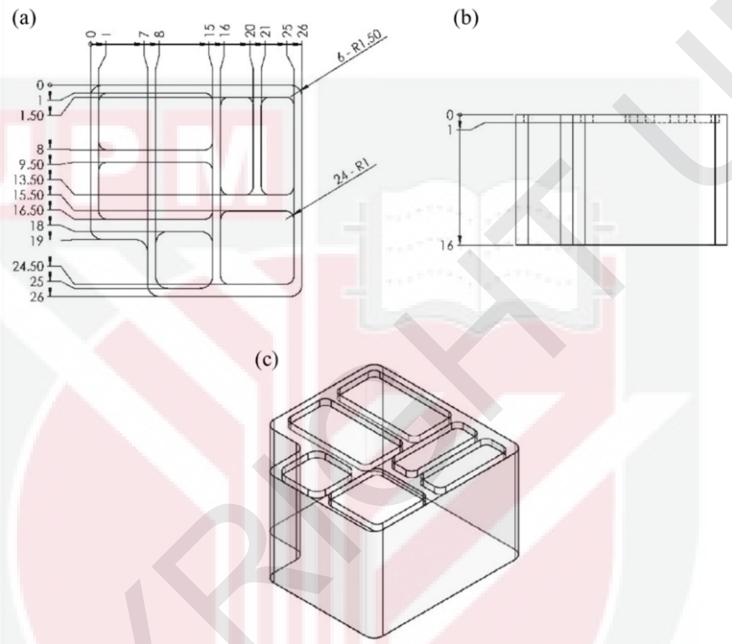


**Figure 3.19: Dosimeter holder (D1) design: (a) Top view, (b) side view, (c) orthographic view**

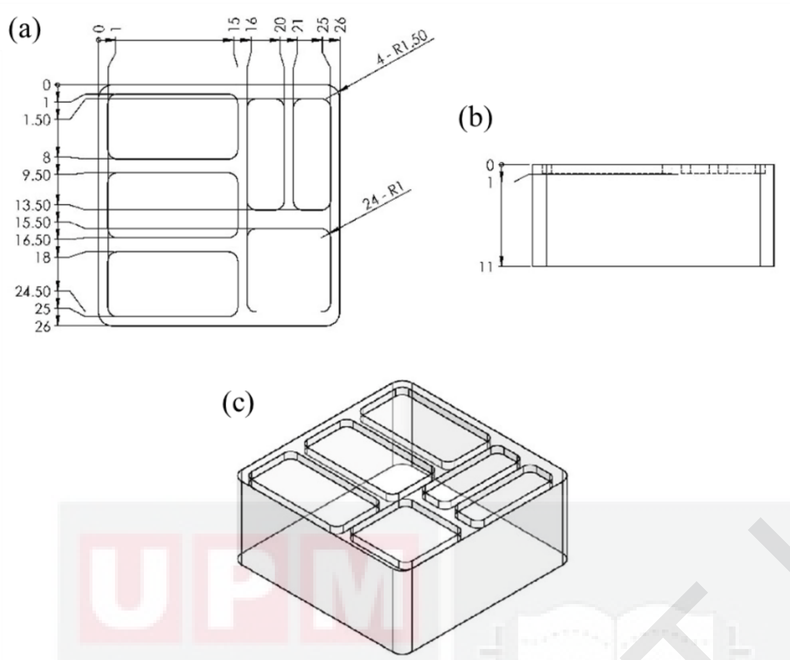


**Figure 3.20: Dosimeter holder (D2) design: (a) Top view, (b) side view, (c) orthographic view**

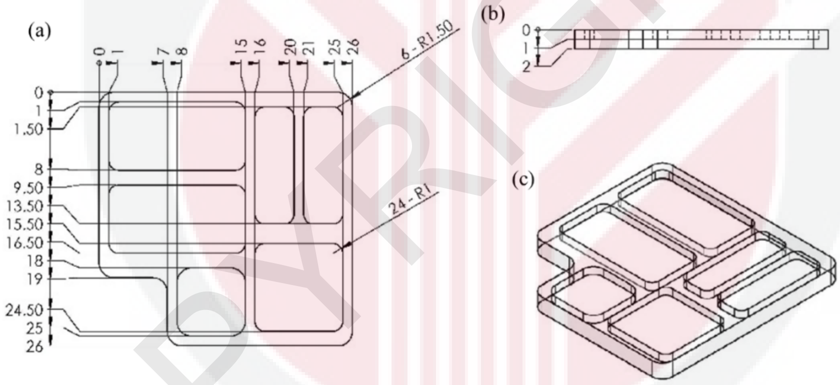


**Figure 3.21: Dosimeter holder (D3) design: (a) Top view, (b) side view, (c) orthographic view**

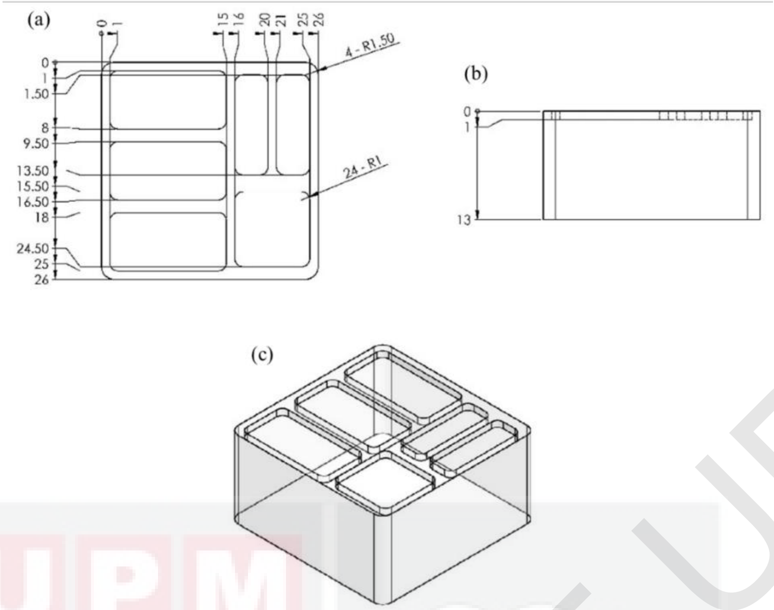


**Figure 3.22: Dosimeter holder (D4): (a) Top view, (b) side view, (c) orthographic view**

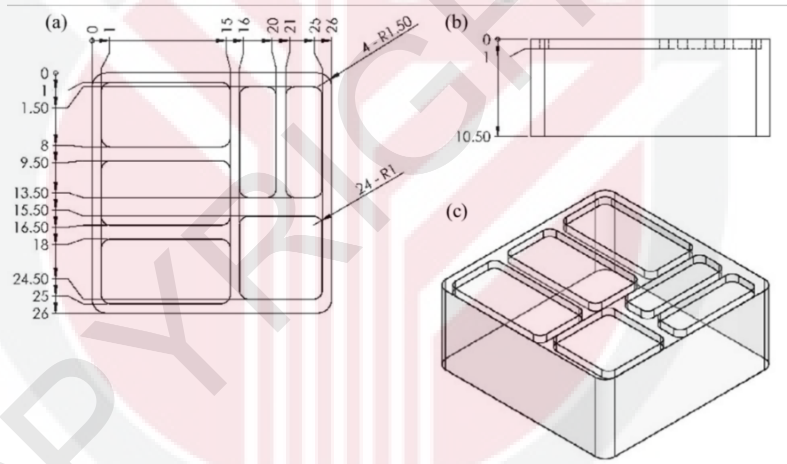


**Figure 3.23: Dosimeter holder (D5): (a) Top view, (b) side view, (c) orthographic view**

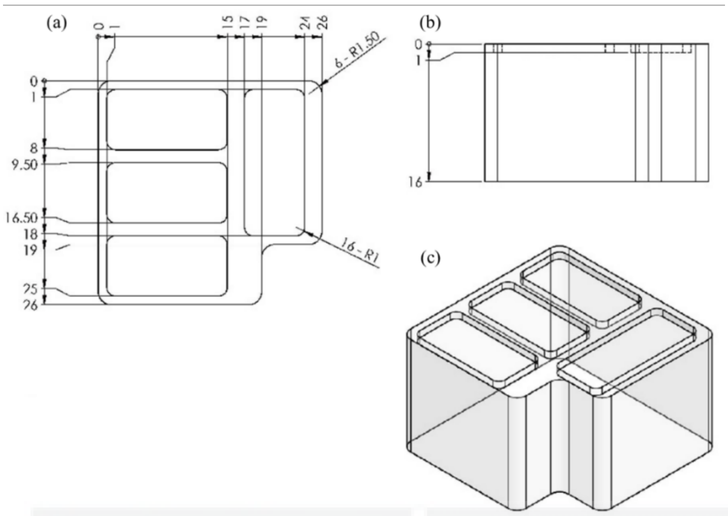


**Figure 3.24: Dosimeter holder (D6): (a) Top view, (b) side view, (c) orthographic view**

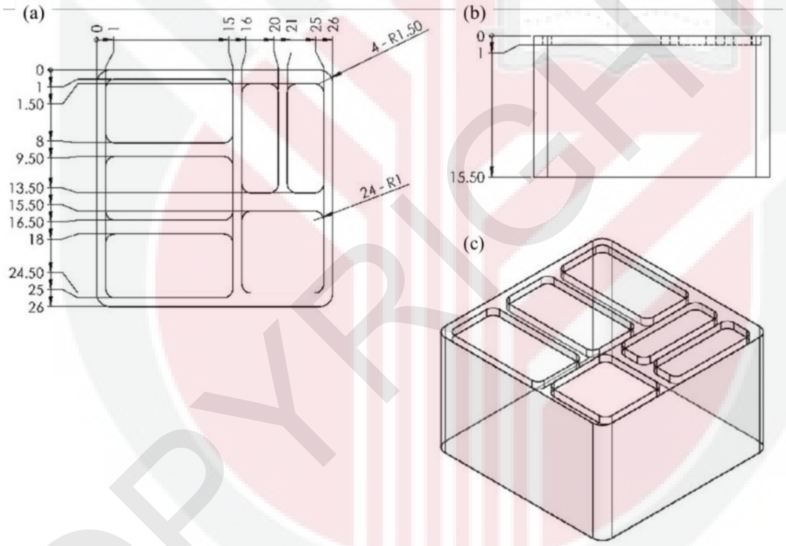


**Figure 3.25: Dosimeter holder (D7): (a) Top view, (b) side view, (c) orthographic view**

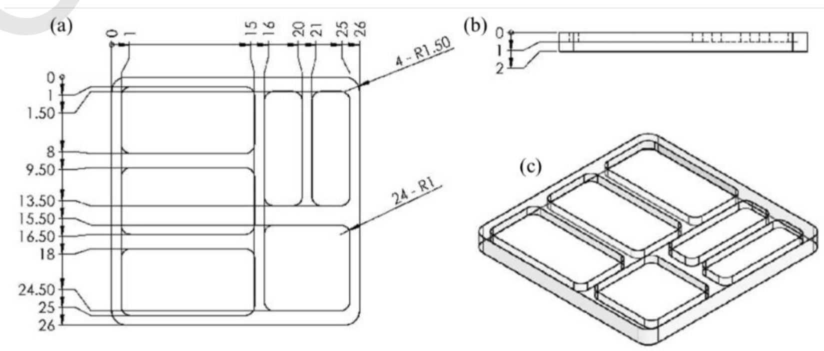


**Figure 3.26: Dosimeter holder (D8): (a) Top view, (b) side view, (c) orthographic view**

**Table 3.12: Parts of SOFPADS**

| Parts Label | Parts Name | Width or Diameter [mm] | Length [mm] | Height [mm] | Number |
|---|---|---|---|---|---|
| MB1 | Case cover | 99.00 | 99.00 | 2.50 | 1 |
| MB2 | Case main body | 99.00 | 99.00 | 17.00 | 1 |
| L1 | Countersunk M3 screw | 5.00 | | 12.00 | 4 |
| L2 | C-clip | 5.00 | | 0.40 | 4 |
| D1 | Dosimeter holder | 26.00 | 26.00 | 16.00 | 2 |
| D2 | Dosimeter holder | 26.00 | 26.00 | 11.00 | 1 |
| D3 | Dosimeter holder | 26.00 | 26.00 | 2.00 | 1 |
| D4 | Dosimeter holder | 26.00 | 26.00 | 13.00 | 1 |
| D5 | Dosimeter holder | 26.00 | 26.00 | 10.50 | 1 |
| D6 | Dosimeter holder | 26.00 | 26.00 | 16.00 | 1 |
| D7 | Dosimeter holder | 26.00 | 26.00 | 15.50 | 1 |
| D8 | Dosimeter holder | 26.00 | 26.00 | 2.00 | 1 |
| D9-1 | 6 mol% Ge-doped CUSOF (CF) | 0.48 | 6.00 | | 248 |
| D9-2 | 6 mol% Ge-doped CUSOF (CF) | 0.61 | 6.00 | | 192 |
| D9-3 | 6 mol% Ge-doped CUSOF (FF) | 0.62 | 6.00 | 0.17 | 192 |
| D9-4 | 10 mol% Ge-doped CUSOF (CF) | 0.60 | 6.00 | | 24 |
| D9-5 | 2.3 mol% Ge-doped CUSOF (CF) | 0.48 | 6.00 | | 31 |
| D9-6 | 2.3 mol% Ge-doped CUSOF (FF) | 0.63 | 6.00 | 0.36 | 37 |
| D9-7 | 4 mol% Ge-doped COMOF | 0.13 | 6.00 | | 120 |
| D10-1 | TLD-100 | 3.20 | 3.20 | 0.89 | 32 |
| D10-2 | TLD-600 | 3.20 | 3.20 | 0.89 | 24 |
| D10-3 | TLD-700 | 3.20 | 3.20 | 0.89 | 24 |
| F1 | W filter | 25.00 | 25.00 | 3.20 | 1 |
| F2 | W filter | 25.00 | 25.00 | 0.50 | 2 |
| F3 | Al filter | 25.00 | 25.00 | 5.00 | 2 |
| F4 | Al filter | 25.00 | 25.00 | 14.00 | 1 |
| F5 | PE filter | 25.00 | 25.00 | 14.00 | 1 |
| C1 | Mesh with 35 µm opening | - | - | 0.10 | 9 |
| C2 | Kapton tape | - | - | 0.07 | - |

**Table 3.13: Items to be placed inside the sections corresponding to the sections in (all sections will have stainless steel mesh (C1) and Kapton tape (C2))**

| Section | Filter material | | Dosimeter holder | Dosimeters |
|---|---|---|---|---|
| A | No filter | | D1 | D9-1, D9-2, D9-3, D10-1, D10-2 and D10-3 |
| B | F3 | 5 mm Al | D2 | D9-1, D9-2, D9-3, D10-1, D10-2 and D10-3 |
| C | No filter | | D1 | D9-1, D9-2, D9-3, D10-1, D10-2 and D10-3 |
| D | F4 | 14 mm Al | D8 | D9-1, D9-2, D9-3, D10-1, D10-2 and D10-3 |
| E | F2 | 0.5 mm W | D7 | D9-1, D9-2, D9-3, D10-1, D10-2 and D10-3 |
| F | F1 | 3 mm W | D4 | D9-1, D9-2, D9-3, D10-1, D10-2 and D10-3 |
| G | No filter | | D6 | D9-4, D9-5, D9-6 and D9-7 |
| H | F3 + F2 | 5 mm Al + 0.5 mm W | D5 | D9-1, D9-2, D9-3, D10-1, D10-2 and D10-3 |
| I | F5 | 14 mm PE | D3 | D9-1, D9-2, D9-3, D10-1, D10-2 and D10-3 |

### 3.7.6 Building: Fabrication and Assembly

Table 3.14 presents the material and supplier for each part. The properties of the materials were taken from the materials safety data sheet (MSDS) are shown in Table 3.15. The main bodies, dosimeter holders and PE filter were fabricated using the same method in the previous iteration. The screws, c-clips, W filters and Al filters are used as purchased. The stainless-steel wire mesh and Kapton tape were cut using scissors into desired dimensions. The SOFPADS was cut into 6 mm long using a ruby scriber. The TLD was used as it is.

**Table 3.14: Material and supplier for each part**

| Parts Label | Material | Supplier |
|---|---|---|
| MB1, MB2, D1, D2, D3, D4, D5, D6, D7 | PEEK Ketron 1000 | Quadrant Engineering Plastic Product |
| L1, L2 | Stainless steel | MISUMI Malaysia |
| D9-1, D9-2, D9-3, D9-4, D9-5, D9-6, | $SiO_2$: Ge | Multimedia University (MMU) |
| D9-7 | $SiO_2$: Ge | Coractive Inc. |
| D10-1, D10-2, D10-3 | LiF: Mg, Ti | Thermo Fisher Scientific |
| F1, F2 | 99% Tungsten | Luoyang Combat Tungsten and Molybdenum Material Co. Ltd. |
| F3, F4 | 7075 Alloy | K&M Infinity Engineering |
| F5 | Polymer | |
| C1 | 304L Stainless steel | Hebei Huan Yu Metal Products Co.,Ltd |
| C2 | Polymer | 3M |

**Table 3.15: Properties of filter materials**

| Properties | PEEK | W | 7075 Al | PE |
|---|---|---|---|---|
| Density [g/cm$^3$] | 1.31 | 19.20 | 2.71 | 0.95 |
| Melting temperature [°C] | 340 | 3410 | 582-652 | 125 |
| Tensile Yield Strength [MPa] | 110 | | 241 | 20 |
| Tensile Strain at break [%] | 20 | | | |
| Tensile Strain at yield [%] | | | 25 | 10 |
| Tensile Modulus [GPa] | 4.40 | | 0.24 | 0.70 |
| Compressive Stress at 1% strain [MPa] | 29 | | | |
| Compressive Stress at 2% strain [MPa] | 57 | | | |

Table 3.16 shows the total mass of each part in the fourth iteration totalling to a 310.28 g which exceeded the initial mass limitation provided by JAXA. Before changing any design concept, this value is used for further FGD with JAXA for the next iteration.

**Table 3.16: Mass of parts in the fourth iteration**

| Parts Label | Singular Mass [g] | Number | Total Mass [g] |
|---|---|---|---|
| MB1 | 32.51 | 1 | 32.51 |
| MB2 | 85.01 | 1 | 85.01 |
| L1 | 0.59 | 4 | 2.35 |
| L2 | 0.03 | 4 | 0.12 |
| D1 | 12.51 | 2 | 25.03 |
| D2 | 9.10 | 1 | 9.10 |
| D3 | 1.07 | 1 | 1.07 |
| D4 | 10.85 | 1 | 10.85 |
| D5 | 8.66 | 1 | 8.66 |
| D6 | 12.52 | 1 | 12.52 |
| D7 | 13.06 | 1 | 13.06 |
| D8 | 1.20 | 1 | 1.20 |
| D9-1 | 0.0024 | 248 | 0.60 |
| D9-2 | 0.00375 | 192 | 0.72 |
| D9-3 | 0.0014 | 192 | 0.27 |
| D9-4 | 0.00 | 24 | 0.12 |
| D9-5 | 0.00 | 31 | 0.09 |
| D9-6 | 0.00 | 37 | 0.11 |
| D9-7 | 0.00 | 120 | 0.02 |
| D10-1 | 0.02 | 24 | 0.57 |
| D10-2 | 0.02 | 24 | 0.57 |
| D10-3 | 0.02 | 32 | 0.76 |
| F1 | 38.50 | 1 | 38.50 |
| F2 | 6.26 | 2 | 12.51 |
| F3 | 8.44 | 2 | 16.88 |
| F4 | 25.31 | 1 | 25.31 |
| F5 | 9.10 | 1 | 9.10 |
| C1 | 0.12 | 9 | 1.05 |
| C2 | 0.05 | 36 | 1.66 |
| | | **Total [g]** | **310.28** |

The eyes size of the stainless steel wire mesh was measured using an Olympus BX51M microscope, and the image obtained is analysed using Olympus AnalySIS software.

From the image obtained in Figure 3.27, the wire mesh had an opening varying between 31.82 -38.07 µm while the wire diameter was varied between 28.93-34.30 µm. Therefore, the eyes size of the stainless-steel wire mesh is less than 50 µm which satisfy the requirement R2-5.

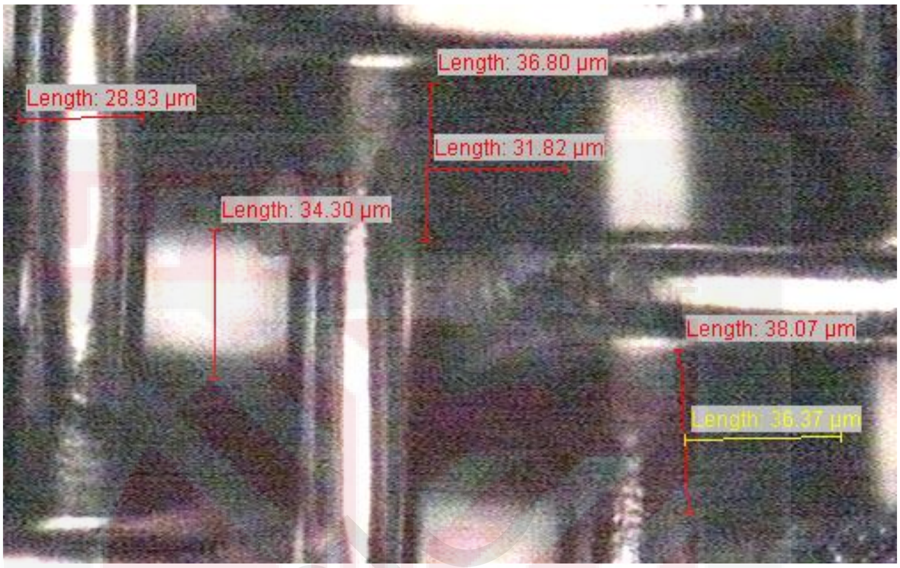


**Figure 3.27: Stainless steel mesh hole dimension**

The SOFPADS was assembled by placing the PD into the dosimeter holder using a vacuum tweezer (Figure 3.28 (a)). Then the PD was secured to the dosimeter holder using the wire mesh and Kapton tape as shown in Figure 3.28 (b)-(d).

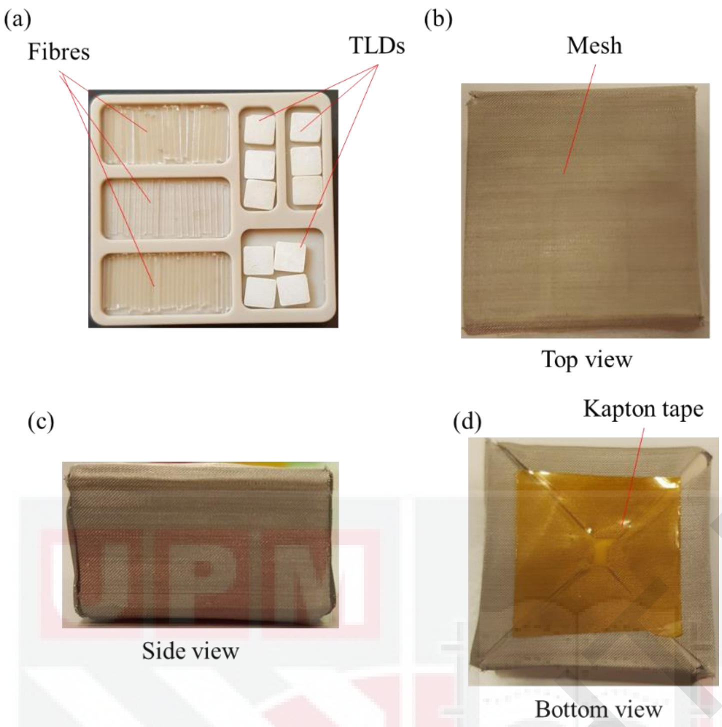


**Figure 3.28: Assembly of SOFPADS. (a) PD placement. (b) Top view, (c) side view, and, (d) bottom view after mesh placement**

In the next assembly process, the filter materials were placed inside MB2, followed by assembled dosimeter holders. The screws were attached to the MB1 using the c-clips (Figure 3.29 (a)) and finally MB1 is secured onto MB2 as shown in Figure 3.29 (b). The assembled SOFPADS is shown in Figure 3.29(c) and Figure 3.29 (d). This completed PADCIOF is then used for further SUI and FGD with JAXA.

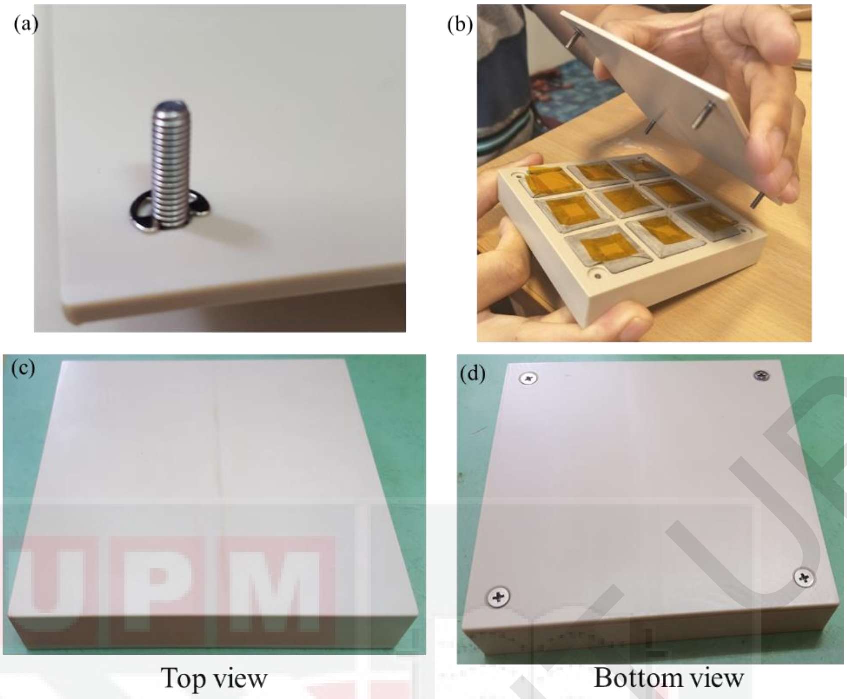

**Figure 3.29: Assembly of SOFPADS. (a) Attachment of screws onto MB1**

## 3.8 Fifth Iteration

### 3.8.1 Evaluation of Previous Design

There are issues raised from the SUI and FGD from the previous design as follows:

1) The application of stainless-steel wire mesh was clustered.

2) No vent holes for the case cover for outgassing.

3) The mass exceeded the initial mass limitation.

The result for the SUI and FGD is presented in the next section.

### 3.8.2 Ideation: Requirement Specification

Table 3.17 shows the additional and amended requirements for the fifth iteration. After FGD with JAXA experts, the initial mass limitation was raised to 434 g (R2-2). This is because the Japanese Experiment Module Remote Manipulator System (JEMRMS) can use a Small Fine Arm (SFA) that can carry up to 22.68 kg payload. The JEMRMS-SFA will carry ExHAM and attach the ExHAM to the experiment site. The mass of ExHAM is 14 kg and it can carry up to 20 experiment modules. As such, at maximum each module can reach up to 434 g.

**Table 3.17: Additional and amendment of requirements for the fifth iteration**

| Code/ Subcode | Requirements Type | Justification |
|---|---|---|
| **R2** | **Space exposure utilising ExHAM** | |
| R2-2 | The total mass of SOFPADS shall be less than 434 g. | Initial mass limitation lifted by JAXA. |
| R2-9 | Each section and compartment shall comply to a venting requirement as follows: $\mathrm{MEVR} = \frac{V}{A} = \leq 5080\ \mathrm{cm}$ | Vent holes for depressurisation and pressurisation. |
| R2-10 | Consideration shall be made on method of securement of PD within the dosimeter holder. | To improve the securement of PD. |

R2-9 is a requirement provided by NASA through JAXA. The maximum effective vent hole ratio (MEVR) is the value of the internal volume (V) over effective vent area (A). The differential pressure ( $\Delta$ P) can be determined using Equation (3.6) where g is gravity acceleration, R is the gas constant for air, T is temperature in Kelvin, C is the orifice discharge coefficient, dp/dt is the pressure decaying rate, and P is the external pressure where the rapid change of pressure occurs (Scialdone, 1998). Figure 3.30 shows the $\Delta P$ vs MEVR relation from Equation (3.6). The lower the MEVR is, the lower $\Delta P$ will be. With a constant internal volume, lower MEVR implies small vent holes area with capability to contain the parts inside. If the internal parts can be contained, any value of MEVR $\leq 5080$ cm is acceptable. In this case, the requirement R2-5 (Table 3.11) had described the MEVR and containment requirement for the dosimeter holder. In this iteration, the vent holes should be added on MB1 to satisfy the requirement R2-9.

$$\Delta P = \frac{1}{2gRT\left(\frac{V}{AC}\right)^2 (\frac{dp}{dt})^2/P} \tag{3.6}$$

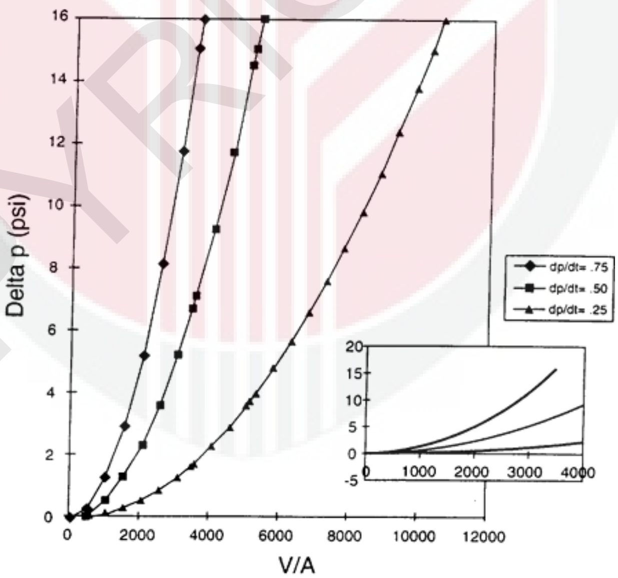


**Figure 3.30: $\Delta P$ vs V/A (MEVR) where P = 6 psi, T = 298 K, and, C = 0.65** (Scialdone, 1998)

### 3.8.3 Ideation: Conceptualisation

To satisfy R2-9, a 2 mm diameter through hole in the MB1 is proposed for each section. Table 3.18 shows the MEVR calculated from the proposed vent hole diameter which is lower than 5080 cm for each section.

**Table 3.18: MEVR for each section**

| Sections | Internal volume [cm$^3$] | Vent holes diameter [cm] | Vent holes area [cm$^2$] | MEVR [cm] |
|---|---|---|---|---|
| A, C, G, and I | 10.88 | 0.2 | 0.13 | 346.3 |
| B, D, E, F, and H | 11.66 | 0.2 | 0.13 | 371.3 |

The proposed method for the application of stainless-steel wire mesh is by cutting the wire mesh to the size of the outer dimension of the dosimeter holder and applying the Kapton tape on the perimeter of the wire mesh. In this method, the wire mesh will have an exposed area about 10 mm × 10 mm. The outcome of the proposed method is shown in Figure 3.31.

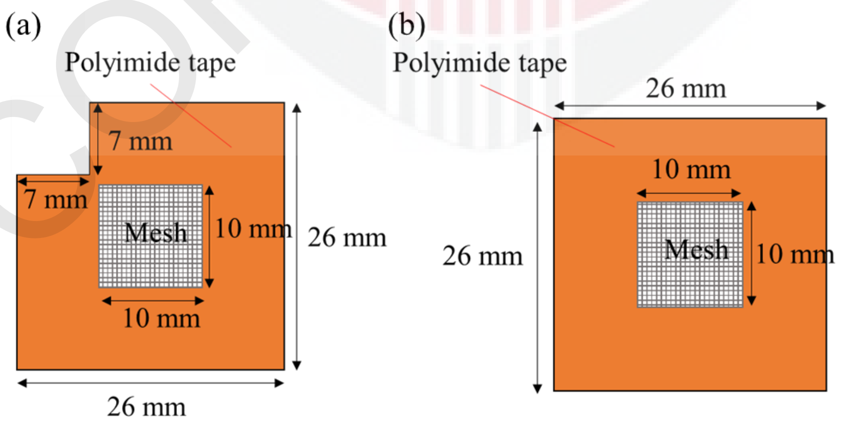


**Figure 3.31: Mesh application on top of the dosimeter holder. (a) Sections A, C, G and I, (b) sections B, D, E, F, and H**

The MEVR for the stainless-steel wire shown in Figure 3.31 is calculated by considering the exposed area of the wire mesh ($A_{tm}$) in Figure 3.32. Accordingly, the area of hole covered by the wire is 65 µm × 65 µm ($A_{mh}$). The opening of the wire mesh which equates to a single vent hole area ($A_h$) is 35 µm × 35 µm. Thus, the total number of holes (N) is $A_{tm}/A_{mh}$ and the total vent area ($A_t$) is $A_h \times N$.

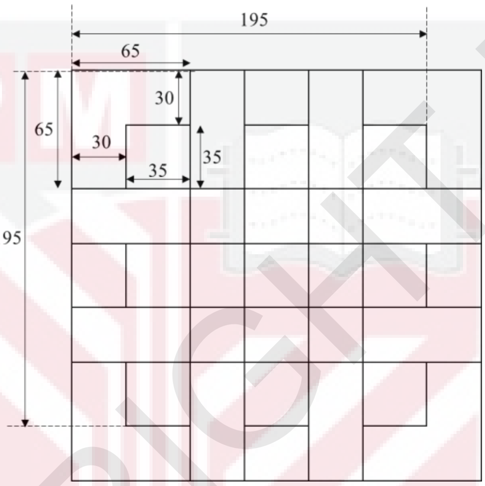


**Figure 3.32: Configuration of stainless-steel mesh (unit: µm)**

For dosimeter holders, total internal volume of the air (V) is considered as Figure 3.33. The Table 3.19 tabulated the calculated MEVR were found 5080 cm. This satisfied the requirement R2-9.

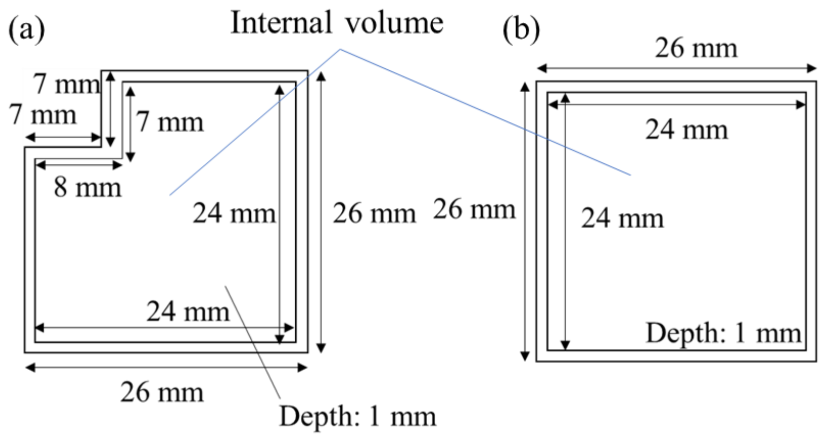


**Figure 3.33: Internal volume of dosimeter holders. (a) Sections A, C, G and I, (b) sections B, D, E, F, and H**

**Table 3.19: MEVR of assembled dosimeter holders**

| Sections | $A_h$ ×10$^{-5}$ [cm$^2$] | N | $A_t$ [cm$^2$] | V [cm$^3$] | MEVR [cm] |
|---|---|---|---|---|---|
| A, C, G, I | 1.23 | 23669 | 0.29 | 0.52 | 1.79 |
| B, D, E, H | 1.23 | 23669 | 0.29 | 0.58 | 1.99 |

### 3.8.4 Prototyping: CAD Drawing

In this new iteration, only MB1 has a change of design. Other parts used the same design as the fourth iteration. Figure 3.34 shows the MB1 with vent holes added while Figure 3.35 shows the CAD drawing of the assembled model.

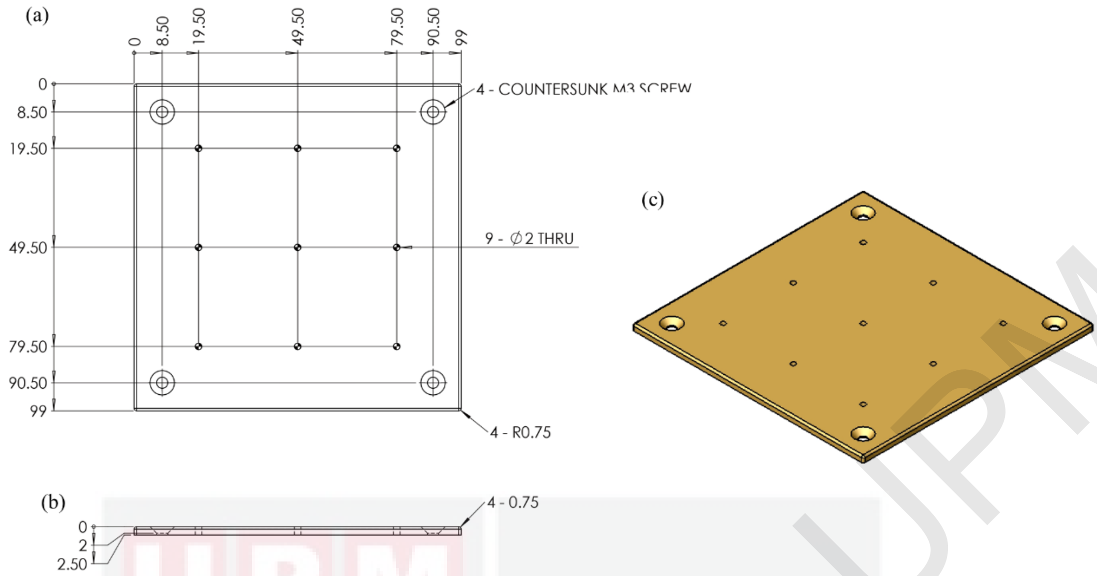


**Figure 3.34: Case cover design for the fifth iteration (MB1): (a) Bottom view, (b) side view and (c) orthographic view**

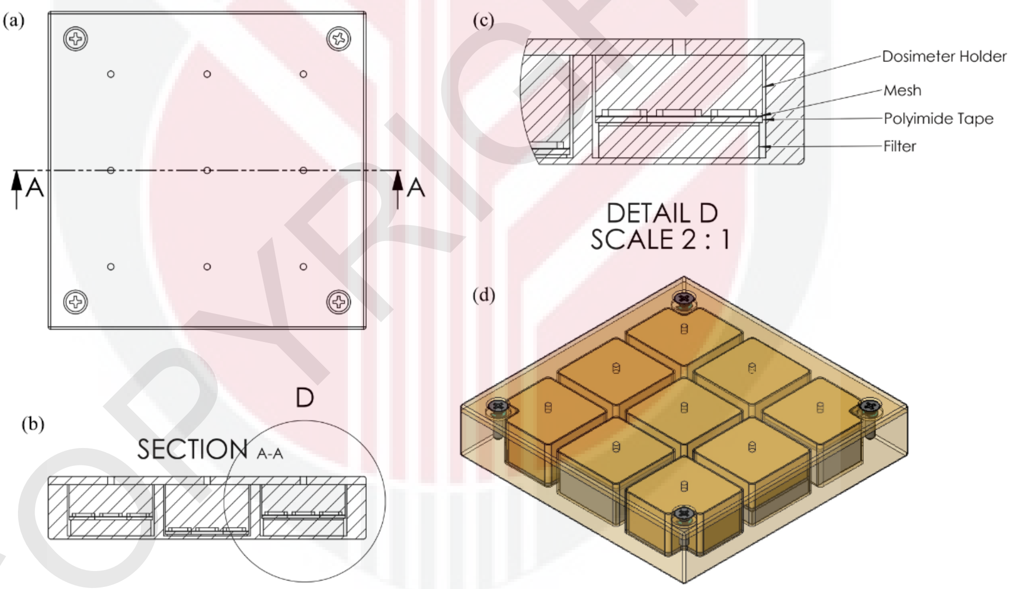


**Figure 3.35: Assembled SOFPADS design for the fifth iteration: (a) Bottom view, (b) side view from A point of view in (a), (c) enlarged view of circle in (b), (d) orthographic view (from the bottom of the model)**

### 3.8.5 Build: Fabrication and Assembly

The MB1 with vent holes is shown in Figure 3.36. The dosimeter holders with mesh attached is shown in Figure 3.37. Figure 3.38 shows the assembled SOFPADS.As can be seen from the figure, the case is slightly bulging in the middle area of MB1. SUI is conducted without FGD to fix the issue of bulging.


**Figure 3.36: MB1 with vent holes**

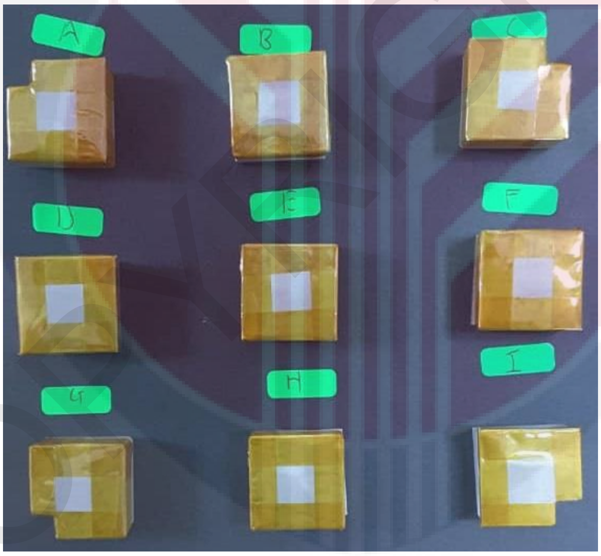

**Figure 3.37: Dosimeter holders with mesh attached**


**Figure 3.38: Assembled SOFPADS for the fifth iteration**

## 3.9 Sixth Iteration (Final Iteration)

### 3.9.1 Evaluation of Previous Design

Issues with previous design are as follows:

1) Bulging of the main body upon assembly.
2) Tightening of the screws with inconsistent torque (using normal screwdriver).

The result of SUI is presented in the subsequent section.

### 3.9.2 Ideation: Requirement Specification

The additional requirement for this iteration is as shown in Table 3.20. For R-11, the internal part heights need to be reduced as to not produce bulging. For R2-12, a torque screwdriver can be used to achieve the value of the torque. The value of the torque is obtained from the PEEL supplier suggesting that a torque value of less than 15 cNm should be used to avoid the breaking of PEEK material.

**Table 3.20: Additional requirements for the sixth iteration**

| Code/ Subcode | Requirements Type | Justification |
|---|---|---|
| **R2** | **Space exposure utilising ExHAM** | |
| R2-11 | The case shall not be bulging. | Quality control. |
| R2-12 | The screws shall be tightened with a torque value of 10 cNm. | To ensure sufficient tightening of screws to a specified torque. |

### 3.9.3 Ideation: Conceptualisation

To remove the bulging, 1 mm of height from the dosimeter holder should further be removed. For sections D and I, the filter materials can be cut instead since the dosimeter holders are at the lowest possible heights (1 mm depth for PD and 1 mm bottom thickness with a total of 2 mm in height). Table 3.21 shows the recommended heights for new parts.

**Table 3.21: List of parts with height reduced**

| Parts Label | Height [mm] | Number |
|---|---|---|
| D1 | 15.00 | 2 |
| D2 | 10.00 | 1 |
| D4 | 12.00 | 1 |
| D5 | 9.50 | 1 |
| D6 | 15.00 | 1 |
| D7 | 14.50 | 1 |
| F4 | 13.00 | 1 |
| F5 | 13.00 | 1 |

### 3.9.4 Build: Fabrication and Assembly

The dosimeter holders and filter materials were machined to reduce the heights by 1 mm. Then, the assembly process was conducted similar with the fifth iteration. The tightening process of the screws was conducted using a 1/4" Hex drive torque screwdriver with a torque value of 10 cNm as shown in Figure 3.39.

**Figure 3.39: 1/4" Hex drive torque screwdriver**

Figure 3.40 (a) shows the PD placement within each dosimeter holder. Figure 3.40 (b) shows the placement of dosimeter holders within the MB2. The filters are placed underneath the dosimeter holders. Figure 3.40 (c) shows the fully sealed SOFPADS using the torque screwdriver.

This iteration was the final iteration and sent for JAXA approval. Upon approval, all PADCIOF fabrication and assembly processes were followed the same as those used in this iteration. Table A1 in Appendix A shows every requirement used to develop PADCIOF.

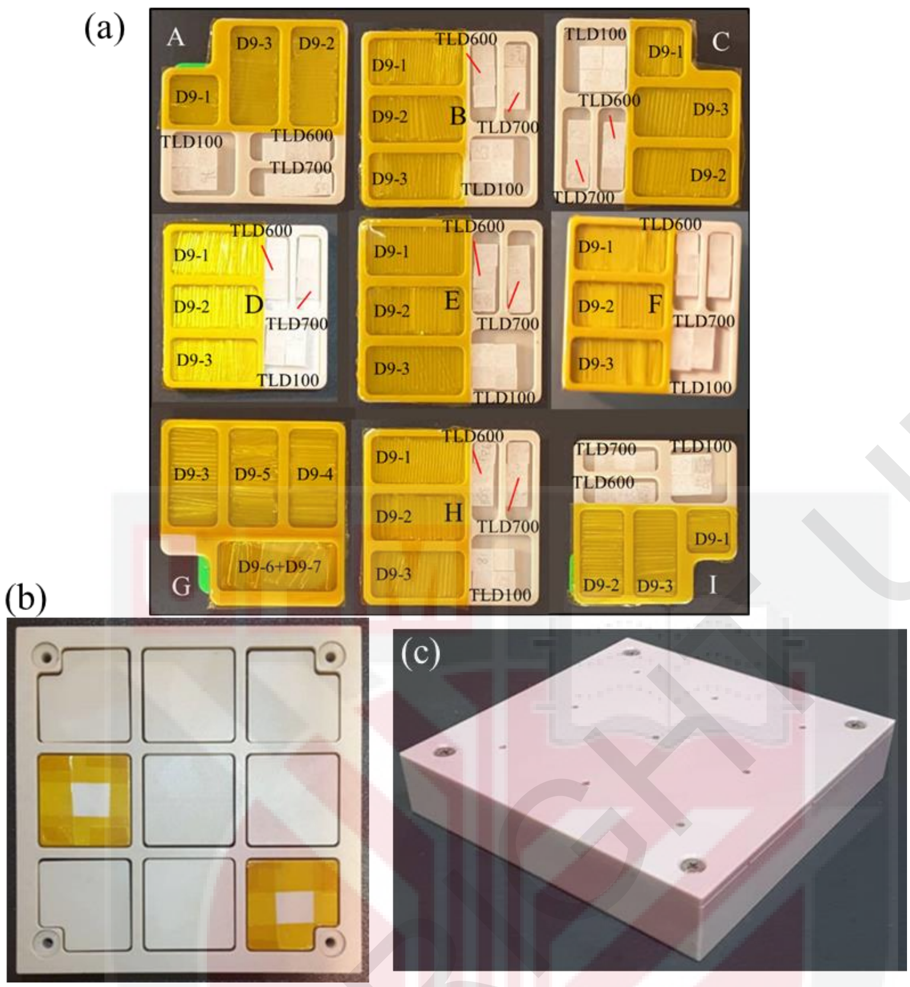


**Figure 3.40: Assembly of SOFPADS of the sixth iteration. (a) PD placement for each section, (b) condition of the MB2 internal part before sealing, (c) the casing has been sealed**

In total, five PADCIOF were fabricated according to Table 3.22. Resultantly, V1, V2 and V3 will be used for destructive quality test (QT) structural test. Specifically, the V1 is used to conduct the QT random vibration test and sine burst test. After the vibration test, V1 is used to conduct the puncture tests until a safety factor (SF) of 2.0. V2 and V3 are used to conduct puncture tests until failure. Flight Model (FM) is the actual model that will be used for space exposure. Prior to launching, the model is subjected to AT to assess the workmanship of the model. Finally, the Control Model (CM) is kept in a dark place as a control for background radiation on Earth.

**Table 3.22: List of SOFPADS versions and its application**

| Structure Model Number | Measurement |
|---|---|
| V1 | Random Vibration Test and Sine Burst Test under Qualification Level, Structural Load Test |
| V2 and V3 | Structural Load Test |
| FM | For ExHAM Utilisation, Random Vibration Test, Static Load Test under Acceptance Level |
| CM | Control on Earth |

## 3.10 Stage 2: Structural Integrity of the Developed SOFPADS

At this stage, the PADCIOF design had been approved by JAXA. The assembled PADCIOF are subjected to two types of structural tests: (1) vibration tests, and (2) structural load tests.

### 3.10.1 Vibration Tests for Qualification and Acceptance

The vibration tests were conducted at the Satellite Assembly, Integration and Test Facility (AIT), MySA for QT random vibration and sine burst. The purpose of QT level random vibration test is to verify PADCIOF ability to sustain the lift-off environment (García-Sánchez et al., 2024) while the sine burst test was to assess the effect of quasi-static load produced by ExHAM. The acoustic test (AT) random vibration test was conducted at the Dynamics & Vibration Laboratory, UPM due to breakdown of MySA's shaker. The tests were conducted under the guidance of MySA's personnel where the MySA's personnel provided with various technical expertise from the test setup to software input. Both QT and AT used the control software provided by MySA. JAXA provided the vibration profiles required as per NASA GEVS standard. The standard provides a procedure for the spectrum measurement of random vibration should be based on magnitude/levels measured at the component mounting locations during previous subsystem or payload testing (Goddard Technical Standard, 2021).

The schematics for the vibration tests conducted at MySA (QT) are shown in Figure 3.41. The vibration control software produces the initial signal according to the user input profile. The amplifier amplifies the controller's signal and drives the shaker. The payload is placed on top of the shaker (vibrator) where an accelerometer is placed near the payload for feedback to the controller to maintain the vibration profile. Table 3.23 shows the performance parameter of the LDS SPA 176 K amplifier used for QT. The amplifier is connected to the LDS V9 shaker where the performance parameter is shown in Table 3.24. The experimental setup of the vibration test is shown in Figure 3.42 where one accelerometer is connected to the payload and the vibration jig each. Figure 3.43 shows the vibration jig mounting the payload onto the slip table. The accelerometer on the jig is used for control while the accelerometer on the payload is used for the observation.

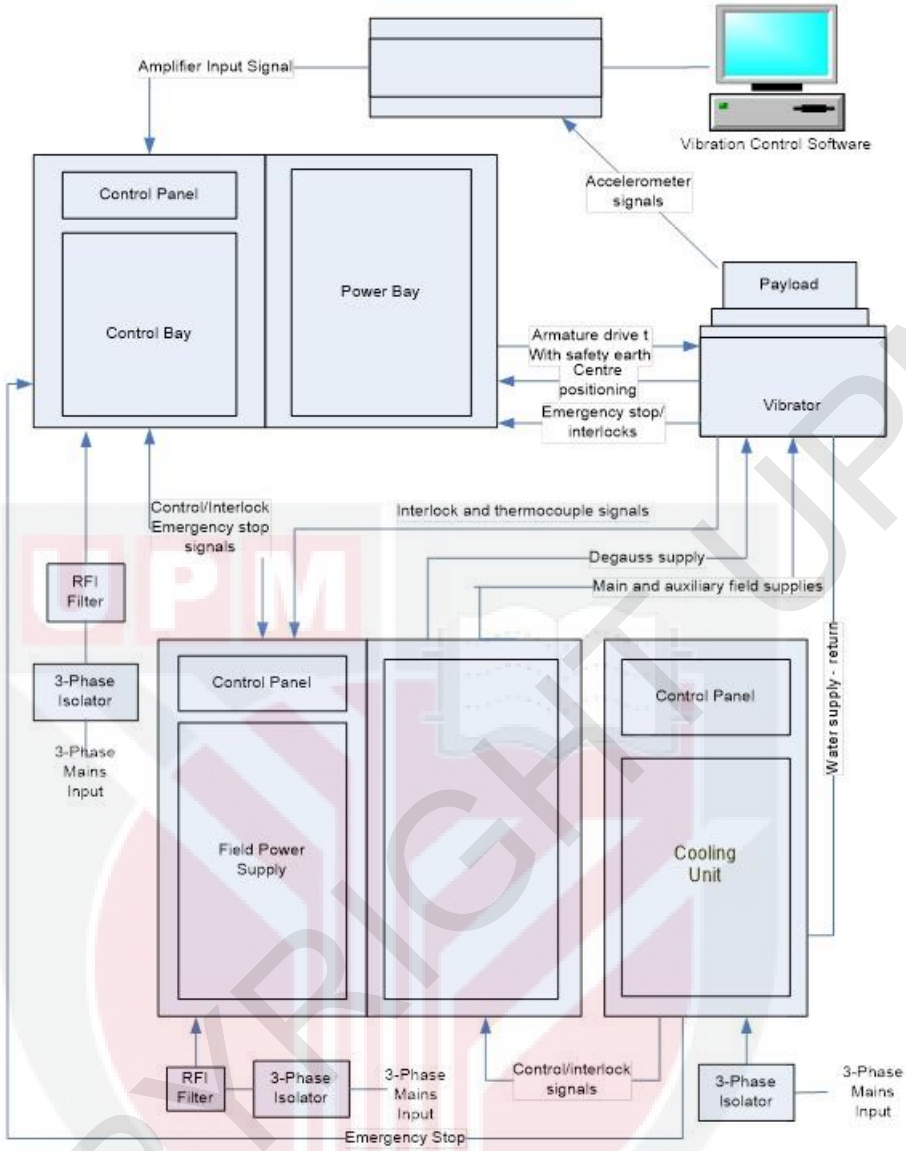


**Figure 3.41: Schematic for vibration test**

**Table 3.23: Performance parameters of amplifier**

| Performance Parameters | LDS SPA 176 K | MPA101 |
|---|---|---|
| Classification | Class D switching amplifier | |
| Amplifier Output [kVA] | 152-176 (8 kVa increments) | 2 |
| Total Harmonic Distortion (at rated Output) | -3 dB for 0.02-3 kHz | Less than 0.5% for d.c. (0.1 Hz)-0.5 kHz; Less than 1.0% for 0.5-5.0 kHz |
| Signal-Noise-Ratio | -68 dB | More than 65 dB at 100 Vrms output, 10 kΩ input termination with rated resistive load |

**Table 3.23: Continued**

| Performance Parameters | LDS SPA 176 K | MPA101 |
|---|---|---|
| DC stability | | Less than 0.05% of full output voltage with 10% change in line voltage |
| Input Drive | | 4 Vrms into 10 kΩ for full output (120 Vrms) |
| Input Sensitivity | 1.0 V for 100 Vrms output | |
| Amplifier Frequency Response | 20 Hz-3.0 kHz, ±1.5 dB | d.c.-4.5 kHz, ±3 dB |
| Switching frequency [kHz] | 150 | 112 |
| Modulation Range [kHz] | d.c.-10 | |
| Rated Output Voltage [Vrms] | 100 (sine) | |
| Maximum No-load Voltage [V] | 110 (sine) | |
| Output Offset voltage [mV] | ±100 (5-40°C) | |
| Maximum Output Voltage [Vrms] | | 120 |
| Continuous Output Current [Arms] | 80 | |
| Maximum Continuous Output Current [Arms] | | 50 |
| Maximum Transient Output Current [Arms] | | 150 |
| Input Impedance [kΩ] | 10 | |
| Efficiency [%] | >90 (not including field power supply) | |
| Power Factor | 0.95 | |

**Table 3.24: Performance parameters of shakers**

| Performance Parameters | LDS V9 | L215M |
|---|---|---|
| Armature Diameter [mm] | 440 | 150 |
| Sine Force (peak) [kN] | 105 | 1.96 |
| Random Force (rms) [kN] | 105 | 1.96 |
| Maximum half sine Shock Force [kN] | 193.1 | 3.92 |
| Armature Resonance ($f_n$) [kHz] | 2.0 | |
| Usable Frequency Range [kHz] | d.c.–2.7 | d.c. –4.5 |
| Mass of Moving Element (raised inserts) [kg] | 49.8 | |
| Velocity (sine peak) – full-field [m/s] | 3.0 | 1.8 |
| Acceleration (sine peak) [g] | 150 | |
| Acceleration (random rms) [g] | 70 | 10 |
| Displacement (pk-pk) – continuous [mm] | 76 | |
| Useable Shock – 20 kg payload [g] | >300 | |
| Useable Shock – 30 kg payload [g] | >200 | |
| Amplifier | LDS SPA 176 K | MPA101 |

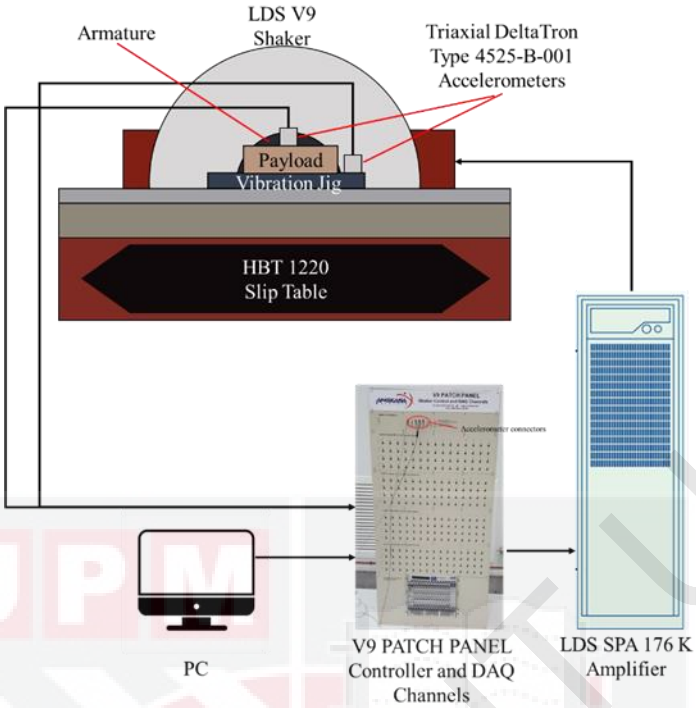


**Figure 3.42: Experimental setup of vibration test**

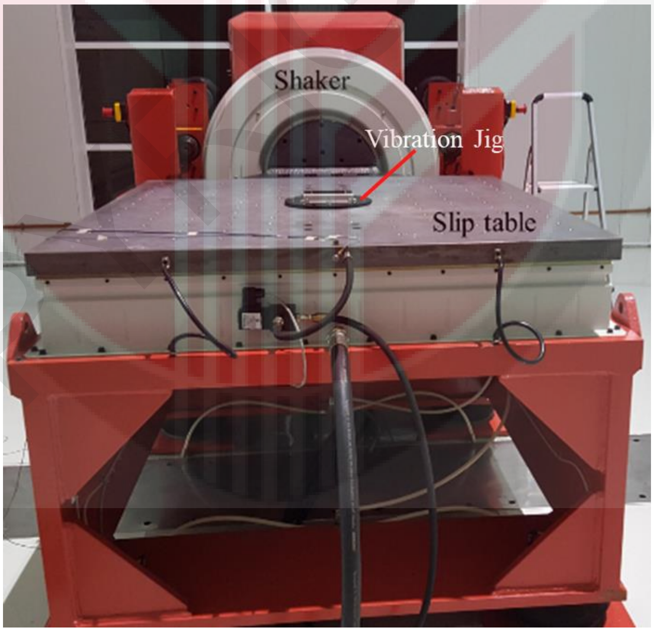


**Figure 3.43: Vibration jig mounted onto the slip table**

This work uses type 4525-B-001 Triaxial DeltaTron Accelerometers by Brüel & Kjær Sound & Vibration Measurement for both control and observation. The dynamic characteristics of the accelerometers are gathered in Table 3.25. For QT, in the x-axis and y-axis vibration tests, the payload is mounted to the vibration jig and is then mounted to the slip table. The slip table is connected to the armature of the shaker. For the vibration test in the z-axis direction, the shaker is rotated 90° and the jig is mounted directly to the armature of the shaker as shown in Figure 3.44.

**Table 3.25: Dynamic characteristics of type 4525-B-001 Triaxial DeltaTron Accelerometer**

| Parameters | X-axis | Y-axis | Z-axis |
|---|---|---|---|
| Reference Sensitivity at 159.2 Hz, 20 $m/s^2$ RMS, 4 mA supply current and 22.4°C [mV/g] | 93.14 | 99.40 | 94.49 |
| Frequency Range [kHz]<br>Amplitude (±10%)<br>Phase (±5%) | 0.001-5.5<br>0.002-3.0 | 0.001-5.5<br>0.002-3.0 | 0.001-10.0<br>0.002-3.0 |
| Measuring Range [g] | ±50 | ±50 | ±50 |
| Mounted Resonance Frequency [kHz] | 18 | 18 | 30 |
| Maximum Transverse Sensitivity at 30 Hz, 100 $m/s^2$ [%] | <5 | <5 | <5 |
| Residual Noise [mg] | 0.5 | 0.5 | 0.5 |

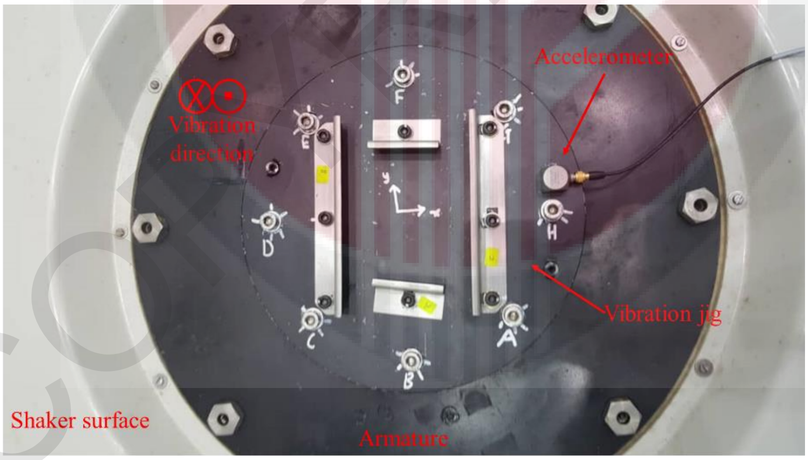


**Figure 3.44: Configuration of vibration jig for the z-axis tests**

AT random vibration test was conducted with the same experimental setup as Figure 3.41 but with different equipment. The amplifier used were MPA101 and L215M shaker. The performance parameters of the amplifier and shaker are shown in Table

3.23 and Table 3.24, respectively. The slip table used was GT300M slip table. The amplifier, shaker and slip table are all manufactured by ETS solutions. The accelerometers and control software were provided by MySA. The method of mounting is the same except for the z-axis, where the vibration jig was mounted onto a head expander as shown in Figure 3.45.

**Table 3.23: Performance parameters of amplifier**

| Performance Parameters | LDS SPA 176 K | MPA101 |
|---|---|---|
| Classification | Class D switching amplifier | |
| Amplifier Output [kVA] | 152-176 (8 kVa increments) | 2 |
| Total Harmonic Distortion (at rated Output) | -3 dB for 0.02-3 kHz | Less than 0.5% for d.c. (0.1 Hz)-0.5 kHz; Less than 1.0% for 0.5-5.0 kHz |
| Signal-Noise-Ratio | -68 dB | More than 65 dB at 100 Vrms output, 10 kΩ input termination with rated resistive load |

**Table 3.23: Continued**

| Performance Parameters | LDS SPA 176 K | MPA101 |
|---|---|---|
| DC stability | | Less than 0.05% of full output voltage with 10% change in line voltage |
| Input Drive | | 4 Vrms into 10 kΩ for full output (120 Vrms) |
| Input Sensitivity | 1.0 V for 100 Vrms output | |
| Amplifier Frequency Response | 20 Hz-3.0 kHz, ±1.5 dB | d.c.-4.5 kHz, ±3 dB |
| Switching frequency [kHz] | 150 | 112 |
| Modulation Range [kHz] | d.c.-10 | |
| Rated Output Voltage [Vrms] | 100 (sine) | |
| Maximum No-load Voltage [V] | 110 (sine) | |
| Output Offset voltage [mV] | ±100 (5-40°C) | |
| Maximum Output Voltage [Vrms] | | 120 |
| Continuous Output Current [Arms] | 80 | |
| Maximum Continuous Output Current [Arms] | | 50 |

| Performance Parameters | LDS SPA 176 K | MPA101 |
|---|---|---|
| Maximum Transient Output Current [Arms] | | 150 |
| Input Impedance [kΩ] | 10 | |
| Efficiency [%] | >90 (not including field power supply) | |
| Power Factor | 0.95 | |


**Figure 3.45: AT random vibration test setup with an expander attached to the armature of the shaker**

### 3.10.2 Vibration Jig

The vibration jig is designed in house to mount the PADCIOF to the slip table/armature/expander for vibration tests. The CAD drawing of the vibration jig for QT is shown in Figure 3.46. The vibration jig consists of a 10 mm thickness base plate made of mild carbon steel with eight 9 mm-diameter through holes for mounting purposes. Another set of 6 mm-diameter threaded through holes used to attach the stainless-steel brackets that were used to hold the PADCIOF. The CAD drawings of the side brackets are shown in Figure 3.47 and Figure 3.48 for the centre bracket. The vibration jig was fabricated by I Pro Skill Engineering Sdn. Bhd that machined the materials into the desired dimensions. Figure 3.44 shows the fabricated vibration jig.

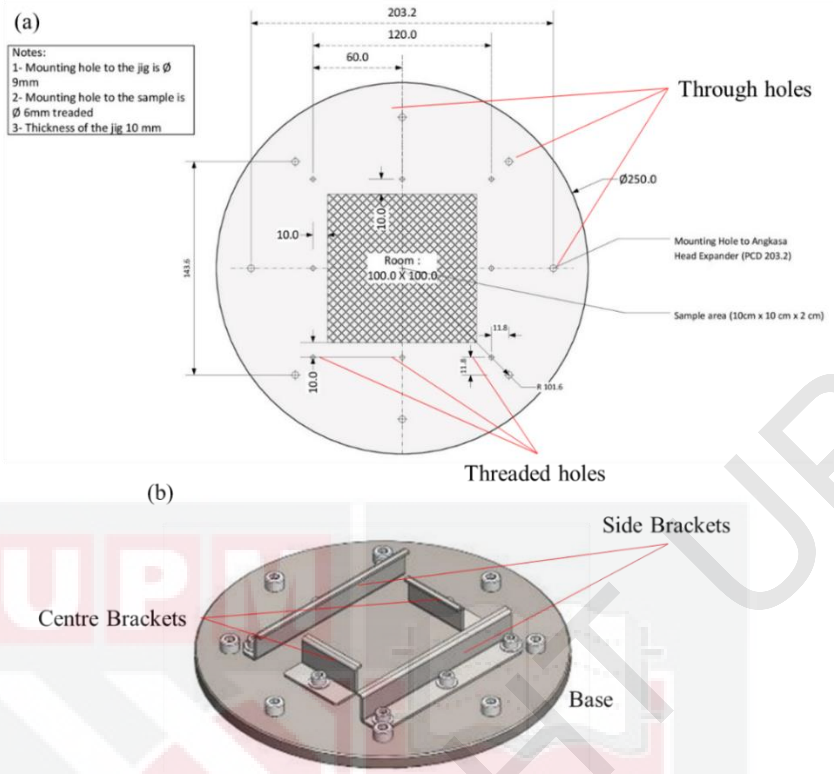


**Figure 3.46: CAD drawing of vibration jig for random vibration test and static load test. (a) Top view, (b) orthographic view**

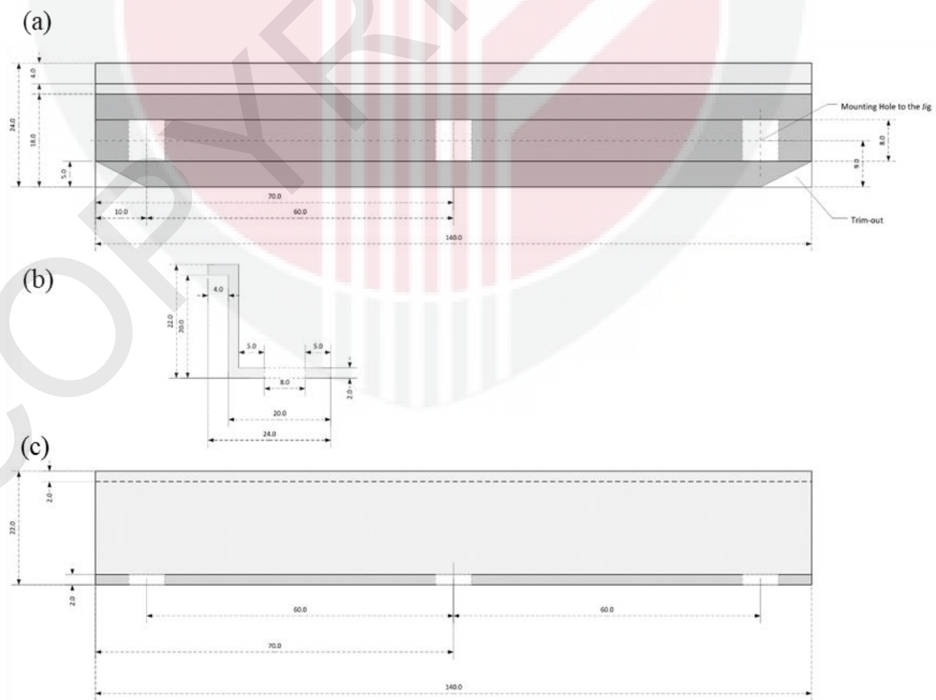


**Figure 3.47: Schematics of the side bracket. (a) Top view, (b) side view and (c) front view**

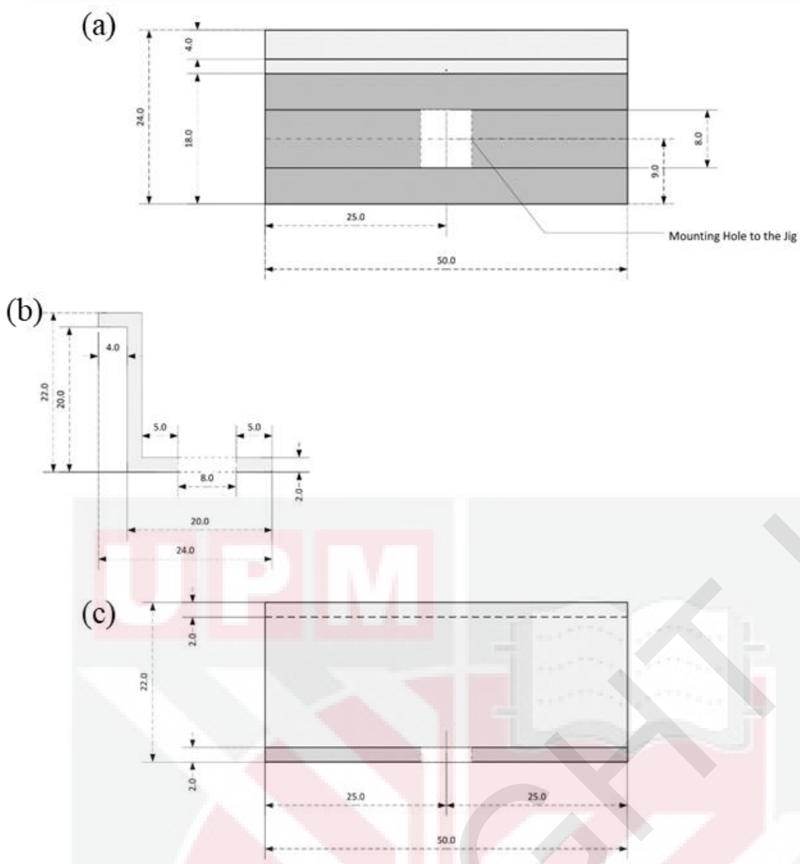


**Figure 3.48: Schematics of the centre bracket. (a) Top view, (b) side view and (c) front view**

For AT, the fabricated vibration jig in Figure 3.44 was modified to fit the GT300M slip table and expander. Figure 3.49 shows the schematic showing the new locations to place the screws for mounting purpose. The vibration jig was sent to I Pro Skill Engineering again for modification. Brackets were carved to have space for washers and screws during mounting of the jig onto the slip table as can be seen in Figure 3.50.

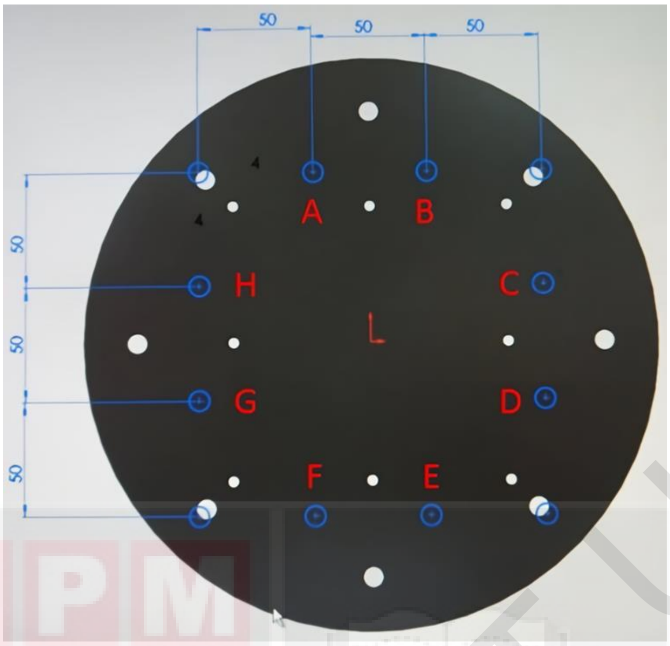


**Figure 3.49: Schematics for new holes drilled into vibration jig (A-H). Unit is in mm**

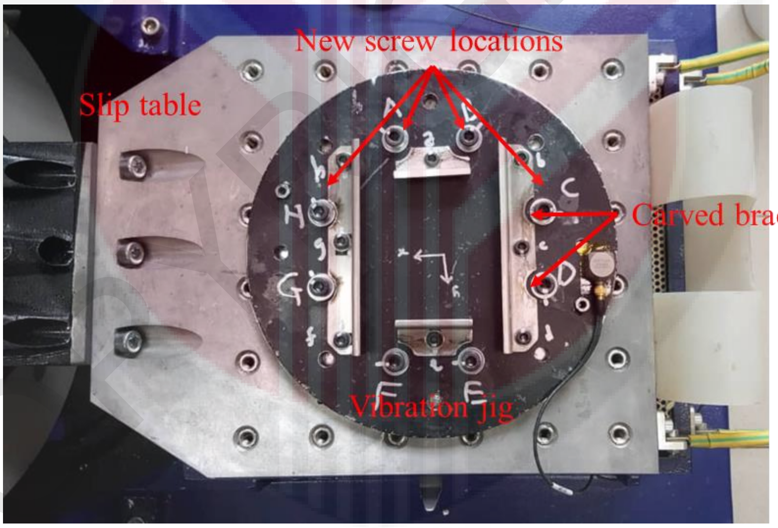


**Figure 3.50: Vibration jig after modification for mounting onto GT300M slip table**

The vibration jig is mounted to the slip table or armature of the shaker using M8 black socket head screws and its corresponding washers. The screws are tightened using a torque wrench with a torque value of 47 Nm. Minimum and maximum torque value for M8 stainless steel screw is 38.7 and 47.3 Nm respectively (Torque Specifications, n.d.). An Artline 990 XF Silver metallic ink marker was used to observe any loosening of the screws after each vibration test is completed.

## 3.11 Vibration Profiles

There are three types of vibration profiles used for the vibration tests: (1) QT level random vibration profile, (2) AT level random vibration profile, and (3) QT level sine-burst vibration profile. All profiles are provided by JAXA as the service provider.

### 3.11.1 Random Vibration Profiles

Figure 3.51 shows the QT level random vibration profile while Figure 3.52 shows the AT level random vibration profile. Table 3.26 shows the quantification of the vibration profile in the figures. According to NASA GEVS standard, the acceleration spectral density should be maintained within ±3 dB of the specified level at all frequencies within the test range and the overall RMS level is within ±10% of the specified level (Goddard Technical Standard, 2021). I the figures the high and low abort level is set at ±3 dB where the test will be aborted upon the PSD exceeding the high and low abort lines. The high and low alarm is at ±1.5 dB from the vibration profile.

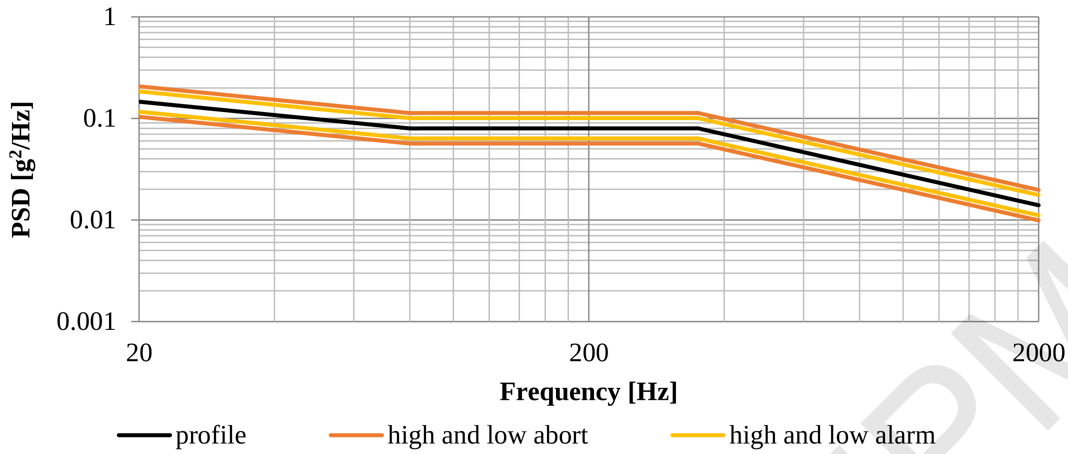


**Figure 3.51: QT random vibration profiles**

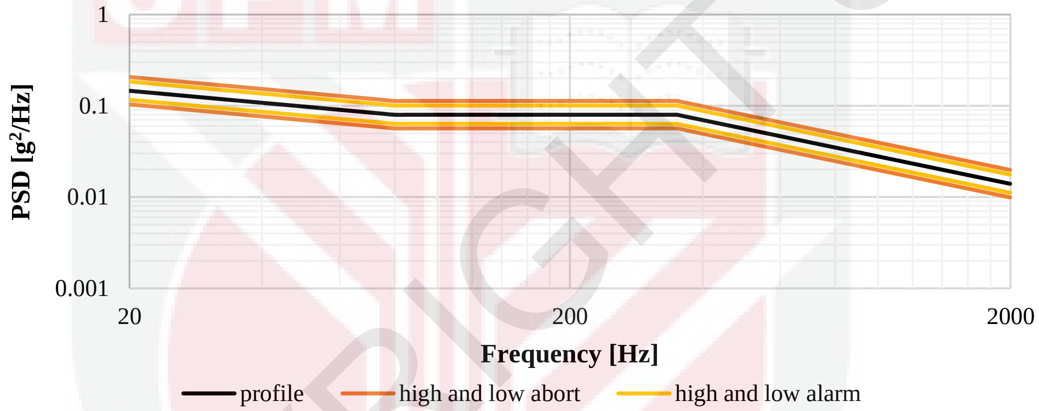


**Figure 3.52: AT random vibration profile**

**Table 3.26: Random vibration profiles**

| Frequency [Hz] | | QT | | | AT | | |
|---|---|---|---|---|---|---|---|
| | | PSD [$g^2$/Hz] | | Slope [dB/Oct] | PSD [$g^2$/Hz] | | Slope [dB/Oct] |
| From | To | From | To | | From | To | |
| 20 | 80 | 0.1465 | 0.08 | -1.31 | 0.037 | 0.04 | 0.17 |
| 80 | 350 | 0.08 | 0.08 | 0 | 0.04 | 0.04 | 0 |
| 350 | 2000 | 0.08 | 0.014 | -3.01 | 0.04 | 0.007 | -3.01 |
| Overall [Grms] | | 8.75 | | | 6.12 | | |
| Duration for each axis [min] | | 3 | | | 1 | | |

### 3.11.2 Sine-burst Vibration Profile

The sine-burst vibration profile only consists of one frequency of sinusoidal wave at varying amplitude. The sine-burst vibration profile is shown in Figure 3.53. The parameters are tabulated in Table 3.27.

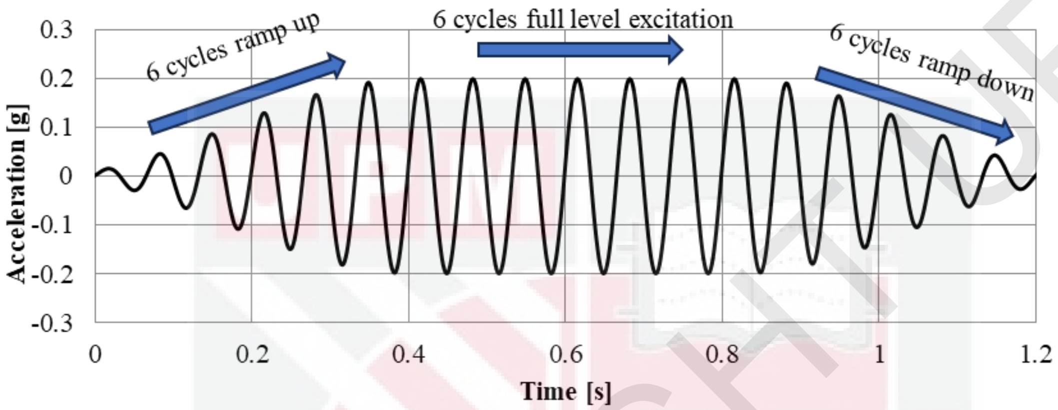


**Figure 3.53: Sine-burst vibration profile**

**Table 3.27: Sine-burst parameters**

| Parameter | Value |
|---|---|
| Maximum acceleration [g] | ±0.2 |
| Frequency [Hz] | 15 |
| Ramping cycles | 6 |
| Maximum level cycles | 6 |
| Total duration [s] | 1.2 |

## 3.12 Control Strategy and Accelerometer Placement

NASA-STD-7001B mentions that the control accelerometer shall be mounted on the test fixture near the attachment points (NASA Technical Standard, 2017). This coincides with MIL-STD-810G standard for acceleration input control strategy (Department of Defense Test Method Standard, 2008). Here the exciter motion is controlled from the feedback of the control accelerometers to provide defined vibration levels at the fixture/test item interface (Department of Defense Test Method Standard, 2008). Figure 3.54 shows the control accelerometer location of about 4 cm from the test item. The accelerometer is attached by applying Kapton tape to the test surface, then applying Loctite 431 cyanoacrylate adhesive on the backing of the tape before attaching the accelerometer.

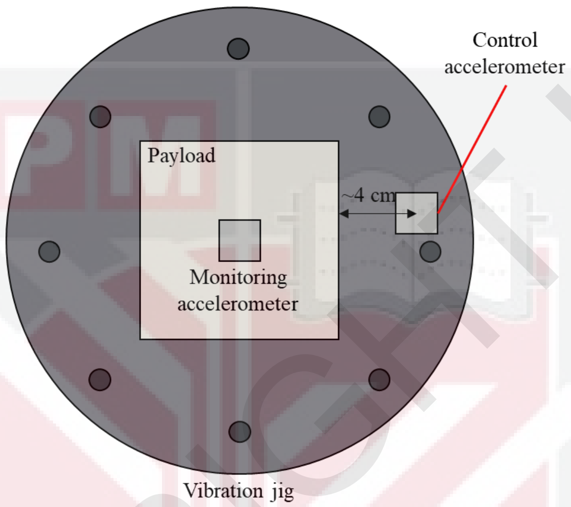


**Figure 3.54: Accelerometer mounting locations**

NASA-STD-7001B require the control accelerometer shall be mounted on the test fixture near the attachment points (NASA Technical Standard, 2017). This coincides with MIL-STD-810G standard for acceleration input control strategy (Department of Defense Test Method Standard, 2008). Here the shaker motion is controlled from the feedback of the control accelerometers to provide defined vibration levels at the fixture/test item interface (Department of Defense Test Method Standard, 2008). Figure 3.54 shows the control accelerometer location of about 4 cm from the test item. The accelerometer is attached by applying Kapton tape to the test surface, then applying Loctite 431 cyanoacrylate adhesive on the backing of the tape before attaching the accelerometer.

For accelerometer on the payload, there is no specific mention in the standards on the best location for mounting. In a CUBESAT there are electronic components such as pin connector, sensors, and LEDs (Brummit, 2010). The accelerometers for observation are placed near the vicinity of the electronic components (Brummit, 2010). For general observation, an accelerometer is placed in the middle of the bottom part of the PCB (Brummit, 2010). In this work, the measurement accelerometer is used for the observation of the PADCIOF response to the input vibration. As such, the accelerometer is placed on the centre of the PADCIOF as shown in Figure 3.54. This ensure the vibration from each part in the PADCIOF can be easily evaluated later.

## 3.13 Measurement Procedure

The random vibration test is conducted by dwelling at 25%, 50% and 75% level for 10 s each prior to vibrating at QT level for 3 min. For FM the same procedure is followed at AT level. Similarly for sine-burst test, excitations at 25%, 50% and 75% level were conducted.

For random vibrations, measurements were conducted for: (1) Vibration jig only without the payload, and (2) vibration jig and payload. This adheres to NASA GEVS to evaluate the dynamics of the experiment jig and the PADCIOF. Each test was done twice after a 90° rotation. Setup for QT for the payload is shown in Figure 3.55 for x- and y-axes, and Figure 3.56 for the z-axis. Setup for AT for the payload is shown in Figure 3.57 for x- and y-axes, and Figure 3.58 for the z-axis.

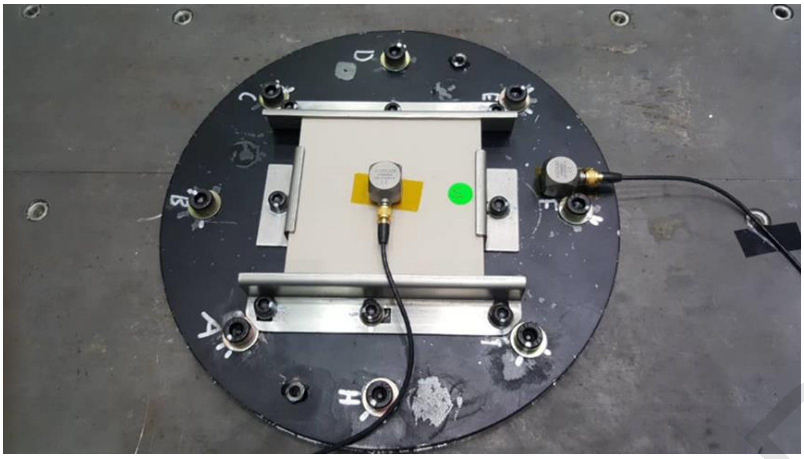

**Figure 3.55: Vibration test setup in the x- and y-axes direction (90° rotated)**

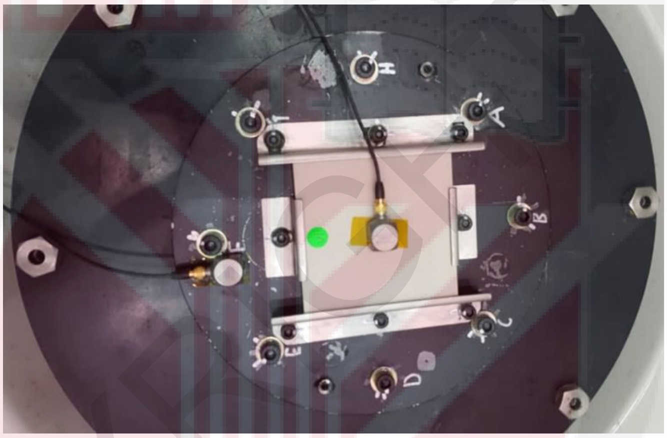

**Figure 3.56: Vibration test setup in the z-axis direction**

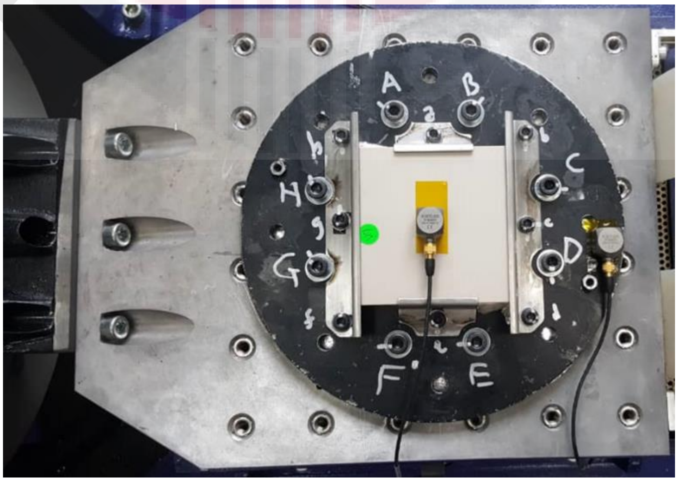

**Figure 3.57: X- and y-axes direction (90° rotated) AT random vibration test setup**

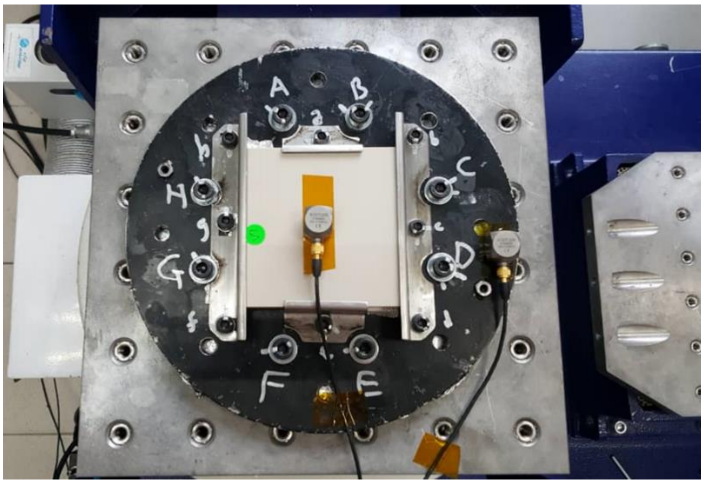


**Figure 3.58: Z-axis direction test setup for AT random vibration. Vibration jig is attached to the expander, not to the slip table**

As per NASA GEVS, the payload is examined before and after the vibration test. Unlike CUBESAT, SOFPADS does not have any printed circuit board (PCB). In terms of functionality of the PD before the vibration test, preliminary tests by irradiating the PD using electron, neutron and gamma radiations are considered. The functionality of PD after vibration tests is considered after space exposure as the irradiations and sample readout require the extraction of the PD from the case. Furthermore, SOFPADS's mechanical joints are the interfaces of MB1 (case cover) and MB2 (main body) only that is joined using screws and c-clips. Other parts are not mechanically joined. The PD are sealed using Kapton tape adhesive. As such, the only concern is in terms of damage done to each part after the vibration tests.

## 3.14 Structural Load Test

Structural load test is conducted to assess the SOFPADS ability to receive external force in the event of accidents occurring. Here, the NASA GEVS is used to evaluate the design strength qualification (Goddard Technical Standard, 2021). Additionally, NASA-STD-5001 standard is used for the minimum factors of safety for flight approval (NASA Technical Standard, 1996).

The structural load tests were conducted using the INSTRON universal testing machine (UTM) by applying load onto the payload. There were two different loading tip diameters operate at specific working loads as provided by JAXA based on the JEMRMS-SFA load and astronaut’s kick load during EVA as presented in Table 3.28. Two stainless steel rods with the loading diameter as per JAXA’s requirements were purchased from I Pro Skill Engineering and used as the loading tip during the test. As both NASA GEVS and NASA-STD-5001 did not provide the necessary loading rate, a similar loading rate to ASTM D695 was used. The structural's safety factor (SF) is calculated using Equation (3.7). Figure 3.59 shows the structural load test setup. The test is started by bringing the load tip as close to the surface of the PADCIOF without touching. In total, there were four types of tests conducted on all sides of SOFPADS on each section as summarised below:

1) Structural load on V1 using Tip 1 up to SF of 2.0.
2) Structural load on V1 using Tip 2 up to SF of 2.0.
3) Structural load on V2 using Tip 1 until failure/break.
4) Structural load on V3 using Tip 2 until failure/break.

**Table 3.28: Parameter for structural load test**

| Parameter | Tip 1 | Tip 2 |
|---|---|---|
| **Working Load [N]** | 208 | 556 |
| **Tip Diameter [mm]** | 2.0 | 12.7 |
| **Loading Rate [mm/min]** | 1.0 | 1.0 |
| **SF** | 2.0 | 2.0 |

$$\mathrm{SF} = \frac{\text{Actual Load}}{\text{Working Load}} \quad (3.7)$$

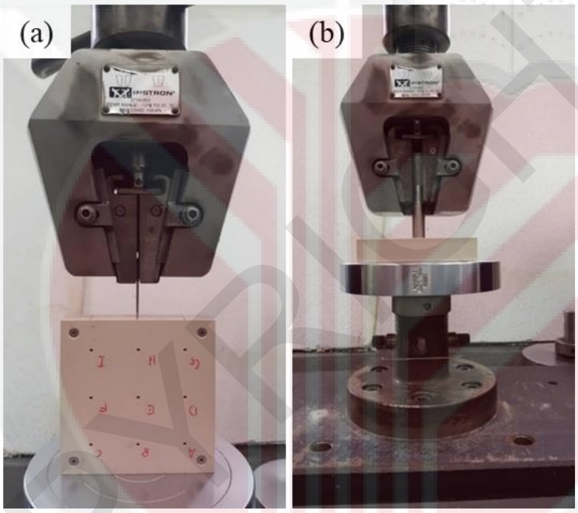


**Figure 3.59: Structural load test setup. (a) Using Tip 1, and (b) using Tip 2.**

## 3.15 Stage 3: Sample Preparation of PD

In this stage, the PD are prepared for irradiation, preliminarily irradiated to low electron, neutron-gamma sources for functionality at low dose radiation exposure, and, screened to sort out the responses of each PD.

### 3.15.1 Preparation of the PD

The CUSOF (D9-1 to D9-6) were purchased from MMU in a roll and then broken down to long strips as shown in Figure 3.60 (a). The long fibres were cut into 6 mm using a S90R ruby fibre scribe by Thorlabs at the Medical Physics Laboratory, Faculty of Medicine and Health Sciences (FPSK), UPM. The cut fibres are shown in Figure 3.60 (b). The COMOF (D9-7) were purchased from Coractive. COMOF were cut using the same method as CUSOF. However, prior to cutting, the outer plastic layer is removed using a fibre stripper.


**Figure 3.60: CUSOF: (a) Long strips, (b) cut down to 6 mm**

TLD (TLD-100, TLD-600 and TLD-700) are purchased from Thermo Fisher Scientific with the dimensions of 3.2 mm× 3.2 mm × 0.89 mm as shown in Figure 3.61. All TLD are undistinguishable from each other as they are the same in colour and shape.

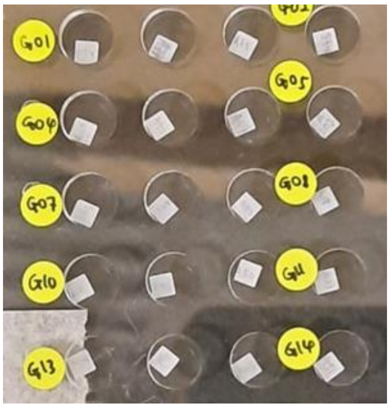


**Figure 3.61: TLD**

### 3.15.2 Morphology of Optical Fibres

The cross sections of CUSOF are analysed using Hitachi SU1510 Scanning Electron Microscope (SEM) to understand the physical structure of the fibres. Subsequently, Electron Dispersive X-ray (EDX) scans were conducted at three points within the CUSOF's core using HORIBA EMAX to find the elemental composition of the fibres. Some SEM or SEM/EDX analyses conducted on other types of fibres can be found in articles such as Mohd Noor et al. (2016) for D9-2 and Lam et al. (2019) for D9-1. From the EDX results, the effective atomic number ($Z_{eff}$) of the optical fibres is calculated using Equation (2.1 in Chapter 2.

The normalisation in this used the dosimeters' core volume. For TLDs, since the dopants are spread throughout the material, the volume of the TLD itself was used. This method was used by Hassan et al. (2018) too. The core area of the CUSOF is measured using ImageJ software from the SEM images to calculate the core volume of the fibres. SEM image of the fibres cross section was viewed using the software. Then the scale was set relative to the pixel value of the image. The setting of the scale is important since the software measures the area by pixel value and then converts it back to the attributed unit. Threshold function was used on the image obtained from SEM to select the area of measurement. Thresholding process was conducted using grayscale image. The Threshold function select the area of measurement from the difference in coloration inside the image. Thus, to improve the accuracy of core area selection, the core area seen from the SEM images were highlighted in white manually using paint software. After selection of core area, the value of core area was obtained using Analyze particles function of the ImageJ software. An imaginary fibre core dimension of 2 cm × 6 cm is drawn to validate the core area results obtained from the software. For CFs, the core volumes are calculated using the core diameter obtained by measurement from the SEM images since the fibre core's cross section is circular in nature.

### 3.15.3 Annealing

Annealing is a process applied onto TLDs to erase any irradiation background through thermal treatment (Furetta, 2010). All PD are annealed prior to any irradiation using the method in Hassan et al. (2019). The OF were annealed at 400°C for 1 h in a Carbolite furnace at the Physics Department, UPM by placing them in a brass plate as shown in Figure 3.62 (a), and then covering the brass plate with Al sheet (Figure 3.62 (b)), followed by placing the brass plate into the furnace. On the other hand, D10-1, D10-2, and D10-3 were sent to Agensi Nuklear Malaysia (ANM) for annealing at 400°C for 1 h and continued with further dwelling at 80°C for 16 h as they provide the standard annealing procedure for these commercial TLD.

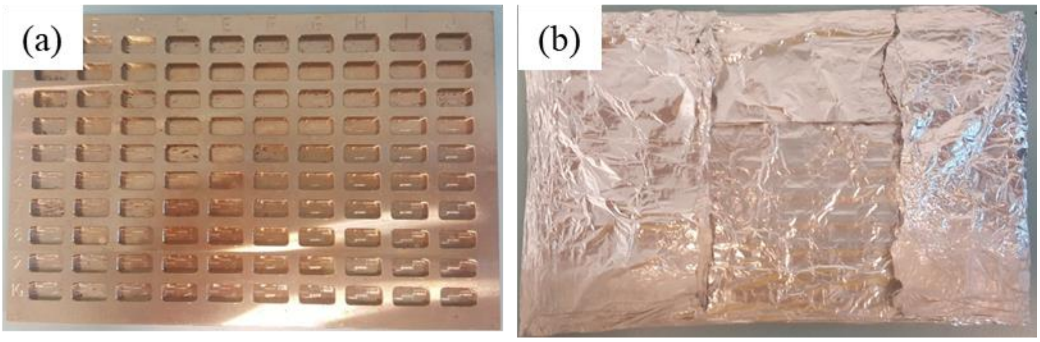


**Figure 3.62: Brass plate to place the OF for annealing, and (b) brass plate covered using Al foil**

### 3.16 Sample Readout

Sample readout is conducted after irradiation of the PD to any radiation source. Sample readout is conducted using Harshaw TLD Model 3500 Readers by Thermo Fisher Scientific. Table 3.29 shows the time-temperature profile (TTP) used for sample readout. The TL responses of the OF and commercial TLD are normalised using their core volume as calculated/measured in section 3.5.1.2. Commercial TLD (D10-1, D10-2 and D10-3) were readout using a TTP as suggested by the manufacturer while for OF, the TTP chosen is based on the glow curve characteristics.

**Table 3.29: TTP for sample readout**

<table>
<tr><th rowspan="3">TTP Label</th><th colspan="7">Procedure</th></tr>
<tr><th colspan="2">Preheating</th><th colspan="3">Acquisition</th><th colspan="2">Annealing</th></tr>
<tr><th>Temperature [°C]</th><th>Time [s]</th><th>Maximum temperature [°C]</th><th>Heating rate [°C/s]</th><th>Time [s]</th><th>Temperature [°C]</th><th>Time [s]</th></tr>
<tr><td>TLD_High</td><td>50</td><td>0</td><td>300</td><td>10</td><td>33.33</td><td>-</td><td>-</td></tr>
<tr><td>P60</td><td>60</td><td rowspan="4">10</td><td rowspan="4">400</td><td rowspan="4">30</td><td rowspan="4">13.33</td><td rowspan="4">400</td><td rowspan="4">10</td></tr>
<tr><td>P80</td><td>80</td></tr>
<tr><td>P100</td><td>100</td></tr>
<tr><td>P120</td><td>120</td></tr>
</table>

## 3.17 Preliminary Exposure

Preliminary exposure of the PD is conducted to understand the PD responses to various radiation. In the following section, details of each process are discussed.

### 3.17.1 Beta Irradiation

Beta irradiation of the PD was conducted using two equipment. The first one is using Stereo Mono Turntable (Lenco) located at the Radiation Lab, Department of Physics, University of Surrey. The second beta irradiation is conducted using Risø TL/OSL reader (Risø National Laboratory) also located at the same laboratory.

### 3.17.2 Stereo Mono Turntable Beta Irradiator

A Strontium-90 ($^{90}Sr$) beta irradiator was used to irradiate the PD to absorbed doses of 0.1, 1, 5, 10, 60, 150, 200 and 450 mGy. The PD is placed inside the 30 positions on the rotating carousel and the irradiation is performed when the sample is rotated to designated $^{90}$Sr beta irradiator location. The sample was removed from the carousel when the target doses is radiated on the sample. The stereo mono turntable with beta irradiator is shown in Figure 3.63.

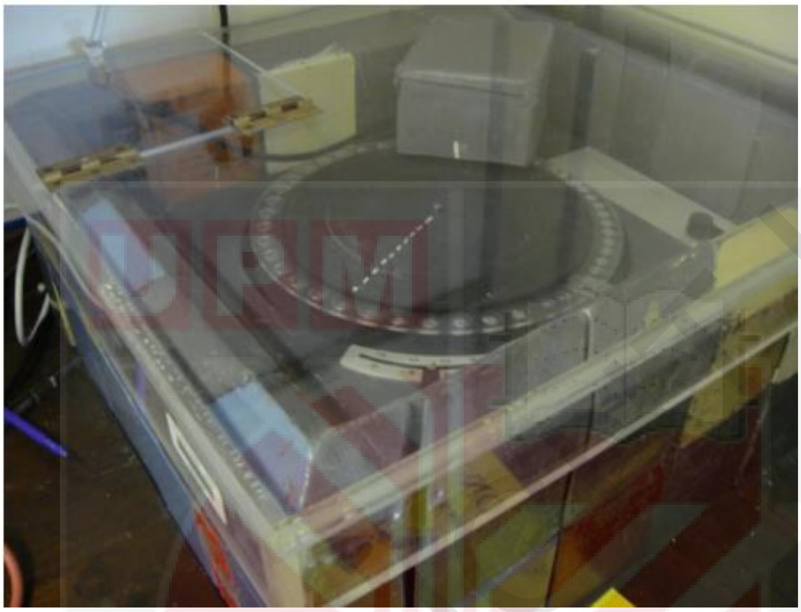

**Figure 3.63: Stereo mono turntable with $^{90}$Sr source mounted above the carousel** (Noor, 2012)

### 3.17.3 Risø TL/OSL Reader based Beta Irradiator

Risø TL/OSL reader is used to analysed irradiated TLD and OSLD as shown in Figure 3.64. The reader also equipped with a detachable beta irradiator of $^{90}$Sr located above the sample carousel. The PD are irradiated to absorbed doses of 20, 40, 80, 150, 400, 700 and 1000 mGy.

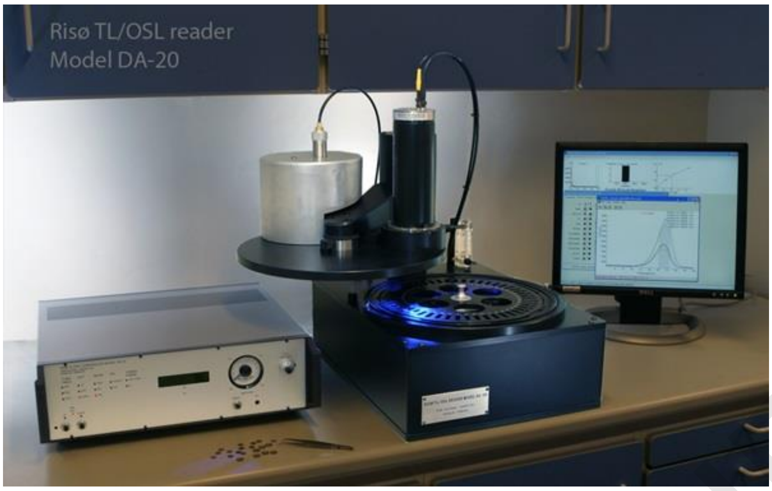


**Figure 3.64: Risø TL/OSL reader equipped with beta irradiator**
(Nielsen, 2023)

### 3.17.4 Neutron-Gamma Irradiation

Since the irradiation was conducted inside a water bath, the OF were placed inside polyoxymethylene (POM) capsules while the D10-1, D10-2 and D10-3 are sealed inside polypropylene (PP) plastic bag using a heat sealer as shown in Figure 3.65. Usage of POM capsules or gelatinous capsules has been employed in various irradiations of CUSOF (Lam et al., 2019; Noor et al., 2016; Hassan et al., 2019). Then, the sealed dosimeters are carefully attached onto PP sheet cut into a circle with 10 cm diameter with four holes punched near the opposite edges using double sided tapes as the adhesive that held the capsules and TLD filled plastics. Three sets of polypropylene sheets (PPS) with samples attached were prepared. They were tied with each other using nylon strings.

**Figure 3.65: D10-1, D10-2 and D10-3 are sealed inside PP bag using heat sealer**

The irradiation setups are depicted in Figure 3.66 and Figure 3.67. The irradiation was performed by using an 11 GBq Americium-Beryllium ($^{241}$AmBe) source placed inside a water bath located at the University of Surrey, United Kingdom. The distance between each PPS was 15 cm with the lowest sheet just next to the $^{241}$AmBe source. Each layer of sheet was labelled as a $PPS_0$, $PPS_{15}$ and $PPS_{30}$ relative to the distances of the sheets from $^{241}$AmBe source which were 0 cm, 15 cm and 30 cm, respectively. The distances were chosen to observe the PD responses at different doses. The samples were irradiated up to a designated time of 24, 48, 66 and 72 hours (h) where at each point of time some samples will be removed from each PPSs.

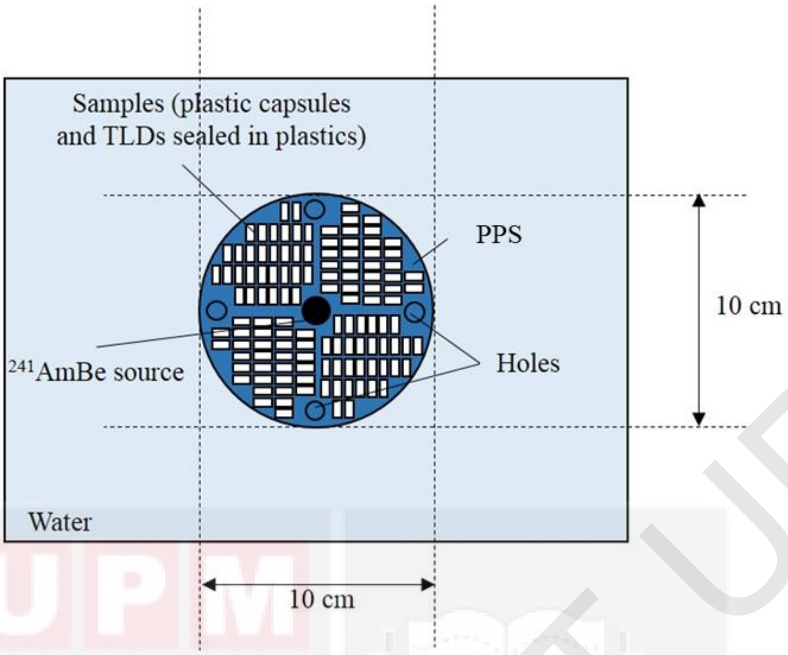


**Figure 3.66: Top view of neutron-gamma irradiation setup**

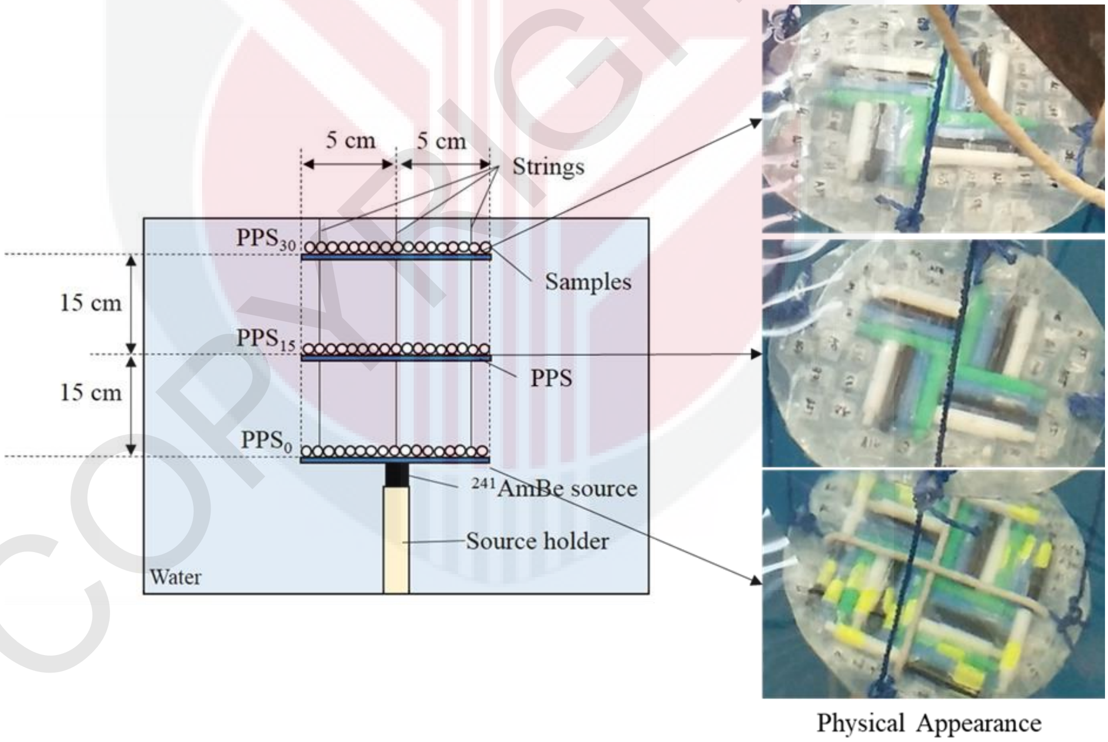


**Figure 3.67: Side view of neutron-gamma irradiation setup**

### 3.18 Screening of the Passive Dosimeters

CUSOF (D9-1, D9-2 and D9-3) and commercial TLD (D10-1, D10-2 and D10-3) are screened to sort the sensitivity of each PD piece in detecting radiation.

#### 3.18.1 Screening of Customised Optical Fibres

CUSOF was screened from the radiation of Caesium-137 ($^{137}$Cs) gamma source. The CUSOF was irradiated to a low dose of 5 mGy to analyse the sensitivity of the CUSOF in detecting low dose radiation. Approximately, 500 pieces from each type of CUSOF were irradiated. From the screening results, actual CUSOF used for FM and CM was determined starting from the most sensitive piece.

#### 3.18.2 Screening of Commercial Thermoluminescent Dosimeter (TLD)

Commercial TLD was screened using $^{241}$AmBe neutron-gamma source located at Nuclear Science Building, Universiti Kebangsaan Malaysia. The TLD was irradiated with a neutron-gamma dose is to measure the sensitivity of each type of commercial TLD towards neutron detection and to help segregate the commercial TLD in the event of accidental mixed up. The irradiation setup is shown in Figure 3.68. The commercial TLD was placed inside gelatine capsules and attached to a cardboard. Then the cardboard was inserted into the tube and pushed down until it reached the $^{241}$AmBe neutron-gamma source. The maximum activity of the source is 0.33 TBq with surface doses of 15 μSv/h for gamma and 17.3 μSv/h for neutron. Approximately 100 pieces of each type of commercial TLD were irradiated for 48 h.

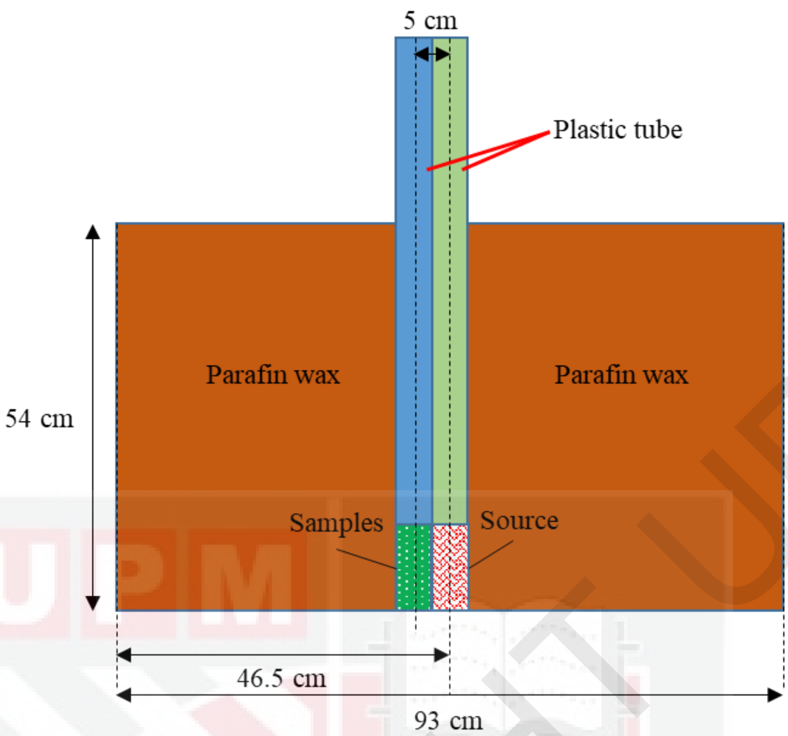


**Figure 3.68: Neutron-gamma setup for commercial TLD screening**

## 3.19 Stage 4: Space Exposure of SOFPADS on the International Space Station

PD prepared in Stage 3 is used for assembly of FM and CM in Stage 2 and later to be used for space exposure in Stage 4. The timeline of space exposure is also presented and discussed as shown in Table 3.30.

**Table 3.30: FM timeline**

| Date | Time (UTC) | Location | Remarks |
|---|---|---|---|
| 2/11/2018 | | Malaysia→TKSC | Hand carried |
| 4/5/2019 to 6/5/2019 | 0645 (launch time) | US Air Force Base, Cape Canaveral→ISS berth | SpX-17 Spacecraft |
| 24/5/2019 | | ISS→ExHAM Platform 2 | Still inside ISS |
| 30/5/2019 | | ExHAM Platform 2→Exposed Facility (Kibo) | Commencement of exposure outside of ISS |
| 30/7/2020 | 828 | Detachment by crew | FM is carried into ISS |
| | 1026 | FM stored in Kibo | |
| 12/1/2021-14/1/2021 | | ISS→Earth (Water landing) | Via SpX-21 Spacecraft |
| 16/5/2021 | | UPM, Malaysia | |
| 22/5/2021 | | Readout starts | |

## 3.20 Launching and Exposure of Flight Model

The assembled FM is hand carried to JAXA's Tsukuba Space Center (TKSC) inside a plastic container filled with acoustic sponge to reduce the impact during travel. The upper part of the container is covered with Al sheet to attenuate any possible radiation the hardware might be exposed to during travel. A special permission was obtained from the Kuala Lumpur International Airport's (KLIA) Royal Malaysian Customs Department to allow the transport of FM without going through the X-ray machine.

Upon arrival at TKSC, the fit checking of FM was conducted to make sure the hardware perfectly fitted the ExHAM as shown in Figure 3.69. After that, the FM was tagged (Figure 3.70) and stored at TKSC for transport to NASA.

**Figure 3.69: Fit checking of FM to ExHAM mock** (JAXA, 2018)


**Figure 3.70: Bottom side of FM is tagged for recording purposes**

FM was launched from the US Air Force Base in Cape Canaveral, Florida to the ISS using the SpaceX Dragon CRS-17 (SpX-17) spacecraft on 4 May 2019 as shown in Figure 3.71. The spacecraft docked at ISS berth on 6 May 2019. On 24 May 2019, the FM is successfully attached to ExHAM platform 2 by the ISS crew. Finally, the ExHAM is attached onto the Exposed Facility of the Kibo module on 30 May 2019. During the exposure duration, the FM top side was faced to the zenith of ISS to directly detect the space radiation. Figure 3.72 shows the condition of FM during space exposure.

**Figure 3.71: Launching of SpX-17 carrying FM** (JAXA, 2019)

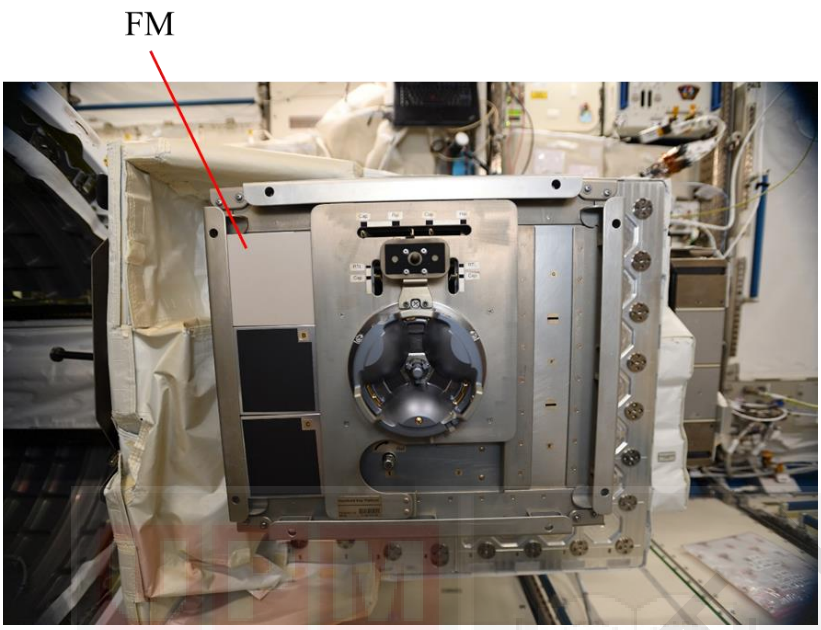


**Figure 3.72: FM attached to the ExHAM at the Exposed Facility of Kibo facing zenith** (JAXA, 2019)

The ExHAM was carried back inside the ISS on 30 May 2020 and the FM is stored in Kibo module until it is carried back the Earth. The FM was sent back via SpaceX Dragon CRS-21 (SpX-21) spacecraft on the 12 January 2021 and arrived on 14 January 2021. After that, FM is sent back to JAXA, then returned to UPM via courier. Finally, the PD readout process inside the FM was started on 22 May 2021. Table 3.30 summarises the location and status of FM throughout the exposure duration. In total, the FM was exposure to space radiation for about 427 days.

### 3.21 Disassemble of FM

The exposed FM was protected from external radiation not related to space radiation using three layers of Al package during the transportation back to UPM as shown in Figure 3.73.


**Figure 3.73: Packaging used to protect FM from external radiation**

Figure 3.74 shows the physical condition of PADCIOF after space exposure. The top side of FM has shown some discolouration compared to CM due to solar exposure, as shown in Figure 3.74 (a). The colour of FM's bottom side shown mostly remained the same since it was not facing the zenith (Figure 3.74 (b)). Detailed inspection on the internal parts found no existing physical damage (Figure 3.74 (c)). The PD also remained physically unchanged (Figure 3.74 (d)). This shows that the PADCIOF and SOFPADS were able to withstand space exposure at LEO altitude.

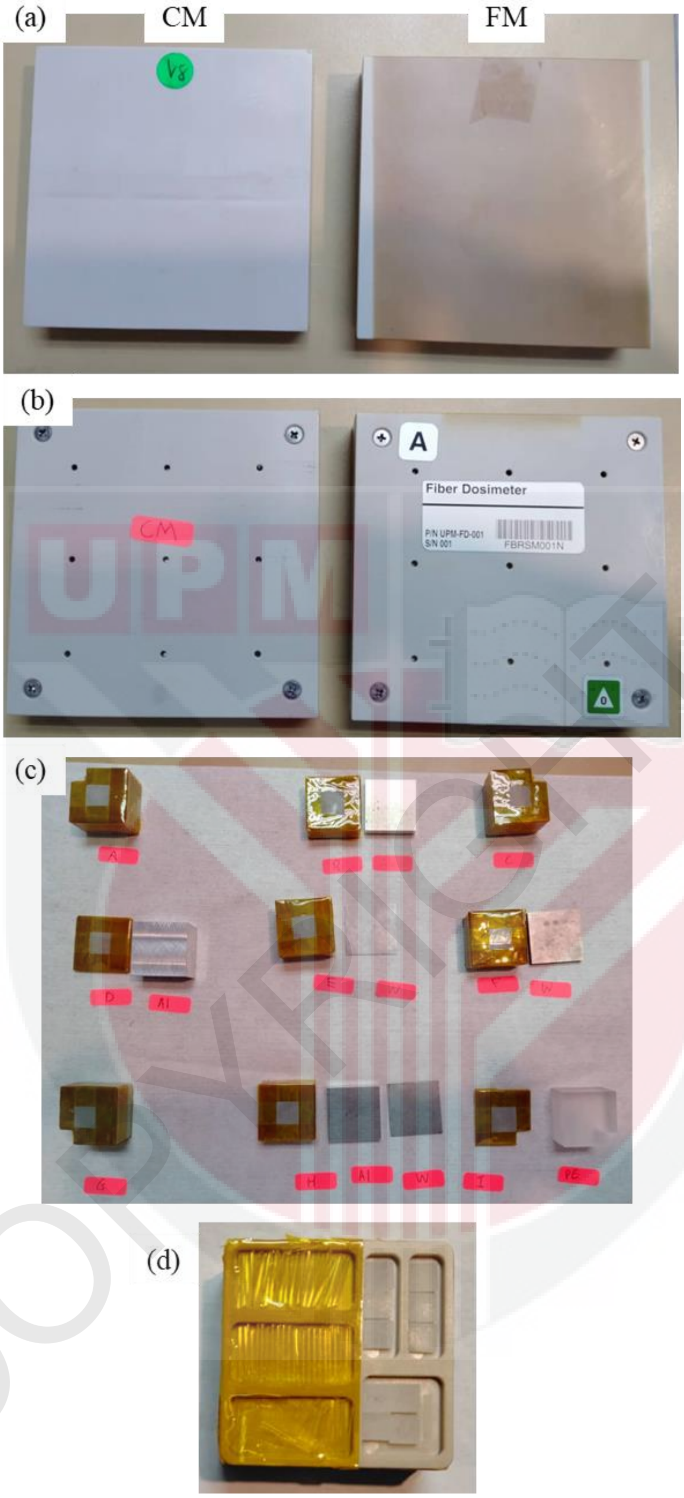


**Figure 3.74: PADCIOF after exposure. (a) Top side of CM and FM, (b) bottom side of CM and FM, (c) FM's dosimeter holders and filters condition, and (d) PD condition of FM**

The PD was disassembled from the dosimeter holder before readout process. The adhesion on the Kapton tape was removed from the dosimeter holder by the aid of

Acetone in glass petri dish as shown in Figure 3.75. Then the PD was carefully transferred glass containers accordingly as shown in Figure 3.76. Similarly, the PD from CM was also disassembled and sent for readout process for comparison process to determine the actual doses detected by the PD during space exposure.

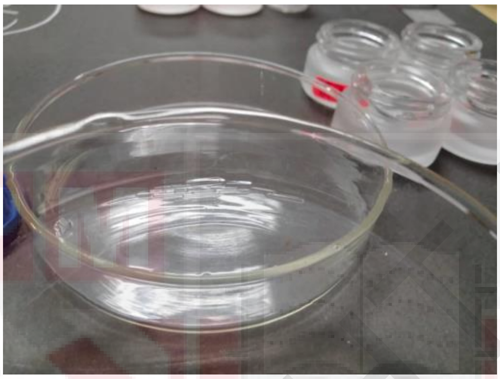

**Figure 3.75: PD soaked in Acetone inside a petri dish**

**Figure 3.76: Glass containers with PD inside**

## 3.22 Calibration Using Proton

The used PD for FM and CM was employed again for proton irradiations. The PD were sent to Hyogo Ion Beam Medical Center (HIBM), Japan and irradiated using proton synchrotron. The irradiation set up shown in Figure 3.77 was used, similar with set up by Hassan et al. (2017; 2019). The dose rate of the proton was 4 Gy/min, the beam field size was 15 cm × 15 cm, and the sample to source distance (SSD) was 270 cm. During the irradiation process, a solid water phantom with a thickness of 11.1 cm was placed on top of the passive dosimeters and an additional 10 cm was placed underneath the passive dosimeters, as presented in Figure 3.77.

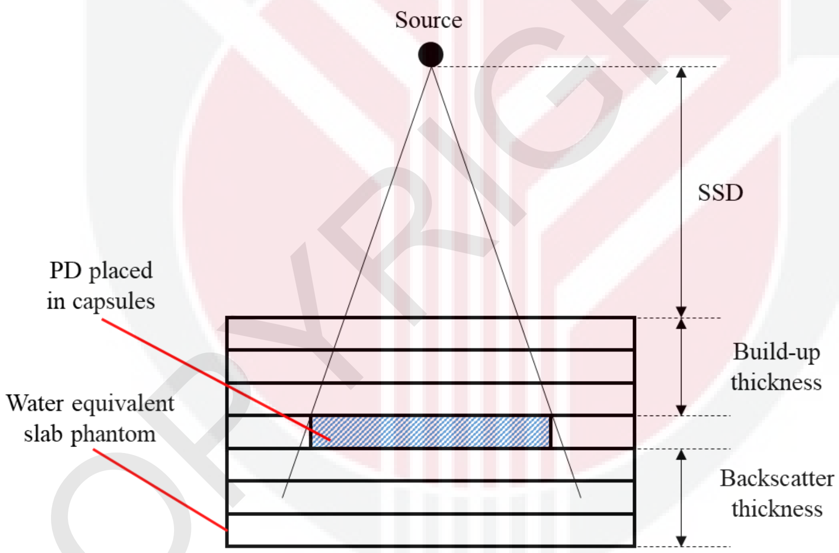


**Figure 3.77: Proton irradiation test setup** (Image adapted and modified from Hassan et al., 2017)

Phantom placed on the bottom of the passive dosimeters serves to block backscatter radiations from the surrounding (Hassan et al., 2023). The PD was characterised for dose linearity, energy response, and fading effect. Table 3.31 lists out the absorbed doses and energies exposed to the PD, and the read-out days after irradiations. The measurement to determine the fading effect was conducted until 358 days analogous to delay on readout process for PD from space exposure.

**Table 3.31: Characteristics of PD responses analysed for proton irradiation**

| Characteristics | Absorbed dose [Gy] | Energy [MeV] | Read-out days after irradiation [days] |
|---|---|---|---|
| Dose linearity | 0.5, 1.0, 1.5, 2.0, 2.5, 3.0 | 150 | 22 |
| Energy response | 2.0 | 80, 150, 190 | 22 |
| Fading effect | 1.0 | 150 | 22, 55, 142, 250, 358 |

## 3.23 Summary

Overall, in this work, PADCIOF was designed in the Stage 1. Upon design acceptance, the PADCIOF was fabricated, assembled and then QT was conducted and assessed in the next Stage 2. Stage 3 consists of the preparation of the PD and exposure under various types of radiation for calibration process. Finally, in Stage 4, the PD in the PADCIOF was sent to ISS and exposed to space radiation in LEO and the final calibration using proton was conducted.

# CHAPTER 4

# RESULTS AND DISCUSSION

## 4.1 Overview

In this chapter, results pertaining to works done in Chapter 3 are discussed. Initially, the filtered radiation energies from the SOFPADS developed are presented. Then, the structural test results and workmanship are presented followed by the preliminary irradiation results of the PD. The final space exposure results and correlation to proton doses are presented to show the PD usability to detect space radiation.

## 4.2 Stage 1: Attenuated Radiation Energies due to Filters

The calculated energies by each filter for each type of radiation is presented in this section.

### 4.2.1 Proton and Electron Filtered Energies

From the calculation made using Equation 3.1, W is the best proton and electron shield up to the thicknesses that are used in this work as shown in Figure 4.1. Table 4.1 summarised the shielded energies of proton and electron for each filter based of Figure 4.1. W with a thickness of 3.2 mm provided highest energies of protons and electrons filtered where protons with energies of less than 57.5 MeV and electrons with energies of less than 10 MeV unable to penetrate the material. Due to its low thickness, W with

0.5 mm shielded the least number of energies at <4.5 MeV for protons and < 1.25 MeV for electrons.

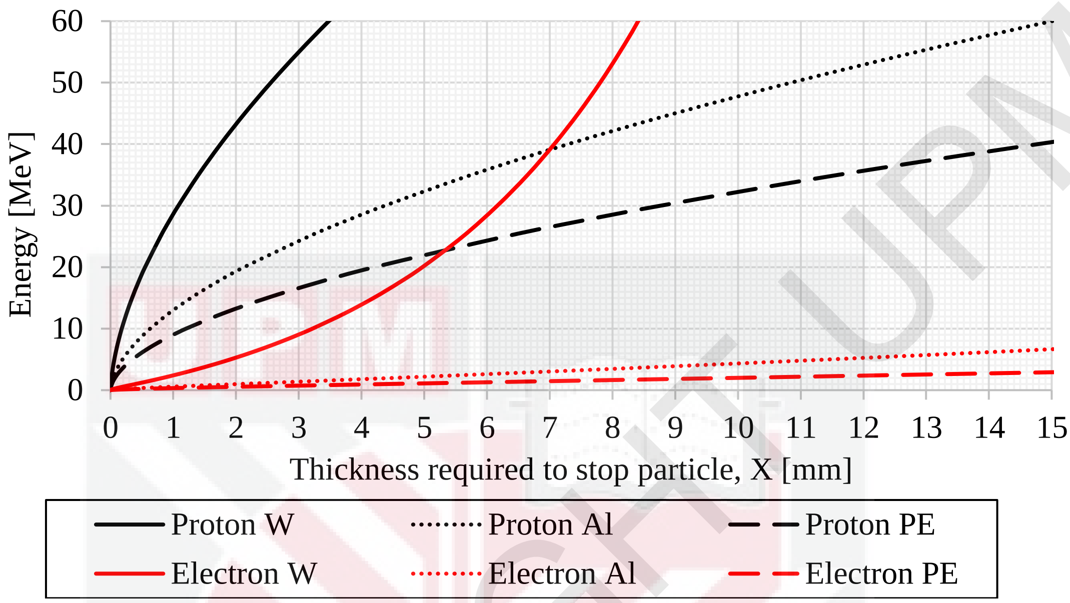


**Figure 4.1: Thicknesses required to stop proton and electron of filter materials as calculated using Equation 3.1 and the CSDA range obtained from NIST**

**Table 4.1: Shielded proton and electron energies of the filters**

| Material | Thickness [mm] | Shielded Radiations | |
|---|---|---|---|
| | | Proton [MeV] | Electron [MeV] |
| Al | 5 | <32.5 | <2.25 |
| | 13 | <55 | <5.75 |
| W | 0.5 | <4.5 | <1.25 |
| | 3.2 | <57.5 | <10 |
| PE | 13 | <37 | <2.5 |

### 4.2.2 Photon Attenuation

Figure 4.2 shows the thicknesses required by Al, W and PE to attenuate 50% and 95% of the incident photon. In the figure, the thicknesses required by W to attenuate up to 50% and 95% the intensity of incident photon is the lowest. For example, to attenuate

20 keV photon by 50%, approximately 0.5 mm of W or 9.0 mm of Al or slightly more than 15.0 mm of PE (the figure shows the attenuation up until 15 mm since the thickest filter is 13 mm) is required. The thickness of W needed is the lowest. Table 4.2 summarises the photon energies that are attenuated at least 95% or more, or 50% or more. From the table, 3.2 mm W is the filter that attenuates photon the most.

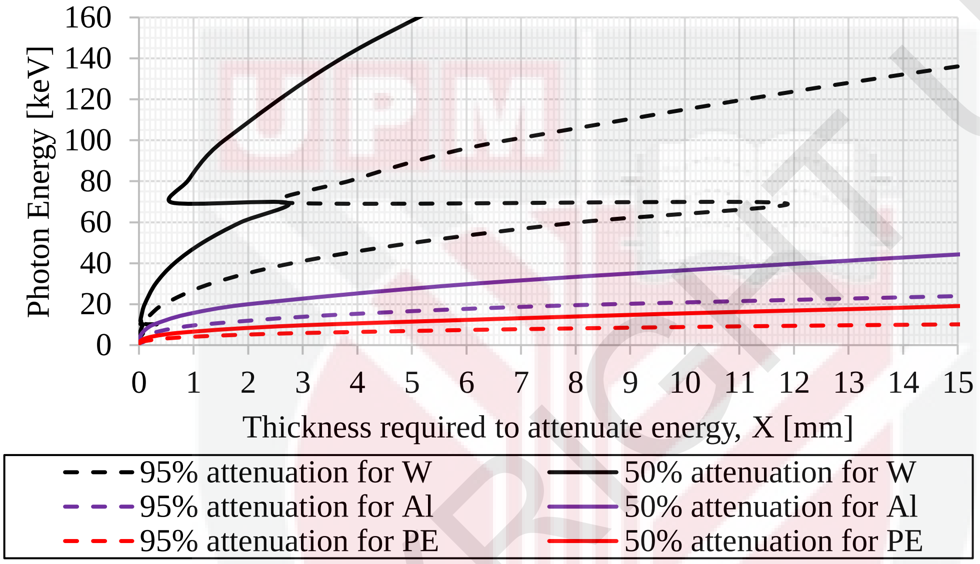


**Figure 4.2: Energies of photon that is attenuated by 95% or more, or, 50% or more**

**Table 4.2: Energies of photon shielded by material with 95% and higher intensity reduction of 50% and higher intensity reduction**

| **Material** | **Thickness [mm]** | **Photon of ≧95% Attenuation [keV]** | **Photon of ≧50% Attenuation [keV]** |
|---|---|---|---|
| Al | 5 | <17.6 | <27.9 |
| | 13 | <23.9 | <41 |
| W | 0.5 | <20.5 | <35.5, 70-72 |
| | 3.2 | <42, 69-76 | <131.5 |
| PE | 13 | <9.5 | <17.5 |

Rearranging the Lambert-Beer's equation (Equation 3.2), the attenuated photon for each energy is shown in Equation 4.1. Here *I* is the intensity of the attenuated incident photon, $I_o$ is the intensity of incident photon, and $X$ is the thickness of material. Using Equation 4.1, the percentage of $I_o$ attenuated for each energy is shown in Figure 4.3. Due to the exponential nature of the equation, when $(\mu/\rho)X \rightarrow \infty$, $e^{-(\mu/\rho)X} = 0$. At lower energies, the photon $\mu/\rho$ is significantly higher. This is translated in Figure 4.3 as lower energy photons are attenuated by 100%. 5 mm Al filter provided the least range of photon shielded at almost 100% up to 4 keV while 3.2 mm W shields almost 100% of photon up to 150 keV. 3.2 mm W is the better photon attenuator until an approximate of 260 keV photon, then 13 mm Al provides better photon attenuation on the higher range of energy spectrum due to its thickness. In Figure 4.3, at higher energy photons, W generally has higher $\mu/\rho$ in comparison to Al except around 1000-2500 keV where both materials possess similar $\mu/\rho$. If both materials were at the same thickness, at higher photon energies, W and Al will be similar photon attenuator.

$$\text{Attenuated photon [\%]} = (1 - I/I_o) \times 100 = (1 - e^{-(\mu/\rho)X}) \times 100 \qquad 4.1$$

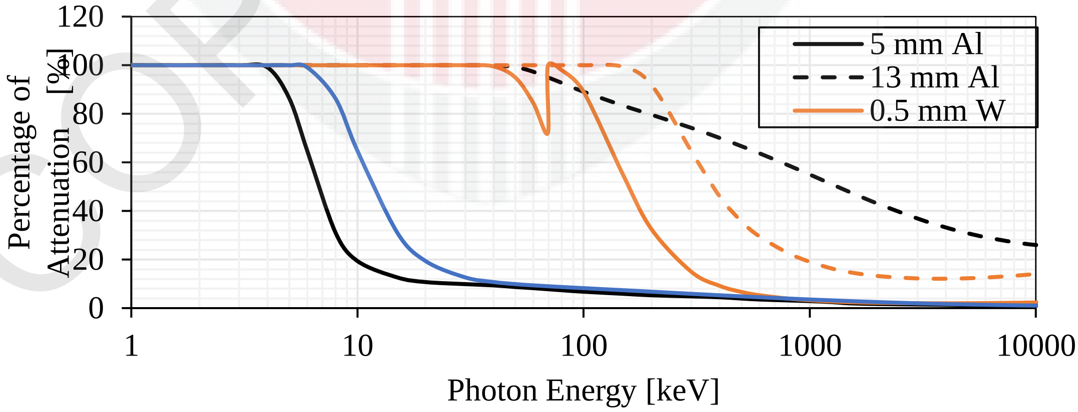


**Figure 4.3: Percentage of photon attenuation until $10^4$ keV for each filter**

### 4.2.3 Neutron Attenuation

The percentage of attenuation for each neutron energies is calculated using Equation 4.2. The equation is a modification from the Lambert-Beer's equation by McAlister (2016). Here, $N$ is atomic or molecular density of a compound which can be calculated using Equation 4.3 where $N_A$ is the Avogadro's constant and $M$ is the atomic or molecular weight of a compound (Nuclear power, 2023). Figure 4.4 shows the attenuated percentage for every filter for each incident neutron energy. At lower energies, 13 mm PE provided the best neutron shielding ability where almost 100% of neutrons are attenuated up to 0.014 eV. For thermal neutron (~0.025 eV) about 95% of incident neutron will be attenuated. Up until the resonance neutron energies, both W and Al attenuate neutron significantly lower than PE.

$$\text{Attenuated neutron [\%]} = (1 - I/I_o) \times 100 = (1 - e^{-(N\sigma)X}) \times 100 \qquad 4.2$$

$$N = \rho N_A / M \qquad 4.3$$

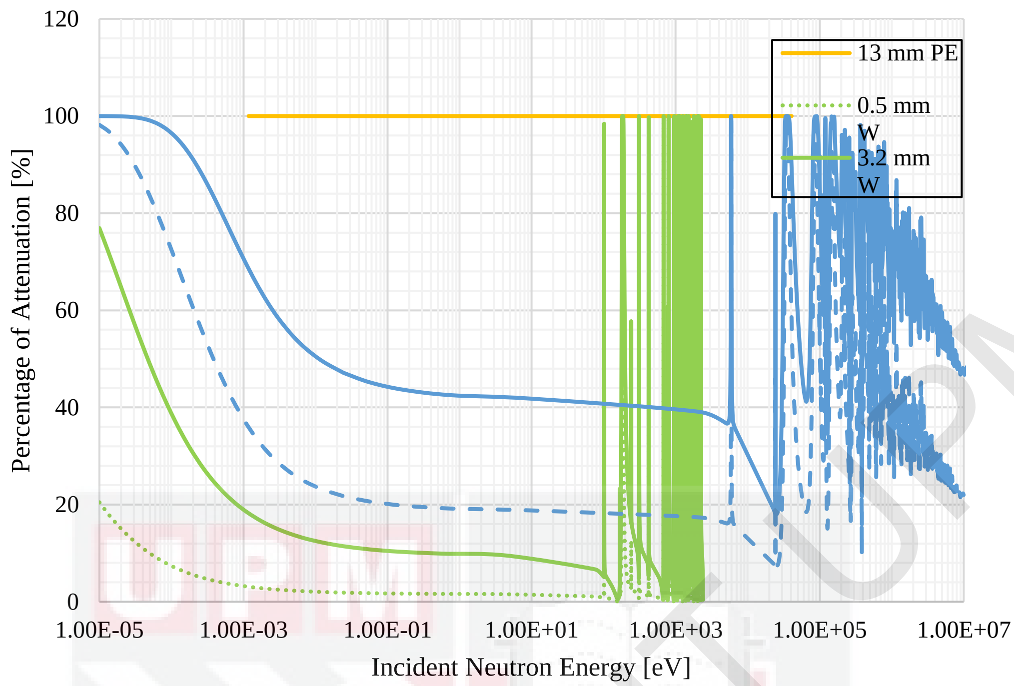


**Figure 4.4: Percentage of neutron attenuated up to $10^7$ eV incident neutron**

## 4.3 Stage 2: Structural Integrity of the Developed SOFPADS

In this section, the structural properties of SOFPADS in terms of random vibration test, sine burst test, and structural load tests are presented.

### 4.3.1 Vibration Test Results for Qualification and Acceptance

As additional measure to tightening the bolts using torque wrench, before and after condition of every bolt of the random vibration jig is assessed after the vibration tests are conducted to see whether they are loosened or not. Figure 4.5 shows an example of the bolts before and after test. The connected silver line after the vibration tests (Figure 4.5 (b)) shows that the bolt is not loosened after conducting the vibration tests. Condition of the bolts for each test is shown in Appendix B.

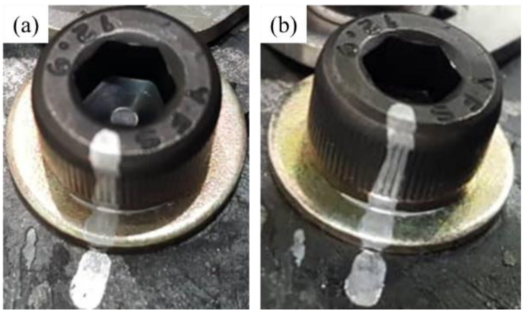


**Figure 4.5: Condition of bolt (a) before experiment, (b) after experiment of the vibration jig**

### 4.3.2 Random Vibration Test Results on Vibration Jig

The QT level vibration test on the vibration jig only without the payload is shown in Figure 4.6. The purpose of the test is to observe the vibration profile transmitted to the payload. This is important to assure that the payload is not being over or under tested. From the figure, in all axes, the vibrations produced by the vibration jig is within the high and low abort which is $\pm 3$ dB from the vibration profile. This reaffirms that the vibrations being transmitted onto the payload is within the high and low abort range.

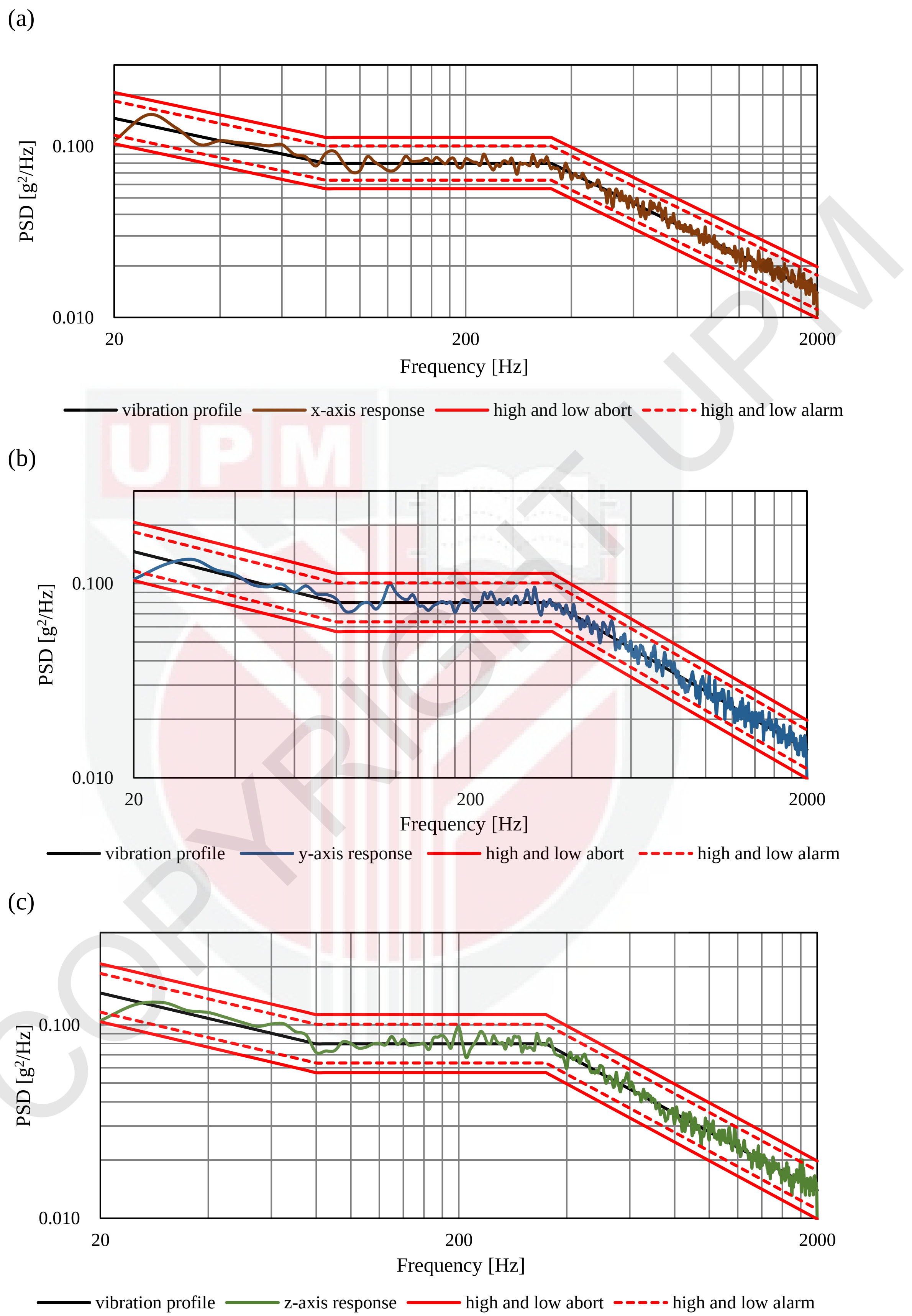


**Figure 4.6: QT level random vibration on vibration jig by LDS V9 shaker system: (a) x-axis, (b) y-axis, and (c) z-axis**

Similarly, the responses of the vibration jig for the AT are shown in Figure 4.7. Like the QT vibration jig, for AT, the vibration jig responses are within the high and low abort of the AT profile. This make certain that the FM is not being over or under tested.

(a)

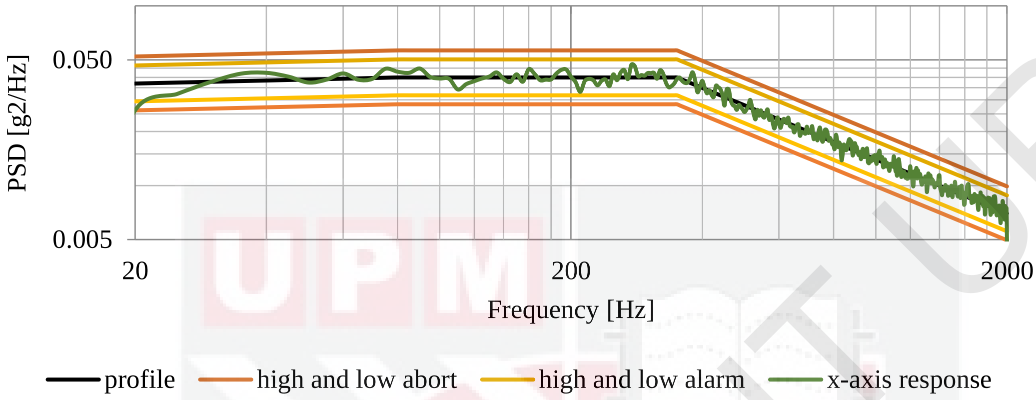


(b)

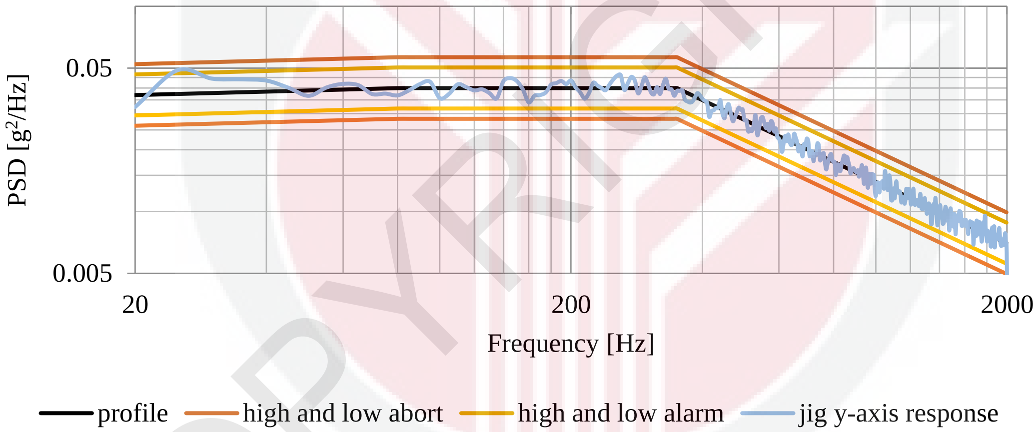


(c)

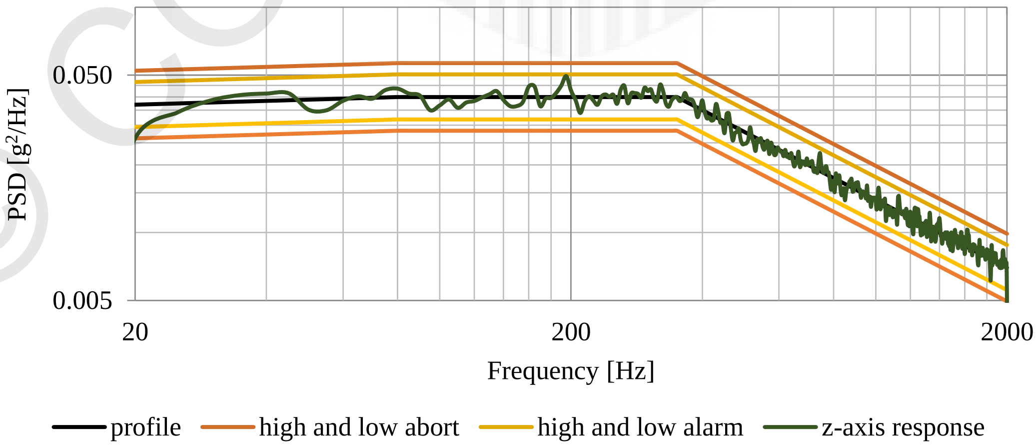


**Figure 4.7: AT level random vibration on vibration jig by MPA101 shaker system: (a) x-axis, (b) y-axis, and (c) z-axis**

### 4.3.3 Random Vibration at QT Level

Figure 4.8 shows the accelerometer responses for QT level random vibration test. In the x-axis, the resonance peaks occurring at the natural frequencies of the system have two modes at 540 Hz and 1120 Hz where the amplitudes were 0.1849 $g^2$/Hz and 0.1033 $g^2$/Hz respectively as shown in Figure 4.8 (a). In the y-axis, as expected, the accelerometer detected no responses within the high and low abort as the response amplitude is even lower. While the x-axis response is expected to be high, the z-axis response is not expected to produce even higher amplitude of resonance. This occurs at 1115 Hz (similar to the x-axis resonance frequency) with an amplitude of 0.2222 $g^2$/Hz as shown in Figure 4.8 (b).

The jig responses in axis of interest are within the high and low abort (Figure 4.8 (a)). In other axes, the jig responses are well below the low abort amplitude that within the range presented in Figure 4.8 (b), the responses could not be seen. The amplitude range presented in Figure 4.8 (b) covers the responses of the axis of interest.

(a)

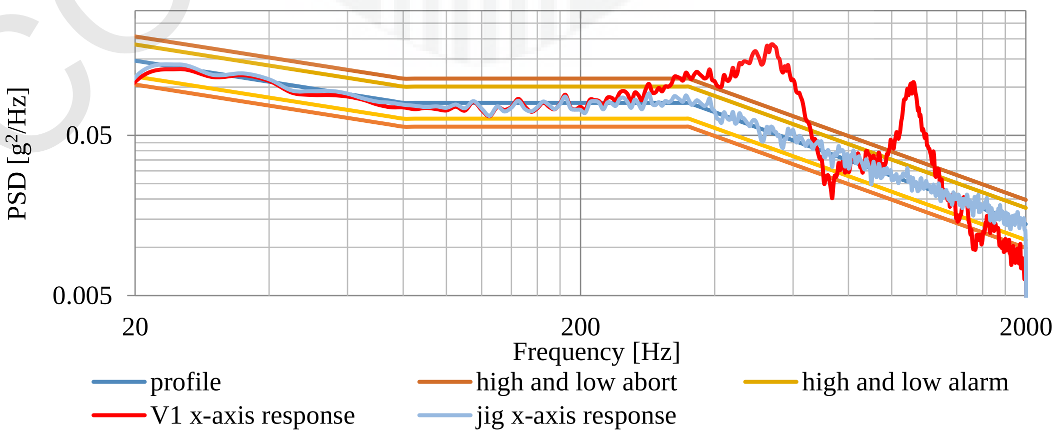

(b)

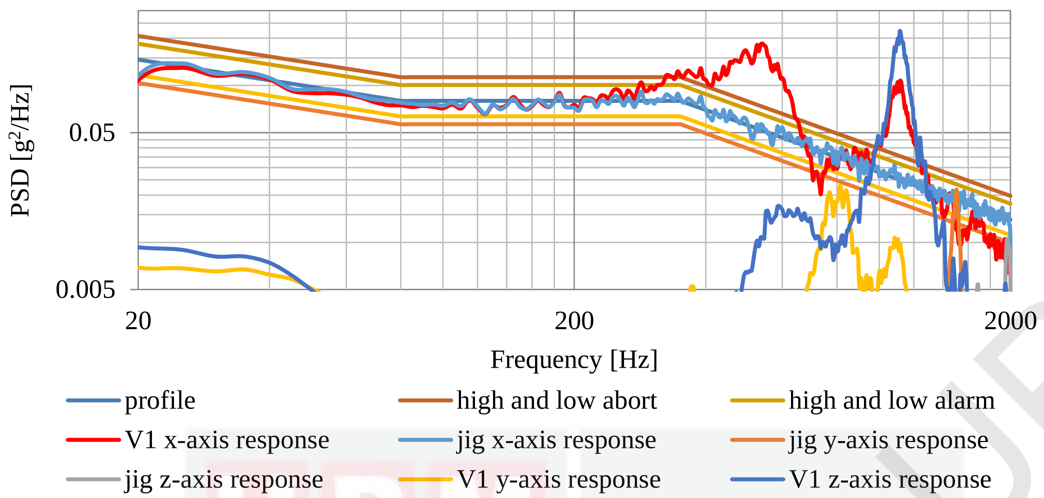


**Figure 4.8: QT level x-axis response of V1 payload. (a) X-axis response, (b) all axes responses**

Quality factors of the resonance ($Q_A$) and antiresonance ($Q_B$) are calculated using the method shown in Appendix C. $Q_A$ is also known as amplification factor. $Q_A$ shows the mechanical gain of the system during forced vibration at the system natural frequency (Forgrave et al., 1998). The value of $Q_A$ and $Q_B$ is shown in Table 4.3 and Table 4.4, respectively. In the tables, $Y_{max}$ and $Y_{min}$ is the amplitude of the resonance and antiresonance frequency respectively. ω is the frequency where the resonance or antiresonance occur. ω occurring at the resonance frequency is also the natural frequency of the system. $\omega_1$ is the lower frequency at ±3 dB of the $Y_{max}$ or $Y_{min}$, and $\omega_2$ is the higher frequency at ±3 dB of the $Y_{max}$ or $Y_{min}$.

The $Q_A$ of the resonance peak in the z-axis is higher at 17.15 than in the x-axis at 14.00 for the similar vibration frequency (1115-1120 Hz). $Q_B$ only occurs in the x-axis since there is only one mode of vibration occurring for the z-axis.

**Table 4.3: $Q_A$ for x-axis during QT**

| $Y_{max}$ [g²/Hz] | $Y_{max}/\sqrt{2}$ [g²/Hz] | ω [Hz] | $\omega_2$ [Hz] | $\omega_1$ [Hz] | $Q_A$ |
|---|---|---|---|---|---|
| **X-axis** | | | | | |
| 0.1849 | 0.1307 | 540 | 565 | 450 | 4.70 |
| 0.1033 | 0.0730 | 1120 | 1140 | 1060 | 14.00 |
| **Z-axis** | | | | | |
| 0.2222 | 0.1571 | 1115 | 1145 | 1080 | 17.15 |

**Table 4.4: $Q_B$ for x-axis during QT**

| $Y_{min}$ [g²/Hz] | $\sqrt{2}Y_{min}$ [g²/Hz] | ω [Hz] | $\omega_2$ [Hz] | $\omega_1$ [Hz] | $Q_B$ |
|---|---|---|---|---|---|
| **X-axis** | | | | | |
| 0.0202 | 0.0286 | 735 | 755 | 715 | 18.38 |
| 0.0097 | 0.0136 | 1540 | 1625 | 1495 | 11.85 |

For the QT in y-axis, single mode resonance peak at 775 Hz and 0.8408 $g^2$/Hz and an antiresonance at 1365 Hz and 0.0007 $g^2$/Hz can be seen in Figure 4.9 (a). The resonance and antiresonance frequency in the y-axis differ from the x-axis that have two modes of resonance frequencies.

From Figure 4.9 (b), while some axes apart of the axis of interest show responses near profile amplitude, they were under the high abort. As such, the $Q_A$ of the other axes are not considered.

(a)

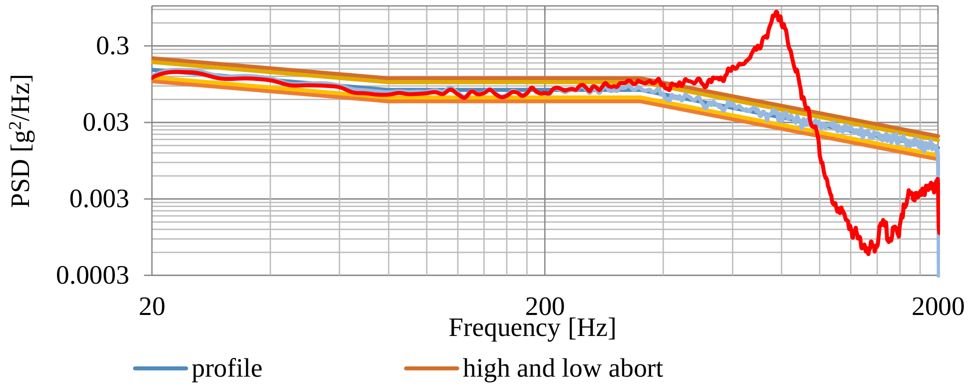


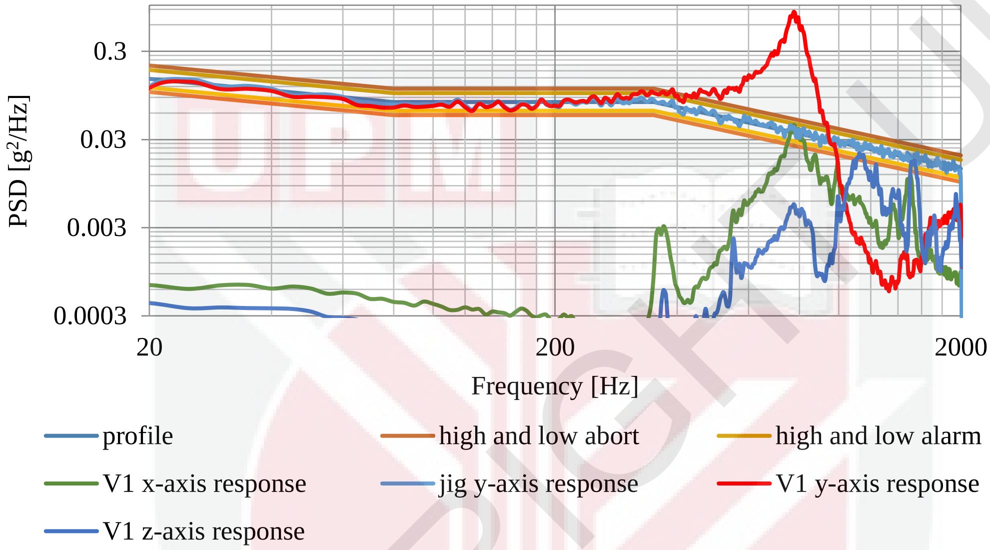


(b)

**Figure 4.9: QT level y-axis response of V1 payload. (a) Y-axis response, (b) all axes responses**

The value of $Q_A$ and $Q_B$ of QT in y-axis is shown in Table 4.5 and Table 4.6, respectively.

**Table 4.5: $Q_A$ for y-axis during QT**

| $Y_{max}$ [$g^2$/Hz] | $Y_{max}/\sqrt{2}$ [$g^2$/Hz] | $\omega$ [Hz] | $\omega_2$ [Hz] | $\omega_1$ [Hz] | $Q_A$ |
|---|---|---|---|---|---|
| 0.8408 | 0.5945 | 775 | 800 | 750 | 15.50 |

**Table 4.6: $Q_B$ for y-axis during QT**

| $Y_{min}$ [$g^2$/Hz] | $\sqrt{2}Y_{min}$ [$g^2$/Hz] | $\omega$ [Hz] | $\omega_2$ [Hz] | $\omega_1$ [Hz] | $Q_B$ |
|---|---|---|---|---|---|
| 0.0007 | 0.0010 | 1365 | 1410 | 1305 | 13.00 |

For the z-axis, two modes of resonance peaks can be seen by the payload at 490 Hz, 0.2014 $g^2$/Hz and 955 Hz, 2.3288 Hz as shown in Figure 4.10 (a). Unlike the other axes, no antiresonance region can be seen as the responses were within or over the high and low abort. Both x- and y-axes also produced resonances as shown in Figure 4.10 (b).

(a)

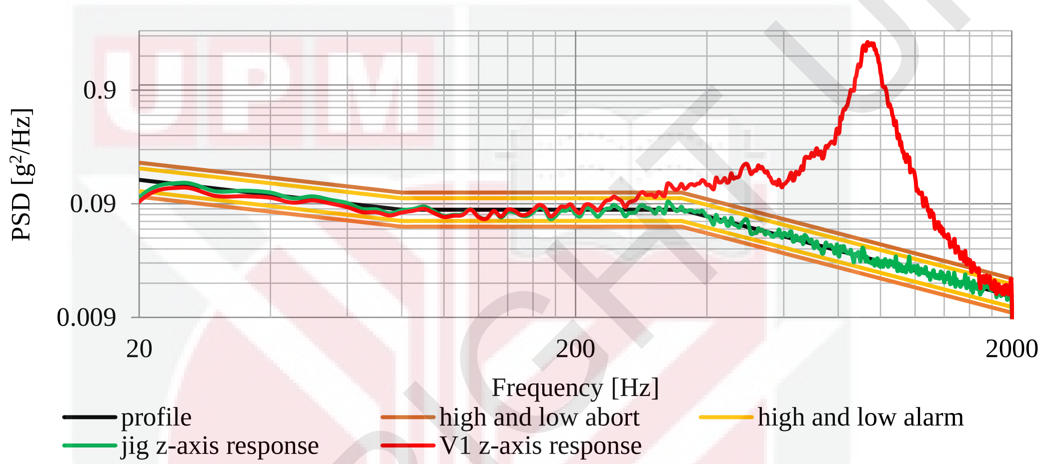


(b)

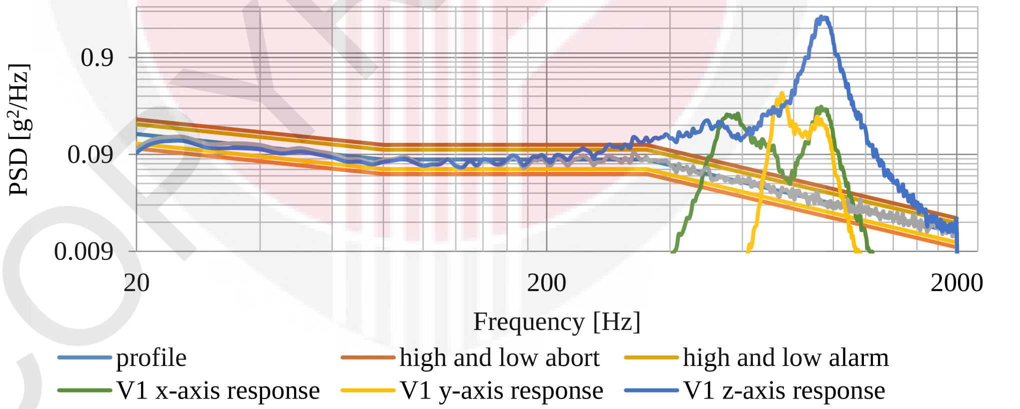


**Figure 4.10: QT level z-axis response of V1 payload. (a) Z-axis response, (b) all axes responses**

The resonance frequencies and $Q_A$ during z-axis QT is presented in Table 4.7. All three axes produced two modes of resonance frequencies within the tested bandwidth. The second mode of resonance frequencies of all three axes are similar at 935 Hz, 915 Hz and 955 Hz respective to x-axis, y-axis and z-axis. The $Q_A$ of the second mode for all three axes are also similar at 10.17-11.00.

**Table 4.7: $Q_A$ for z-axis during QT**

| $Y_{max}$ [$g^2$/Hz] | $Y_{max}/\sqrt{2}$ [$g^2$/Hz] | ω [Hz] | $\omega_2$ [Hz] | $\omega_1$ [Hz] | $Q_A$ |
|---|---|---|---|---|---|
| **X-axis** | | | | | |
| 0.2295 | 0.162 | 560 | 615 | 520 | 5.89 |
| 0.2798 | 0.198 | 935 | 985 | 900 | 11.00 |
| **Y-axis** | | | | | |
| 0.3889 | 0.2750 | 750 | 775 | 720 | 13.64 |
| 0.2214 | 0.1565 | 915 | 970 | 880 | 10.17 |
| **Z-axis** | | | | | |
| 0.2014 | 0.1424 | 490 | 565 | 455 | 4.45 |
| 2.3288 | 1.6467 | 955 | 990 | 900 | 10.61 |

### 4.3.4 Random Vibration at AT Level

Like the QT, the random vibration test at AT level responses were obtained as shown in Figure 4.11 for the x-axis. As presented in Figure 4.11 (b) in x-axis AT the payload produced responses in all axes. The resonance frequencies and $Q_A$ is gathered Table 4.8. For x-axis AT, in all axes, the resonance frequencies occur at the same frequency of 780 Hz for the first mode and at 1250-1265 Hz for the second mode. The accelerometer in on the vibration jig only produces response within the high and low abort in the x-axis. In the y- and z-axes the responses were considerably lower than the low abort amplitude. The $Q_A$ values of first mode of vibration were also similar, ranging from 19.50 to 26.00 while the second mode of vibration ranged from 14.71 to 15.8. As the y- and z-axis are not expected to produce large responses, the $Q_B$ of the axes were not determined. Gathered in Table 4.9 are the $Q_B$ of the x-axis at 20.10 for the first antiresonance of 1005 Hz and 16.70 for the second antiresonance frequency of 1670 Hz.

(a)

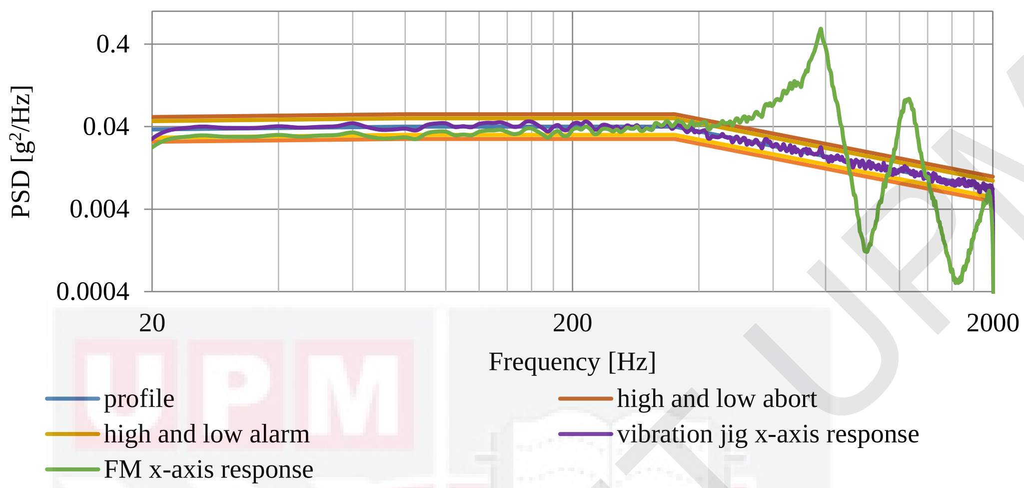


(b)

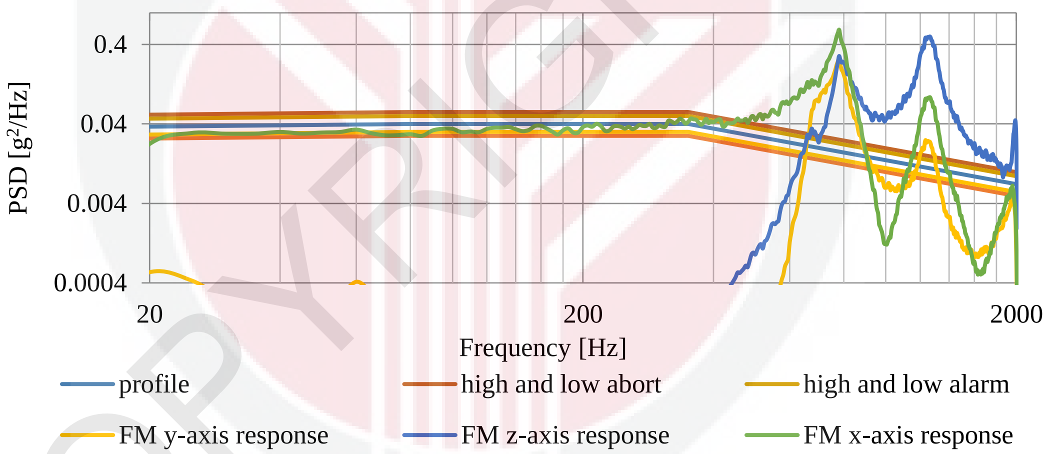


**Figure 4.11: AT level x-axis response of FM payload. (a) X-axis response, (b) all axes responses**

**Table 4.8: $Q_A$ for x-axis during AT**

| $Y_{max}$ [g²/Hz] | $Y_{max}/\sqrt{2}$ [g²/Hz] | ω [Hz] | $\omega_2$ [Hz] | $\omega_1$ [Hz] | $Q_A$ |
|---|---|---|---|---|---|
| **X-axis** | | | | | |
| 0.6134 | 0.4338 | 780 | 790 | 760 | 26.00 |
| 0.0866 | 0.0612 | 1265 | 1300 | 1220 | 15.81 |
| **Y-axis** | | | | | |
| 0.2694 | 0.1905 | 780 | 795 | 760 | 22.29 |
| 0.0245 | 0.0173 | 1250 | 1285 | 1200 | 14.71 |

**Table 4.8: Continued**

| $Y_{max}$ [$g^2$/Hz] | $Y_{max}/\sqrt{2}$ [$g^2$/Hz] | ω [Hz] | $\omega_2$ [Hz] | $\omega_1$ [Hz] | $Q_A$ |
|---|---|---|---|---|---|
| **X-axis** | | | | | |
| 0.6134 | 0.4338 | 780 | 790 | 760 | 26.00 |
| 0.0866 | 0.0612 | 1265 | 1300 | 1220 | 15.81 |

**Table 4.9: $Q_B$ for x-axis during AT**

| $Y_{min}$ [$g^2$/Hz] | $\sqrt{2}Y_{min}$ [$g^2$/Hz] | ω [Hz] | $\omega_2$ [Hz] | $\omega_1$ [Hz] | $Q_B$ |
|---|---|---|---|---|---|
| 0.0012 | 0.0017 | 1005 | 1030 | 980 | 20.10 |
| 0.0005 | 0.0007 | 1670 | 1700 | 1600 | 16.70 |

Figure 4.12 shows the responses in y-axis in the axis of interest (Figure 4.12 (a)) and all axes (Figure 4.12 (b)). Like the x-axis vibration, the payload produced responses in all axes with resonances and antiresonances gathered in Table 4.10 and Table 4.11, respectively. In the region of interest (y-axis), resonances occur in three modes (650 Hz, 790 Hz and 1770 Hz). On the other hand, in the x-and z-axes the resonances occur in two modes with similar frequencies (790 Hz and 1220/1235 Hz). The second mode of y-axis, and, first and second mode of the x- and z-axes during y-axis AT show similarities to the modes of the x-axis AT results. This shows that the natural frequencies of the system in different axes are similar implying that the internal structure of the casing in both x- and y-axes being similar.

(a)

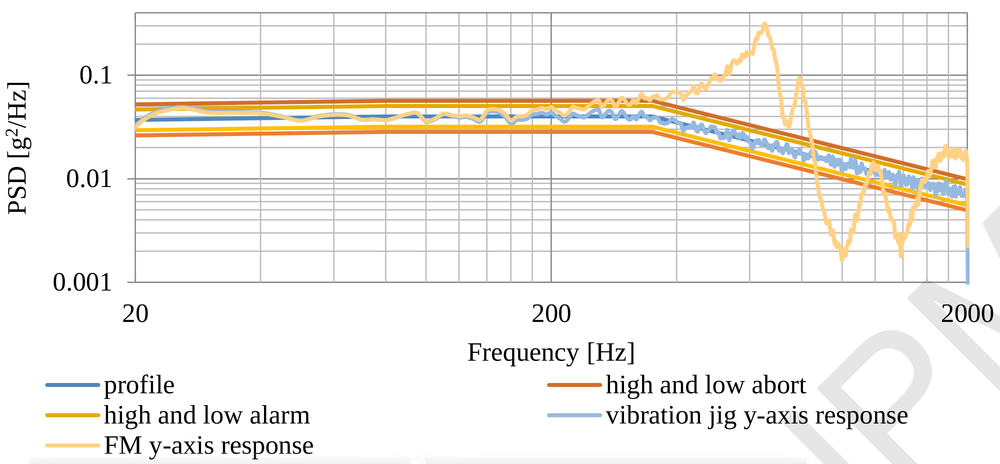


(b)

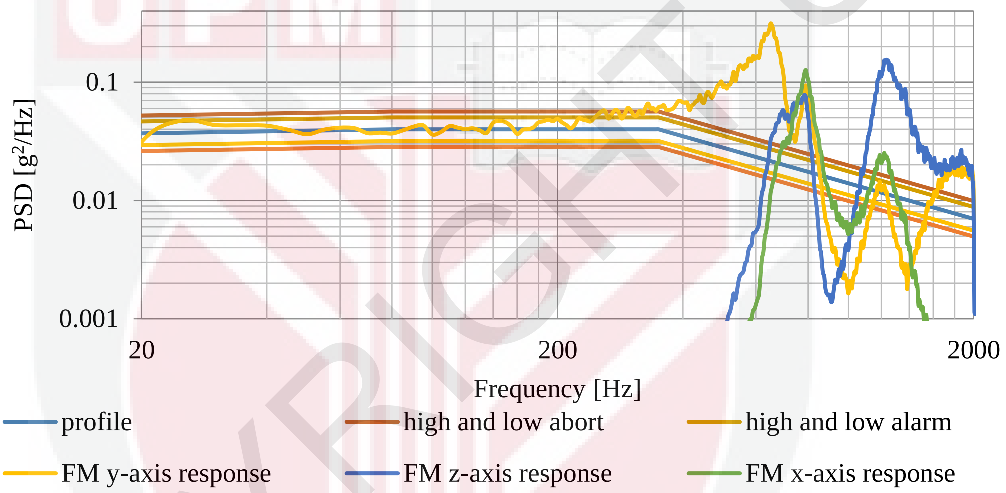


**Figure 4.12: AT level y-axis response of FM payload. (a) Y-axis response, (b) all axes responses**

**Table 4.10: $Q_A$ for y-axis during AT**

| $Y_{max}$ [g²/Hz] | $Y_{max}/\sqrt{2}$ [g²/Hz] | ω [Hz] | $ω_2$ [Hz] | $ω_1$ [Hz] | $Q_A$ |
|---|---|---|---|---|---|
| **X-axis** | | | | | |
| 0.0752 | 0.0532 | 790 | 800 | 730 | 11.29 |
| 0.0252 | 0.0178 | 1220 | 1255 | 1155 | 12.20 |
| **Y-axis** | | | | | |
| 0.3132 | 0.2214 | 650 | 675 | 615 | 10.83 |
| 0.0941 | 0.0665 | 790 | 810 | 775 | 22.57 |
| 0.0206 | 0.0146 | 1770 | 2000 | 1680 | 5.53 |
| **Z-axis** | | | | | |
| 0.1266 | 0.0895 | 790 | 810 | 770 | 19.75 |
| 0.1547 | 0.1094 | 1235 | 1285 | 1185 | 12.35 |

**Table 4.11: $Q_B$ for y-axis during AT**

| $Y_{min}$ [$g^2$/Hz] | $\sqrt{2}Y_{min}$ [$g^2$/Hz] | ω [Hz] | $\omega_2$ [Hz] | $\omega_1$ [Hz] | $Q_B$ |
|---|---|---|---|---|---|
| 0.0016 | 0.0023 | 1000 | 1035 | 980 | 18.18 |
| 0.0018 | 0.0025121 | 1385 | 1395 | 1375 | 69.25 |

As per the x- and y-axes the z-axis AT responses in presented in Figure 4.13. Unlike the x- and y-axes however, there is no antiresonance region where the amplitude falls under the low abort (Figure 4.13 (a)). While there are some discrepancies in the resonance frequencies, the first mode for all axes occurs at similar frequency of 580-605 Hz as shown in Figure 4.13 (b) and gathered in Table 4.12. The axis of interest (z-axis) produced the most resonance frequencies with four modes where apart from the first mode, the third mode also occurred in x- and y-axes at 1150 Hz.

(a)

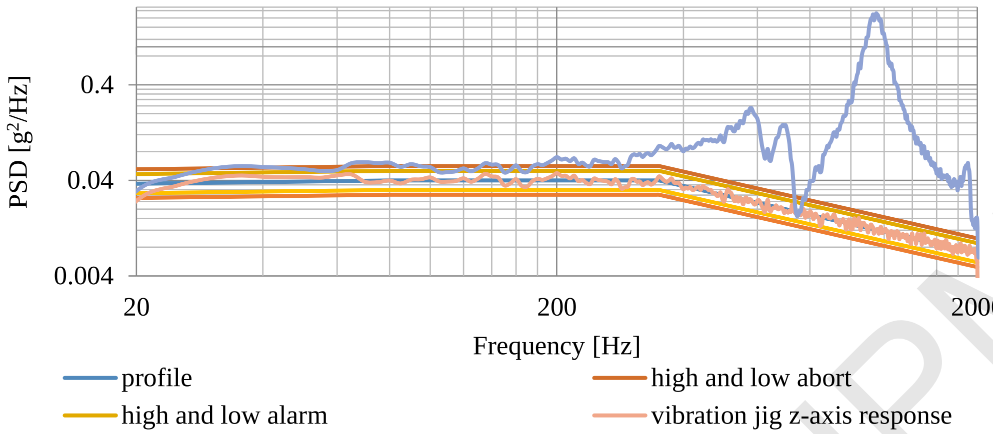


(b)

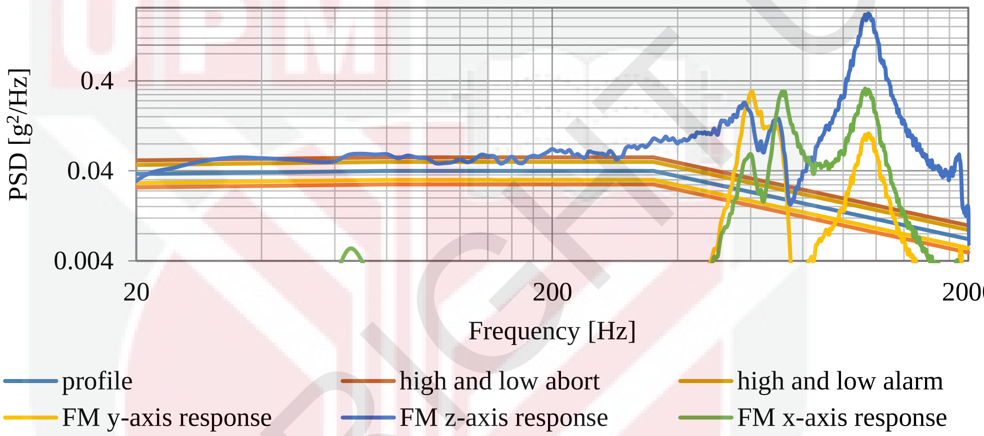


**Figure 4.13: AT level z-axis response of FM payload. (a) Z-axis response, (b) all axes responses**

**Table 4.12: $Q_A$ for z-axis during AT**

| $Y_{max}$ [g²/Hz] | $Y_{max}/\sqrt{2}$ [g²/Hz] | ω [Hz] | $\omega_2$ [Hz] | $\omega_1$ [Hz] | $Q_A$ |
|---|---|---|---|---|---|
| **X-axis** | | | | | |
| 0.0614 | 0.0434 | 600 | 615 | 570 | 13.33 |
| 0.3042 | 0.2151 | 715 | 735 | 695 | 17.88 |
| 0.3203 | 0.2265 | 1150 | 1185 | 1100 | 13.53 |
| **Y-axis** | | | | | |
| 0.3045 | 0.2153 | 605 | 620 | 585 | 17.29 |
| 0.1046 | 0.0740 | 1150 | 1190 | 1105 | 13.53 |
| **Z-axis** | | | | | |
| 0.2293 | 0.1621 | 580 | 605 | 555 | 11.60 |
| 0.1527 | 0.1079 | 690 | 715 | 660 | 12.55 |
| 2.2387 | 1.5830 | 1150 | 1185 | 1105 | 14.38 |
| 0.0610 | 0.0432 | 1900 | 1920 | 1850 | 27.14 |

### 4.3.5 Sine Burst Test Results

The sine burst responses of the accelerometers attached onto vibration jig and payload are shown in Figure 4.14 in time domain and Figure 4.15 in frequency domain. Table 4.13 summarises the resonance frequencies of both vibration jig and hardware. Both vibration jig and V1 shows similar responses with each other. For x-axis and y-axis static load, in x-axis and y-axis vibration direction, during ramp up/ramp down, both vibration jig and hardware had acceleration of lower than the profile (Figure 4.14 (a) and (b)). However, at full level excitation of ±0.2 g at 15 Hz, the acceleration of vibration jig and hardware were higher than the profile of up to ± 0.4822 g for x-axis and ±0.5219 g for y-axis. Z-axis static load test is an exception where even during ramp up/ramp down the vibration jig and hardware had a higher acceleration than the profile up to ±0.2837 g (Figure 4.14 (c)).

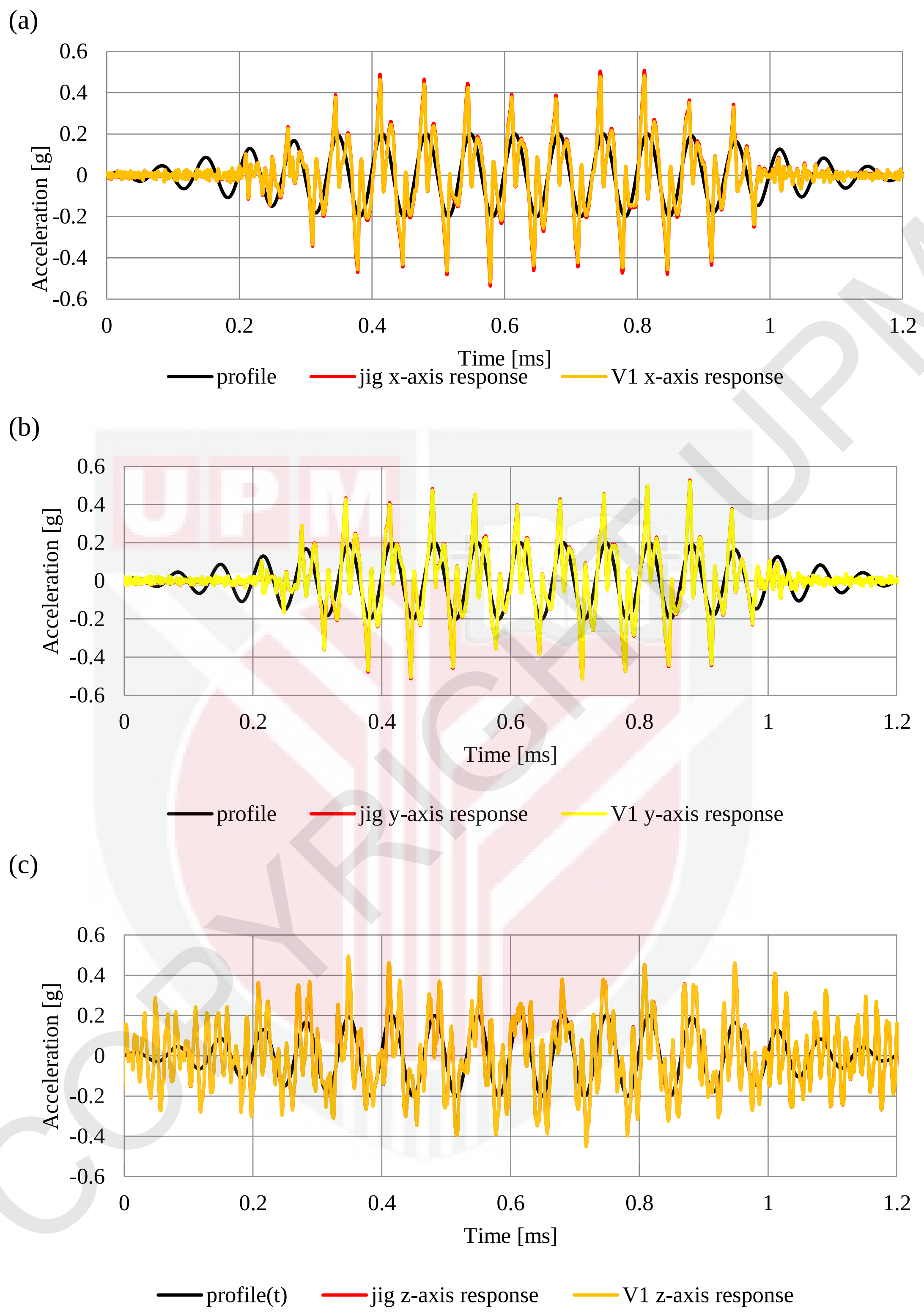


**Figure 4.14: Sine burst responses (time domain): (a) x-axis, (b) y-axis and (c) z-axis**

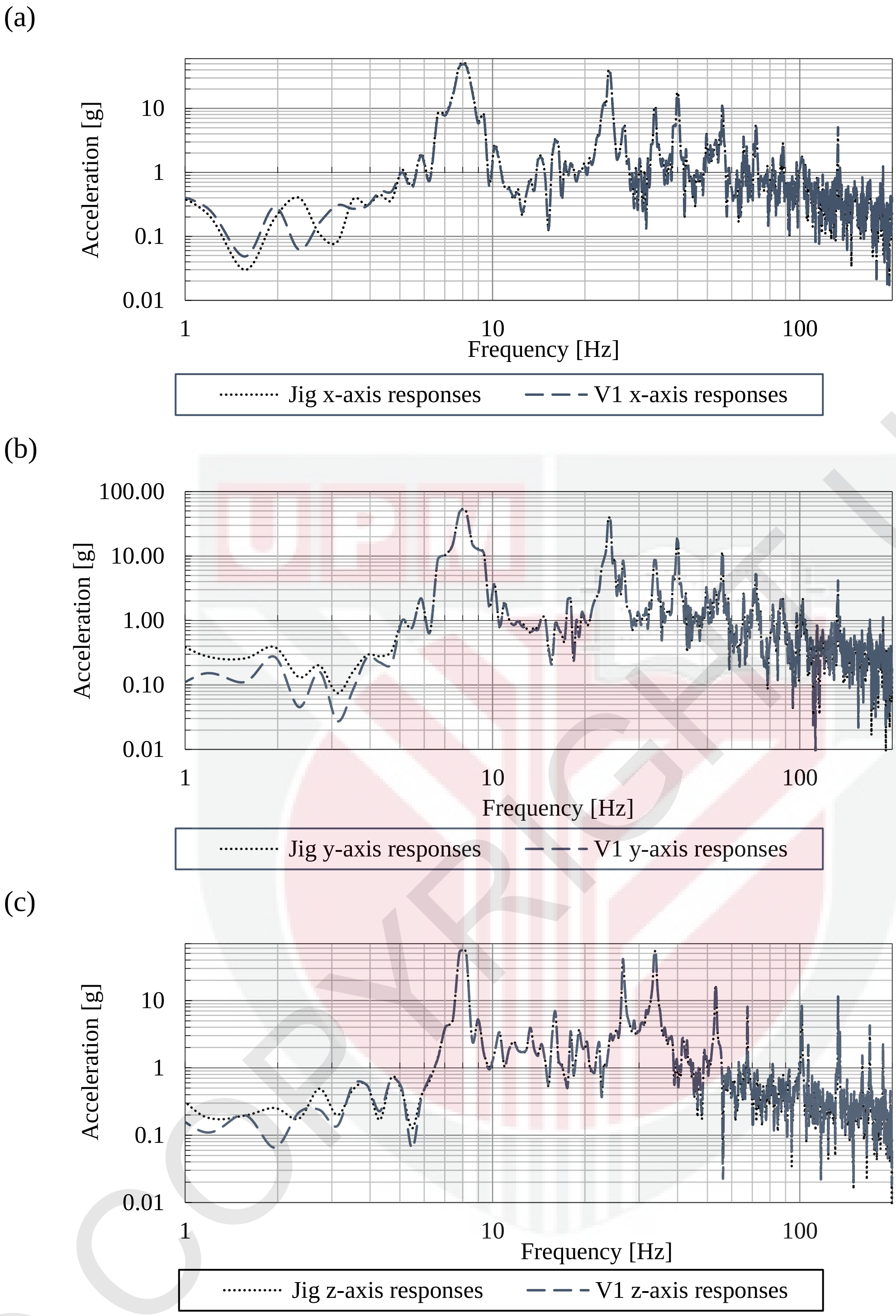


**Figure 4.15: Sine burst responses (frequency domain): (a) x-axis, (b) y-axis, and (c) z-axis**

From Table 4.13, in the x- and y-axis, both jig and hardware had similar resonance frequency and acceleration. Even between the x-axis vibration and the y-axis vibration, the resonance frequency and acceleration were similar. However, for z-axis vibration, while the hardware and vibration jig had similar responses like the x-axis and y-axis counterparts, the resonance frequency and acceleration were slightly different (Figure 4.15 (a) and Figure 4.15 (b)). For example, for V1, at 23.83 Hz, there is a resonance at 37.25 × $10^{-4}$ $g^2$/Hz and 39.09 × $10^{-4}$ $g^2$/Hz respective to the x-axis and y-axis vibration (accelerometer response in the vibration direction). However, there is no resonance at 23.83 Hz in z-axis vibration. Nearby the resonance at 23.83 Hz, there is another peak at 26.56 Hz. Here, both the x-axis and y-axis had low acceleration at 4.75 and 9.94 × $10^{-4}$ $g^2$/Hz while the acceleration for the z-axis was much higher at 40. 73 × $10^{-4}$ $g^2$/Hz.

The resonance frequencies and amplitude of V1 are similar to the vibration jig. Since the V1 and vibration jig produced similar responses, there is no amplification produced by the payload meaning that the resonance peaks are purely produced from the vibration jig. Compared with the previous random vibration results, the natural frequency of the system at minimum occurs at 490 Hz (Table 4.7). As such, the payload responded to the profile given by the vibration jig. However, the vibration jig did not produce the profile as driven by the shaker. This can be due to the mass of the vibration jig as compared to the load given.

**Table 4.13: Resonance frequencies in every axis during a static load test in the axis direction**

| Accelerometer location | Resonance frequency in vibration direction [Hz] | | | Acceleration [g] | | |
|---|---|---|---|---|---|---|
| | x-axis | y-axis | z-axis | x-axis | y-axis | z-axis |
| Vibration jig | 8.2 | 8.2 | 7.81 | 48.88 | 49.96 | 52.12 |
| | 16.01 | 17.58 | 16.02 | 3.37 | 2.02 | 6.72 |
| | 23.83 | 23.83 | - | 39.18 | 39.62 | - |
| | 26.59 | 26.56 | 26.56 | 5.01 | 8.5 | 40.46 |
| | 33.59 | 33.59 | 33.98 | 10.41 | 8.37 | 54.37 |

**Table 4.13: Continued**

| Accelerometer location | Resonance frequency in vibration direction [Hz] | | | Acceleration [g] | | |
|---|---|---|---|---|---|---|
| | x-axis | y-axis | z-axis | x-axis | y-axis | z-axis |
| | 39.84 | 39.84 | - | 17.57 | 18.52 | - |
| | 55.86 | 55.86 | 53.13 | 10.82 | 11.38 | 16.54 |
| | 71.87 | 71.88 | 67.58 | 5.51 | 5.17 | 7.94 |
| | - | - | 101.56 | - | - | 8.27 |
| | 133.2 | 131.2 | 133.2 | 4.32 | 3.74 | 10.3 |
| | - | - | 169.14 | - | - | 3.39 |
| | - | - | 186.72 | - | - | 1.87 |
| V1 | 8.2 | 8.2 | 7.81 | 46.42 | 48.93 | 52.19 |
| | 16.02 | 17.58 | 16.02 | 3.19 | 2.13 | 6.87 |
| | 23.83 | 23.83 | - | 37.25 | 39.09 | - |
| | 26.56 | 25 | 26.56 | 4.75 | 9 | 40.73 |
| | 33.59 | 33.59 | 33.98 | 9.94 | 8.51 | 54.74 |
| | 39.84 | 39.84 | - | 16.83 | 18.23 | - |
| | 55.86 | 55.86 | 53.13 | 10.59 | 11.44 | 16.84 |
| | 71.87 | 71.88 | 67.58 | 5.46 | 5.24 | 8.12 |
| | - | - | 101.56 | - | - | 8.83 |
| | 133.2 | 133.2 | 133.2 | 4.64 | 4.05 | 11.54 |
| | - | - | 169.14 | - | - | 4.12 |
| | - | - | 186.33 | - | - | 1.21 |

### 4.3.6 Criteria of Acceptance of the Vibration Test Results

There are two criteria for acceptance of vibration testing: (1) Structural damages on the casing itself, and (2) the functionality of the PD incorporated within the casing.

In terms of structural damages, the assessment can be made by comparing the condition of V1 before conducting the test and post-test. V1 condition prior and post random vibration test and sine burst test are shown in Table 4.14. From the table, there are no scratches that can be seen externally or internally (internal parts of the casing). As for screws, the casing was sealed using 10 cNm torque for consistency in applying torque for tightening the screws. Additional observations were made using a marker as shown in the table to see that there was no loosening occurring.

Brummit (2010) conducted random vibration with NASA GEVS profile where at the input of 0.04 $g^2$/Hz (20-2000 Hz), the amplitude of the PCB integrated into the CubeSAT had an amplification of up to 44.27 $g^2$/Hz in the z-axis excitation with broken capacitor, loose nut and staking compound. Even after modification, the final 1U CubeSAT qualification for Brummit (2010) had a maximum amplification of 15.22 $g^2$/Hz in the z-axis excitation at an approximate input amplitude of 0.70 $g^2$/Hz (815 Hz) without any loosening of spring plunger. This work agrees with the final 1U CubeSAT with a lower maximum amplification amplitude at 2.33 $g^2$/Hz for QT where the input amplitude was 0.03 $g^2$/Hz. A significant factor of acceptance also lies on the condition of the casing after test where the casing look the same as the condition prior to testing showing that the external parts and internal parts were undamaged.

Like Brummit (2010), this work's z-axis direction random vibration produced the highest amplification. Several factors affect z-axis amplification: 1) placement of accelerometer on the thinnest section of the casing. The thinnest part of the casing is 1 mm meaning that this section has the lowest stiffness causing the most deformation. In the x-axis and y-axis vibration, the vibration is parallel to the surface, hence the amplification may be caused by out-of-plane deformation. However, for the z-axis where the vibration direction is perpendicular to the surface, apart from the natural deformation occurring due to the casing structure and internal parts within the casing, the mass of the accelerometer itself may contribute to the additional amplification. This also agrees with Brummit (2010) where the PCB is the thinnest part during vibration in the z-axis producing the highest amplification. 2) Lack of securement. The casing is secured near four edges. As can be seen during the fifth iteration (Chapter 3 subsection 3.3.6), there was a bulging occurring in the middle of the case cover. This implies that without sufficient securement, enough force (in the case of vibration, acceleration producing force) will be able to cause deformation to the case cover. Hence, during random vibration test in z-axis especially in the middle of the case cover that is not secured, additional vibration might be produced causing the highest amplification.

**Table 4.14: Case condition before and after random vibration test and static load test**

| Parts | Before Test | After Test | Remarks |
|---|---|---|---|
| **Top** |   |   | No scratches or other damages can be seen apart of the remnant of Kapton tape and adhesive used to attach accelerometer. |
| **Inner part of case cover** | 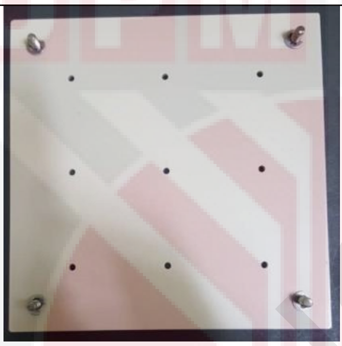 | 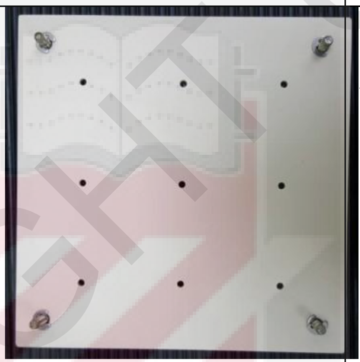 | No visible damages can be seen |
| **Bottom** | 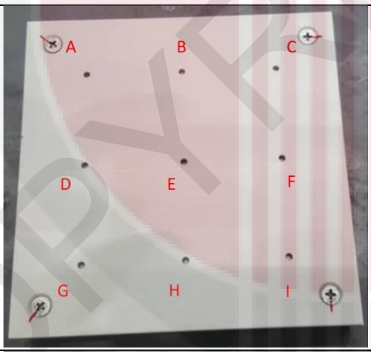  | 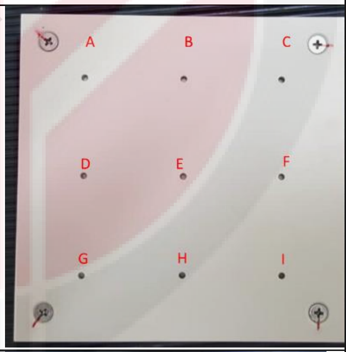  | No loosening of screws. No damages. |
| **Bottom (A screw)** |  | 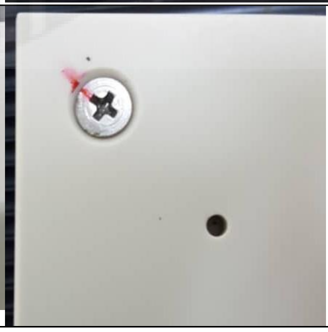 | No loosening. Marker smudged due to isopropyl alcohol by handler. |

**Table 4.14: Continued**

| Parts | Before Test | After Test | Remarks |
|---|---|---|---|
| **Bottom (C screw)** |  |  | No loosening |
| **Bottom (G screw)** |  | 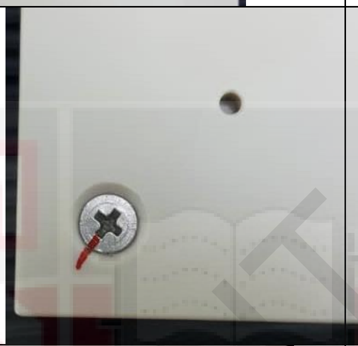 | No loosening |
| **Bottom (I screw)** | 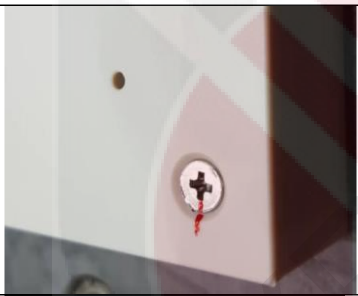 | 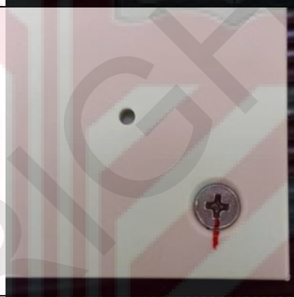 | No loosening |
| **Inner** | 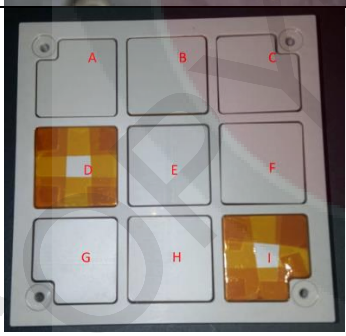  | 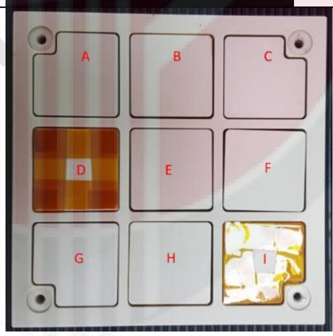  | No shatter able materials can be seen. (The alphabets represent case main body's sections) |

In terms of functionality, the CubeSATs can be tested immediately as they use and active system. In this work the functionality only falls to the PD that is incorporated within the casing. Due to the passive nature of the sensor, functionality testing requires extraction of the materials from the casing, irradiation and sample read-out which requires a set of experiment, thus, time consuming. The functionality of the PD prior to the vibration test, hence, is assumed to be the preliminary irradiations (Stage 3) which are conducted concurrently with the Stage 1 of the research before being incorporated into the casing for structural tests.

While ideally, the functionality of the post-structural tests of the PD should be considered before the space exposure, FM (casing used for AT) is used directly after conducting the tests without modification to preserve to condition of the casing, thus, not allowing for the functionality to assessed. However, for PD, even if the material is shattered, it is expected to not lose the function of detecting radiation. This is due to the TL nature of the material that is based on the energy band of said material, not requiring the material to be at a specific geometry (Bos, 2006). This also further agrees with the existence of TLD-100 in powder form and other TL materials such as TLD-MSO-S (Fadzil et al. 2022; Nagamatsu et al., 2013). As such, the physical form of the PD is expected to affect the radiation detection capabilities of the PD used in this work. Furthermore, in Chapter 3, subsection 3.6.2, the PD that has underwent AT level vibration and space exposure was not deformed physically.

## 4.4 Structural Load Test Results

The points of loading on V1 are shown in Figure 4.16. Each point is compressed under Tip 2 then followed by Tip 1.

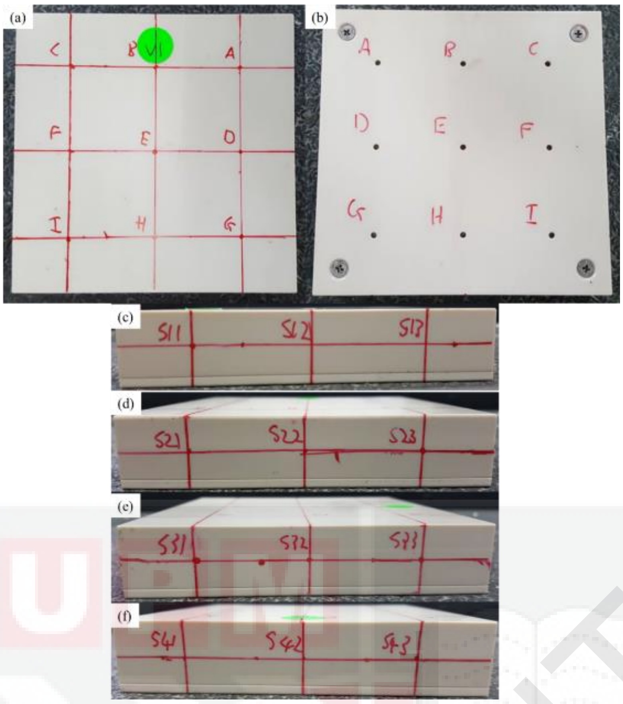


**Figure 4.16: V1 compression point. (a) top, (b) bottom, (c) side from points C, F, I, (d) side from points I, H, G, (e) side of points, A, D, G, (f) side from points C, B, A**

Figure 4.17 (a) shows the load-time curve of robotic arm collision load test on the top side of V1. At the top side of the case on point E, failure occurred at 304 N (SF 1.46) while on other points at top part of the hardware, the case structure can withstand the load up to 416 N (SF 2.0) as shown in the figure. At point E, even though the curve showed sign of failure at 304 N, only slight scratches can be seen as shown in Figure 4.18. This indicates that the failure occurred internally. Displacements at point A, G and I were larger than point C with multiple drops on the load. At these points A, G and I, small indentation can be seen as presented in Figure 4.19. Since there were no major physical failure found in the load-displacement curves, these results show that the hardware structure does not follow plastic deformation (where a major drop in load occurred after reaching a maximum load). This can be expected as the structural load test is not applied on sample conditioned for mechanical testing. Instead, the load is applied on the designed hardware. The internal structure of the hardware will influence the deformation of the hardware.

For bottom part of V1, Tip 1 load is applied at points approximately 3 mm from the outer end of the vent holes. From Figure 4.17 (b), at any point, the bottom part of the hardware can withstand force of up to 416 N without any failure occurring. There is no visible damage can be seen at each point tested.

For side part of V1, the results are shown in Figure 4.17 (c). From the figure, the side part of the hardware can withstand force of up to 416 N without any failure occurring. Again, there is no visible damage that can be seen at each point tested. Compared to the top (1 mm thick), both bottom (2.5 mm thick) and sides (minimum of 6 mm thick) did not produce any failure due to their thicknesses.

(a)

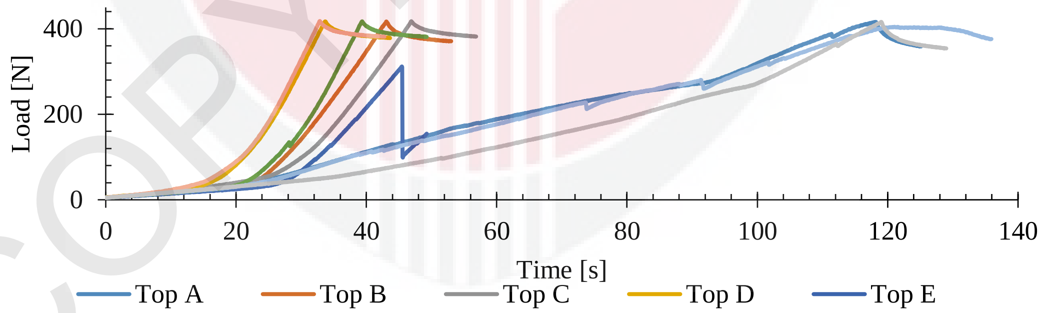


(b)

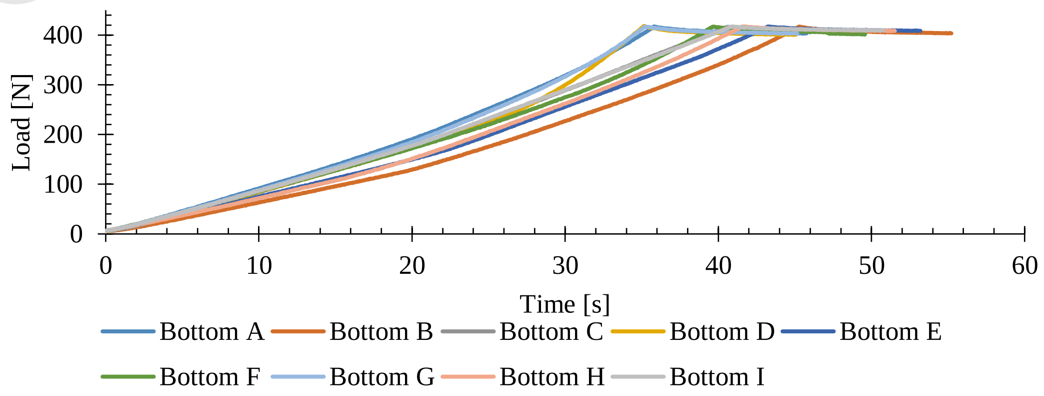

(c)

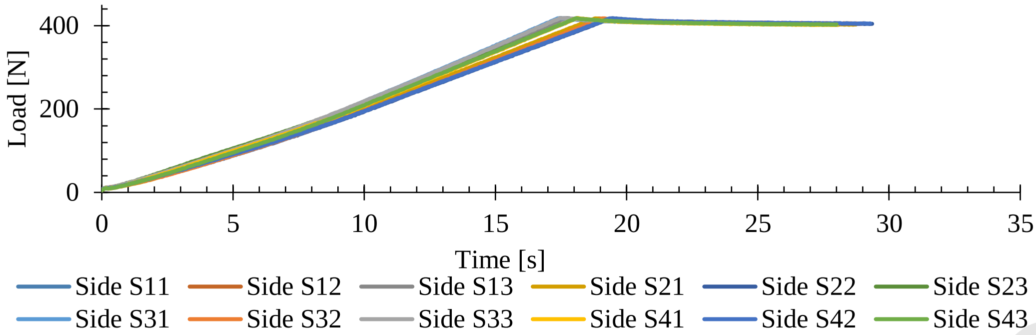


**Figure 4.17: Load-time curve of using tip 1 on V1: (a) Top, (b) bottom, and (c) sides**

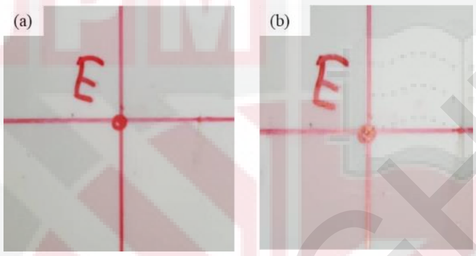


**Figure 4.18: Condition of point E on the top of V1 (a) before and (b) after structural load test using Tip 1**

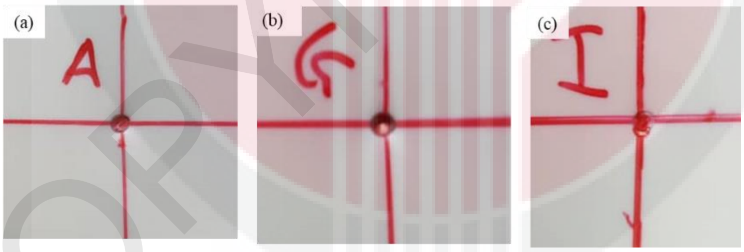


**Figure 4.19: Conditions of point (a) A, (b) G and (c) I after structural load test using Tip 1**

For V2, rather than conducting the test on all point only points, A, C, E, G and I are tested. For the top part, test on point G is considered as a failed test due to bent shaft. The same test could not be conducted since point G is already deformed. Figure 4.20 (a) shows the resultant load curve upon top part of V2. This time point E and point I both had internal failure at 309 N (SF = 1.49) and 320 N (SF = 1.50). Point A had a sudden drop in load at 407 N (safety factor 1.96) while top C point had a drop in load at 576 N which is well past of safety factor 2.0. At most the load increased up to 1366 N.

For the bottom part of the hardware, from Figure 4.20 (b), at all points tested, a drop in load can be seen well past 416 N (SF = 2.0). However, the drop in load was not due to failure of the case part, it was due to the stainless-steel rod bending at around 1000 N. The penetration occurred during the rise of load up to 1000 N. From the same test conducted on V1, it can be assumed that the penetration occurred at a higher load than 416 N since during the test conducted on V1, no visible damage can be seen.

Since the side parts of the hardware of the hardware possess the thickest wall, it is the part that can withstand the highest load. From Figure 4.20 (c), at all points tested at a particular load, sudden drop in load can be seen. This sudden drop of load is not due to failure of the case part; but it is due to unbuckling of the hardware since the side part of the hardware is not thick enough to prevent the hardware from moving due to pressure. Before the hardware unbuckles, at minimum, 534 N force was applied at S42 which is higher than SF = 2.0.

Figure 4.21 shows the inner condition of V2 after conducting structural load test using Tip 1. The main take is that the failure mechanism was penetration rather than cracking. The most worrisome part is the top part of the SOFPADS due to the part being the thinnest. However, at every point the structure can at least withstand more than SF = 1.0 which is the expected load applied in the event of robotic arm collision.

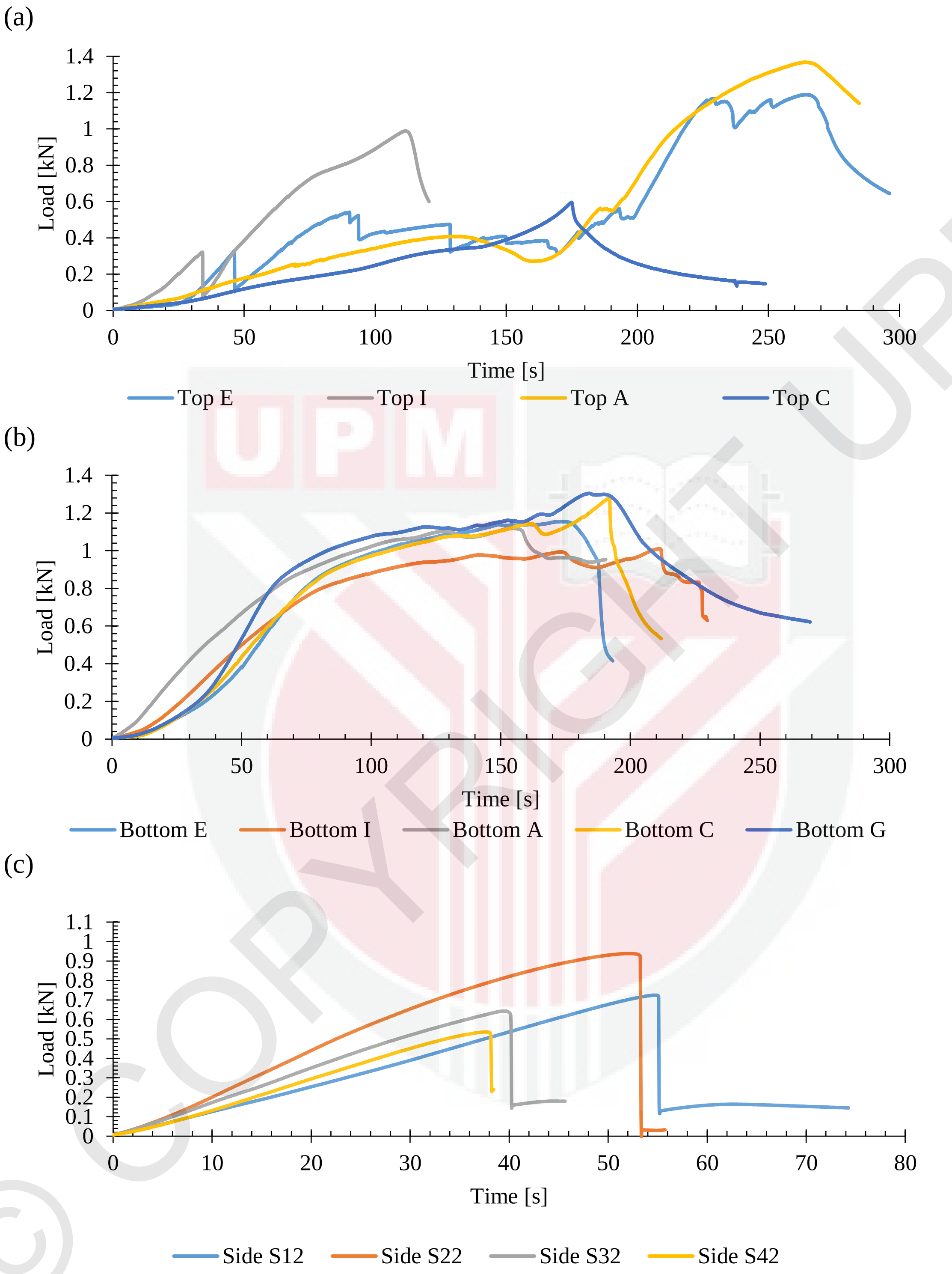


**Figure 4.20: Load-time curve of using tip 1 on V2: (a) Top, (b) bottom, and (c) sides**

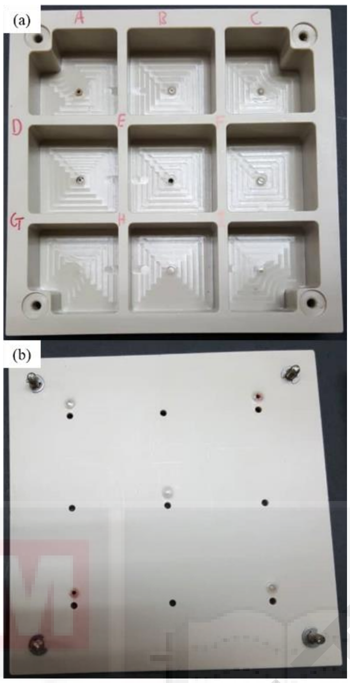


**Figure 4.21: Condition of the (a) inner bottom side and (b) inner top side of V2 after robotic arm collision load test**

Load-time curves of tests up to SF = 2.0 on V1 using Tip 2 are shown in Figure 4.22. During the increment of load, slight drop in load can be seen in some of the curves such as observed at position Top F and Top G (Figure 4.22 (a)). During the slight drop, a small crack sound can be heard. However, upon test completion no visible damage can be seen. This indicates that slight internal failure occurred during load increment. Since the bottom side of the V1 is thicker, no slight drop observed at any points tested as presented in Figure 4.22 (b). As expected, as shown in Figure 4.22 (c), since the sides are the thickest part, like Tip 1 structural load test results, after reaching the force equal to SF = 2.0, the force remains constant compared to the top and bottom of V1 where the force slightly falls after reaching SF = 2.0. It is also noted that the sides of V1 reached SF = 2.0 the earliest at about 16 s. The jig applied a load by moving at a constant rate of 1 mm/min. This means that VI had an approximate of 0.27 mm deformation, which was the lowest deformation at the sides of the case.

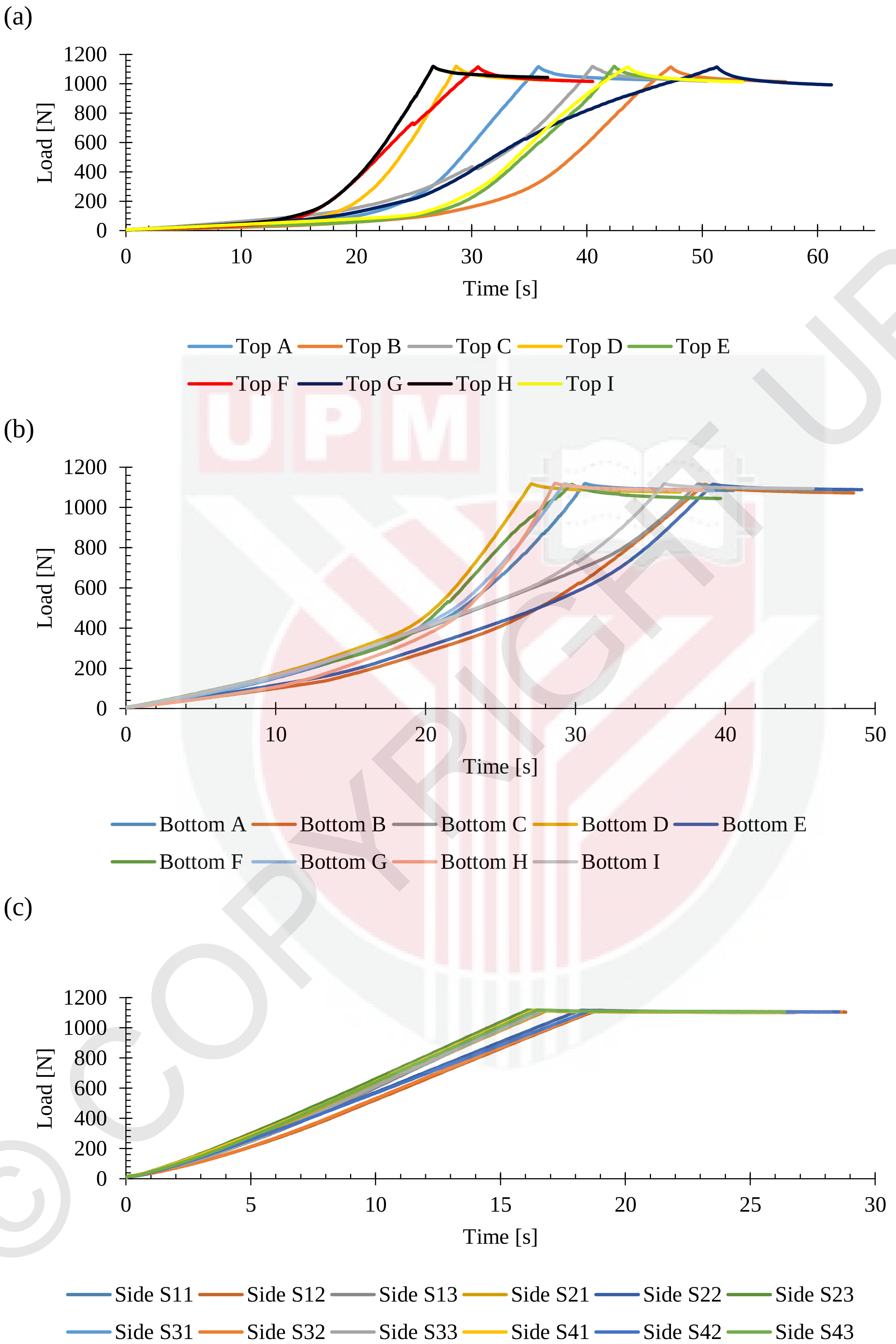


**Figure 4.22: Load-time curve of using Tip 2 on V1: (a) Top, (b) bottom, and (c) sides**

Like V2, EVA kick load test is not conducted on every point of V3. From Figure 4.23, the load needs to exceed well beyond SF = 2.0 (1112 N) before any drop can be seen. Even after a drop in load which usually indicates failure of a structure, for point G (Figure 4.23a) after 4171 N (load before drop) is applied, only slight damage can be seen (Figure 4.24). Even after receiving 10 kN force (point C), no major damage can be seen. Only at points A and E penetrations can be seen after receiving 33 kN and 40 kN forces respectively. Receiving 40 kN of force at point E caused deformations on the opposite side of the case too. Even after being deformed, the test at bottom part of the hardware is continued. For bottom part of case, the maximum force applied at each point tested was higher than 44 kN. From the results conducted, it seems that the case does not produce propagating cracks on top and bottom part of the case even at high level load. Instead, the case is penetrated by the material that provides the load. Even after applying extremely high load, only small number of debris can be seen. Only the side part of the case shows plastic deformation as can be seen in Figure 4.24. After receiving 24 kN the case is shattered as producing large parts after failing at a load well over the SF.

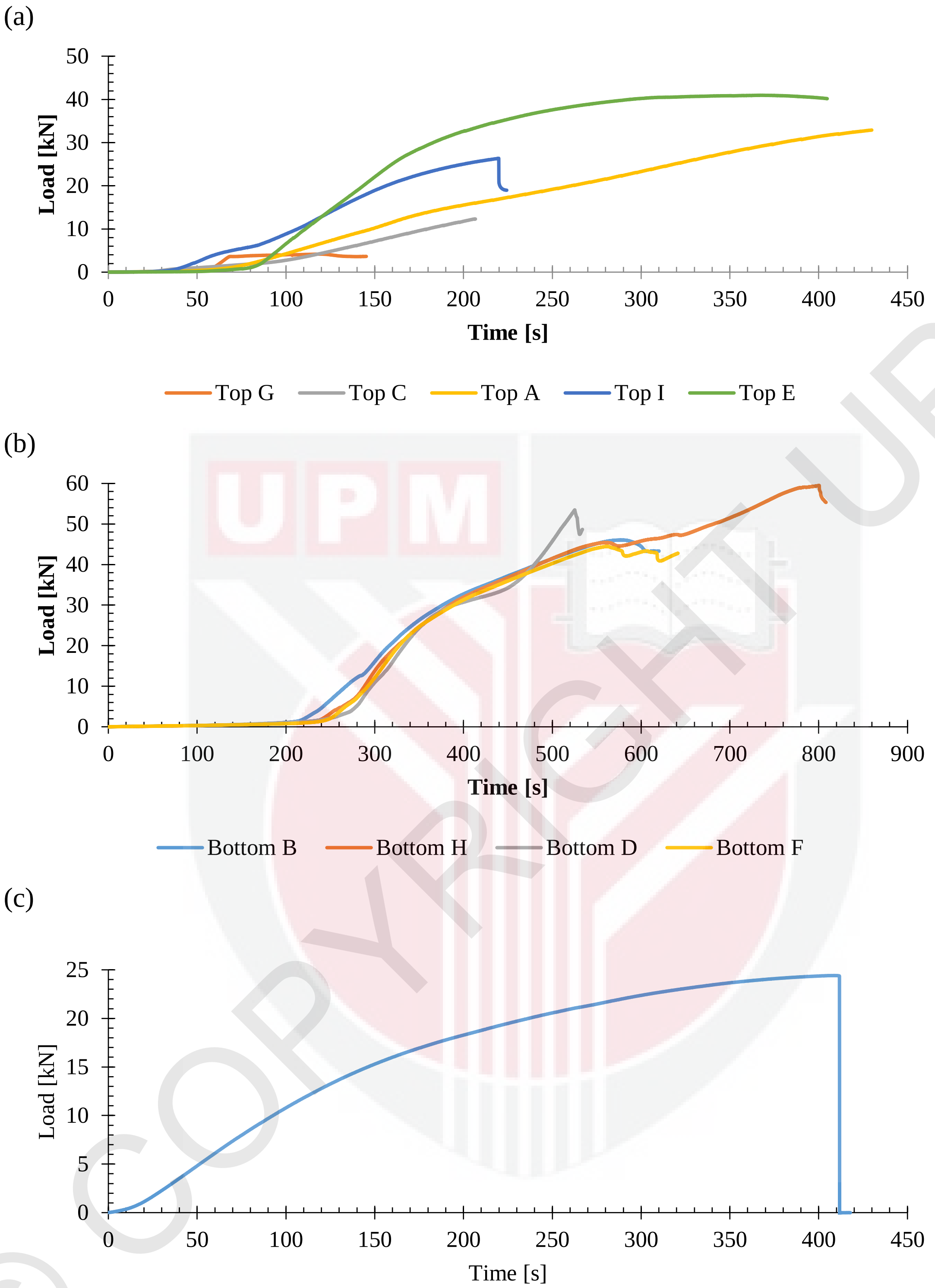


**Figure 4.23: Load-time curve of using Tip 2 on V3: (a) Top, (b) bottom, and (c) sides**


**Figure 4.24: Condition of V3 after on top side of section E (top-side view)**

## 4.5 Workmanship Evaluation

Workmanship is important to assess the consistency of work. In terms of this research, workmanship of fabrication and the resulting assembled hardware is important because the results of any experiment conducted on a particular hardware can be interpreted to be the same throughout any hardware. If multiple hardware shows different quality of workmanship, interpretation of the experiment results is different due to changes in the product's nature. As such, here the assessment of each is conducted quantitatively in terms of mass measurement and dimension measurement. Additionally for Flight Model (FM), the hardware is further assessed qualitatively in terms of visual inspection and touch test.

### 4.5.1 Mass Measurement

The mass measurements are made for individual parts and after assembling the case. Then the mass deviation is calculated using Equation 4.4. Here, $FM_m$ is the mass of each part of FM, $V1_m$ is the mass of each part of V1, $V2_m$ is the mass of each part of V2, $V3_m$ is the mass of each part of V3, $CM_m$ is the mass of each part of Control Model (CM). The mass measured for each part and the assembled hardware is shown in Table 4.15. The total combined mass is the mass of each part measured separately and combined to calculate the mass of the whole hardware. Total mass of assembled case is the mass of whole assembled case measured as a single item. The value between total combined mass and total mass of assembled case is different due to the usage of different balances. The A&D HR-250A Analytical Balance used to measure each singular part is more accurate with limitation of measurement up to 220 g. Thus, another balance (SHIMADZU precision balance UX4200H) that can measure up to 4200 g is used to measure the whole case. For separate parts like mesh and tape for section I, the deviation can be up to 20.462%. This is due to:

1) Low mass: slight variation is a huge difference in percentage.

2) Manual assembly: especially the usage of polyimide tape which depends on the assembler. The tape is used as much as needed thus for some sections; the mass may be higher/lower than other sections.

For parts that weigh more than 10 g, the mass deviations were 0.054-1.462%. This deviation low (lower than 5%). With tungsten (W) filter having the highest deviation at 1.462%. Due to having the highest density of 19.3 g/cm$^3$ in comparison to other parts, slight variation in the dimension of the W filter will affect its weight significantly. Even then the deviation is still under 5% meaning that the W filter still possess good workmanship. Ignoring W filter, parts weigh large than 10 g had a maximum deviation of 0.483% which is considerably low.

For FM, total combined mass had a deviation of 0.24% while total mass of assembled case had a deviation of 0.098% compared to the other hardware. Overall, the mass deviation of the assembled FM is extremely low in comparison to the other hardware with higher deviation in smaller parts which ultimately do not affect the whole SOFPADS significantly. As such, it can be said that the workmanship of SOFPADS is good in term of mass measurement.

$$\text{Mass deviation} = \left| \frac{\text{FM}_m}{\left(\frac{\text{V1}_\text{m} + \text{V2}_\text{m} + \text{V3}_\text{m} + \text{CM}_\text{m}}{4}\right)} - 1 \right| \times 100\ [\%] \qquad 4.4$$

The total combined mass is the mass of each part measured separately and combined to calculate the mass of the whole hardware. Total mass of assembled case is the mass of whole assembled case measured as a single item. The value between total combined mass and total mass of assembled case is different due to the usage of different balances. The A&D HR-250A Analytical Balance used to measure each singular part is more accurate with limitation of measurement up to 220 g. Thus, another balance (SHIMADZU precision balance UX4200H) that can measure up to 4200 g is used to measure the whole case. For separate parts like mesh and tape for section I, the deviation can be up to 20.462%. This is due to:

1) Low mass: slight variation is a huge difference in percentage.

2) Manual assembly: especially the usage of polyimide tape which depends on the assembler. The tape is used as much as needed thus for some sections; the mass may be higher/lower than other sections.

The mass measurements for each hardware part are shown in Table 4.15 . For parts that weigh more than 10 g, the mass deviations were 0.05-1.46%. This deviation low (lower than 5%). With W filter having the highest deviation at 1.46%. Due to having the highest density of 19.3 $mg/m^3$ in comparison to other parts, slight variation in the dimension of the W filter will affect its weight significantly. Even then the deviation is still under 5% meaning that the W filter still possess good workmanship. Ignoring W filter, parts weigh large than 10 g had a maximum deviation of 0.483% which is considerably low.

For FM, total combined mass had a deviation of 0.24% while total mass of assembled case had a deviation of 0.10% compared to the other hardware. Overall, the mass deviation of the assembled FM is extremely low in comparison to the other hardware with higher deviation in smaller parts which ultimately do not affect the whole SOFPADS significantly. As such, it can be said that the workmanship of SOFPADS is good in term of mass measurement.

**Table 4.15: Mass measurement of FM in comparison to other hardware**

| **Part Name** | **Parts Label** | **Mass [g]** | | | | | **Mass deviation [%]** |
|---|---|---|---|---|---|---|---|
| | | **$V1_m$** | **$V2_m$** | **$V3_m$** | **$CM_m$** | **$FM_m$** | |
| Case main body | MB2 | 83.77 | 83.48 | 83.95 | 83.82 | 83.92 | 0.20 |
| Case cover | MB1 | 34.08 | 34.22 | 33.73 | 34.21 | 34.12 | 0.18 |
| Screw | L1 | | | | | | |
| C-clip | L2 | | | | | | |
| Dosimeter holder section A | D1-1 | 11.67 | 11.70 | 11.68 | 11.61 | 11.69 | 0.18 |

**Table 4.15: Continued**

| Part Name | Parts Label | Mass [g] | | | | | Mass deviation [%] |
|---|---|---|---|---|---|---|---|
| | | $V1_m$ | $V2_m$ | $V3_m$ | $CM_m$ | $FM_m$ | |
| Dosimeter holder section C | D1-2 | 11.68 | 11.65 | 11.67 | 11.54 | 11.64 | 0.05 |
| Dosimeter holder section B | D2 | 8.13 | 8.07 | 8.13 | 8.23 | 8.11 | 0.33 |
| Dosimeter holder section D | D3 | 1.15 | 1.15 | 1.16 | 1.24 | 1.14 | 3.26 |
| Dosimeter holder section F | D4 | 9.91 | 9.91 | 9.91 | 9.38 | 9.93 | 1.58 |
| Dosimeter holder section H | D5 | 7.70 | 7.70 | 7.70 | 7.98 | 7.69 | 1.00 |
| Dosimeter holder section G | D6 | 11.69 | 11.69 | 11.69 | 11.95 | 11.70 | 0.48 |
| Dosimeter holder section E | D7 | 11.96 | 11.99 | 11.97 | 12.41 | 12.05 | 0.31 |
| Dosimeter holder section I | D8 | 1.06 | 1.08 | 1.07 | 1.64 | 1.07 | 12.00 |
| 6% Ge-CF 1 | D9-1 | 0.43 | 0.45 | 0.44 | 0.38 | 0.42 | 1.64 |
| 6% Ge-CF 2 | D9-2 | 0.63 | 0.67 | 0.61 | 0.60 | 0.60 | 3.48 |
| 6% Ge-FF | D9-3 | 0.21 | 0.26 | 0.26 | 0.20 | 0.21 | 8.52 |
| 10% Ge-CF | D9-4 | 0.08 | 0.08 | 0.09 | 0.08 | 0.08 | 8.16 |
| 2.3% Ge-CF | D9-5 | 0.06 | 0.07 | 0.07 | 0.05 | 0.05 | 11.84 |
| 2.3% Ge-FF | D9-6 | 0.07 | 0.06 | 0.07 | 0.07 | 0.08 | 11.94 |
| COMOF | D9-7 | 0.01 | 0.01 | 0.01 | 0.02 | 0.01 | 9.43 |
| TLD-100 | D10-1 | 0.77 | 0.75 | 0.76 | 0.72 | 0.73 | 2.17 |
| TLD-600 | D10-2 | 0.57 | 0.58 | 0.58 | 0.58 | 0.57 | 1.17 |
| TLD-700 | D10-3 | 0.58 | 0.58 | 0.58 | 0.58 | 0.57 | 1.21 |
| Tungsten (W, 3.2 mm) | F1 | 36.85 | 38.64 | 36.85 | 36.72 | 36.72 | 1.46 |
| W (0.7 mm) | F2-1 | 83.77 | 83.48 | 83.95 | 83.82 | 83.92 | 0.20 |
| Aluminium (Al) filter | F2-2 | 34.08 | 34.22 | 33.73 | 34.21 | 34.12 | 0.18 |

| Part Name | Parts Label | Mass [g] | | | | | Mass deviation [%] |
|---|---|---|---|---|---|---|---|
| | | $V1_m$ | $V2_m$ | $V3_m$ | $CM_m$ | $FM_m$ | |
| Al filter | F3-1 | 8.64 | 8.63 | 8.64 | 8.63 | 8.62 | 0.13 |

**Table 4.15: Continued**

| Part Name | Parts Label | Mass [g] | | | | | Mass deviation [%] |
|---|---|---|---|---|---|---|---|
| | | $V1_m$ | $V2_m$ | $V3_m$ | $CM_m$ | $FM_m$ | |
| Polyethylene (PE) filter | F3-2 | 8.64 | 8.62 | 8.64 | 8.63 | 8.56 | 0.84 |
| Mesh | F4 | 11.67 | 11.70 | 11.68 | 11.61 | 11.69 | 0.18 |
| Polyimide tape | F5 | 11.68 | 11.65 | 11.67 | 11.54 | 11.64 | 0.05 |
| Mesh + Tape section A | C1-1 +C2-2 | 8.13 | 8.07 | 8.13 | 8.23 | 8.11 | 0.33 |
| Mesh + Tape section B | C1-2 +C2-1 | 1.15 | 1.15 | 1.16 | 1.24 | 1.14 | 3.26 |
| Mesh + Tape section C | C1-3 +C2-2 | 9.91 | 9.91 | 9.91 | 9.38 | 9.93 | 1.58 |
| Mesh + Tape section D | C1-4 +C2-1 | 7.70 | 7.70 | 7.70 | 7.98 | 7.69 | 1.00 |
| Mesh + Tape section E | C1-5 +C2-1 | 11.69 | 11.69 | 11.69 | 11.95 | 11.70 | 0.48 |
| Mesh + Tape section F | C1-6 +C2-1 | 11.96 | 11.99 | 11.97 | 12.41 | 12.05 | 0.31 |
| Mesh + Tape section G | C1-7 +C2-2 | 1.06 | 1.08 | 1.07 | 1.64 | 1.07 | 12.00 |
| Mesh + Tape section H | C1-8 +C2-1 | 0.43 | 0.45 | 0.44 | 0.38 | 0.42 | 1.64 |
| Mesh + Tape section I | C1-9 +C2-2 | 0.63 | 0.67 | 0.61 | 0.60 | 0.60 | 3.48 |
| **Total combined mass [g]** | | 296.46 | 0.21 | 0.26 | 0.26 | 0.20 | 0.21 |
| **Total mass of assembled case [g]** | | 296.56 | 0.08 | 0.08 | 0.09 | 0.08 | 0.08 |

### 4.5.2 Dimension Measurement

Figure 4.25 shows the outer dimensions of the assembled hardware that are measured. The dimension deviations of FM in comparison to other hardware is calculated using Equation 4.5. Here $FM_d$ is each outer dimensions of FM, $V1_d$ is each outer dimensions of V1, $V2_d$ is each outer dimensions of V2, $V3_d$ is each outer dimensions of V3 and $V8_d$ is each outer dimension of V8.

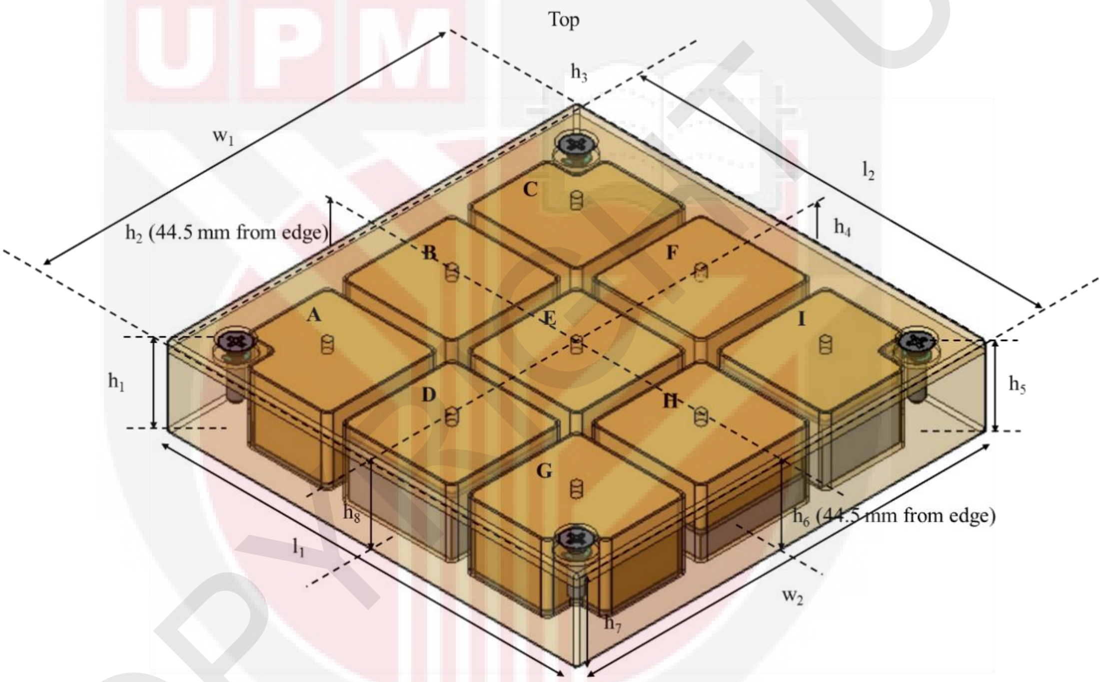


**Figure 4.25: Outer dimension measurements of SOFPADS hardware**

$$\text{Dimension deviation} = \left| \frac{FM_d}{\left( \frac{V1_d + V2_d + V3_d + CM_d}{4} \right)} - 1 \right| \times 100\ [\%] \qquad 4.5$$

From Table 4.16 every height of FM measured falls within 19.52 to 19.71 mm which is within the tolerable range of ExHAM of 20 (+0/-2) mm. For side measurements, the dimension is within 99.01 to 99.13 mm. The side dimensions required for ExHAM utilization is 100 (+0/-1) mm which means that UPM's FM is within the required side dimensions. The deviation between FM and other models is only 0.0048% for height measurement and 0.0177% for side measurements. This reaffirms the workmanship of the hardware fabricated in term of outer dimensions since they are of similar value in dimensions with each other.

**Table 4.16: Outer size measurement of FM in comparison to other hardware**

| Parts Label | Dimension [mm] | | | | | | | | | | Deviation [%] |
|---|---|---|---|---|---|---|---|---|---|---|---|
| | $V1_d$ | | $V2_d$ | | $V3_d$ | | CM | | FM | | |
| | Value | Average | Value | Average | Value | Average | Value | Average | Value | Average | |
| $h_1$ | 19.67 | 19.58 ±0.08 | 19.6 | 19.65 ±0.04 | 19.57 | 19.65 ±0.03 | 19.46 | 19.53 ±0.06 | 19.57 | 19.60 ±0.05 | 0.005 |
| $h_2$ | 19.52 | | 19.62 | | 19.65 | | 19.60 | | 19.71 | | |
| $h_3$ | 19.53 | | 19.71 | | 19.61 | | 19.58 | | 19.60 | | |
| $h_4$ | 19.65 | | 19.68 | | 19.62 | | 19.46 | | 19.57 | | |
| $h_5$ | 19.53 | | 19.63 | | 19.64 | | 19.47 | | 19.58 | | |
| $h_6$ | 19.52 | | 19.7 | | 19.59 | | 19.59 | | 19.60 | | |
| $h_7$ | 19.7 | | 19.64 | | 19.65 | | 19.48 | | 19.59 | | |
| $h_8$ | 19.52 | | 19.62 | | 19.67 | | 19.57 | | 19.60 | | |
| $l_1$ | 99.13 | 99.10 ±0.03 | 99.01 | 99.05 ±0.03 | 99.05 | 99.04 ±0.01 | 99.05 | 99.04 ±0.02 | 99.03 | 99.04 ±0.02 | 0.02 |
| $l_2$ | 99.06 | | 99.06 | | 99.03 | | 99.02 | | 99.06 | | |
| $w_1$ | 99.11 | | 99.07 | | 99.04 | | 99.01 | | 99.06 | | |
| $w_2$ | 99.09 | | 99.07 | | 99.03 | | 99.06 | | 99.01 | | |

### 4.5.3 Visual Inspection

Visual inspection under light is important to see whether the hardware is reflecting harsh light (glare) or not. Glare will disrupt the effectiveness of visual capturing device. Figure 4.26 shows that the image captured is affected by the glare. In space, glares are harsher due to the high intensity of sunlight as compared to on the surface of the Earth.

**Figure 4.26: Image of ExHAM captured during attachment onto the Exposed Facility of Kibo module showing the effect of glare reducing the image quality** (Image courtesy of JAXA)

Table 4.17 shows the glare test on FM by pointing the high energy light and capturing the images of the hardware. From the image, it can be seen that FM hardware does not reflect harsh light meaning that the material is not a glare producing material.

**Table 4.17: Confirmation of glare for FM**

| Part | Images | Remarks |
|---|---|---|
| Top |  | No glare |

### 4.5.4 Touch Test

A touch test using non-woven glove to assess the surface of SOFPADS is conducted by stroking each part of the surface with emphasis on the edges, vent holes and disconnected parts like the screws and interface between the case cover and main body. The criterion of having smooth surface is the cloth oof the glove not getting caught on the hardware. Table 4.18 shows each location that is stroked and remarks on the condition of the surfaces and edges. Most importantly the vent holes, edges and the screw areas did not present any rough or uneven surface that cause the cloth to be stuck. If the surface of the hardware had any rough surface that may penetrate a crew member of the International Space Station (ISS).

**Table 4.18: Location and condition of each part stroked using cotton glove**

| Parts | Location | Remarks |
|---|---|---|
| Top surface |  | Smooth surface |
| Top pointed edges (4 sides) | 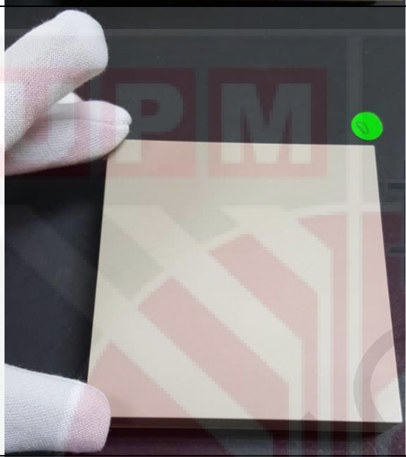 | Cloth not caught on the edges of the hardware |
| Top edges (4 sides) | 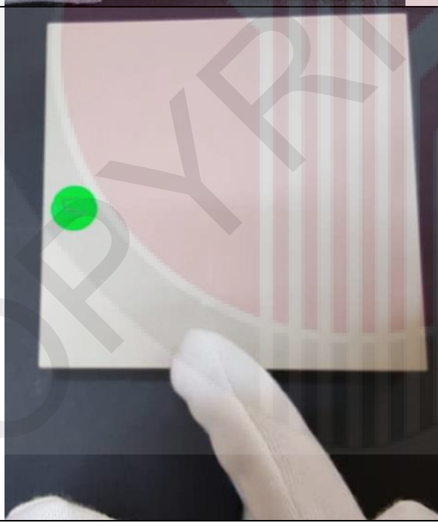 | Smooth edges |

**Table 4.18: Continued**

| Parts | Location | Remarks |
|---|---|---|
| Bottom surface | 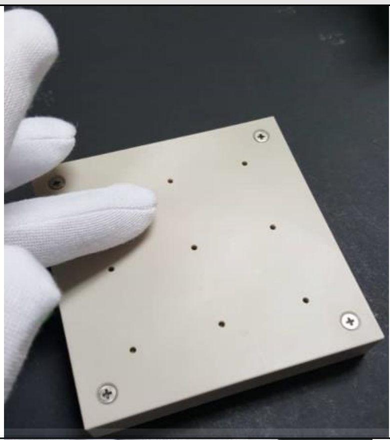 | Smooth surface |
| Bottom vent holes (9 holes) |  | Cloth not caught on the vent holes |
| Bottom screw surface (4 screws) | 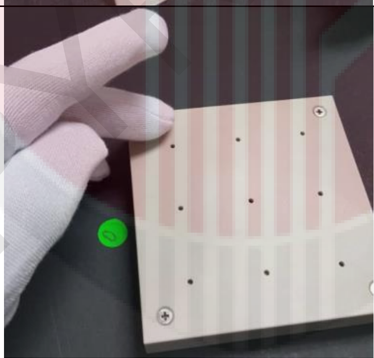 | Cloth not caught on the screw |
| Bottom pointed edges (4 sides) | 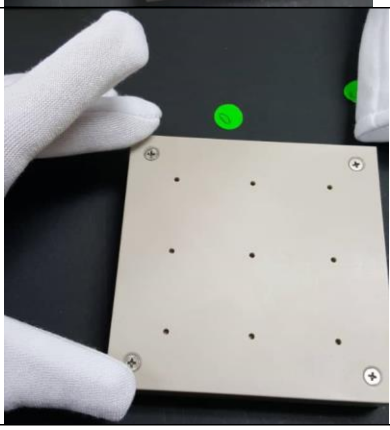 | Cloth not caught on bottom edges |

**Table 4.18: Continued**

| Parts | Location | Remarks |
|---|---|---|
| Bottom edges (4 sides) | 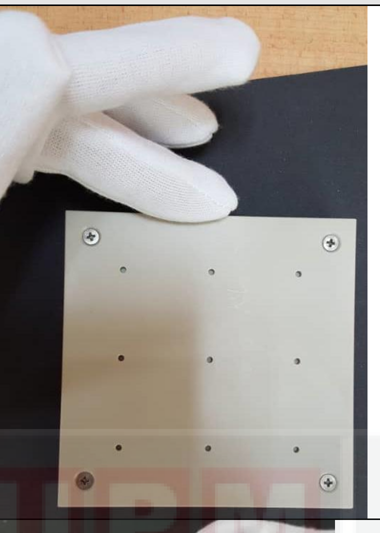 | Smooth edges |
| Side surface (4 sides) |  | Smooth surface |
| Side edge (4 sides) | 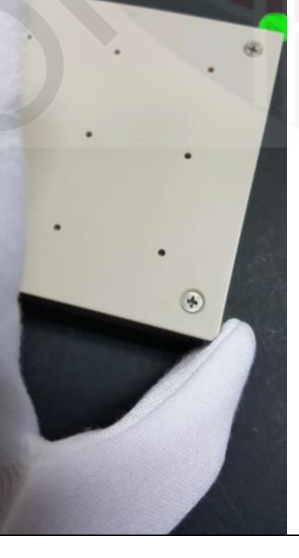 | Cloth not caught on side edges |

### 4.6 Morphological Analysis and Preliminary Irradiation Results of PD

In this section the morphological analysis of the CUSOF is presented. This is followed by the preliminary irradiation results of beta and neutron-gamma mixed field irradiations and finally the screening of the PD used for space exposure.

#### 4.6.1 Morphological Analysis of CUSOF

In this section, the SEM images of CUSOF fabricated for space exposure is analysed. The core dimension is used for normalisation while the resulting effective atomic number ($Z_{eff}$) is compared with human. Figure 4.27, Figure 4.28, and Figure 4.29 respectively show the SEM image of D9-3, D9-4 and D9-6. Figure 4.30 show the imaginary fibre with rectangular core used to compare the accuracy of ImageJ area measurement. CF has a geometric circular core, meaning that the core area can be calculated easily from the diameter of the core measured from the SEM images. However, FF's core is more of an organic shape with bulbous sides and a thin line in between the sides. D9-6 seems more organic where the shape of the sides is both irregular and different from each other. D9-4 has bulbous sides that are similar in shape. In this work, the normalisation of the TL responses of the passive dosimeters is conducted using the core volume. As such, for FF, an alternative method for measuring the fibre's core area using ImageJ is needed.

shows the measured core areas of the CUSOF and the imaginary fibre. Measurement made by ImageJ of the imaginary fibres is 99.95% like the theoretical area calculation of the geometric shape which reaffirms the accuracy of the software at measuring the

CUSOF's core area. Other OF used in this work has been analysed by Zakaria et al. (2023) which is gathered in Table 4.19 too. Since all OF are cut into 6 mm, the core volume is calculated by multiplying the core area with the OF length. For TLD-100, TLD-600 and TLD-700, the whole dosimeter is considered are the volume due to the dopant being distributed evenly. As such, the volume of the commercial TLD will be 3.2 mm ×3.2 mm × 0.89 mm.

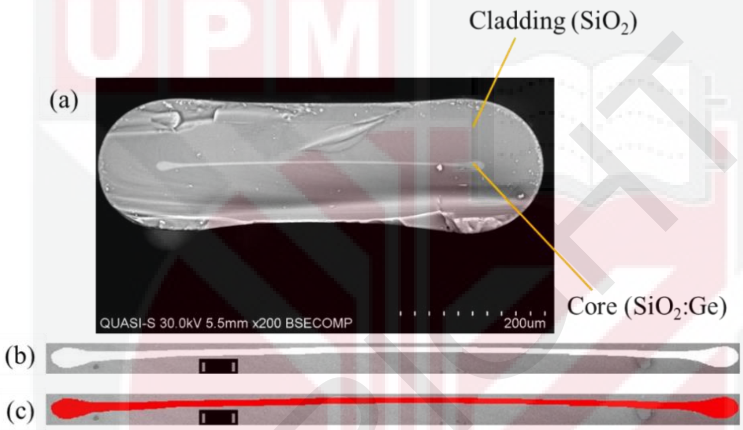


**Figure 4.27: D9-3 SEM image (a) cross section of whole fibre, (b) core area enlarged and highlighted (adjacent scale distance is 20 µm), (c) area measured by ImageJ threshold function is highlighted from (b)**

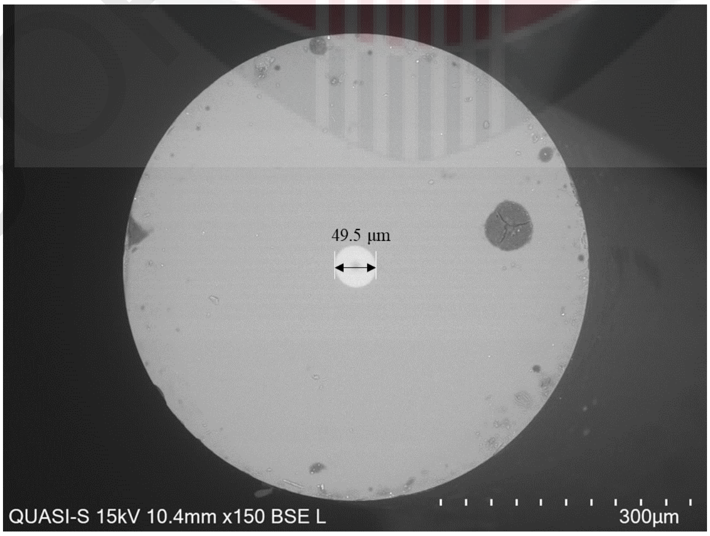


**Figure 4.28: D9-4 SEM image**

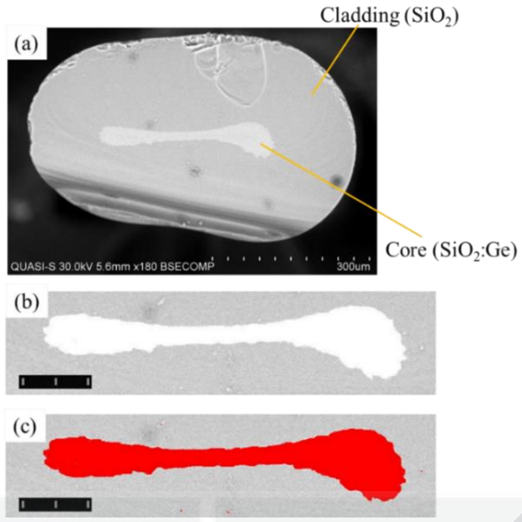


**Figure 4.29: D9-6 SEM image (a) cross section of whole fibre, (b) core area enlarged and highlighted (adjacent scale distance is 30 µm), (c) area measured by ImageJ threshold function is highlighted from (b)**


**Figure 4.30: Imaginary fibre cross section**

**Table 4.19: Core dimension of the PD used in this work**

| PD | Core Diameter [µm] | Core Area × $10^4$ [µm²] | Theoretical Area [cm²] | Source |
|---|---|---|---|---|
| **CF** | | | | |
| D9-1 | 78.5 | 0.484 | n.a | Zakaria et al., 2023 |
| D9-2 | 96.4 | 0.730 | n.a | Zakaria et al., 2023 |
| D9-4 | 49.5 | 0.192 | | This work |
| D9-5 | 125 | 1.23 | | Zakaria et al., 2023 |
| D9-7 | 50 | 0.196 | | Manufacturer |
| **FF** | | | | |
| D9-6 | | 1.00±0.04 | | This work |
| D9-3 | | 0.230±0.005 | | This work |
| Imaginary | | 11.95 [cm²] | 12 | |

The Electron Dispersive X-ray (EDX) spots for D9-4, D9-4 and D9-6 are shown in Figure 4.31, Figure 4.32, Figure 4.33, respectively with their EDX results presented underneath. The elemental composition and $Z_{eff}$ of each CUSOF is gathered in Table 4.20. From the table the $Z_{eff}$ value for CUSOF is from 13.6 to 14.76. The values of $Z_{eff}$ of the CUSOF are comparable to the human skeletons such as cranium at 15.19, femur at 14.77 and sacrum at 13.77 (Manjunatha & Rudraswamy, 2013). The importance of $Z_{eff}$ is to estimate the interaction of radiations with human. Section 4.3 has shown that the Z of a matter will affect its interaction (shielding) with a particular radiation. This means that since CUSOF's $Z_{eff}$ is similar to human skeletons, the OF is suitable to be used in estimating human skeleton radiation exposure.

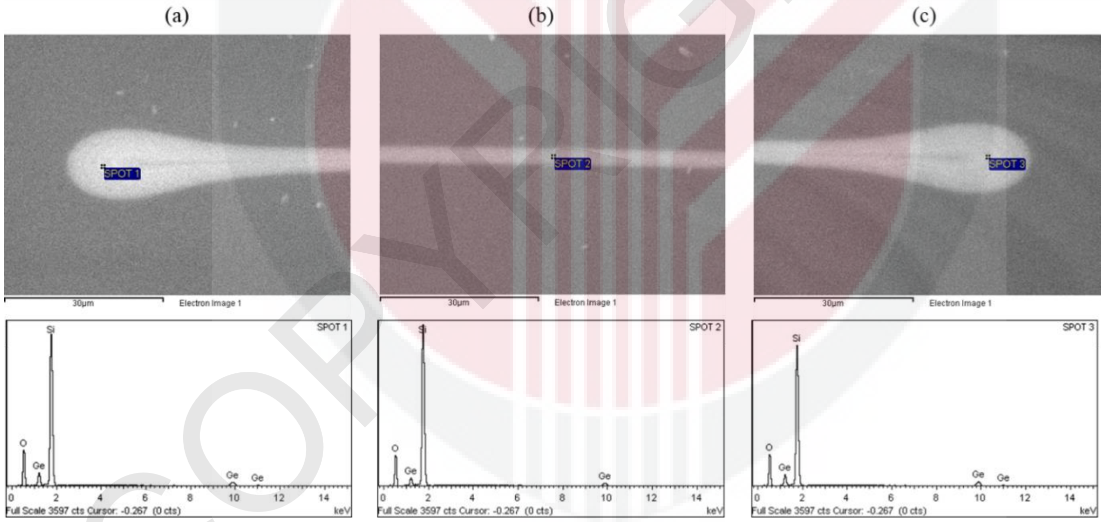


**Figure 4.31: EDX spots for D9-3 where (a) spot 1, (b) spot 2 and (c) spot 3**

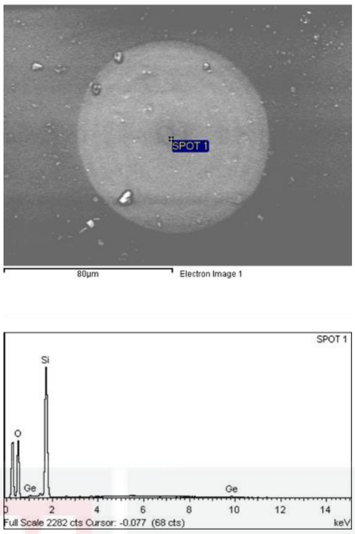

**Figure 4.32: EDX spot for D9-4**

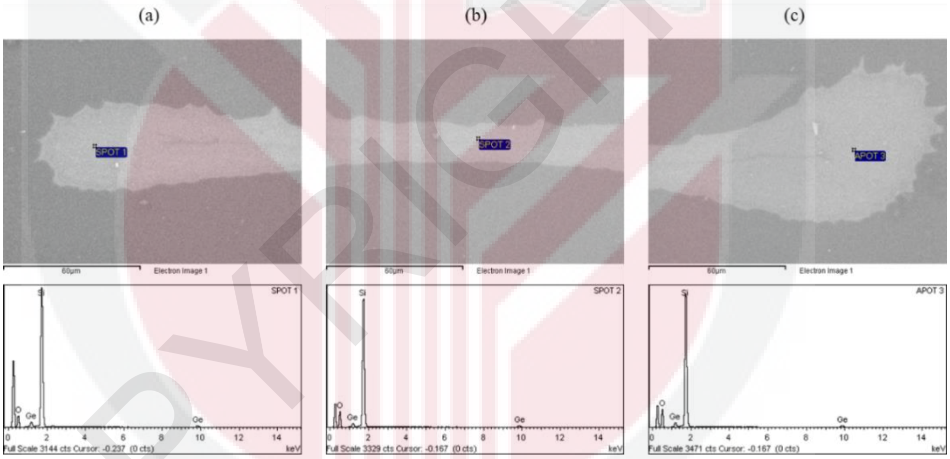

**Figure 4.33: EDX spots for D9-6 where (a) spot 1, (b) spot 2 and (c) spot 3**

**Table 4.20: The elemental composition and $Z_{eff}$ used in this work**

| **Fibre Type** | **Spot** | **Fractional Weight, $W_i$ [%]** | | | **$Z_{eff}$** | **Average $Z_{eff}$** | **Source** |
|---|---|---|---|---|---|---|---|
| | | Si | O | Ge | | | |
| D9-1 | | 54.45 | 42.98 | 2.58 | 13.6 | 13.6 | Zakaria et al., 2023 |
| D9-2 | | 52.54 | 44.82 | 2.65 | 13.6 | 13.6 | Zakaria et al., 2023 |
| D9-3 | 1 | 40.76 ±0.05 | 52.65 ±0.17 | 6.60 ±0.12 | 14.81 ±0.07 | 14.76 ±0.30 | This work |

**Table 4.20: Continued**

| Fibre Type | Spot | Fractional Weight, $W_i$ [%] | | | $Z_{eff}$ | Average $Z_{eff}$ | Source |
|---|---|---|---|---|---|---|---|
| | | Si | O | Ge | | | |
| | 2 | 43.12 ±0.42 | 51.80 ±0.45 | 5.09 ±0.02 | 14.23±0.04 | | |
| | 3 | 42.40 ±0.75 | 52.45 ±1.24 | 5.16 ±1.99 | 15.25 ±0.14 | 3 | |
| D9-4 | | 50.02 | 44.14 | 5.84 | 14.81 | 14.81 | This work |
| D9-5 | | 52.54 | 44.82 | 2.65 | 13.6 | 13.6 | Zakaria et al., 2023 |
| D9-6 | 1 | 40.00 ±2.52 | 56.31 ±2.94 | 3.69 ±0.42 | 13.40 ±0.46 | 13.80 ±0.20 | This work |
| | 2 | 46.81 ±2.38 | 48.84 ±2.51 | 4.35 ±0.13 | 14.01 ±0.21 | | |
| | 3 | 46.20 ±1.75 | 49.40 ±1.84 | 4.40 ±0.09 | 14.01 ±0.15 | | |

## 4.7 Results of Beta Irradiation of PD

For stereo turntable beta irradiation, the linearity of dose responses is observed while for the Risø TL/OSL Reader beta irradiation, both the linearity and fading responses is observed.

### 4.7.1 Stereo Mono Turntable Beta Irradiator Analysis

Figure 4.34 shows the responses of PD irradiated using Strontium-90 ($^{90}$Sr) source through stereo irradiation. Figure 4.35 shows the TLD-100, TLD-600 and TLD-700 responses while Figure 4.36 shows OF responses only. From these figures, D9-1, apart from producing the greatest TL responses per unit volume also possesses high coefficient of determination ($R^2$) at 0.9905 meaning that the PD responses is very linear. TLD-100, TLD-600 and TLD-700 show similar responses in term of TL responses per unit volume. TLD-600 had the highest $R^2$ out of all PD at 0.9965. Having a high linearity is a very important aspect of a PD to measure and unknown dose from a known TL response. Using the linear regression equation shown in Figure 4.34, the absorbed dose can be determined easily by finding the value of x-axis (absorbed dose) from a known y-axis value (TL response). $R^2$ shows the level of confidence during conversion where $R^2 = 1$ means that conversion from TL response to absorbed dose is perfectly linear.

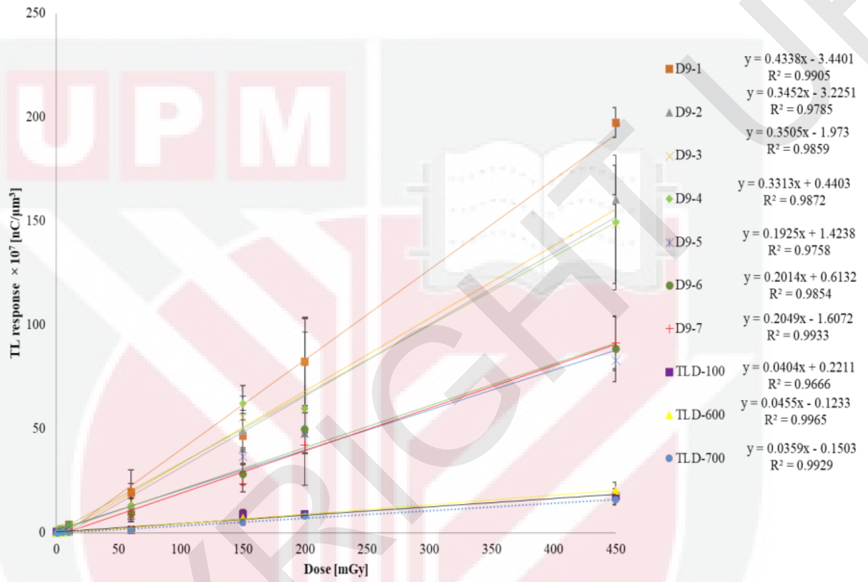


**Figure 4.34: TL responses of all PD irradiated using beta (Stereo)**

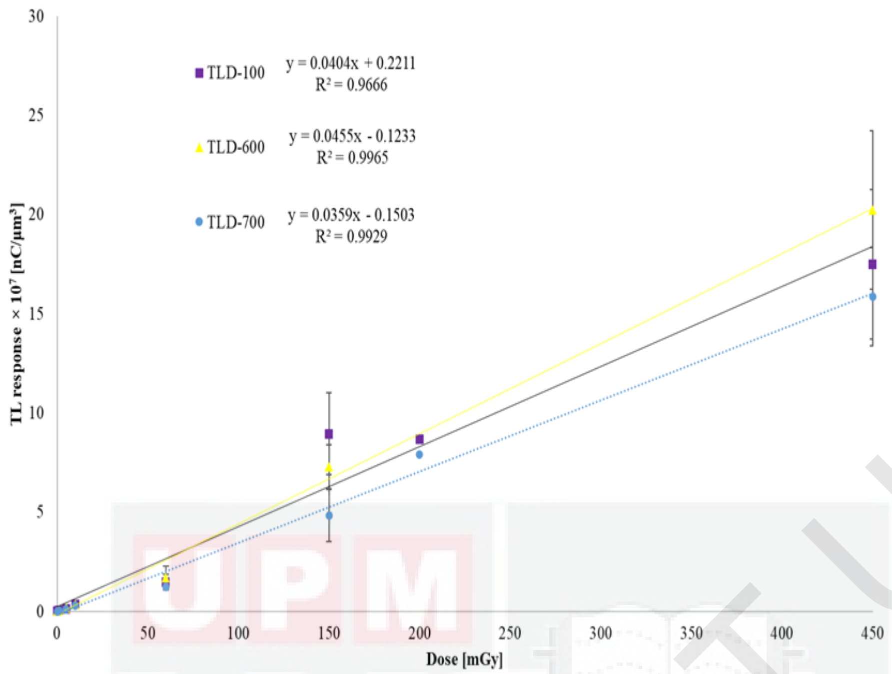


**Figure 4.35: TLD-100, TLD-600 and TLD-700 responses to beta (Stereo)**

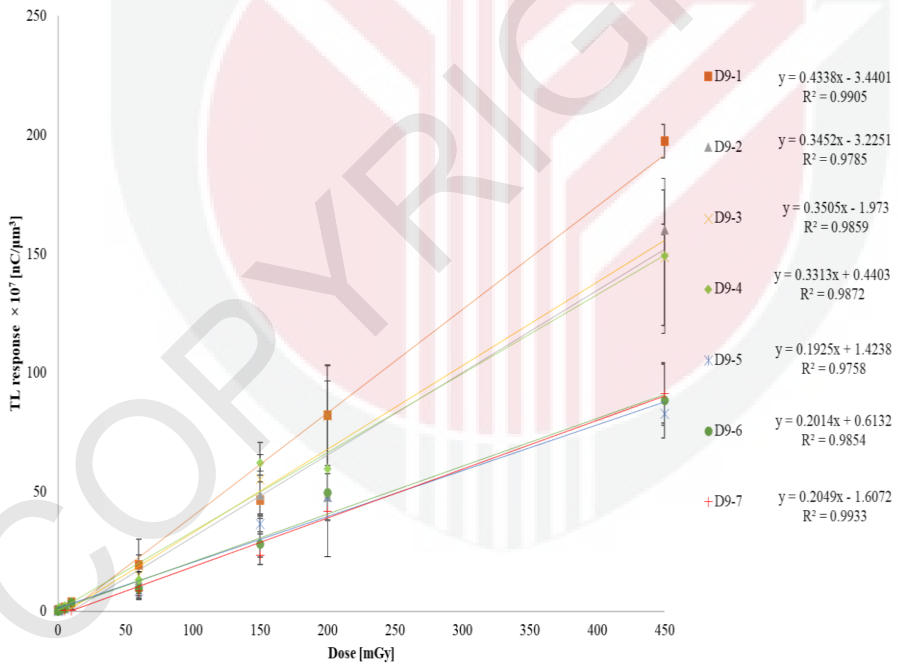


**Figure 4.36: OF responses to beta (Stereo)**

### 4.7.2 Risø TL/OSL Reader based Beta Irradiator Analysis

Figure 4.37 shows all PD irradiated by beta using Risø TL/OSL reader. To clarify the responses of the PD, the figure is further separated into commercial TLD only (Figure 4.38) and CUSOF only (Figure 4.39). From these figures, commercial optical fibre (COMOF) showed the highest thermoluminescence (TL) response per unit volume. However, compared to other PD, COMOF had a low $R^2$ value of 0.907. What this means is, COMOF's TL responses are less likely to be linear compared to the commercial TLD with $R^2$ of 0.9968 to perfectly linear at 1. While the commercial TLD (TLD-100 and TLD-600) had the highest $R^2$ value, they are the lowest in sensitivity from the low TL responses per unit volume in comparison to OF. From Figure 4.38 the commercial TLD showed similar TL responses especially at lower doses. D9-1, D9-2 and D9-5 had a high $R^2$ value of >0.99. CUSOF doped with 6 mol% Ge is said to possess higher responses compared to 2.3 mol% Ge doped CUSOF due to the increment of trapping centres in the OF when the concentration level of Ge increases (Hassan et al., 2019).

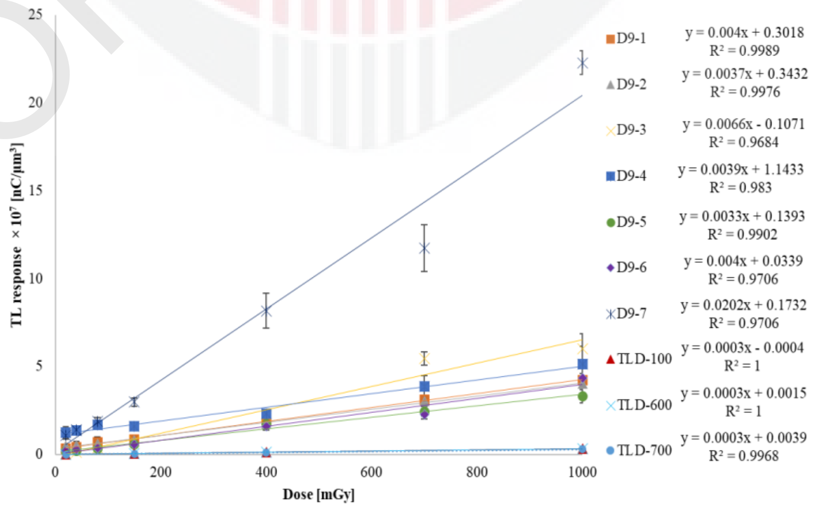


**Figure 4.37: TL responses of all PD irradiated using beta (Risø)**

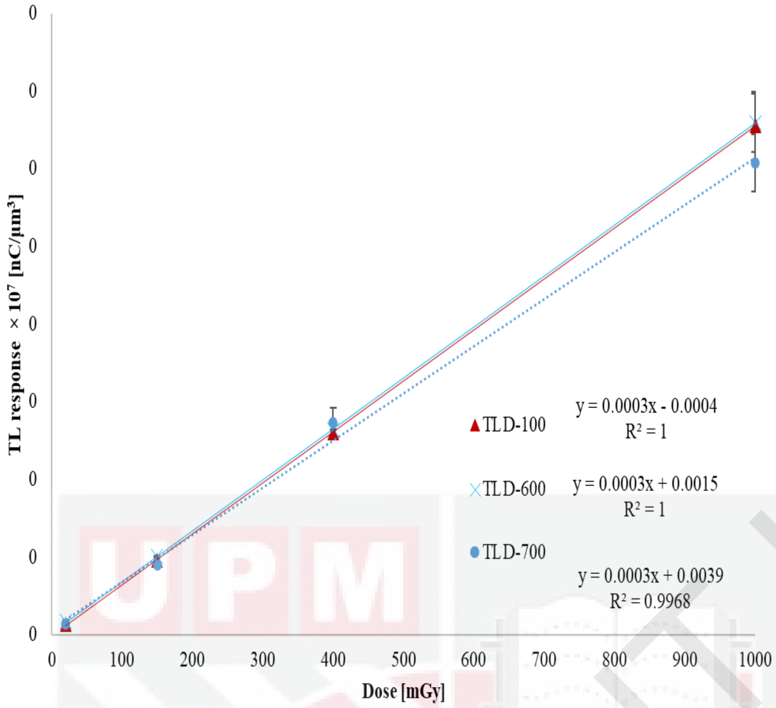


**Figure 4.38: TLD-100, TLD-600 and TLD-700 responses to beta (Risø)**

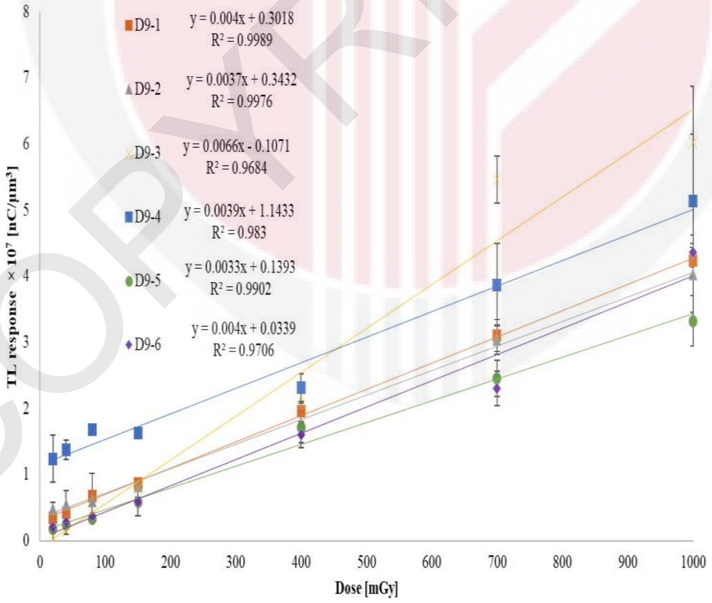


**Figure 4.39: CUSOF responses to beta (Risø)**

Figure 4.40 shows the fading rate of each PD after irradiation of beta particles using Risø TL/OSL Reader based Beta Irradiator. D9-6 had the least amount of fading at

2.9% (Figure 4.40 (f)) after 429 days post-irradiation. TLD-100 unexpectedly had a high fading rate of 13.3% after 429 days post irradiation, however, TLD is being compared to its reading at 17 days post-irradiation rather than 69 days post-irradiation by the OF. In Figure 4.40 (j), the absence of reading at 130 days after irradiation is due to accidental reading without the flow of nitrogen gas. This invalidates the reading and since the number of samples is limited, no other reading was mas mat for TLD-100 130 days post-irradiation. Overall, considering the long-term fading duration, all PD did not show significant drop in TL responses which is an important characteristic since post-space exposure, the duration it takes for FM to arrive to its origin was 294 days.

(a)

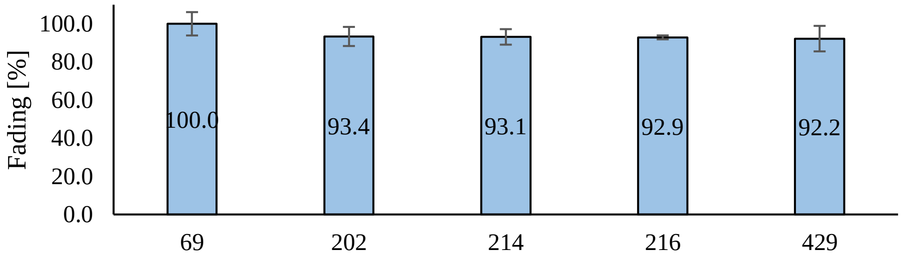

Fading [%]
100.0
80.0
60.0
40.0
20.0
0.0
100.0
93.4
93.1
92.9
92.2
69
202
214
216
429


(b)

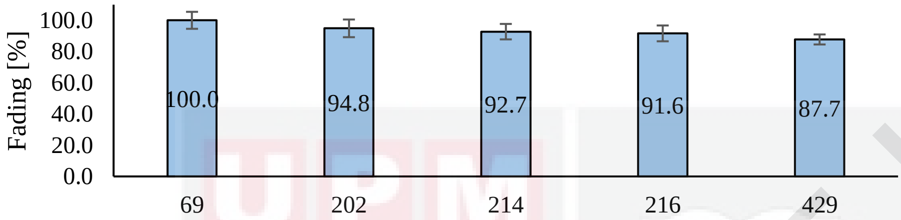

Fading [%]
100.0
80.0
60.0
40.0
20.0
0.0
100.0
94.8
92.7
91.6
87.7
69
202
214
216
429


(c)

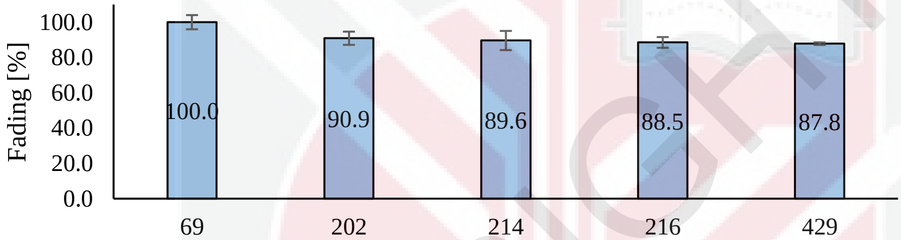

Fading [%]
100.0
80.0
60.0
40.0
20.0
0.0
100.0
90.9
89.6
88.5
87.8
69
202
214
216
429


(d)

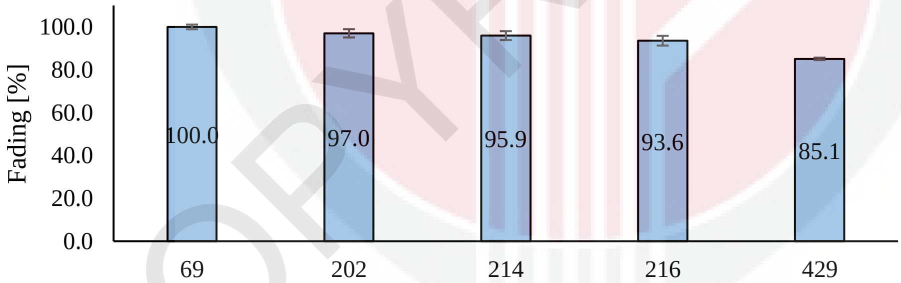

Fading [%]
100.0
80.0
60.0
40.0
20.0
0.0
100.0
97.0
95.9
93.6
85.1
69
202
214
216
429


(e)

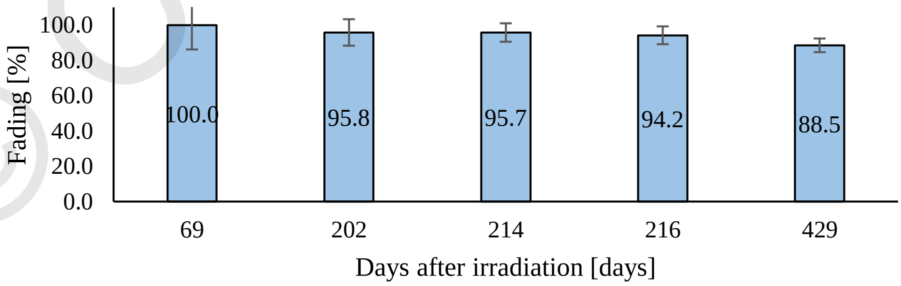

Fading [%]
100.0
80.0
60.0
40.0
20.0
0.0
100.0
95.8
95.7
94.2
88.5
69
202
214
216
429
Days after irradiation [days]

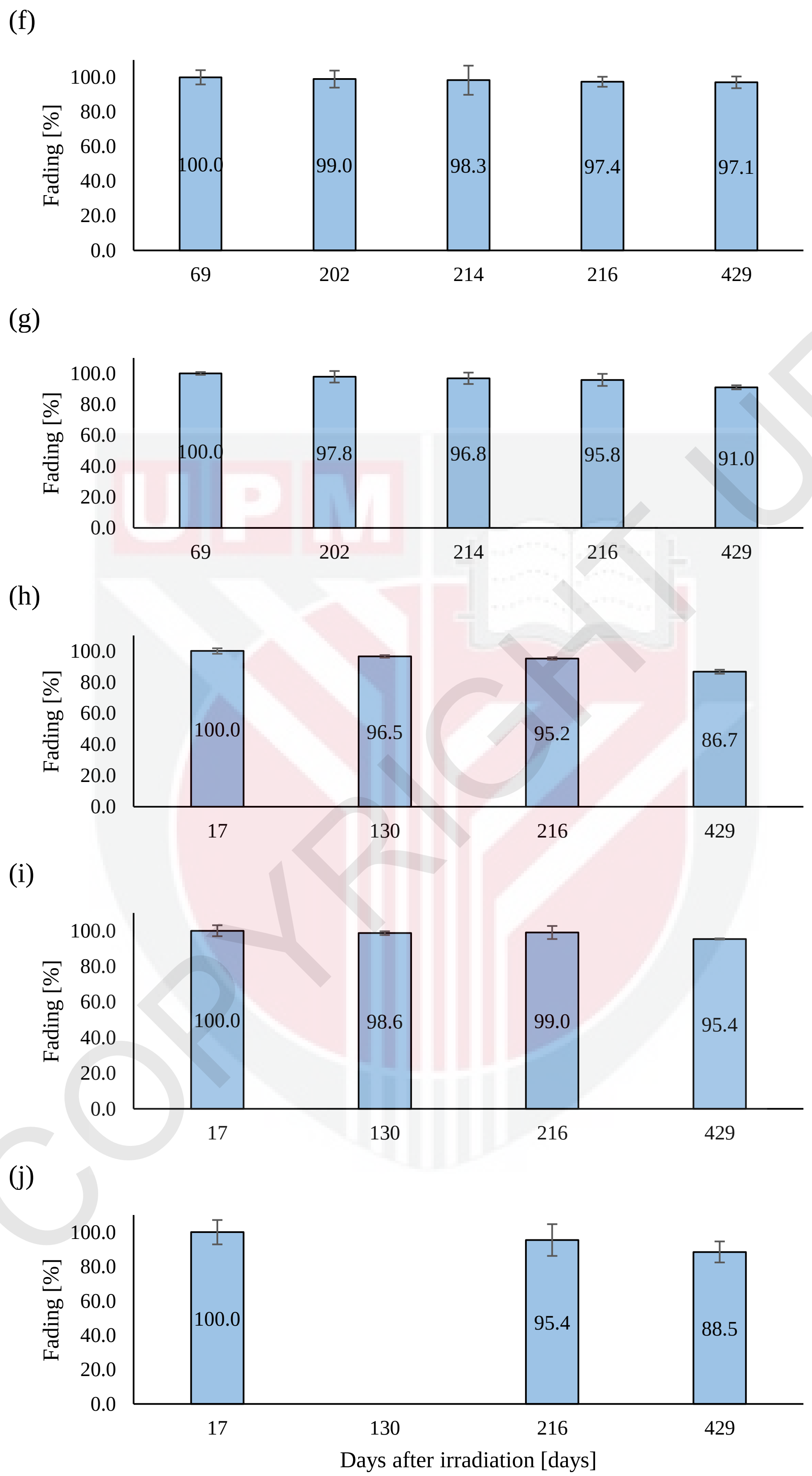


**Figure 4.40: Fading of PD under 400 mGy beta radiation (Risø): (a) D9-1, (b) D9-2, (c) D9-3, (d) D9-4, (e) D9-5, (f) D9-6, (g) D9-7, (h) TLD-100, (i) TLD-600, (j) TLD-700**

## 4.8 Neutron-gamma Irradiation Analysis

Figure 4.41 to Figure 4.43 display the linearity of the CusOF and TLD when irradiated with $^{241}$AmBe source. To avoid convoluting the figures, the linear fits of the responses are gathered in Table 6. From the normalised TL signal to irradiation time responses D9-3 shows the highest TL signal towards the radiation produced by $^{241}$AmBe. FF has been found to have higher sensitivity because of their collapsed surface structures that may have introduced an increased amount of defect sites during the fabrication process (Zakaria et al., 2020). The normalised TL signals of the 6 mol% doped FF were higher than the thermal neutron sensitive TLD-600 at approximately 2950 nC/mm$^3$ compared to 425 nC/mm$^3$ at 0 cm from the source. At distances of 15 cm and 30 cm, the TL signals of the passive dosimeters decreased significantly (Figure 4.42 and Figure 4.43). Inverse-square law that affects point-like radiation describes that the intensity of radiation, I at a distance, r, will become I/r$^2$ at 2r (Vodoukis and Oikonomidis, 2017). To simplify the matter, if the distance of the dosimeters were 1 cm next to the source, at 15 cm and 30 cm the intensity of radiation absorbed by the dosimeters will drop to an extremely low value of 0.0044 and 0.0011 respectively compared to that at 1 cm distance. Another method to estimate the radiation intensity at a certain distance is by using Lambert-Beer's equation as shown in Equation 4.6 (Raventos et al., 2017).

$$I = I_o e^{-\Sigma_r X} \quad 4.6$$

Here, $\Sigma_r$ is the macroscopic neutron removal cross section of the material passed through by the radiation. From the NBS 63 handbook, the $\Sigma_r$ of water is 0.108 cm$^{-1}$ (NBS Handbook, 1957). Also, the effective neutron removal cross section is considered to be approximately constant for neutron energies between 2 and 12 MeV (El Abd and Elkady, 2014). By using Equation 4.6, at 15 cm and 30 cm from the source with water as a medium, the intensity of neutron with 2-12 MeV energies will be reduced to 0.20 and 0.04, respectively, from the intensity at source.

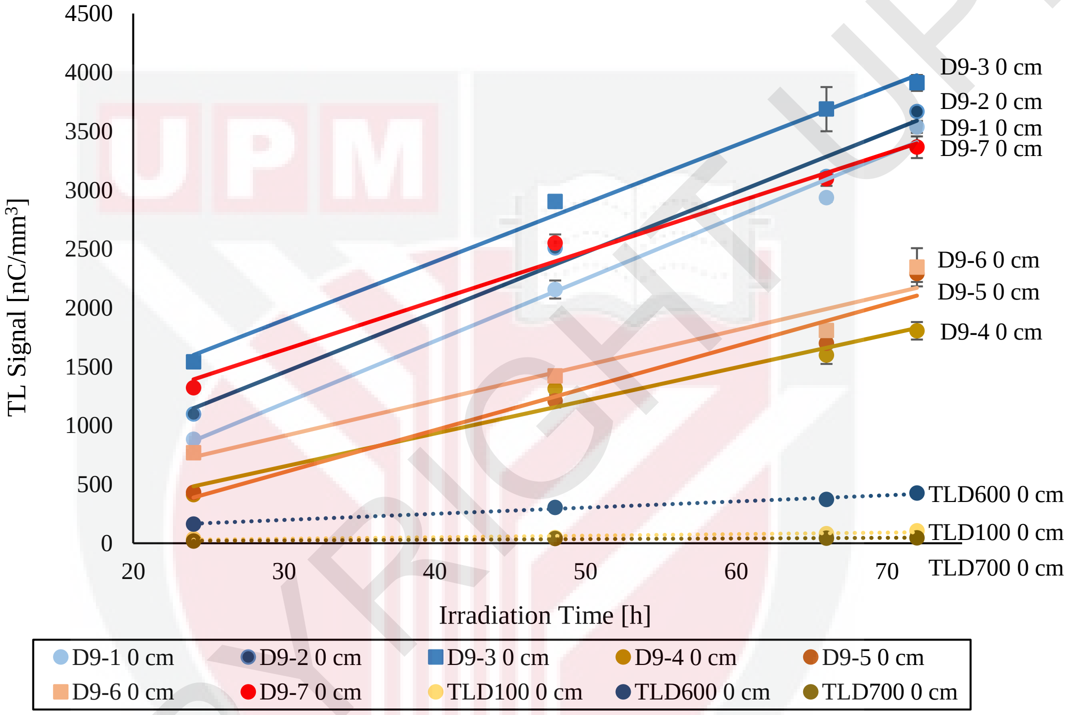


**Figure 4.41: Normalised TL signal of CUSOF and TLD irradiated using $^{241}$AmBe source over time right next to the source (0 cm)**

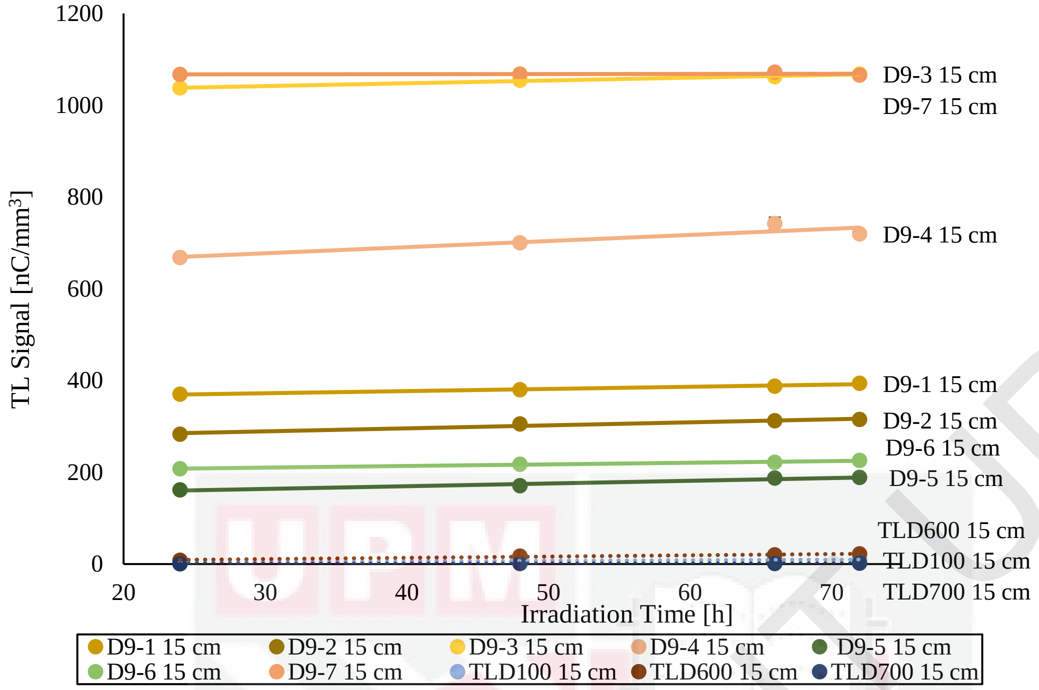


**Figure 4.42: Normalised TL signal of CUSOF and TLD irradiated using $^{241}$AmBe source over time 15 cm from the source**

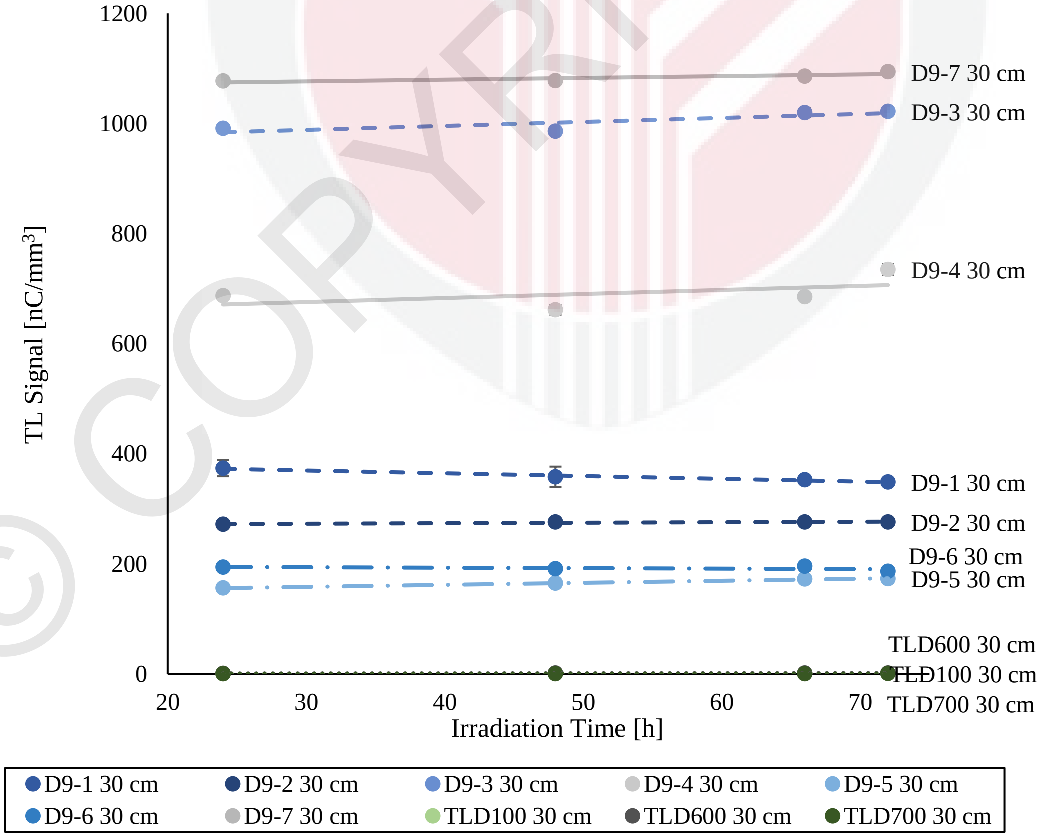


**Figure 4.43: Normalised TL signal of CUSOF and TLD irradiated using 241AmBe source over time 30 cm from the source**

For gamma, Equation 4.6 can be applied to by replacing $\Sigma_r$ with the $\mu/\rho$ written in Equation 4.7 (Yıldırım et al., 2016). The $\mu/\rho$ of photon (X-ray) with 4 and 5 MeV energy passing through water, obtained from NIST (2023), are 82.78 and 42.58 $cm^2/g$, respectively. NIST (2023) does not provide the $\mu/\rho$ of photon with 4.4 MeV energy produced by $^{241}$AmBe, hence, the usage of 4 and 5 MeV. By using Equation 4.7 at 15 cm and 30 cm distance from source in water medium, the intensity of 4 and 5 MeV gamma would drop to almost non-existence compared to the intensity at source.

$$I = I_o e^{-\frac{\mu}{\rho}x} \qquad 4.7$$

This explains the significant drop in the values of gradient and TL signal from 0 cm to 30 cm (Table 4.21). Also, higher $R^2$ values can be seen at distances nearer to the source where the $R^2$ values were about 0.95 to 0.99 at 0 cm and 15 cm from the source. D9-6 had the worst $R^2$ value and gradient at 30 cm from source of 0.1904 and -0.08 $nC/mm^3h$, respectively. At this point, it can be considered that the dose was too low for the fibre to detect, and the negative gradient may have just been due to the inconsistencies of the background readings. In general, CUSOF shows better sensitivity and good $R^2$ values when compared with the commercial TLDs. Even TLD-600 which is enriched with $^6$Li that possesses a large neutron cross section gave a lower normalised TL signal (El-Faramawy et al., 2021). Due to the extremely low percentage of $^6$Li existing in TLD-700, the dosimeter's normalised TL signal from $^{241}$AmBe irradiation was quite low where the gradient was 0.55 $nC/mm^3h$ as compared to 1.32 and 5.24 $nC/mm^3h$ for TLD-100 and TLD-600 respectively at 0 cm from the source. TLD-100 normalised TL signal was in between TLD-600 and TLD-700 as expected since the $^{6}$Li percentage of TLD-100 is also in between both dosimeters. Paiva et al. (2015) found that the dose contribution of neutrons in TLD-100, TLD-600 and TLD-700 due to $^{241}$AmBe source irradiation were 95.32, 99.21 and 20.7% respectively while the rest were from photons. From this information, while $^{241}$AmBe produces gamma rays too, apart from neutrons, the dose of the gamma rays was much lower compared to neutron since both TLD-100 and TLD-700 produced much lower normalised TL signals in comparison to TLD-600.

**Table 4.21: Linear fit of CusOF and TLD irradiated using $^{241}$AmBe source**

| TLD Type | Distance from source [cm] | $R^2$ | Gradient [nC/mm$^3$h] | y intercept [nC/mm$^3$] |
|---|---|---|---|---|
| D9-1 | 0 | 0.9896 | 52.87 | -699.45 |
| | 15 | 0.9717 | 0.47 | 57.07 |
| | 30 | 0.9776 | -0.50 | 83.46 |
| D9-2 | 0 | 0.9846 | 50.89 | -301.53 |
| | 15 | 0.9546 | 0.66 | 111.81 |
| | 30 | 0.7851 | 0.09 | 43.06 |
| D9-3 | 0 | 0.9939 | 49.52 | -552.78 |
| | 15 | 0.9896 | 0.61 | 60.01 |
| | 30 | 0.6839 | 0.72 | 3.21 |
| D9-4 | 0 | 0.9698 | 28.02 | -188.98 |
| | 15 | 0.8398 | 1.33 | 637.33 |
| | 30 | 0.2645 | 0.73 | 653.52 |
| D9-5 | 0 | 0.9599 | 35.73 | -617.10 |
| | 15 | 0.9525 | 0.59 | -1.85 |
| | 30 | 0.9945 | 0.37 | -0.94 |
| D9-6 | 0 | 0.9496 | 29.95 | -142.02 |
| | 15 | 0.9819 | 0.36 | 44.02 |
| | 30 | 0.1904 | -0.08 | 40.73 |
| D9-7 | 0 | 0.9868 | 41.77 | 389.51 |
| | 15 | 0.0473 | 0.03 | 1066.65 |
| | 30 | 0.7399 | 0.32 | 1066.86 |
| TLD-100 | 0 | 0.8672 | 1.32 | -1.82 |
| | 15 | 0.9824 | 0.12 | 1.46 |
| | 30 | 0.9899 | 0.01 | 0.19 |
| TLD-600 | 0 | 0.9881 | 5.24 | 40.56 |
| | 15 | 0.9619 | 0.27 | 2.67 |
| | 30 | 0.9714 | 0.01 | 0.45 |
| TLD-700 | 0 | 0.9185 | 0.55 | 7.53 |
| | 15 | 0.9548 | 0.02 | 0.21 |
| | 30 | 0.8015 | 0.00 | 0.21 |

Figure 4.44 shows the TL signals of the passive dosimeters at 0 cm after being irradiated for 72 h. By comparing the TL signals of the TLDs, it's obvious that the main radiation contribution from the $^{241}$AmBe source was neutron rather than gamma since TLD-700 TL signal was significantly lower than that of TLD-600. Since both TLDs can be used to detect gamma ray, the 426 nC/mm$^3$ response of TLD-600 was contributed by both neutron and gamma. The 45 nC/mm$^3$ response of TLD-700 was

contributed by gamma only since TLD-700 is insensitive towards neutrons. An approximation of 381 nC/mm$^3$ contribution from neutron is considered for TLD-600. Nawi et al. (2015) has found that optical fibres with the same properties as 6FF had a relative sensitivity of 0.42 with respect to TLD-100 when irradiated to a $^{60}$Co gamma source. What this imply is that since 6FF has a lower sensitivity towards gamma, it will produce lower TL signal compared to TLD-100 if the gamma radiation from $^{241}$AmBe was the main TL signal contributor. Instead, 6FF had a notably higher respond compared to TLD-100 which means that neutron is the major contributor to the fibre's respond. Unfortunately, CUSOF at present lacks the ability to differentiate accurately between the neutron and gamma radiation. However, the objective of this work is to observe whether CUSOF is capable to detect neutron since the target application of the CUSOF is space radiation. From this work we know that neutron contributions from space environment should not be neglected when CUSOF is employed as the radiation detector. Another concern is that $^{60}$Co produces gamma energies of 1.173 and 1.332 MeV which is different from the gamma energy produced by $^{241}$AmBe of 4.4 MeV (Parsons, 2012). However, Entezam et al. (2016) found that OF doped with Ge had minimal dependency on photon energies of 6 MV and 10 MV for X-ray up to 1.25 MeV for gamma.

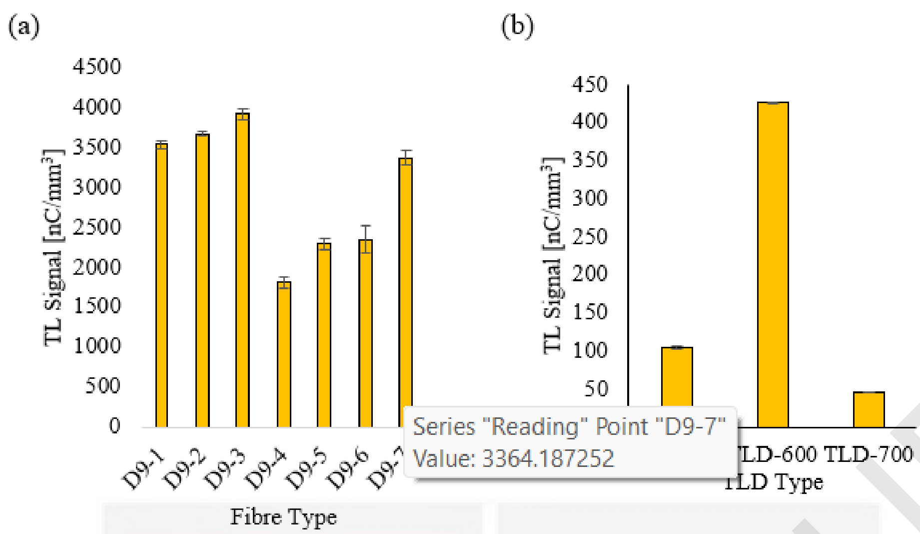


**Figure 4.44: TL signal at 0 cm after 72 h of irradiation for (a) OF, and, (b) commercial TLD**

Figure 4.45 represent the glow curve respective to CUSOF commercial TLD used in this work. CUSOF exhibited wide range of temperature where electrons are thermally excited to produce luminescence starting from approximately 151°C (2.5 s) up to 400°C (10.86 s until the end of acquisition time of 13.33 s). On the other hand, TLDs had shown smaller range of electron thermal excitation temperature of 135°C (2.6 s) up to 300°C (7.9 s to 9 s) as shown in Figure 4.46. Hassan et al. (2018) attributed this phenomenon due to the amorphous nature of the silica glass (CUSOF main constituent) and crystalline nature of the TLDs. CUSOF mainly display a single broad peak that is affected near 400°C due to the background planchet (BGP) reading influence. Since the maximum temperature for TLD's TTP is 300°C, the glow curve is not influenced by the BGP reading. TL intensity increase of the BGP may be induced from the light produced by the TLD reader itself through the phosphorescence in the glass envelope of the photomultiplier or by the interactions in the photocathode material (German and Weinstein, 2002). The maximum TL intensity will increase with exposure duration and occurred at similar temperature for each dosimeter. TLDs had significantly larger volume compared to CUSOF as presented in hence the TL intensity produced by TLDs were substantial compared to CUSOF.

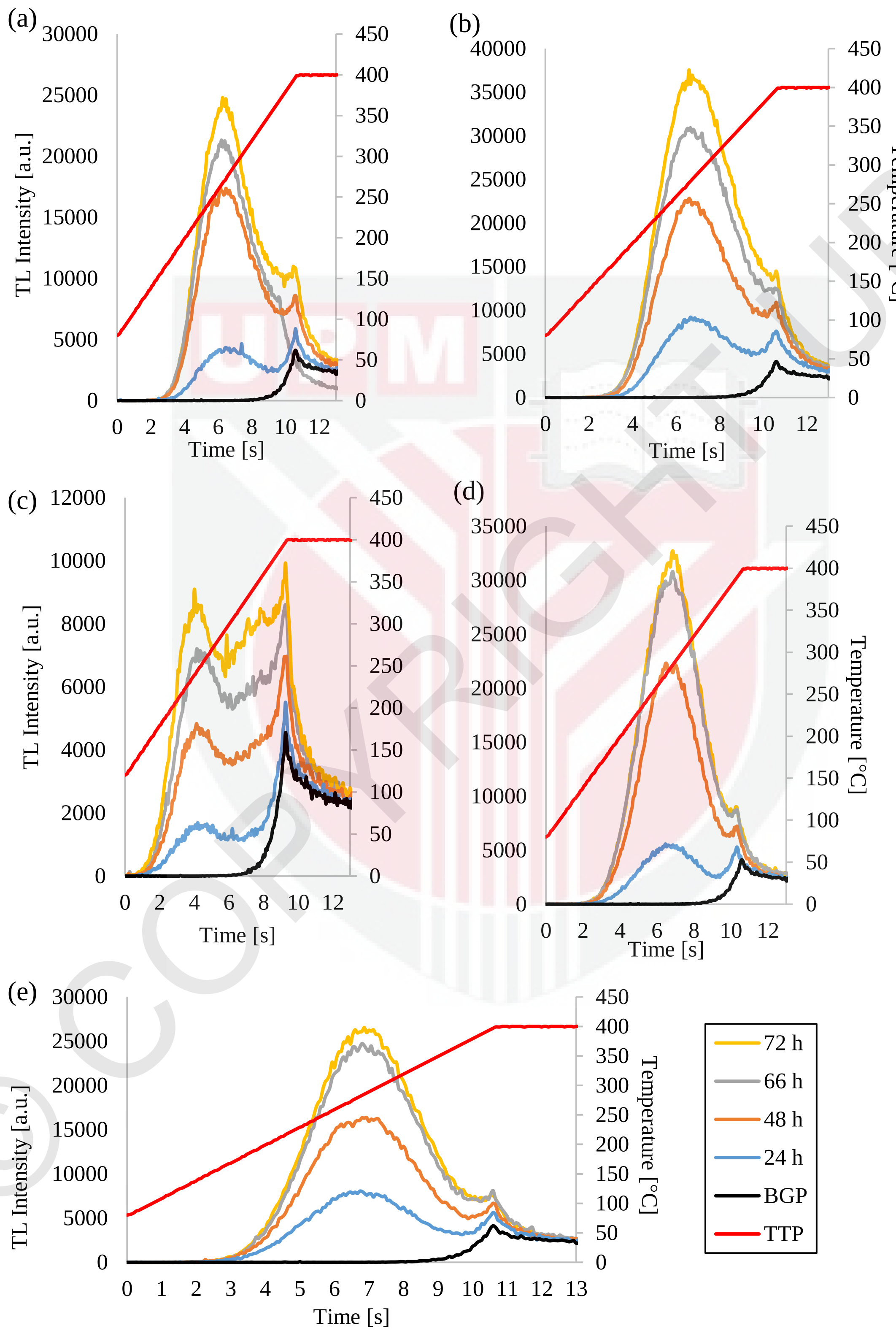


**Figure 4.45: Glow curve of (a) D9-1, (b) D9-2, (c) D9-3, (d) D9-5, and (e) D9-6 at 0 cm**

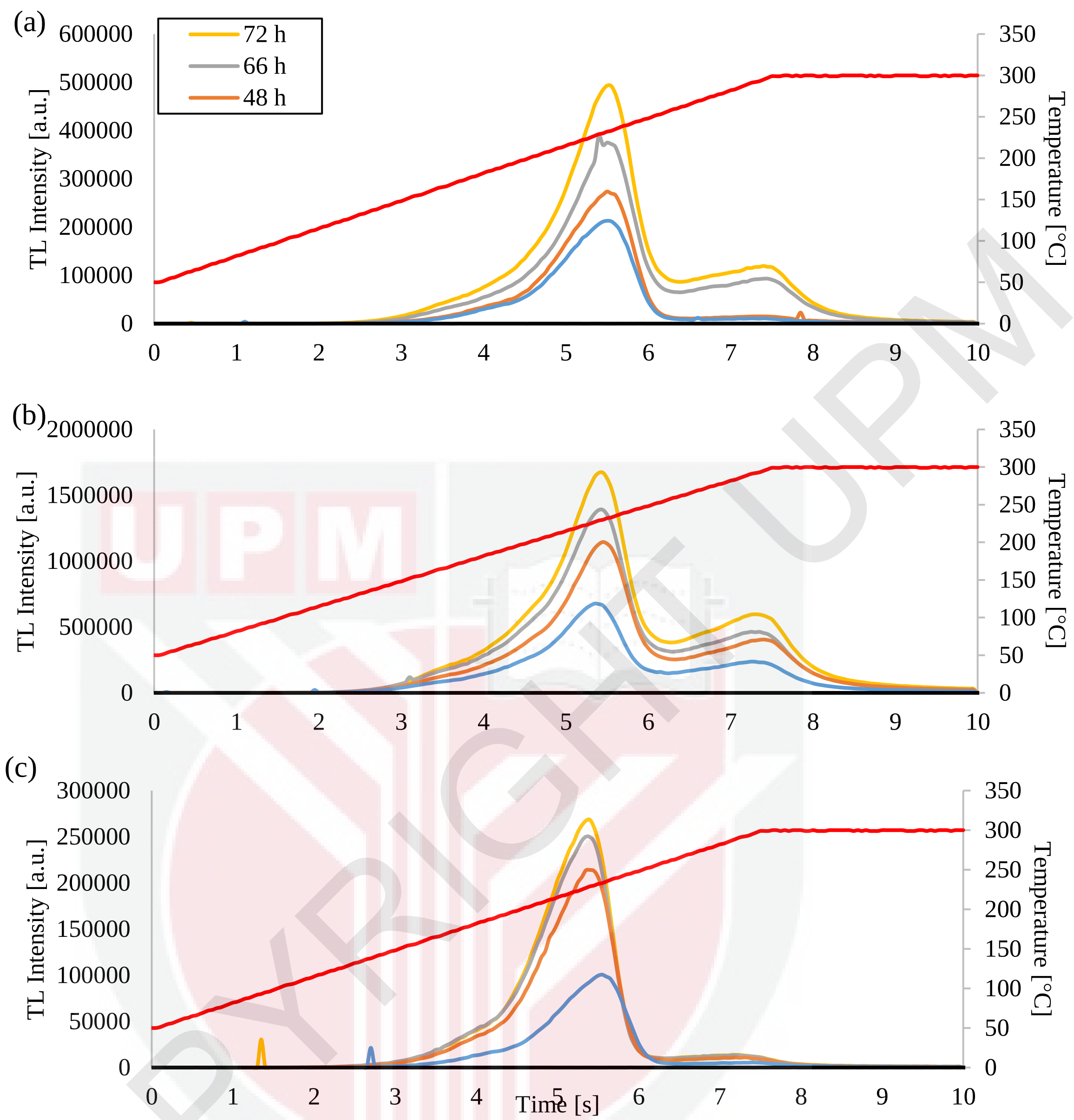


**Figure 4.46: Glow curve of (a) TLD-100, (b)TLD-600 and (c) TLD-700 at 0 cm**

## 4.9 Screening of Passive Dosimeters Analysis

For CUSOF, D9-1, D9-2 and D9-3 are irradiated to Caesium-137 ($^{137}Cs$) to a low gamma dose of 5 mGy to assess the sensitivity of each fibre on radiation detection. Figure 4.47 shows the glow curve of D9-2 irradiated to 5 mGy gamma. In the figure, the CUSOF shows a small response to the radiation in comparison to the background planchet reading. The more sensitive the fibre is, the bigger the response will be. While

LEO's radiation is higher than that of the Earth's surface, compared to other dosimetry application such as radiotherapy, the dose is smaller. As such, rather than using CUSOF with responses that is close to average, here the usage of a more sensitive CUSOF is chosen for FM with decreasing sensitivity for CM where the extra screened fibres are used for calibration alongside the exposed fibres as shown in Figure 4.48.

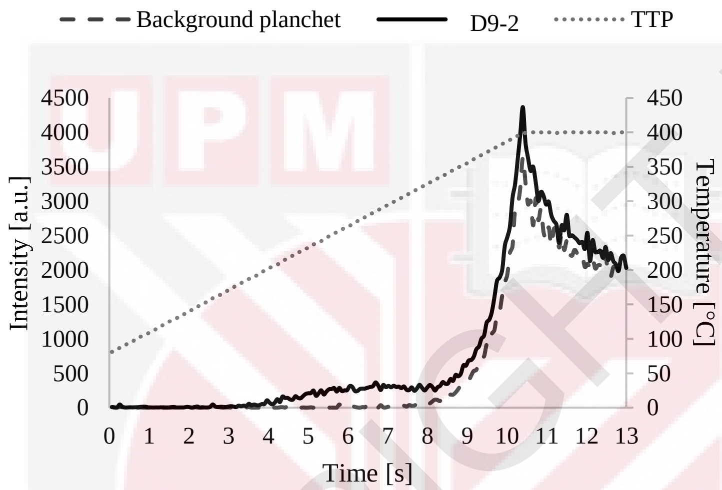


**Figure 4.47: D9-2 irradiated to 5 mGy gamma ($^{137}$Cs)**

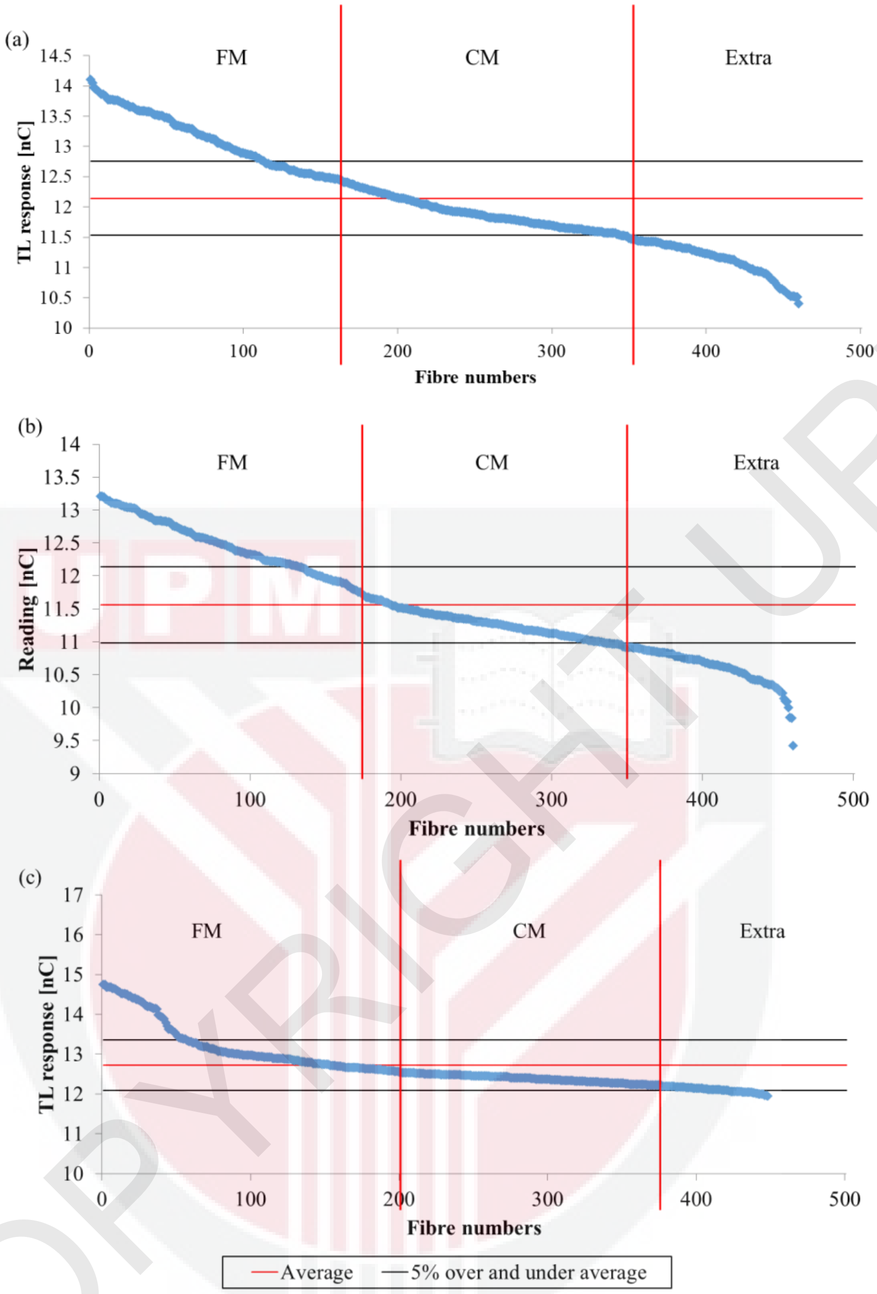


**Figure 4.48: Screening results of (a) D9-1, (b) D9-2 and (c) D9-3 using gamma ($^{137}$Cs)**

For TLD-100, TLD-600 and TLD-700, about 100 pieces of each type of dosimeter are screened using $^{241}$AmBe. While screening the PD, simultaneously, irradiation using the neutron-gamma source will help segregate the PD in the event of accidental mix up. For TLD-100, TLD-600 and TLD-700, about 100 pieces of the PD are screened with the results shown in Figure 4.49. As can be expected, TLD-600 yielded the highest TL response followed by TLD-100 then TLD-700. For FM and CM, 32 pieces of TLD-100 are used for each hardware. For TLD-600 and TLD-700, each hardware used 24 pieces of the materials each. Hence, a significantly smaller number of the commercial TLD are screened. Also, each screened commercial TLD is labelled accordingly for future usage.

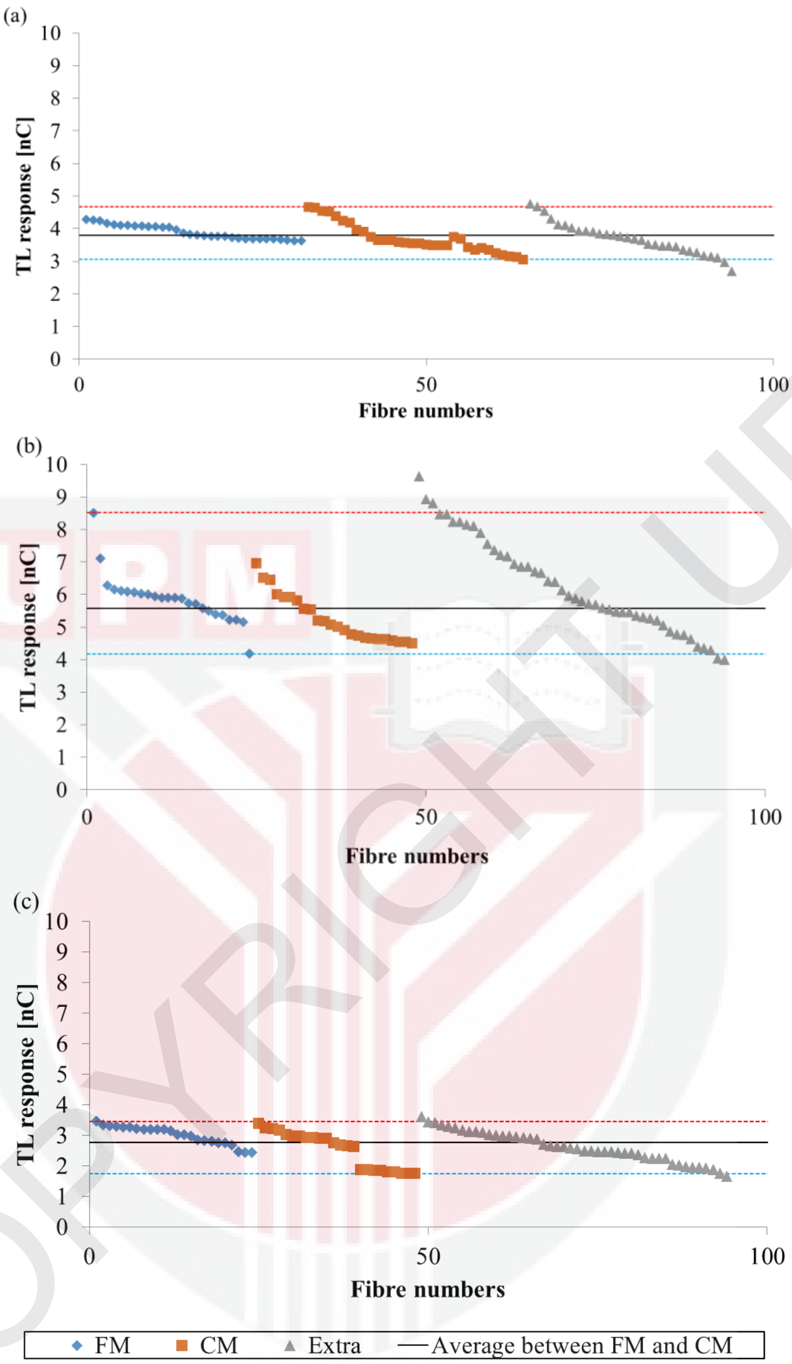


**Figure 4.49: Screening results of (a) TLD-100, (b) TLD-600 and (c) TLD-700 using neutron-gamma ( $^{241}$AmBe)**

## 4.10 Results of Space Exposed SOFPADS

In this section, the PD within FM and CM are readout. Then their readout results are analysed. The same PD are irradiated and calibrated with proton since proton is the main constituent of space radiation at LEO. At the same time, the PD responses to proton can be further investigated. Table 4.22 shows the time-temperature profile (TTP) used for space exposure and proton irradiation of each PD. The TTP labelling in the table corresponds to the TTP shown in Table 3.29 in the previous chapter.

**Table 4.22: TTP used for space exposed samples and proton irradiation**

| PD | Irradiation | TTP |
|---|---|---|
| D9-1 | Space Exposure | P60, P80, P100, P120 |
| | Proton | P100 |
| D9-2 | Space Exposure | P60, P80, P100, P120 |
| | Proton | P100 |
| D9-3 | Space Exposure | P60, P80, P100, P120 |
| | Proton | P120 |
| D9-4 | Space Exposure | P60, P80, P100, P120 |
| | Proton | P120 |
| D9-5 | Space Exposure | P60, P80, P100, P120 |
| | Proton | P120 |
| D9-6 | Space Exposure | P60, P80, P100, P120 |
| | Proton | P100 |
| D9-7 | Space Exposure | P60, P80, P100, P120 |
| | Proton | P100 |
| TLD100 | All | TLD_High |
| TLD600 | | |
| TLD700 | | |

## 4.11 Space Exposed SOFPADS Analysis

The readout results of space exposed samples are shown in Figure 4.50. The readout results in the figure are obtained by subtracting the TL responses of FM with the readout responses from the figure, D9-5 produced the highest TL readings at 228 to $283\times10^{6}$ [nC/μm$^{3}$] depending on the TTP followed by D9-3. Both D9-5 and D9-3 being FF and having the highest reading agree with results from Zakaria et al., (2020) and Mat Nawi et al., (2015) where FF have higher sensitivity in comparison to TLD-

100 and CF. Comparing results from section A and C, all samples with various TTP for OF were statistically insignificant with a p-value > 0.05 where the confidence level is 95%. D9-3 that are placed in section A, C and G also did not show statistical significance (p-value > 0.05) for P60, P100 and P120. While radiations coming from the zenith are expected to be the highest, secondary radiations from various directions could be affecting the total absorbed dose received by the passive dosimeters. Having no statistical significance imply that the probability of the positioning of the passive dosimeters within the SOFPADS affecting the total dose received by the passive dosimeters is low.

Comparison of TTP have shown that in terms of preheat temperature, generally no statistical significance (p-value > 0.05) is shown regarding TL readings, except for D9-2 placed in section E. The preheat temperature, however, affects the position of the peaks in the glow curves as shown in Figure 4.51. Higher preheat temperature will cause the glow curve to reach its maximum intensity earlier, basically shifting the glow curve to the left as evidenced by the figure. Ideally, a singular peak glow curve should have its peak occurring in the middle while for two peaks glow curve, adjustment should be made where the glow curve occur in the middle of the acquisition channels (approximate 6.67 s after the start of acquisition) (Fadzil et al., 2011). For D9-1 and D9-2, P100 is the ideal TTP while for other OF, P120 is more suitable. A higher preheat temperature might be more fitting for D9-4 and D9-6 but number of samples limit the availability of testing. Thus, currently for both D9-4 and D9-6 P120 is chosen to be the best TTP for space exposure.

Additionally, as shown in Figure 4.50(e) in section I, TLD600 presented a TL reading of $2.4 \times 10^5$ nC/μ$m^3$, while TLD700 presented a TL reading of $1.7 \times 10^5$ nC/μ$m^3$. The difference of the reading is the thermalised neutron (kinetic energy of about 0.025 eV) detected by TLD600 as the material is sensitive to thermal neutron while TLD700 is insensitive the particle (El-Faramawy et al., 2021; Brahme, 2014). Both TLD are insensitive to fast neutrons (El-Faramawy et al., 2021). The averaged difference of responses of TLD600 and TLD700 in section A and C is $0.35 \pm 0.05 \times 10^5$ nC/μ$m^3$. The difference between the responses of the both TLD in section I is $0.7 \times 10^5$ nC/μ$m^3$. This means that there is an additional $0.35 \times 10^5$ nC/μ$m^3$ difference as compared to section A and C, proving the existence of higher energy neutrons that is thermalised and detected by the PD.

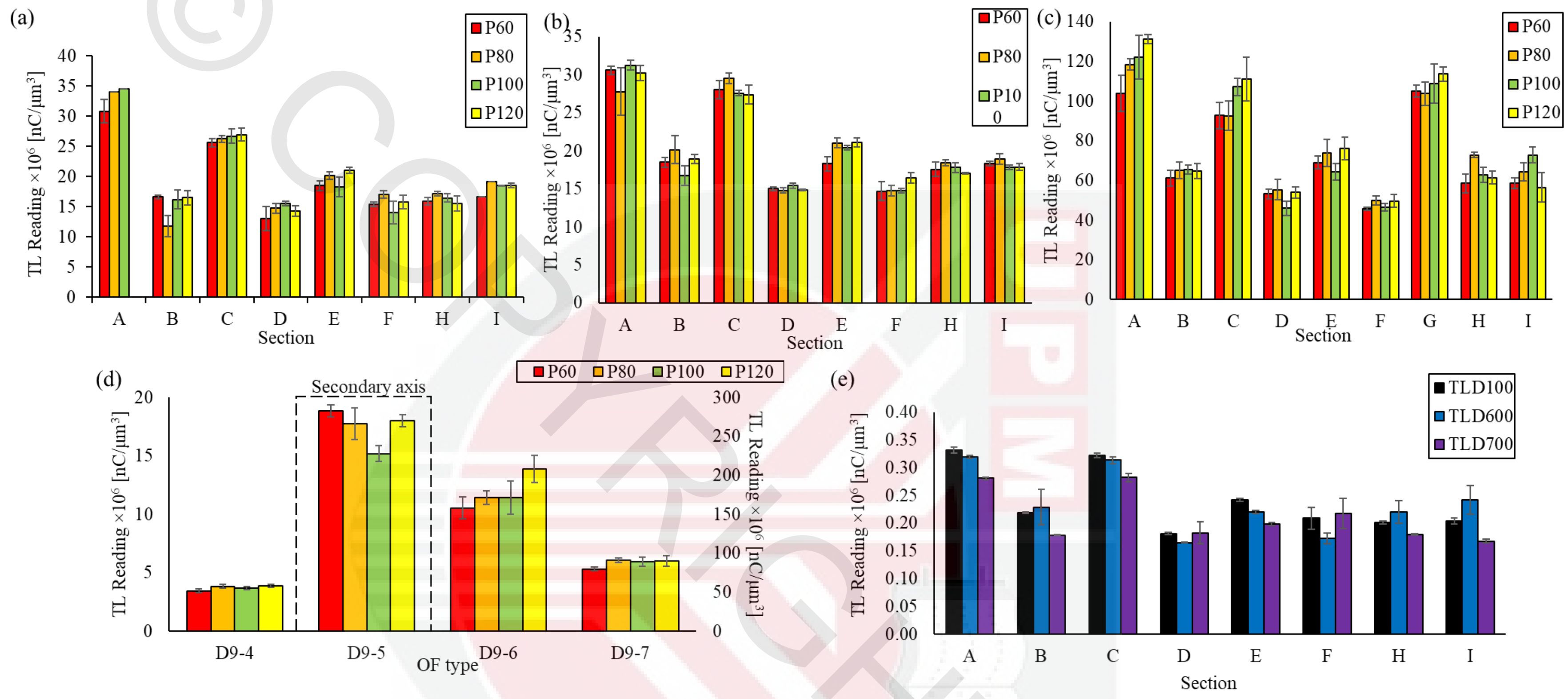


Figure 4.50: TL responses of space exposed samples: (a) D9-1, (b) D9-2, (c) D9-3, (d) PD in section G (D9-4, D9-5 and D9-6), (e) TLD-100, TLD-600 and TLD-700

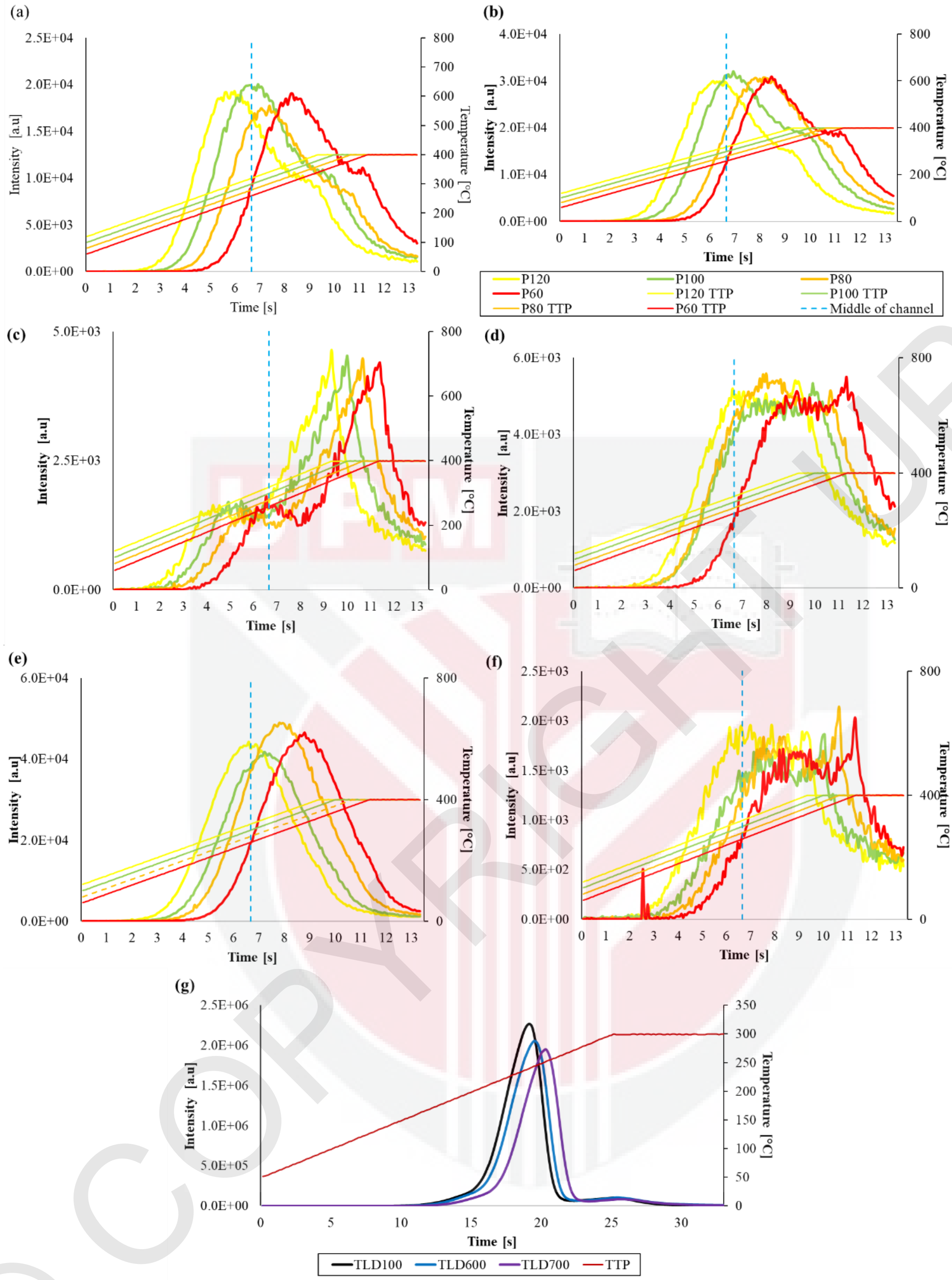


**Figure 4.51: Glow curves for space exposed samples for section C for (a) D9-1, (b) D9-2 and (c) D9-3. For (d) D9-4, (e) D9-5 and (f) D9-7, the CUSOF are in section G of FM. The glow curves of (g) TLD-100, TLD-600 and TLD-700 are from readout of section C**

## 4.12 Proton Exposed Passive Dosimeters used for Space Exposure

The PD irradiated using proton is not normalised since it will be used for calibration. The space exposed PD results shown in Figure 4.50 is normalised but during calibration calculation, the original TL response in nC is used. The reasoning behind this is to reduce the number of steps required for calculation to promote less calculation mistake from happening. Furthermore, between the same PD, normalisation is unneeded since without normalisation, the same result is produced. Normalisation is needed for comparison between PD with different (core) dimensions.

Figure 4.52 shows the linearity responses of the PD irradiated using proton of 150 MeV in energy. The regression is compared between same PD exposed in space (FM) and left as a control on Earth (CM). This is to see whether space radiation will alter the PD's responses to radiation after long term exposure in space environment. From the figure, most PD are similar with each other (between FM and CM) in their responses to proton. As such, the combined trendline will be used for dose determination. D9-7 (Figure 4.52 (g)) there are not enough samples to be analysed hence the lack of CM linearity response. Additionally, the small nature COMOF (significantly smaller than CUSOF) makes it hard to be handled (easily lost during handling). Apart from D9-1, D9-2 D9-3, proper dose conversion using linearity, energy dependency and fading response may not be possible due to the small number of samples employed. For calibration, only PD used in FM and CM were irradiated with proton.

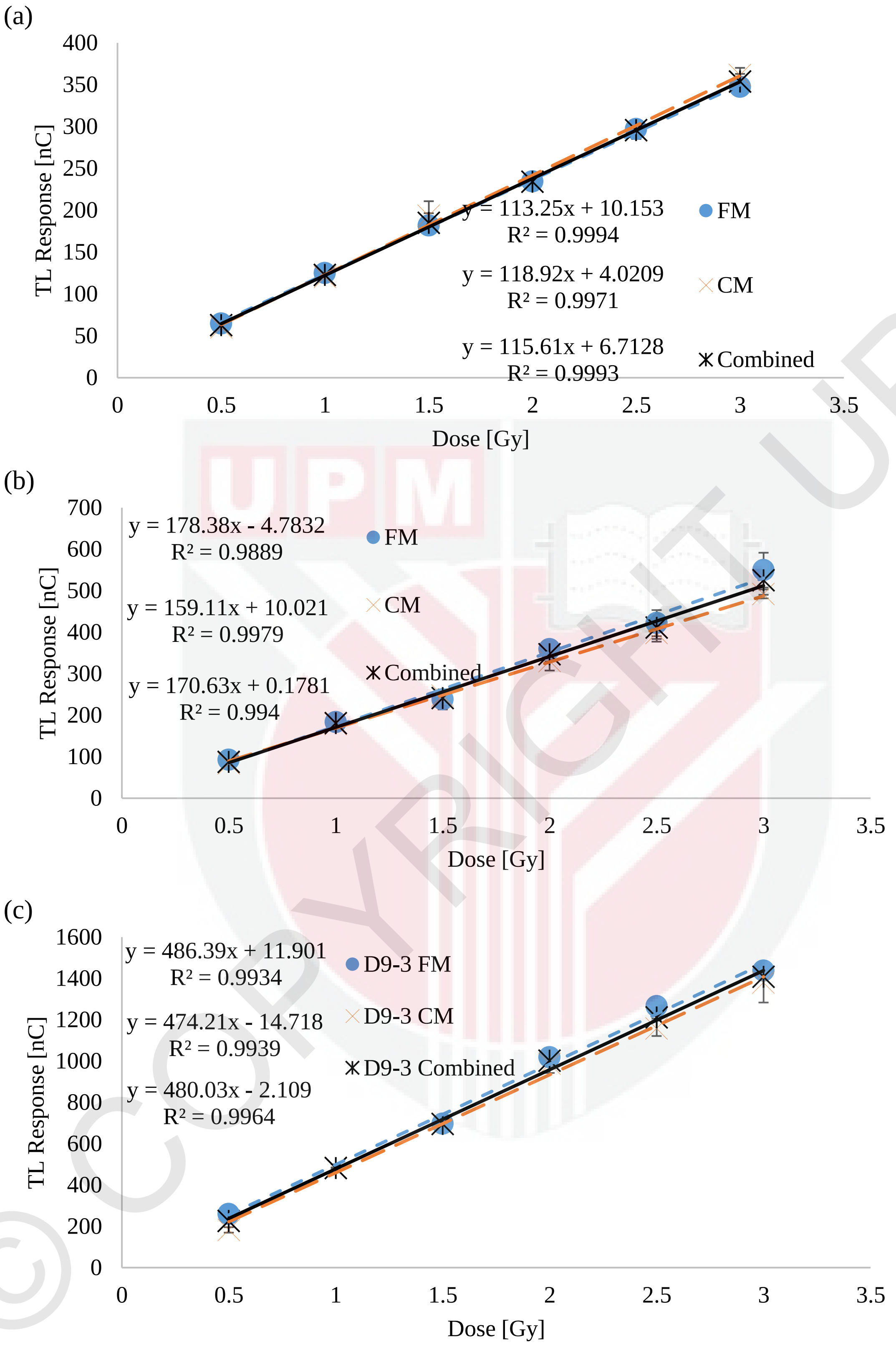
(a)
y = 113.25x + 10.153
R² = 0.9994
y = 118.92x + 4.0209
R² = 0.9971
y = 115.61x + 6.7128
R² = 0.9993
FM
CM
Combined
TL Response [nC]
Dose [Gy]
(b)
y = 178.38x - 4.7832
R² = 0.9889
y = 159.11x + 10.021
R² = 0.9979
y = 170.63x + 0.1781
R² = 0.994
FM
CM
Combined
TL Response [nC]
Dose [Gy]
(c)
y = 486.39x + 11.901
R² = 0.9934
y = 474.21x - 14.718
R² = 0.9939
y = 480.03x - 2.109
R² = 0.9964
D9-3 FM
D9-3 CM
D9-3 Combined
TL Response [nC]
Dose [Gy]

(d)

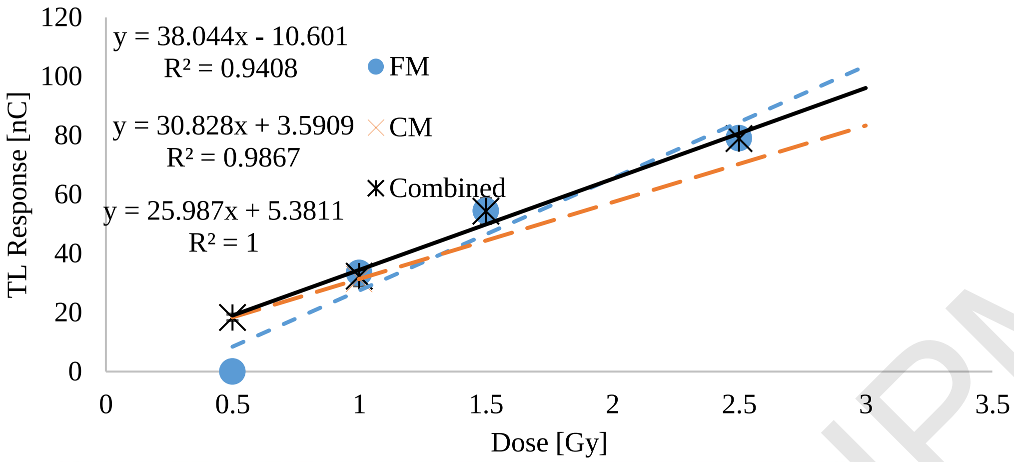

y = 38.044x - 10.601
R² = 0.9408
y = 30.828x + 3.5909
R² = 0.9867
y = 25.987x + 5.3811
R² = 1
FM
CM
Combined
TL Response [nC]
Dose [Gy]
0
20
40
60
80
100
120
0
0.5
1
1.5
2
2.5
3
3.5


(e)

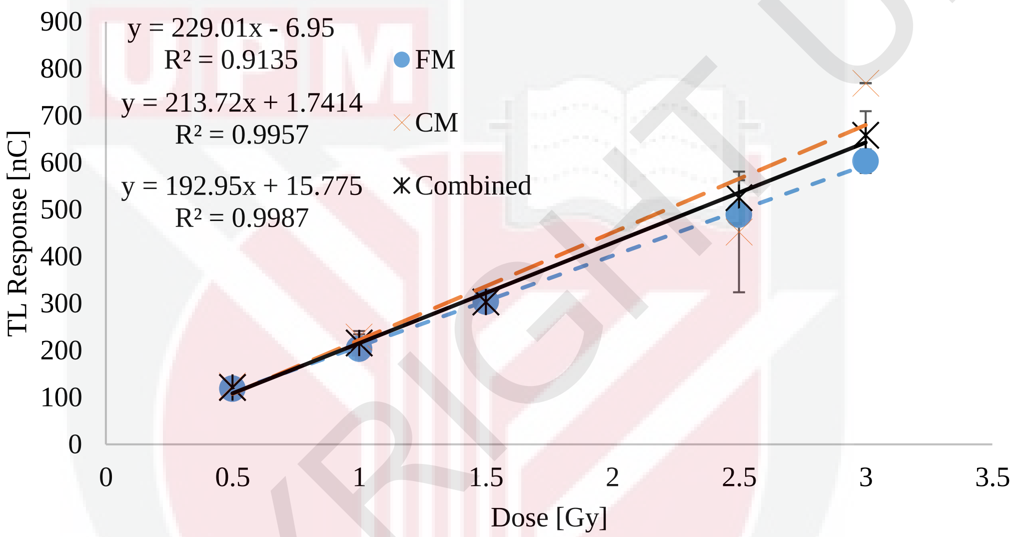

y = 229.01x - 6.95
R² = 0.9135
y = 213.72x + 1.7414
R² = 0.9957
y = 192.95x + 15.775
R² = 0.9987
FM
CM
Combined
TL Response [nC]
Dose [Gy]
0
100
200
300
400
500
600
700
800
900
0
0.5
1
1.5
2
2.5
3
3.5


(f)

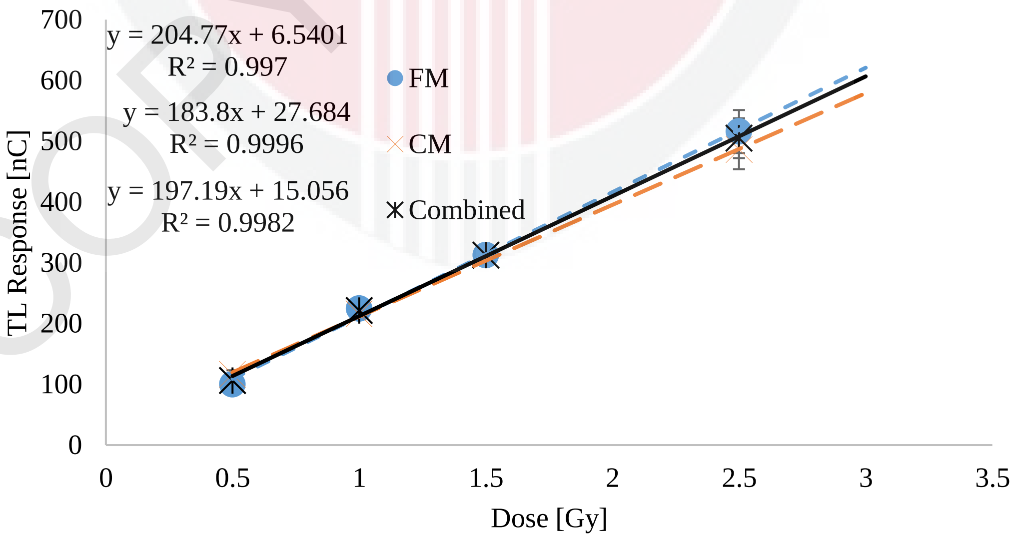

y = 204.77x + 6.5401
R² = 0.997
y = 183.8x + 27.684
R² = 0.9996
y = 197.19x + 15.056
R² = 0.9982
FM
CM
Combined
TL Response [nC]
Dose [Gy]
0
100
200
300
400
500
600
700
0
0.5
1
1.5
2
2.5
3
3.5

(g)

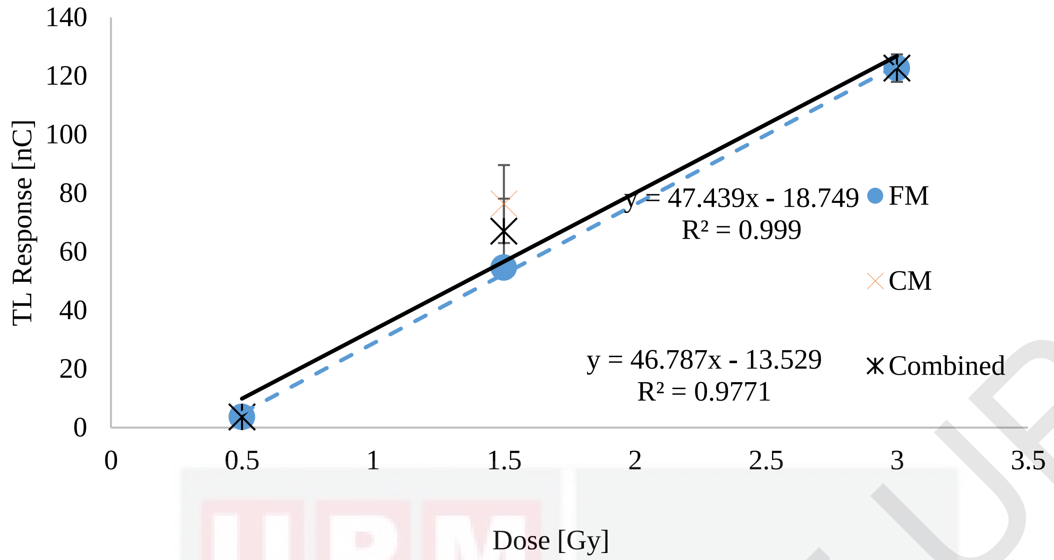

140
120
100
80
60
40
20
0
TL Response [nC]
y = 47.439x - 18.749
R² = 0.999
y = 46.787x - 13.529
R² = 0.9771
FM
CM
Combined
0
0.5
1
1.5
2
2.5
3
3.5
Dose [Gy]


(h)

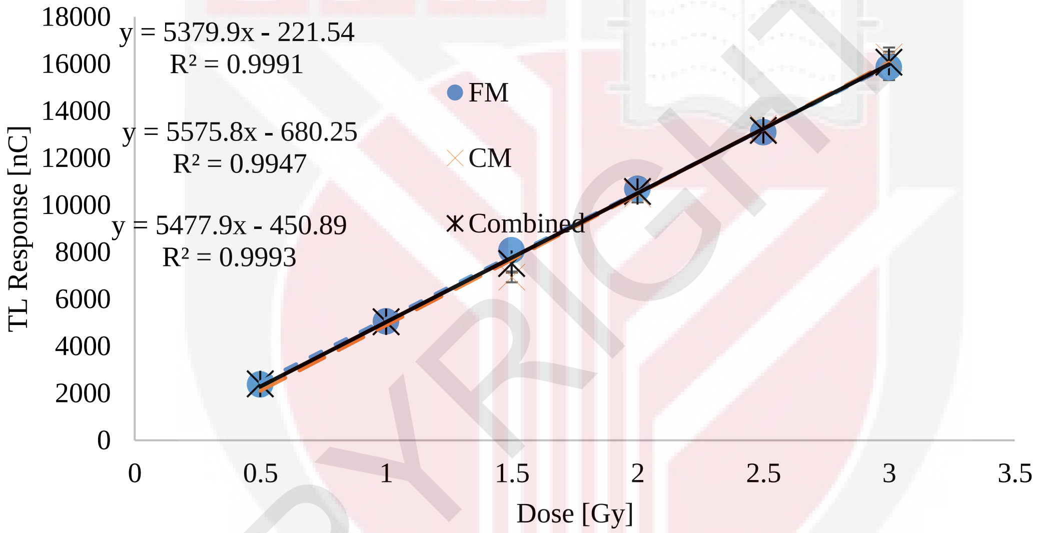

18000
16000
14000
12000
10000
8000
6000
4000
2000
0
TL Response [nC]
y = 5379.9x - 221.54
R² = 0.9991
y = 5575.8x - 680.25
R² = 0.9947
y = 5477.9x - 450.89
R² = 0.9993
FM
CM
Combined
0
0.5
1
1.5
2
2.5
3
3.5
Dose [Gy]


(i)

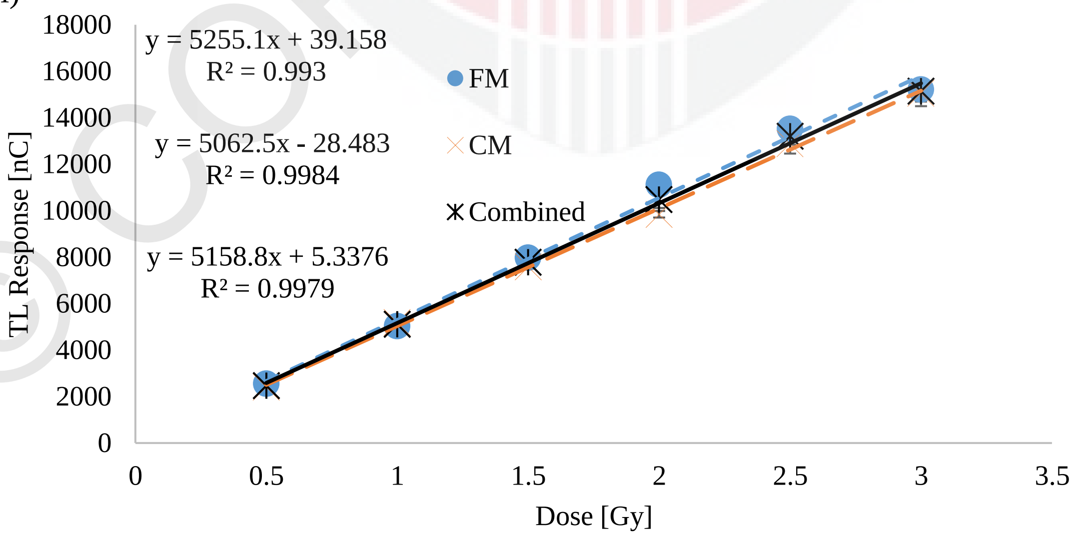

18000
16000
14000
12000
10000
8000
6000
4000
2000
0
TL Response [nC]
y = 5255.1x + 39.158
R² = 0.993
y = 5062.5x - 28.483
R² = 0.9984
y = 5158.8x + 5.3376
R² = 0.9979
FM
CM
Combined
0
0.5
1
1.5
2
2.5
3
3.5
Dose [Gy]

(j)

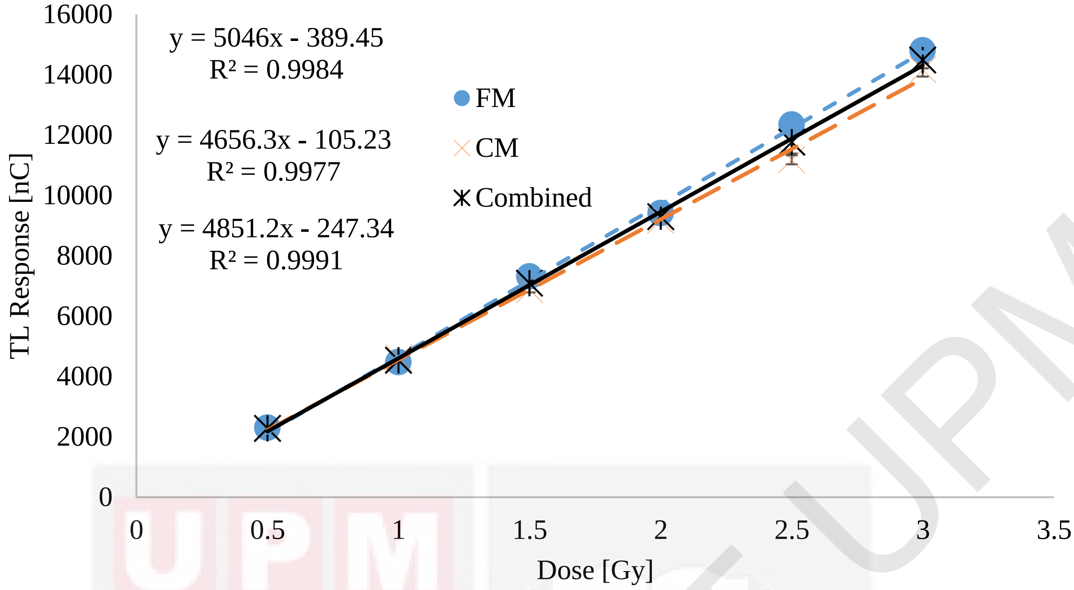


**Figure 4.52: Linearity of the PD used for FM and CM irradiated at proton energy of 150 MeV. (a) D9-1, (b) D9-2, (c) D9-3, (d) D9-4, (e) D9-5, (f) D9-6, (g) D9-7, (h) TLD-100, (i) TLD-600 and (j) TLD-700**

Figure 4.53 shows the normalised responses of each PD irradiated at 2.0 Gy with the energies of 150, 190 and 230 MeV. The responses are normalised to the 150 MeV. D9-4, D9-5, D9-6, and D9-7 did not have any energy dependency responses due to the lack number of samples required to conduct the test. Generally, the PD showed similar responses to each energy except TLD-600.

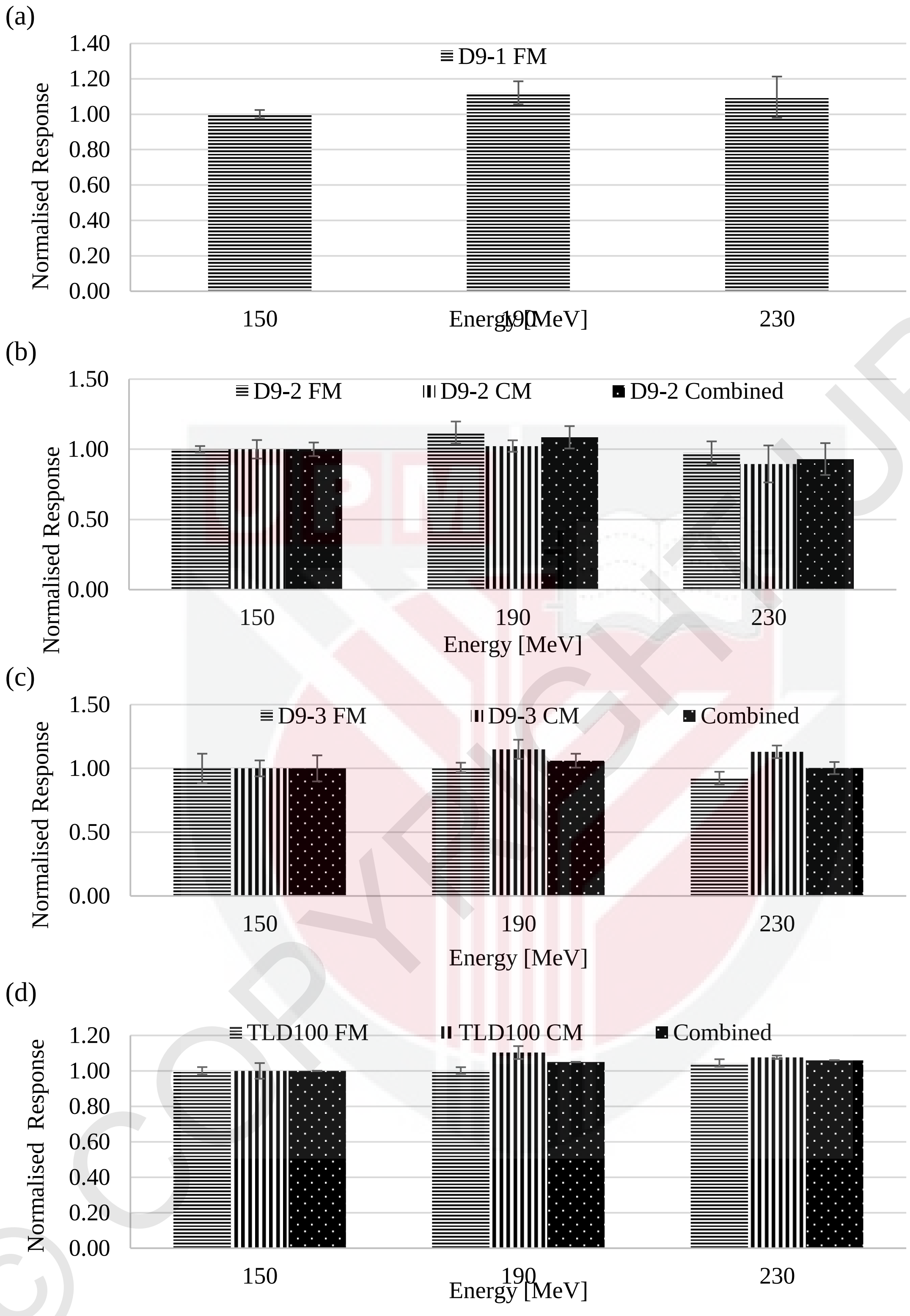
(a)
D9-1 FM
Normalised Response
1.40
1.20
1.00
0.80
0.60
0.40
0.20
0.00
150
190
230
Energy [MeV]
(b)
D9-2 FM
D9-2 CM
D9-2 Combined
Normalised Response
1.50
1.00
0.50
0.00
150
190
230
Energy [MeV]
(c)
D9-3 FM
D9-3 CM
Combined
Normalised Response
1.50
1.00
0.50
0.00
150
190
230
Energy [MeV]
(d)
TLD100 FM
TLD100 CM
Combined
Normalised Response
1.20
1.00
0.80
0.60
0.40
0.20
0.00
150
190
230
Energy [MeV]

(e)

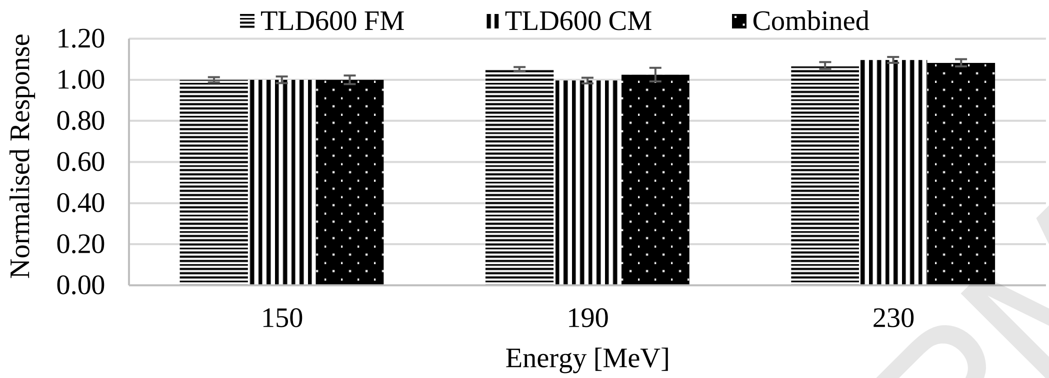


(f)

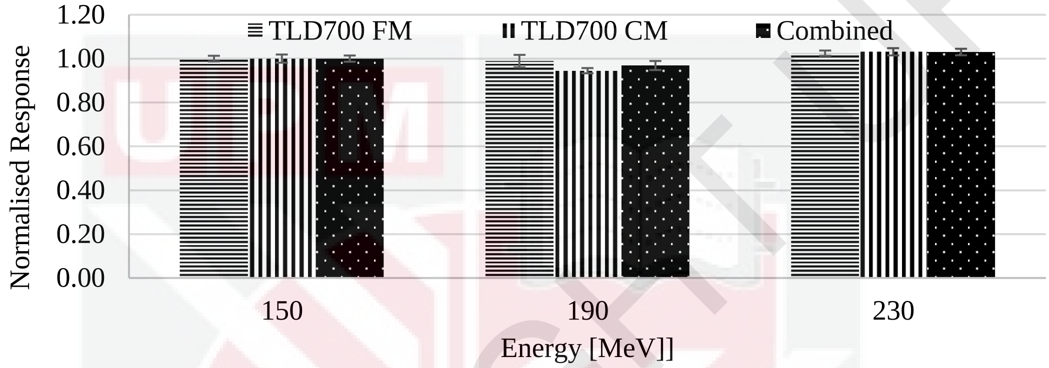


**Figure 4.53: Energy response of 2.0 Gy proton irradiated PD. (a) D9-1, (b) D9-2, (c) D9-3, (e) TLD-100, (f) TLD-600 and (f) TLD-700**

Figure 4.54 shows the fading responses of PD with enough number conduct the test. After 352 days post irradiation, TLD-700 had the lowest fading at about 8% while D9-3 had highest fading of 17% compared to the initial readout value. While high fading rate is an undesirable characteristic, the dose can be corrected by using the fading calibration curve shown in the figure. The trendline is plotted using logarithmic function as used by Ghomeishi et al. (2015).

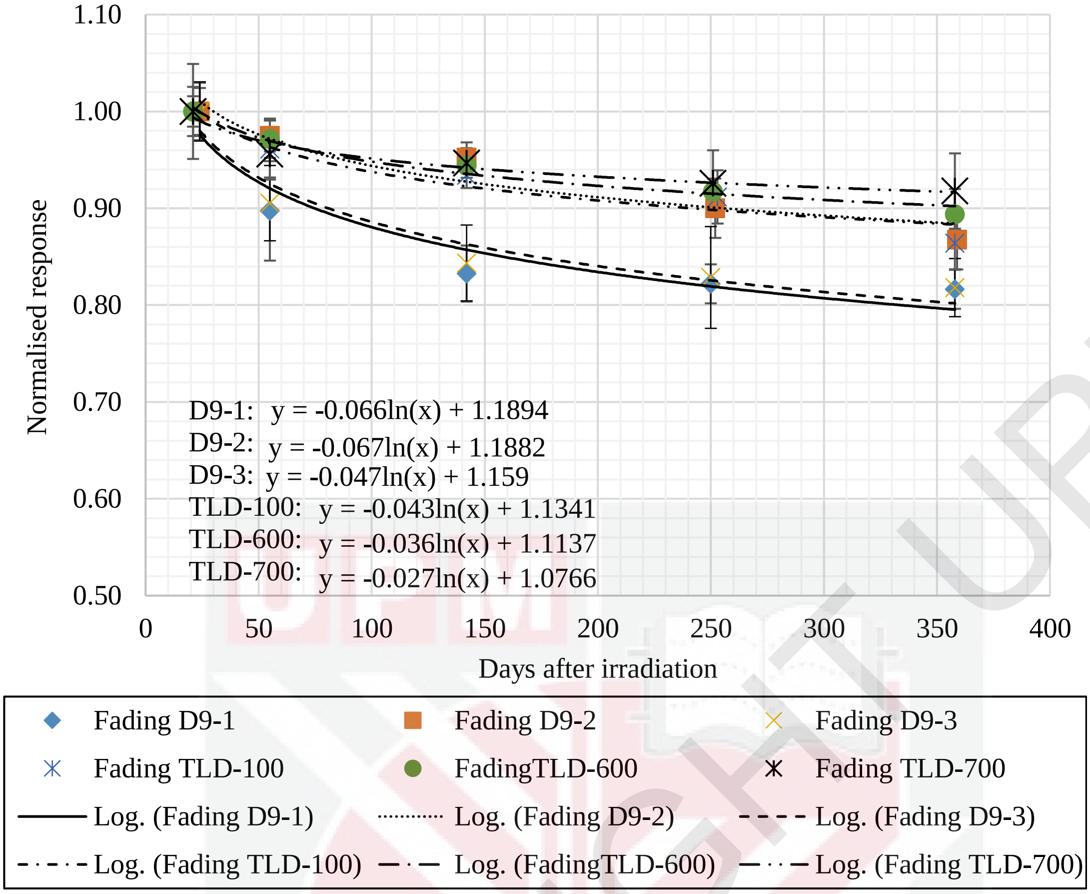


**Figure 4.54: Fading responses of the PD exposed to 1.0 Gy proton at 150 MeV**

## 4.13 Absorbed Dose Conversion of Space Exposed Passive Dosimeters

The absorbed dose is correlated using the calibration curve in Figure 4.52. The trendline is shown in Equation 4.8 where y is the TL response, m is the slope of the curve, x is the dose given to the PD and c is the y-intercept. The rearranged equation is shown in Equation 4.9.

$$y = mx + c \qquad 4.8$$

$$x = \frac{y - c}{m} \qquad 4.9$$

Then measurement is corrected by the following Equation 4.10. The equation is based on Izewska et al., (2008).

$$D = M \cdot f_{fad} \qquad 4.10$$

Here, D is the absorbed dose. M is the mean reading of space exposed PD. Basically $x = M.\, f_{lin}$ is the linearity correction factor. This value is taken from the trendline function in Figure 4.52.

$f_{fad}$ is the fading correction factor. It is determined with similar method to Noor (2012) as shown in Equation 4.11. Here, $y_{RD}$ is the fading ratio at day the reference day $x_{RD}$, and $y_{PD}$ is the fading ratio at day $x_{PD}$. Both a and b are the coefficients in the trendline. The values of the trendline coefficients are taken from Figure 4.54. For proton irradiated samples, the $x_{RD}$ is at 21 days and the $x_{PD}$ is at 296 days.

$$f_{fad} = \frac{y_{RD}}{y_{PD}} = \frac{a \ln x_{RD} + b}{a \ln x_{PD} + b} \qquad 4.11$$

There is no non-linearity, temperature, angular, dose rate dependence, energy and holder correction factor. This is generally due to the nature of the exposure where the actual exposure condition is unknown. In terms of linearity, in Figure 4.52, the linearity of the PD responses has been shown. As such, there is no non-linearity correction factor.

Table 4.23 shows the absorbed dose correlation of the space exposed PD to 150 MeV proton. Without any filter, the PD detected up to 2211.64 μGy/day absorbed dose rate by D9-2 and 1674.66 μGy/day absorbed dose rate by TLD-100. EXPOSE-R mission measured an absorbed dose rate of 276-381 μGy/day (Berger et al., 2015; Rabbow et al., 2015). It should be noted however, that the dosimeters used during EXPOSE-R mission was placed inside an Al container which means the dosimeters received a shielded radiation. The MTR-1 mission detected a higher range of absorbed doses range from 204 -711 μGy/day (Berger et al., 2013; Zhou et al., 2010). Again, it should be noted that in MTR-1 mission, the dosimeters are placed either inside the poncho or inside the phantom which estimates the part of human that receives radiation. The MTR-1 mission also measured the radiation outside of the container of up to 1000 mGy/day. This shows that the LEO radiation environment varies based the exposure period and location. The variation of radiation environment can be attributed to solar activity during the exposure period. Additionally, the variations in measurements imply that there are other correction factors that should be considered.

**Table 4.23: Absorbed dose conversion**

| PD | Section | TL response, y [nC] | Standard Deviation [nC] | Dose conversion from calibration curve, M [Gy] | Fading calibration factor at 296 days, $f_{fad}$ | Absorbed dose, D [Gy] | Dose rate [µGy/day] | Standard Deviation [µGy/day] |
|---|---|---|---|---|---|---|---|---|
| D9-1 | A | | | | | | | |
| | B | 46.54 | 8.87 | 0.34 | 1.21 | 0.42 | **979.81** | **36.01** |
| | C | 76.66 | 6.82 | 0.61 | 1.21 | 0.73 | **1720.88** | **1.79** |
| | D | 44.86 | 2.15 | 0.33 | 1.21 | 0.40 | **938.67** | **76.17** |
| | E | 53.33 | 9.42 | 0.40 | 1.21 | 0.49 | **1147.05** | **45.18** |
| | F | 40.57 | 10.82 | 0.29 | 1.21 | 0.36 | **832.92** | **68.43** |
| | H | 47.37 | 3.80 | 0.35 | 1.21 | 0.43 | **1000.34** | **48.61** |
| | I | 53.25 | 0.33 | 0.40 | 1.21 | 0.49 | **1145.08** | **106.53** |
| D9-2 | A | 132.29 | 5.31 | 0.77 | 1.22 | 0.94 | **2211.64** | **57.76** |
| | B | 70.99 | 10.96 | 0.41 | 1.22 | 0.50 | **1178.55** | **120.60** |
| | C | 116.84 | 2.86 | 0.68 | 1.22 | 0.82 | **1930.38** | **29.81** |
| | D | 65.22 | 2.73 | 0.37 | 1.22 | 0.46 | **1070.00** | **28.26** |
| | E | 86.23 | 2.42 | 0.49 | 1.22 | 0.60 | **1407.57** | **24.64** |
| | F | 62.29 | 2.52 | 0.35 | 1.22 | 0.43 | **1010.13** | **25.58** |
| | H | 75.30 | 5.34 | 0.43 | 1.22 | 0.52 | **1214.87** | **56.13** |
| | I | 75.33 | 2.83 | 0.42 | 1.22 | 0.52 | **1208.49** | **28.71** |
| D9-3 | A | 17.58 | 0.60 | 0.04 | 1.14 | 0.05 | **109.45** | **11.59** |
| | B | 8.93 | 1.02 | 0.02 | 1.14 | 0.03 | **61.35** | **13.41** |
| | C | 15.20 | 3.03 | 0.04 | 1.14 | 0.04 | **96.21** | **21.98** |
| | D | 7.35 | 0.77 | 0.02 | 1.14 | 0.02 | **52.59** | **12.33** |
| | E | 10.35 | 1.52 | 0.03 | 1.14 | 0.03 | **69.26** | **15.54** |
| | F | 7.05 | 0.91 | 0.02 | 1.14 | 0.02 | **50.90** | **12.94** |
| | G | 15.18 | 0.97 | 0.04 | 1.14 | 0.04 | **96.09** | **13.19** |
| | H | 8.36 | 0.87 | 0.02 | 1.14 | 0.02 | **58.19** | **12.75** |
| | I | 7.68 | 2.02 | 0.02 | 1.14 | 0.02 | **54.41** | **17.69** |

**Table 4.23: Continued**

| PD | Section | TL response, y [nC] | Standard Deviation [nC] | Dose conversion from calibration curve, M [Gy] | Fading calibration factor at 296 days, $f_{fad}$ | Absorbed dose, D [Gy] | Dose rate [µGy/day] | Standard Deviation [µGy/day] |
|---|---|---|---|---|---|---|---|---|
| TLD-100 | A | 3022.01 | 98.52 | 0.63 | 1.13 | 0.72 | **1674.66** | **208.25** |
| | B | 1994.07 | 35.51 | 0.45 | 1.13 | 0.50 | **1178.98** | **184.36** |
| | C | 2936.34 | 65.86 | 0.62 | 1.13 | 0.70 | **1633.35** | **195.87** |
| | D | 1651.76 | 37.00 | 0.38 | 1.13 | 0.43 | **1013.91** | **184.93** |
| | E | 2208.71 | 45.18 | 0.49 | 1.13 | 0.55 | **1282.48** | **188.03** |
| | F | 1903.33 | 368.15 | 0.43 | 1.13 | 0.48 | **1135.23** | **310.44** |
| | H | 1836.17 | 46.94 | 0.42 | 1.13 | 0.47 | **1102.84** | **188.69** |
| | I | 1862.61 | 100.60 | 0.42 | 1.13 | 0.48 | **1115.59** | **209.04** |
| TLD-600 | A | 2908.33 | 56.20 | 0.56 | 1.10 | 0.62 | **1455.98** | **20.90** |
| | B | 2083.03 | 583.49 | 0.40 | 1.10 | 0.44 | **1042.05** | **237.56** |
| | C | 2855.42 | 105.72 | 0.55 | 1.10 | 0.61 | **1429.44** | **41.25** |
| | D | 1505.04 | 13.28 | 0.29 | 1.10 | 0.32 | **752.17** | **3.26** |
| | E | 2004.59 | 54.62 | 0.39 | 1.10 | 0.43 | **1002.71** | **20.25** |
| | F | 1573.02 | 180.04 | 0.30 | 1.10 | 0.34 | **786.26** | **71.78** |
| | H | 2003.99 | 377.06 | 0.39 | 1.10 | 0.43 | **1002.41** | **152.74** |
| | I | 2207.80 | 467.09 | 0.43 | 1.10 | 0.47 | **1104.63** | **189.73** |
| TLD-700 | A | 2562.27 | 36.68 | 0.58 | 1.08 | 0.62 | **1461.32** | **127.26** |
| | B | 1625.33 | 11.72 | 0.39 | 1.08 | 0.42 | **974.01** | **116.08** |
| | C | 2571.05 | 141.46 | 0.58 | 1.08 | 0.63 | **1465.89** | **174.21** |
| | D | 1664.57 | 364.61 | 0.39 | 1.08 | 0.42 | **994.41** | **274.19** |
| | E | 1807.41 | 56.51 | 0.42 | 1.08 | 0.46 | **1068.71** | **136.14** |
| | F | 1986.49 | 498.00 | 0.46 | 1.08 | 0.50 | **1161.85** | **333.97** |
| | H | 1632.17 | 23.80 | 0.39 | 1.08 | 0.42 | **977.56** | **121.49** |
| | I | 1529.01 | 56.58 | 0.37 | 1.08 | 0.39 | **923.91** | **136.18** |

The uncertainty budget is generally based on Ahmad Fadzil (2020) focusing on Type A uncertainty due to variation in measured results. This is due to limitations where the actual source of exposure is unknown.

The uncertainties of the mean reading of space exposed PD ($u(R)$) is determined using Equation 4.12 (Hultqvist, 2006). Here, $\sigma_i$ is the standard deviation of the PD for the *i*th section ($\sigma_A, \sigma_B \ldots\ldots \sigma_I$). *l* is the total number of sections and *n* is the number of PD.

$$u(R) = \frac{\sum_i \sigma_i}{l\sqrt{n}} \qquad 4.12$$

The uncertainty due to fading correction ($u(f_{fad})$ ) is shown in Equation 4.13 where $y_{i(measured)}$ is the measured fading ratio while $y_{i(calculated)}$ is the calculated fading ratio from the trendline equations in Figure 4.54 (JCGM 100, 2008). *N* is the total number of dosimeters used for the measurements. JCGM 100 (2008) notes that individual observations ($y_{i(measured)}$ differ in value because of random variations in the influence quantities of random effects. The random error is presumed to arise from unpredictable or stochastic temporal and spatial variations of influence quantities (JCGM 100, 2008).

$$u(f_{fad}) = \frac{1}{N-2}\sum_{i=1}^{N} y_{i(measured)} - y_{i(calculated)} \qquad 4.13$$

The combined uncertainty is calculated using Equation 4.14 based on Ahmad Fadzil (2020).

$$u_c(D) = \sqrt{u(R)^2 + u(fad)^2} \qquad 4.14$$

The expanded uncertainty is calculated using Equation 4.15 where $k_p$ is the coverage factor having a level confidence of $p$ (JCGM 100, 2008; Ahmad Fadzil, 2020). $k_p$ = 1 have a confidence level of 68%, $k_p = 2$ have a confidence level of 95% and $k_p = 3$ have a confidence level of 99% (Bell, 2001).

$$U_p = k_p u_c(D) \qquad 4.15$$

Table 4.24 gathered the uncertainties of each PD. In combined uncertainty for CUSOF, the $u(R)$ and $u(f_{fad})$ are similar for D9-1 and D9-2 but for D9-3 $u(R)$ is the main contributor of uncertainty. Meanwhile, for TLD, both TLD100 and TLD700 are similar in the uncertainties with $u(f_{fad})$ being the major contributor. TLD600 had the largest $u(R)$ at 0.053.

**Table 4.24: Uncertainties of each PD**

| PD | $u(R)$ | $u(f_{fad})$ | $u_c(D)$ | $U_p\ (k_p = 1)$ | $U_p\ (k_p = 2)$ | $U_p\ (k_p = 3)$ |
|---|---|---|---|---|---|---|
| D9-1 | 0.009 | 0.008 | 0.012 | 0.012 | 0.025 | 0.037 |
| D9-2 | 0.009 | 0.010 | 0.014 | 0.014 | 0.027 | 0.041 |
| D9-3 | 0.014 | 0.007 | 0.015 | 0.015 | 0.030 | 0.046 |
| TLD100 | 0.006 | 0.016 | 0.017 | 0.017 | 0.034 | 0.051 |
| TLD600 | 0.053 | 0.006 | 0.054 | 0.054 | 0.107 | 0.161 |
| TLD700 | 0.005 | 0.014 | 0.015 | 0.015 | 0.030 | 0.045 |

## 4.14 Summary

Overall, in this chapter, initially the calculated filtered energies of each radiated was presented.

The structural test results for analysis of the effect of spacecraft vibrations on the hardware were presented too. From the aftermath of the test, the hardware survived without any scratch. Structural load tests were also conducted on the hardware where the bottom and the sides of the hardware provided with positive outcomes. Only parts of the top of the hardware show some unwanted failure with a load of under SF = 2.0 for Tip 1 but still exceeding the working load during failure. From assessment by JAXA, the hardware was deemed to be suitable for space exposure outside of Kibo.

On the other hand, CUSOF were fabricated and exposed to beta ($^{90}$Sr), neutron-gamma ($^{241}$AmBe), and low dose gamma ($^{137}$Cs) during the PADCIOF designing stage to elucidate the responses of the CUSOF irradiated to various types of radiations due to multiple types of radiations that exist in space. Screened PD were sent for space exposure and the resulting responses were calibrated using proton as the largest constituents of space radiation at lower LEO.

# CHAPTER 5

# CONCLUSION AND FUTURE WORKS

## 5.1 Conclusion

Overall, to employ the PD, namely CUSOF to monitor the space radiation at LEO altitude has resulted in the development of casing carrying the PD that can survive the harsh conditions of LEO with an exposure of up to 427 days. While there are some radiation monitoring missions employed in LEO, there is no standardisation on method of exposure in LEO. Current work provides a space radiation monitoring method that employ a water equivalent casing with the inclusion of filters to estimate the existing radiation energies in LEO. While the external hardware (namely the case main body and case cover) should be changed for each mission due to LEO environment (AO erosion, UV irradiation, etc), some of the internal parts like the filters, mesh, dosimeter holders and the PD itself can be reused for repeated exposure. Same exposure method can be employed with rearrangement of the internal parts.

An iterative development method was used to develop the casing for the exposure of CUSOF. This development procedure involved the contributions of experts in different fields from the perspective of radiation monitoring and space exposure. Requirements collection methods employed were SUI and FGD which guided the final hardware design used for the LEO exposure. From the radiation monitoring perspective, medical physicists, dosimetry experts, photonics and astrophysics experts helped the on the specification of requirements. On the other hand, from the space exposure perspective, apart from the initial member of experts, additionally, JAXA experts on ExHAM, engineers and researchers provided the requirements for the casing development. This iterative requirement specifications and development of the casing of up to the sixth iteration was finally used for the space exposure. From the casing that is exposed to space, there were no internal damage found after the exposure. The only difference, compared to control casing left on Earth is the discoloration due to UV exposure. While no mass or dimension measurement made, it is expected that due to AO erosion, the exposed part of the casing faced a reduction in thickness resulting in mass loss. As such, while the same design can be used, a new hardware should be employed for future works.

To evaluate the developed case for suitability to be employed in LEO via ExHAM utilisation, structural tests were conducted. The random vibration mimics the vibration environment of the launching vehicle while the sine burst test produces the quasi-static load of the ExHAM for attachment and during exposure. While the responses of the casing exceeded the high abort limit of the vibration profile, from JAXA's assessment, since the casing did not produce any damages after conduction the vibration tests, the case was approved for launching. In terms of functionality, the PD is assessed from the preliminary radiation exposure and the post-exposure results. Limitations to assess the functionality exists due to the nature of the PD requiring full dis-assembly of the casing for assessment. The structural load on the casing resulted in an SF of at least 2.00 for Tip 2 at each part where the force is applied. For Tip 1 at the thinnest section of the casing the SF fell under 2.00 at 1.46. Since the value is higher than working load, deformation in terms of piercing without crack propagation, and containment of the PD using mesh, the results were accepted by JAXA for launching. Finally, the workmanship was assessed in which the mass and dimension of each version of the casing was evaluated to be extremely similar with each other, hence the testing on any version of the casing is expected to yield the same results.

In terms of preliminary irradiations, the PD incorporated within the casing were irradiated using low dose of beta minus up to 1000 mGy and mixed neutron-gamma sources. From the responses of the PD, both CUSOF and TLD were highly linear in the doses tested for beta minus where D9-2 and D 9-5 had $R^2 > 0.99$ comparable to the commercial TLD. The fading of CUSOF 429 days after irradiation were comparable to TLD (reading reduced to 86.7-95.4% after initial reading) at TL responses being reduced to 92.2%, 87.7% and 87.8% respective to D9-1, D9-2 and D9-3. For neutron-gamma exposure likewise linearity of the dose responses was maintained at 0 cm from the source. At 15 cm and 30 cm, there were almost no responses as the radiation has been severely attenuated. CUSOF, while being able to detect the low dose neutron-gamma irradiation, were unable to separate the responses contribution due to neutron and gamma unlike the thermal neutron sensitive TLD600 and neutron insensitive TLD700. However, since the TL responses of CUSOF is higher than TLD, it is assumed that neutron also contributed to the TL responses. Overall, from the irradiations of PD with beta minus and neutron-gamma sources, it is established that CUSOF is suitable for low dos radiation detection which is attributed to the environmental radiation at LEO. The correlated absorbed doses detected were up to 2212 μGy/day by D9-2 which is comparable to TLD100 at 1675 μGy/day. The differences in the dose correlation are attributed to correction factors that are not considered in this study. The uncertainty budget considered in this study is due to the uncertainty of the mean reading of the PD for space exposed samples and the uncertainty of the fading after exposure. The extended uncertainties of CUSOF with

99% confidence level is slightly lower than TLD100 (0.051) with 0.0037, 0.041 and 0.046 respective to D9-1, D9-2 and D9-3.

## 5.2 Recommendation for Future Work

While the casing developed in this work has been proven to be able to survive LEO exposure, in terms of design, it can still be improved. For radiation exposure, changes can be made by employing different configuration of the filters. In the current work, the thickest employed filter is 13 mm for Al and PE. W is a better attenuator for photon, proton, and electron than Al. If W with a thickness of 13 mm is employed, wider range of energies can be excluded, and K-edge of the material (occurring at around 70 keV from 2.7-12 mm) can be avoided meaning that all energies below 70 keV is at least 95% attenuated. However, since the density of W is high where the mass of the filter at 13 mm will be 157 g, additional consideration should be given. Higher mass might be allowed but there is a possibility for higher cost alongside the increment of mass.

The design of the developed casing influences the resulting structural tests. The vibration properties of the developed case can be improved to reduce the resonance amplitude and resonance frequency range. To reduce the resonance amplitude, considerations can be made by increasing the natural frequency outside of the test range. This requires materials consideration as the natural frequency is based on the stiffness and mass of the material. Stiffer material with lower density will increase the natural frequency. Another consideration can be made by changing the vibration mode shape by constraining the cover by increasing the number of screws or changing the geometry of the cover. Additionally, the placement of the accelerometer should be considered. In this work, the accelerometer was placed in the middle of the casing to observe the general vibration responses of the casing during random vibration and sine burst test. In hindsight, the amplitude of the z-axis responses was amplified significantly due to the part having the lowest thickness and the accelerometer mass further contributes to the responses. This can be rectified in the future by placing the accelerometer on the part of the casing that is the stiffest or generally with the highest thickness. Another method to verify the most suitable accelerometer placement is by conducting multiple tests with variations in accelerometer locations. This would also produce observations on multiple parts of the casing providing a better understanding on the effects of the vibrations on the case. Lastly, vibrations can be damped by introducing a vibration isolator to reduce the amplitude of the resonance. In terms of structural load, improvement for higher load being sustained before failure can be made by increasing the thickness. However, an increment in thickness means that the configuration within the casing needs to be considered. This also contradicts the space radiation exposure requirement where the lowest thickness is required at the radiation direction. As such, to determine the best suitable thickness that incorporate the consideration of SF and attenuation of radiation, a new iteration of development can be considered.

In terms of CUSOF, discrepancies in detection were seen due to the inadequacy of correction factors. In this work, the absorbed dose conversion was conducted using proton of 150 MeV. The correction factor considered was using fading correction factor only. Nagamatsu et al. (2006) calibrated the developed TLD using various types of radiation to consider the Linear Energy Transfer (LET) of the radiation as the energy rang in space is wide to higher than $10^{11}$ GeV. The author calibrated the TLD by using gamma. Proton and HZE ions up to iron. As such, for future work, as this will require collaboration with international bodies as in Malaysia there is no HZE ion facilities. In fact, there is no proton centre in Malaysia as the proton irradiation in this work was conducted at the Hyogo Ion Beam Center. Further considerations in the method to calibrate the space exposed sample will improve the precision of the dose detection.

## REFERENCES


AbuAlRoos, N. J., Amin, N. A. B., & Zainon, R. (2019). Conventional and new lead-free radiation shielding materials for radiation protection in nuclear medicine: A review. *Radiation Physics and Chemistry*, 165, 108439.

Ahmad Fadzil, M. S. (2020). *Use of fabricated germanium-doped optical fibres for radiotherapy postal dose audit of megavoltage photon beams under non-reference conditions in selected Malaysian radiotherapy facilities* (Doctoral dissertation). Universiti Putra Malaysia.

Air Force Space Command. (2014). *Test requirements for launch, upper-stage and space vehicles*. Space and Missile System Standard SMC-S-016.

Anderson, P. C., Rich, F. J., & Borisov, S. (2018). Mapping the South Atlantic Anomaly continuously over 27 years. *Journal of Atmospheric and Solar-Terrestrial Physics*, 177, 237-246.

Aramrun, P., Beresford, N. A., & Wood, M. D. (2018). Selecting passive dosimetry technologies for measuring the external dose of terrestrial wildlife. *Journal of Environmental Radioactivity*, 182, 128-137.

Attix, F. H. (2008). *Introduction to radiological physics and radiation dosimetry*. John Wiley & Sons.

Aziz, M. A. B., Rahman, M. F., & Prodhan, M. M. H. (2018). Comparison of lead, copper and aluminium as gamma radiation shielding material through experimental measurements and simulation using MCNP version 4c. *International Journal of Contemporary Research and Review*, 9(8), 20193-20206.

Bell, L. T. (2023). Dipole Resonances in the Well-Deformed Even-even Samarium (152,154 Sm) Isotopes (Master's thesis).

Benabdesselam, M., Mady, F., Cieslikiewicz-Bouet, M., Blanc, W., El Hamzaoui, H., Cassez, A., ... & Capoen, B. (2023). Ge-doped optical fibers for passive and active radiation detection modes. IEEE Sensors Journal, 23(7), 6948-6955.

Begum, M., Rahman, A. M., Abdul-Rashid, H. A., Yusoff, Z., Begum, M., Mat-Sharif, K. A., ... & Bradley, D. A. (2015). Thermoluminescence characteristics of Ge-doped optical fibers with different dimensions for radiation dosimetry. *Applied Radiation and Isotopes*, 100, 79-83.

Bell, S. A. (2001). A beginner's guide to uncertainty of measurement.

Berger, T., Bilski, P., Hajek, M., Puchalska, M., & Reitz, G. (2013). The MATROSHKA experiment: results and comparison from extravehicular activity (MTR-1) and intravehicular activity (MTR-2A/2B) exposure. *Radiation Research*, 180(6), 622-637.

Berger, T., Hajek, M., Bilski, P., & Reitz, G. (2015). Cosmic radiation exposure of biological test systems during the EXPOSE-R mission. *International Journal of Astrobiology*, 14(1), 27-32.

Birnbacher, L., Willner, M., Marschner, M., Pfeiffer, D., Pfeiffer, F., & Herzen, J. (2018). Accurate effective atomic number determination with polychromatic grating-based phase-contrast computed tomography. *Optics express*, 26(12), 15153-15166.

Blakstad, K. J., & Tingsborg, O. (2023). The Iterative Development Method: Its aspects and effect on innovation within new product development.

Blasi, P. (2013). The origin of galactic cosmic rays. *The Astronomy and Astrophysics Review*, 21, 1-73.

Bos, A. J. (2006). Theory of thermoluminescence. *Radiation measurements*, 41, S45-S56.

Bradley, D. A., Shafiqah, A. S., Rozaila, Z. S., Sabtu, S. N., Sani, S. A., Alanazi, A. H., ... & Alzimami, K. (2017). Developments in production of silica-based thermoluminescence dosimeters. Radiation Physics and Chemistry, 137, 37-44.

Brown, M., Korte, M., Holme, R., Wardinski, I., & Gunnarson, S. (2018). Earth's magnetic field is probably not reversing. *Proceedings of the National Academy of Sciences*, 115(20), 5111-5116.

Casolaro, P., Campajola, L., Breglio, G., Buontempo, S., Consales, M., Cusano, A., Cutolo, A., Di Capua, F., Fienga, F. and Vaiano, P. (2019). Real-time dosimetry with radiochromic films. *Scientific reports*, 9(1), 5307.

Castillo, F., Espinosa, G., Golzarri, J. I., Osorio, D., Rangel, J., Reyes, P. G., & Herrera, J. J. E. (2013). Fast neutron dosimetry using CR-39 track detectors with polyethylene as radiator. Radiation Measurements, 50, 71-73.

Garcia, M. (2024). *NASA Collins xEVAS Update.* Retrieved from https://blogs.nasa.gov/spacestation/tag/xevas/

CERN. (2024). *What is the difference between an active and a passive dosimeter?* Retrieved from https://dosimetry.web.cern.ch/faqs/what-difference-between-active-and-passive-dosimeter

Chancellor, J. C., Scott, G. B., & Sutton, J. P. (2014). Space radiation: the number one risk to astronaut health beyond low earth orbit. *Life*, 4(3), 491-510.

Cheraghi, E., Shaaer, A., Chen, S., Osei, E., & Yeow, J. T. (2023). Enhanced electron radiation shielding composite developed by well dispersed fillers in PDMS polymer. *Radiation Physics and Chemistry*, 211, 110994.

Clagett, C., Santos, L., Azimi, B., Cudmore, A., Marshall, J., Starin, S., ... & Rodriquez, M. (2017). Dellingr: NASA Goddard Space Flight Center's first 6U spacecraft.

Cooper, R. G., & Sommer, A. F. (2016). Agile-Stage-Gate: New idea-to-launch method for manufactured new products is faster, more responsive. *Industrial Marketing Management,* 59, 167-180.

Cote, T., Spicer, R. L., Kearns, A., Do, N., & Soliman, H. E. (2020). Development and test of an additively manufactured ESPA class satellite. In *AIAA Scitech 2020 Forum* (p. 1668).

Cucinotta, F. A., Wang, H., & Huff, J. L. (2009). Risk of acute or late central nervous system effects from radiation exposure. *Human Health and Performance Risks of Space Exploration Missions: Evidence Reviewed by the NASA Human Research Program, 191*, 212.

De Groh, K. K., & Banks, B. A. (2019). Atomic oxygen erosion data from the MISSE 2-8 missions (No. NASA/TM—2019-219982).

De Groh, K., Banks, B. A., McCarthy, C. E., Rucker, R. N., Roberts, L. M., & Berger, L. A. (2006, November). MISSE PEACE Polymers Atomic Oxygen Erosion Results. In *2006 MISSE Post-Retrieval Conference* (No. NASA/TM-2006-214482).

Department of Defense Test Method Standard. (2008). *Environmental Engineering Considerations and Laboratory Tests (MIL-STD-810G)*. U. S. Department of Defense.

Dhanumalayan, E., & Joshi, G. M. (2018). Performance properties and applications of polytetrafluoroethylene (PTFE)—a review. *Advanced Composites and Hybrid Materials*, 1, 247-268.

DiPaolo, A. J. (2014). The definition and delimitation of outer space: The present need to determine where "space activities" begin. *Annals of Air & Space Law,* 39.

El Abd, A. A., & Elkady, A. S. (2014). A method for simultaneous determination of effective removal cross-section for fast neutrons and mass absorption coefficient for gamma rays. *Materials Science and Engineering*, 2(2), 1-6.

Elburn, D. (2021). LEO Economy. NASA. https://www.nasa.gov/leo-economy/faqs

El Ghazaly, M., & Hassan, N. M. (2018). Characterization of saturation of CR-39 detector at high alpha-particle fluence. Nuclear Engineering and Technology, 50(3), 432-438.

Enginess. (2021). What is iterative design? (And why you should use it). https://www.enginess.io/insights/what-is-iterative-design

ESA. (2020). Types of orbit. https://www.esa.int/Enabling_Support/Space_Transportation/Types_of_orbits

Fadzil, M. S. A. (2020). Use of fabricated germanium-doped optical fibres for radiotherapy postal dose audit of megavoltage photon beams under non-reference conditions in selected Malaysian radiotherapy facilities [Doctoral dissertation, Universiti Putra Malaysia].

Fadzil, M. S. A., Noor, N. M., Min, U. N., Abdullah, N., Dolah, M. T., Pawanchek, M., & Bradley, D. A. (2022). Dosimetry audit for megavoltage photon beams applied in non-reference conditions. *Physica Medica*, *100*, 99-104.

Fadzil, M. S. A., Noor, N. M., Min, U. N., Abdullah, N., Dolah, M. T., Pawanchek, M., & Bradley, D. A. (2022). Dosimetry audit for megavoltage photon beams applied in non-reference conditions. Physica Medica, 100, 99-104.

Furetta, C. (2010). Handbook of thermoluminescence. World Scientific.

Furukawa, S., Nagamatsu, A., Nenoi, M., Fujimori, A., Kakinuma, S., Katsube, T., Wang, B., Tsuruoka, C., Shirai, T., Nakamura, A.J. and Sakaue-Sawano, A. (2020). *Space radiation biology for "Living in Space"*. BioMed Research International. 4703286.

GafchromicTM Dosimetry tools. (2023). http://www.gafchromic.com/documents/PC-11802_Gafchromic_EBT3.pdf

García-Sánchez, E. R., Vargas-Martínez, H. S., Candia-García, F., & Contreras-Lima, J. (2024). Agile Stage-Gate approach for design, integration, and testing of a 1U CubeSat. Aerospace, 11(4), 324.

German, U., & Weinstein, M. (2002). Non-radiation induced signals in TL dosimetry. Radiation Protection Dosimetry, 101(1-4), 81-84.

Ghomeishi, M., Mahdiraji, G. A., Adikan, F. M., Ung, N. M., & Bradley, D. A. (2015). Sensitive fibre-based thermoluminescence detectors for high resolution in-vivo dosimetry. Scientific Reports, 5(1), 13309.

Goddard Technical Standard. (2021). General Environmental Verification Standard (GEVS) for GSFC Flight Programs and Projects (GSFC-STD-7000B). NASA. https://standards.nasa.gov/

Greene, J. P. (2021). Microstructures of polymers. In Automotive Plastics and Composites (pp. 27-37).

Hashim, S., Ibrahim, S. A., Che Omar, S. S., Alajerami, Y. S. M., Saripan, M. I., Noor, N. M., Ung, N. M., Mahdiraji, G. A., Bradley, D. A., & Alzimami, K. (2014). Photon irradiation response of photonic crystal fibres and flat fibres at radiation therapy doses. *Applied Radiation and Isotopes, 90,* 258-260.

Hassan, M. F., Rahman, W. N. W. A., Akagi, T., Sulaiman, N. S., Bradley, D. A., & Noor, N. M. (2023). Thermoluminescence kinetic parameters of proton-irradiated germanium doped flat-shape optical fibres. *Radiation Physics and Chemistry, 202*, 110521.

Hassan, M. F., Rahman, W. N. W. A., Kadir, A. B. A., Isa, N. M., Tominaga, T., Geso, M., Akasaka, H., Bradley, D. A., & Noor, N. M. (2018, December). Fabricated Ge-doped flat optical fibres: Assessing the thermoluminescence glow curves for proton beam irradiation. In *AIP Conference Proceedings* (Vol. 2045, No. 1, p. 020084). AIP Publishing LLC.

Hassan, M. F., Rahman, W. N. W. A., Tominaga, T., Geso, M., Akasaka, H., Bradley, D. A., & Noor, N. M. (2019). Ge-doped silica fibre for proton beam dosimetry. *Radiation Physics and Chemistry, 165*, 108390.

Hopkins, A. R., Labatete-Goeppinger, A. C., Kim, H., & Katzman, H. A. (2016). Space survivability of carbon nanotube yarn material in low Earth orbit. *Carbon*, 107, 77-86.

Howell, E. (2023). International Space Station — Everything you need to know. https://www.space.com/16748-international-space-station.html

Hubbell, J. H., & Seltzer, S. M. (1995). Tables of X-ray mass attenuation coefficients and mass energy-absorption coefficients 1 keV to 20 MeV for elements Z= 1 to 92 and 48 additional substances of dosimetric interest (No. PB-95-220539/XAB; NISTIR-5632). National Institute of Standards and Technology, Gaithersburg, MD (United States), Ionizing Radiation Division.

Hultqvist, M. (2006). Analysis of the uncertainties in the IAEA/WHO TLD postal dose audit programme (Master's thesis). Stockholm University.

Ibrahim, S. A., Omar, S. C., Hashim, S., Mahdiraji, G. A., Bradley, D. A., Kadir, A. B., & Isa, N. M. (2014, November). Assessment of Ge-doped optical fibres subjected to x-ray irradiation. In *Journal of Physics: Conference Series* (Vol. 546, No. 1, p. 012017). IOP Publishing.

Irvine, T. (2009). *An introduction to the vibration response spectrum* (Revision D). Vibrationdata.

Jafferson, J. M., & Chatterjee, D. (2021). A review on polymeric materials in additive manufacturing. *Materials Today: Proceedings, 46*, 1349-1365.

JAXA. (2008). Japanese Experiment Module Remote Manipulator System. https://iss.jaxa.jp/en/kibo/about/kibo/rms/

JAXA. (2015). Free-Space PADLES. https://iss.jaxa.jp/en/kiboexp/pm/padles/free-space-padles/

JAXA. (2018). Exposed Experiment Handrail Attachment Mechanism (ExHAM). https://iss.jaxa.jp/en/kiboexp/ef/exham/

JCGM 100. (2008). Guide to the expression of uncertainty in measurement, JCGM 100: 2008, GUM 1995 with minor corrections. International Organization for Standardization Geneva ISBN.

Kawaguchi, Y., Yokobori, S. I., Hashimoto, H., Yano, H., Tabata, M., Kawai, H., & Yamagishi, A. (2016). Investigation of the interplanetary transfer of microbes in the Tanpopo mission at the exposed facility of the international space station. *Astrobiology*, 16(5), 363-376.

Kim, J. H., Jang, J. I., & Park, S. H. (2019). Vibration Analysis of a Nanosatellite for Microgravity Science Missions. *Journal of the Korean Society of Manufacturing Process Engineers, 18*(12), 104-110.

Kloprogge, T., & Wood, B. (2020). *Handbook of Mineral Spectroscopy Volume 1 X-ray Photoelectron Spectra*.

Kocharov, L., Omodei, N., Mishev, A., Pesce-Rollins, M., Longo, F., Yu, S., Gary, D.E., Vainio, R. and Usoskin, I. (2021). Multiple sources of solar high-energy protons. *The Astrophysical Journal*, 915(1), 12.

Kodaira, S., Naito, M., Uchihori, Y., Hashimoto, H., Yano, H., & Yamagishi, A. (2021). Space radiation dosimetry at the exposure facility of the International Space Station for the Tanpopo mission. *Astrobiology*, *21*(12), 1473-1478.

Kress, B. T., Rodriguez, J. V., & Onsager, T. G. (2020). The GOES-R space environment in situ suite (SEISS): Measurement of energetic particles in geospace. In *The GOES-R Series* (pp. 243-250). Elsevier.

Kua, J., Loke, S. W., Arora, C., Fernando, N., & Ranaweera, C. (2021). Internet of things in space: a review of opportunities and challenges from satellite-aided computing to digitally-enhanced space living. *Sensors*, 21(23), 8117.

Kurudirek, M. (2014). Effective atomic numbers, water and tissue equivalence properties of human tissues, tissue equivalents and dosimetric materials for total electron interaction in the energy region 10 keV–1 GeV. Applied radiation and Isotopes, 94, 1-7.

Lam, S. E., Bradley, D. A., Mahmud, R., Pawanchek, M., Rashid, H. A., & Noor, N. M. (2019). Dosimetric characteristics of fabricated Ge-doped silica optical fibre for small-field dosimetry. *Results in Physics*, *12*, 816-826.

Landauer. (2024). Luxel+® & Neutrak®: High performance integrated neutron dosimeter. Retrieved from https://www.landauer.co.uk/produit/luxel-neutrak-high-performance-integrated-neutron-dosimeter/

Lee, J. H., Kim, H. N., Jeong, H. Y., & Cho, S. O. (2020a). Optimization of shielding to reduce cosmic radiation damage to packaged semiconductors during air transport using Monte Carlo simulation. *Nuclear Engineering and Technology*, *52*(8), 1817-1825.

Lee, J., Nishiyama, J., Hori, J. I., Kimura, R., Sako, T., Yamada, A., & Sano, T. (2020b). Neutron total cross section measurements of polyethylene using time-of-flight method at KURNS-LINAC. *Journal of Nuclear Science and Technology*, *57*(1), 1-8.

Lei, X. F., Chen, Y., Zhang, H. P., Li, X. J., Yao, P., & Zhang, Q. Y. (2013). Space survivable polyimides with excellent optical transparency and self-healing properties derived from hyperbranched polysiloxane. *ACS Applied Materials & Interfaces*, 5(20), 10207-10220.

Liu, J., Mo, Y., Wang, S., Ren, S., Han, D., Xiao, M., ... & Meng, Y. (2019). Ultrastrong and heat-resistant poly (ether ether ketone) separator for dendrite-proof and heat-resistant lithium-ion batteries. *ACS Applied Energy Materials*, *2*(5), 3886-3895.

Liu, T., Sun, Q., Meng, J., Pan, Z., & Tang, Y. (2016). Degradation modeling of satellite thermal control coatings in a low earth orbit environment. *Solar Energy,* 139, 467-474.

Lu, Y., Shao, Q., Yue, H., & Yang, F. (2019). A review of the space environment effects on spacecraft in different orbits. *IEEE Access, 7*, 93473-93488.

Manjunatha, H.C., & Rudraswamy, B. (2013). Study of effective atomic number and electron density for tissues from human organs in the energy range of 1 keV–100 GeV. *Health Physics, 104*(2), 158-162.

Mariano, M. G., Morsch, F. E., Vega, M. S., Oriel, S. L., Kessler, S. L., & Augusto, B. E. (2020). Qualification and validation test methodology of the open-source CubeSat FloripaSat-I. *Journal of Systems Engineering and Electronics*, 31(6), 1230-1244.

Mat Nawi, S.N.B., Wahib, N.F.B., Zulkepely, N.N.B., Amin, Y.B.M., Min, U.N., Bradley, D.A., Md Nor, R.B. and Maah, M.J. (2015). The thermoluminescence response of Ge-doped flat fibers to gamma radiation. *Sensors*, 15(8), 20557-20569.

McAlister, D. R. (2016). Neutron shielding materials. PG Research Foundation.

McDowell, J. C. (2018). The edge of space: Revisiting the Karman Line. *Acta Astronautica*, 151, 668-677.

McDowell, J. C. (2020). The low earth orbit satellite population and impacts of the SpaceX Starlink constellation. *The Astrophysical Journal Letters,* 892(2), L36.

McNulty, P. J., Poole, K. F., & Poole, J. O. (2022). DIME-2 flown as part of NASA's SET-1 on the DSX satellite. *IEEE Transactions on Nuclear Science*, 69(5), 1072-1078.

Mohd Noor, N., Hussein, M., Kadni, T., Bradley, D. A., & Nisbet, A. (2014). Characteristics of Ge-doped optical fibres for MV radiotherapy dosimetry. *Radiation Physics and Chemistry, 98*, 33-41.

Mohd Noor, N., Shukor, N. A., Hussein, M., Nisbet, A., & Bradley, D. A. (2012). Comparison of the TL fading characteristics of Ge-doped optical fibres and LiF dosimeters. *Applied Radiation and Isotopes, 70*, 1384-1387.

Motcheyo, A. T., & Macías-Díaz, J. E. (2020). Energy transmission in the forbidden band-gap of a nonlinear chain with global interactions. *Journal of Physics A: Mathematical and Theoretical, 53*(50), 505701

Muhsin, S. A., Hatton, P. V., Johnson, A., Sereno, N., & Wood, D. J. (2019). Determination of Polyetheretherketone (PEEK) mechanical properties as a denture material. *The Saudi Dental Journal, 31*(3), 382-391.

Munson, C. A., Gottfried, J. L., De Lucia Jr, F. C., McNesby, K. L., & Miziolek, A. W. (2007). Laser-based detection methods of explosives. In Jehuda Yinon

(Ed.), *Counterterrorist Detection Techniques of Explosives* (pp. 279-321). Elsevier Science BV.

Murtazin, R., & Zaborskaya, E. (2014). ISS maneuvering: 15 years of experience. In *Proceedings of the International Astronautical Congress, IAC* (pp. 3113-3120).

Mustafa, S., Saad, F. F. A., Tamchek, N., Mohamed, F., Bajuri, F., & Noor, N. M. (2018). Response of fabricated germanium optical fibre subjected to low dose neutron-gamma irradiation. *International Journal of Nanoelectronics and Materials,* 11, 253-260.

Nagamatsu, A., Masukawa, M., & Kamigaichi, S. (2006). *Development of the space radiation dosimetry system'PADLES'* (No. KEK-PROC--2006-7).

Nagamatsu, A., Murakami, K., Kitajo, K., Shimada, K., Kumagai, H., & Tawara, H. (2013). Area radiation monitoring on ISS Increments 17 to 22 using PADLES in the Japanese Experiment Module Kibo. *Radiation Measurements, 59,* 84-93.

Nakamura, H., Nakamura, T., Noguchi, T., & Imagawa, K. (2006). Photodegradation of PEEK sheets under tensile stress. *Polymer Degradation and Stability, 91*(4), 740-746.

Nakamura, T., Nakamura, H., & Shimamura, H. (2009, January). Effects of LEO environment on tensile properties of PEEK films. In *AIP Conference Proceedings* (Vol. 1087, No. 1, pp. 127-136). American Institute of Physics.

NASA Technical Standard. (1996). *Structural Design and Test Factors of Safety for Spaceflight Hardware* (NASA-STD-5001). NASA. https://standards.nasa.gov/

NASA Technical Standard. (2017). *Payload Vibroacoustic Test Criteria* (NASA-STD-7001B). NASA. https://standards.nasa.gov/

NASA. (1999). *Sine-Burst Load Test*. https://llis.nasa.gov/lesson/730

NASA. (2015). *Best Practices for Use of Sine Burst Testing*. https://www.nasa.gov/wp-content/uploads/2015/04/nesc-tb-15-02-best-practices-for-use-of-sine-burst-testing.pdf?emrc=e1924f#:~:text=Sine%20Burst%20(SB)%20Testing%20is,the%20shaker%20for%20other%20tests.

Navarro, M., Gussy, J., Pack, D., Rowen, D., & Salvaggio, D. (2020). Building satellites in 18 months: lessons learned from the rogue alpha/beta CubeSats.

Nielsen, K. B. (2023). The risø TL/OSL reader - DTU physics. Retrieved from https://www.fysik.dtu.dk/english/research/radphys/research/radiation-instruments/tl_osl_reader

Nishizuka, N., Sugiura, K., Kubo, Y., Den, M., & Ishii, M. (2018). Deep flare net (DeFN) model for solar flare prediction. *The Astrophysical Journal,* 858(2), 113.

NIST. (2023). *Appendix: Significance of Calculated Quantities*. https://physics.nist.gov/PhysRefData/Star/Text/appendix.html#:~:text=CSDA%20range%3A%20a%20very%20close,to%20the%20total%20stopping%20power.

NNDC. (2023). *Evaluated Nuclear Data File (ENDF) Retrieval & Plotting*. https://www.nndc.bnl.gov/sigma/index.jsp

Noor, N. M. (2012). *The use of Ge-doped optical fibres in external beam radiotherapy dosimetry* (Doctoral dissertation, University of Surrey).

Noor, N. M., Fadzil, M. A., Ung, N. M., Maah, M. J., Mahdiraji, G. A., Abdul-Rashid, H. A., & Bradley, D. A. (2016). Radiotherapy dosimetry and the thermoluminescence characteristics of Ge-doped fibres of differing germanium dopant concentration and outer diameter. *Radiation Physics and Chemistry, 126*, 56-61.

Nuclear Power. (2023). *Atomic number density*. https://www.nuclear-power.com/nuclear-power/reactor-physics/nuclear-engineering-fundamentals/neutron-nuclear-reactions/atomic-number-density/

Obodovskiy, I. (2019). *Radiation: fundamentals, applications, risks, and safety*. Elsevier.

Oh, H. U., Kim, T. G., Han, S. H., & Lee, J. (2017). Verification of MEMS fabrication process for the application of MEMS solid propellant thruster arrays in space through launch and on-orbit environment tests. *Acta Astronautica, 131*, 28-35.

Paiva, F., Siqueira, P. T., & Cavalieri, T. A. (2015). Comparing the responses of TLD 100, TLD 600, TLD 700 and TLD 400 in mixed neutron-gamma fields. In *INAC 2015: International Nuclear Atlantic Conference Brazilian Nuclear Program State Policy For A Sustainable World*.

Papaioannou, A., Sandberg, I., Anastasiadis, A., Kouloumvakos, A., Georgoulis, M.K., Tziotziou, K., Tsiropoula, G., Jiggens, P. and Hilgers, A. (2016). Solar flares, coronal mass ejections and solar energetic particle event characteristics. *Journal of Space Weather and Space Climate*, 6, A42.

Parsons, B. J. (2012). Sterilisation of healthcare products by ionising radiation: Principles and standards. In *Sterilisation of Biomaterials and Medical Devices* (pp. 56-70). Woodhead Publishing.

Poole, K. F., McNulty, P. J., & Poole, J. O. (2022). The DIME-1 experiment flown as part of NASA's SET-1 project on the DSX Satellite. *IEEE Transactions on Nuclear Science*, 69(5), 1066-1071.

QB50. (2015). *System Requirements and Recommendations*. Retrieved from https://www.qb50.eu/index.php/tech-docs/category/25-up-to-date-docs?download=89:qb50-docs

Rabbow, E., Rettberg, P., Barczyk, S., Bohmeier, M., Parpart, A., Panitz, C., Horneck, G., Burfeindt, J., Molter, F., Jaramillo, E. and Pereira, C. (2015). The astrobiological mission EXPOSE-R on board of the International Space Station. *International Journal of Astrobiology*, 14(1), 3-16.

Rabbow, E., Rettberg, P., Parpart, A., Panitz, C., Schulte, W., Molter, F., Jaramillo, E., Demets, R., Weiß, P. and Willnecker, R. (2017). EXPOSE-R2: The astrobiological ESA mission on board of the International Space Station. *Frontiers in Microbiology*, *8*, 1533.

Raventos, M., Harti, R. P., Lehmann, E., & Grünzweig, C. (2017). A method for neutron scattering quantification and correction applied to neutron imaging. *Physica Procedia*, *88*, 275-281.

Roberts, K. A. (2018). *Design and Testing of an Additively Manufactured CubeSat Structural Bus* [Doctoral dissertation, Air Force Institute of Technology].

Sarafin, T., Doukas, P., Demchak, L., Browning, M., & Wright, L. (2018). Vibration testing of small satellites: Part 4. Instar Engineering and Consulting, Inc.

Sathish, K. V., Sowmya, N., Munirathnam, R., Manjunatha, H. C., Seenappa, L., & Sridhar, K. N. (2023). Radiation shielding properties of aluminium alloys. *Radiation Effects and Defects in Solids*, 178(9-10), 1301-1320.

Savage, P. (1996, April). User interface evaluation in an iterative design process: A comparison of three techniques. In Conference Companion on Human Factors in Computing Systems (pp. 307-308).

Scialdone, J. J. (1998, October). Spacecraft compartment venting. In *Optical Systems Contamination and Degradation* (Vol. 3427, pp. 23-27). SPIE.

Schulz, M., Lehmann, E., & Losko, A. (2024). Neutron imaging. In Non-Destructive Material Characterization Methods (pp. 205-247). Elsevier.

Seedhouse, E. (2018). *Space radiation and astronaut safety*. Cham, Switzerland: Springer International Publishing.

Share, G. H., Murphy, R. J., Tylka, A. J., Kozlovsky, B., Ryan, J. M., & Gwon, C. (2011). Physics of solar neutron production: Questionable detection of neutrons from the 31 December 2007 flare. *Journal of Geophysical Research: Space Physics*, *116*(A3).

Sharma, S., Fish, S., & Ekblaw, A. (2021, July). Astronaut-in-the-loop: An iterative design research framework for space environments. *50th International Conference on Environmental Systems*.

Shen, Z. N., Qin, G., Zuo, P., & Wei, F. (2019). Modulation of galactic cosmic rays from helium to nickel in the inner heliosphere. *The Astrophysical Journal*, 887(2), 132.

Smith, J. A., Martz, H. E., & Kallman, J. S. (2011). Case for an improved effective-atomic-number for the electronic baggage scanning program (No. LLNL-TR-520312). Lawrence Livermore National Lab (LLNL), Livermore, CA (United States).

SpaceX. (2021). *Falcon user guide*. Retrieved from https://www.spacex.com/media/falcon-users-guide-2021-09.pdf

Tawara, H., Masukawa, M., Nagamatsu, A., Kitajo, K., Kumagai, H., & Yasuda, N. (2011). Characteristics of Mg2SiO4: Tb (TLD-MSO-S) relevant for space radiation dosimetry. *Radiation Measurements, 46*(8), 709-716.

Thukral, V., van Soestbergen, M., Zaal, J. J. M., Roucou, R., Rongen, R. T. H., Driel, W., & Zhang, G. Q. (2022). Board level vibration test method of components for automotive electronics: State-of-the-art approaches and challenges. *Microelectronics Reliability, 139*, 114830.

Tjus, J. B., & Merten, L. (2020). Closing in on the origin of galactic cosmic rays using multimessenger information. *Physics Reports, 872*, 1-98.

Torque Specifications. (n.d.). Retrieved from https://www.melco-service.com/docs/AMAYA_OS_v10/AMAYA/Torque_Specifications.htm

Tsang, P. Y., Chan, P. M., & Yu, K. N. (2017). Measuring diffuse ultraviolet exposures using Gafchromic EBT3 films. *Results in Physics,* 7, 1492-1493.

Uğur, F. A. (2017). New applications and developments in the neutron shielding. In *EPJ Web of Conferences* (154) p. 01022.

Wan Aasim, W. F. A., AlMazrouei, M., Okasha, M., & Jallad, A. H. (2022, April). The structural analysis of AlainSat-1: An earth observation 3U CubeSat. In *4th Symposium on Space Educational Activities*. Universitat Politècnica de Catalunya.

Wang, X., Li, Y., Qian, Y., Qi, H., Li, J., & Sun, J. (2018). Mechanically robust atomic oxygen-resistant coatings capable of autonomously healing damage in low earth orbit space environment. *Advanced Materials,* 30(36), 1803854.

Webb, D. F., & Howard, T. A. (2012). Coronal mass ejections: Observations. *Living Reviews in Solar Physics, 9*(1), 1-83.

Wender, S. A., O'Donnell, J. M., Zavorka, L., & Bhuva, B. (2020). Measured energy-dependent neutron attenuation through the stacked printed circuit boards. *IEEE Transactions on Nuclear Science*, 67(6), 1114-1117.

Wynn, D. C., & Eckert, C. M. (2017). Perspectives on iteration in design and development. *Research in Engineering Design, 28*, 153-184.

Yadav, N., Singh, M., & Mishra, S. P. (2021). Tissue-equivalent materials used to develop phantoms in radiation dosimetry: A review. *Materials Today: Proceedings*, 47, 7170-7173.

Yamagishi, A., Kawaguchi, Y., Yokobori, S.I., Hashimoto, H., Yano, H., Imai, E., Kodaira, S., Uchihori, Y. and Nakagawa, K. (2018). Environmental data and survival data of Deinococcus aetherius from the exposure facility of the Japan experimental module of the international space station obtained by the Tanpopo mission. *Astrobiology,* 18(11), 1369-1374.

Yanagida, T., Okada, G., Kato, T., Nakauchi, D., & Kawaguchi, N. (2022). A review and future of RPL dosimetry. Radiation Measurements, 158, 106847.

Yasaka, T., & Onoda, J. (2003). *Spacecraft structures*.

Yıldırım, S., Tugrul, A. B., Buyuk, B., & Demir, E. (2016). Gamma attenuation properties of some aluminum alloys. *Acta Physica Polonica A*, *129*(4), 813-815.

Yu, X. X., Lu, H., Chen, G. T., Li, X. Q., Shi, J. K., & Tan, C. M. (2015). Detection of solar neutron events and their theoretical approach. *New Astronomy*, 39, 25-35.

Zakaria, Z., Aziz, M. A., Ishak, N. H., Suppiah, S., Bradley, D. A., & Noor, N. M. (2023). Comparison of effective atomic number, output factor, and glow curve of fabricated Ge-doped optical fibers (FGDOFs) for electron beams dosimetry. *Radiation Physics and Chemistry*, *111012*.

Zakaria, Z., Aziz, M. A., Ishak, N. H., Suppiah, S., Bradley, D. A., & Noor, N. M. (2020). Advanced thermoluminescence dosimetric characterization of fabricated Ge-doped optical fibres (FGDOFs) for electron beams dosimetry. *Radiation Physics and Chemistry*, *166*, 108487.

Zhou, D., Semones, E., O'Sullivan, D., Zapp, N., Weyland, M., Reitz, G., Berger, T. and Benton, E.R. (2010). Radiation measured for MATROSHKA-1 experiment with passive dosimeters. *Acta Astronautica*, 66(1-2), 301-308.

Zhuang, Y., Ural, S. O., & Uchino, K. (2014). Methodology for characterizing loss factors of piezoelectric ceramics. *Ferroelectrics, 470*(1), 260-271.

Zuber, S. H., Hashikin, N. A. A., Yusof, M. F. M., Hashim, R., Zahri, M., & Aziz, A. (2021). Effective atomic number based on energy dispersive X-ray (EDX) analysis and carbon hydrogen nitrogen (CHN) analysis for phantom material in medical physics applications. *Malaysian Journal of Medicine and Health Sciences*, 17(4), 116-121.

## APPENDICES

### Appendix A

**Table A1 All requirements for developing SOFPADS**

| Code/ Subcode | Requirements Type | Justification |
|---|---|---|
| **R1** | **Space radiation monitoring** | |
| R1-1 | CUSOF shall be used for radiation monitoring. | PD of interest |
| R1-2 | TLD-100, TLD-600 and TLD-700 shall be used for comparison. | Commercial TLD for comparison |
| R1-3 | The internal area of the casing shall have multiple areas for placing the PD | To determine the consistency of radiation exposure at different locations |
| R1-4 | Structure covering the PD facing the space should be as thin as possible. | To reduce the attenuation of radiations |
| R1-5 | Holes for TLD placement shall accommodate multiple pieces of the PD. | Easier placement and extraction of TLD during assembly |
| R1-6 | Each type of TLD shall have its own designated compartments. | To balance the number of each type of TLD without having to place them in the same section. |
| R1-7 | One section shall be used to place other types of CUSOF. | To evaluate CUSOF of different types that are not the main CUSOF (Table 3.3). |
| R1-8 | The material for the main casing shall be made of water equivalent material. | Used for dosimetric applications. |
| R1-9 | Consideration for filters shall be made based on radiation attenuation capability. | Radiation attenuation to observe the different energies of the radiations. |
| R1-10 | Consideration for filters shall be made based on mass. | Limitation of the mass of filters due to total mass limitation. |
| R1-11 | Calculations on attenuated radiation energies shall be made. | To estimate the radiation energies received by the PD. |
| | | |
| **R2** | **Space exposure utilising ExHAM** | |
| R2-1 | The overall maximum dimension shall be 100 (+0/-1) mm × 100 | ExHAM's sample size with tolerance added. |

| Code/ Subcode | Requirements Type | Justification |
|---|---|---|
| | (+0/-1) mm × 20 (+0/-2) mm (L×W×H). | |
| R2-2 | The total mass of SOFPADS shall be less than 434 g. | Initial mass limitation lifted by JAXA. |
| R2-3 | Case cover shall be secured onto the main body using a double lock mechanism. | Securement of case cover onto main body. |
| R2-4 | Empty spaces between the filters and the main body shall be occupied. | To secure the filters. |
| R2-5 | Shatterable materials shall be contained using mesh with opening of less than 50 $\mu$m. | Shatterable materials containment. |
| R2-6 | Material used for main body and case cover shall be able to sustain AO environment. | Survivability in space. |
| R2-7 | Material used for main body and case cover shall have strength to sustain damage. | Survivability in space. |
| R2-8 | All corners and edges of the case main body and the case cover shall be rounded with at least radius = 0.75 mm. | To protect crew members from sharp edges during all crew operations. |
| R2-9 | Each section and compartment shall comply to a venting requirement as follows: $\mathrm{MEVR} = \frac{V}{A} = \leq 5080\ \mathrm{cm}$ | Vent holes for depressurisation and pressurisation. |
| R2-10 | Consideration shall be made on method of securement of PD within the dosimeter holder. | To improve the securement of PD. |
| R2-11 | The case shall not be bulging. | Quality control. |
| R2-12 | The screws shall be tightened with a torque value of 10 cNm. | To ensure sufficient tightening of screws to a specified torque. |

## Appendix B

**N of bolts before and after vibration tests**

| **Section** | **Before Test** | **After Test** | **Remark** |
|---|---|---|---|
| A |  |  | No loosening |
| **B** | 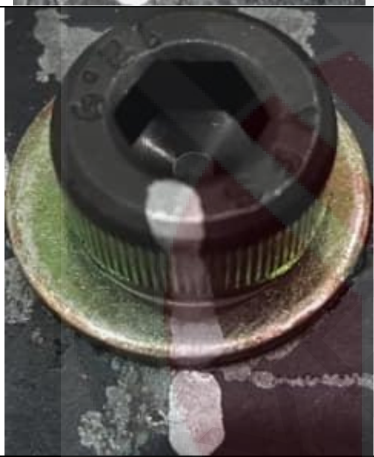 |  | No loosening |
| **C** | 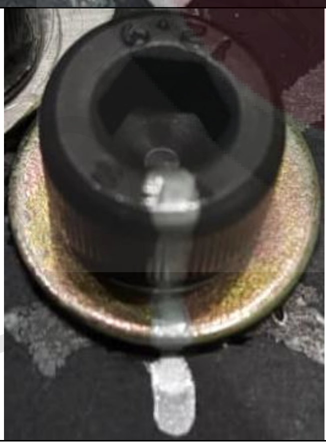 | 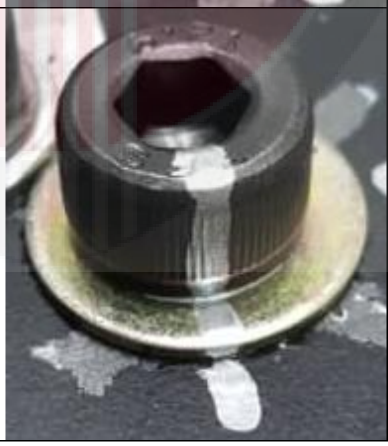 | No loosening |

| Section | Before Test | After Test | Remark |
|---|---|---|---|
| **D** |  | 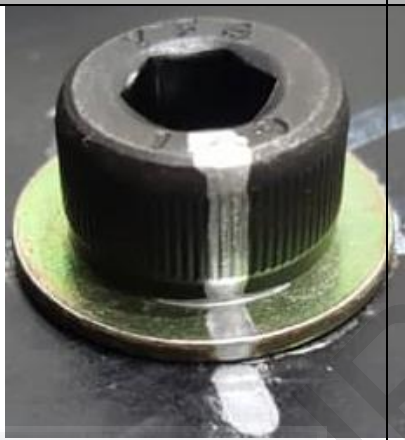 | No loosening |
| **E** |  | 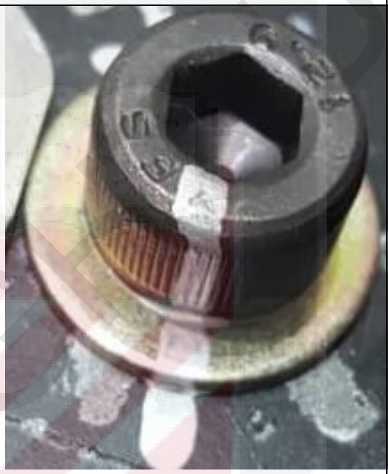 | No loosening |
| **F** | 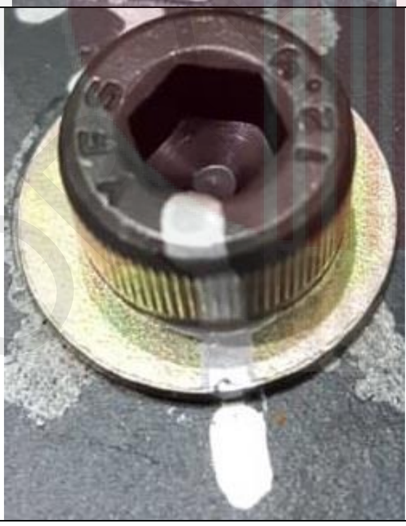 | 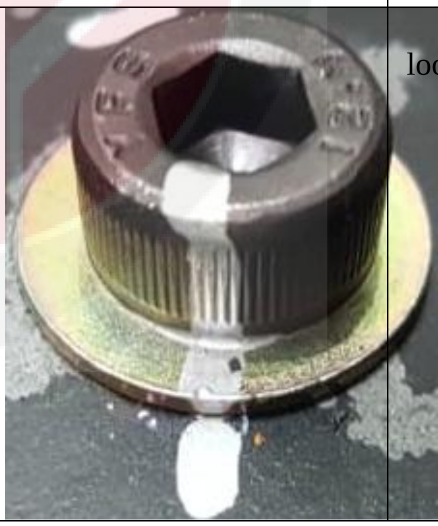 | No loosening |

| Section | Before Test | After Test | Remark |
|---|---|---|---|
| **G** |  |  | No loosening |
| **H** |  |  | No loosening |

## Appendix C

The quality factor (Q) is calculated using method used by Brummit (2010) and Zhuang et al. (2014) as shown in Figure C1.

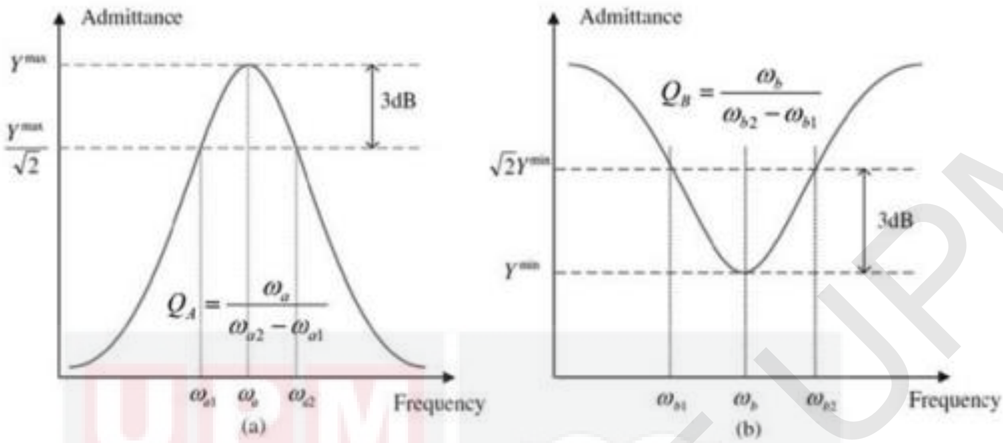


**Figure C1 Q for (a) resonance and (b) antiresonance**

## BIODATA OF STUDENT

Farid Bajuri has a Diploma in Electrical and Computer Engineering (Akita National College of Technology) where he conducted a project in Sound Engineering related field for hearing aid during a loud background noise for his final year project. He also conducted a Sound Engineering related project to detect musical notes for polyphonic musical piece by analysing the overtones of the notes played which was rewarded with a Degree in Electrical and Electronics Engineering (Akita University). He achieved his Masters in Materials Engineering (Universiti Putra Malaysia) where he infused mesoporous silica into kenaf using the impregnation method to strengthen the natural fibre before fabricating the polymer composites. For his PhD, he ventured into the realm of space radiation detection by developing a passive dosimetry casing that carries customised optical fibres fabricated for the purpose of radiation detection.

## LIST OF PUBLICATIONS, CONFERENCE AND PATENT

### Journals

Bajuri, F., Mustafa, S., Hassan, M. F., Dollah, T., Kadir, A. B. A., Tamchek, N., ... & Noor, N. M. (2018). Basic thermoluminescence characteristics of fabricated germanium doped cylindrical optical fibres under low dose particles irradiations. Int. J. Nanoel. and Mat., 11, 169-178.

Bajuri, F., Bradley, D. A., Mustafa, S., Tamchek, N., Saad, F. A., Mazlan, N., & Noor, N. M. (2022). Morphology and thermoluminescence characteristics of customised Ge-doped optical fibre under Am–Be neutron source as a potential to be used for space radiation detector. Radiation Physics and Chemistry, 200, 110378.

### Conference

Bajuri, F., Bradley, D. A., Mustafa, S., Tamchek, N., Saad, F. A., Mazlan, N., & Noor, N. M. (2021). Thermoluminescence characteristics of customised Ge-doped optical fibres (CusOF) under Am-Be neutron source as a potential to be used for space radiation detector. Presented in 15th International Symposium on Radiation Physics (ISRP-15).

### Patent

Bajuri, F., Noor, N. M., Tamchek, N., & Ahmad Saad, F. F. (2019). A System for Housing a Passive Dosimeter. PI2019007076.